



The University of Sheffield

Department of Mechanical Engineering

Towards real-time imaging of strain in soft tissue

Zing Siang Lee

*Submitted for the degree
of
Doctor of Philosophy*

September 2017

Abstract

The study of deformation and strain in soft tissues has always been important in the biomechanics field because it is part of understanding the mechanism on how human body perceives the external or environmental stimulation and also the main cause of superficial injuries or torn soft tissues. In addition, it is particularly challenging to investigate the strain behaviour of the soft tissue undergoing sliding interaction experimentally in real-time due to the limitations of the available measuring equipment. As such, this research introduced a range of high-speed imaging techniques to aim at developing and working towards real-time imaging of deformation and strain in soft tissue.

The imaging techniques used were 3D-digital image correlation (3D-DIC), optical coherence tomography (OCT) and confocal tomography. 3D-DIC was used to find the surface strain profiles of the human skin and also to measure the apparent contact area of the finger pads on a glass plate. OCT was able to measure the roughness profile and the real-to-apparent contact area ratio of the finger pads. Confocal microscopy was used to determine the orientation of the tissue fibres in the porcine aorta before and after the damage was inflicted. Confocal microscopy was not used on the human skin because there were high risks in using this imaging technique on the human skin in vivo tests.

The frictional and the strain behaviour of the finger pad during a sliding interaction with a smooth glass plate are relatable because the normal load has shown to have a linear relationship with the average strain of the contact area in this study. In general, the predominant friction mechanism of the finger pad was adhesion and the edge of the contact area has higher surface strain values than the middle region. It was found that the apparent contact area has a power-law relationship with the normal load and a linear relationship with the shear force during sliding. The roughness profile of the finger pad was influence by the normal load and the sliding state of the finger pad as well. It was found that the moist finger pad had a moisture level similar to the dry finger pad after the acclimatisation period even though the frictional behaviours of the two finger pads were different, highlighting the importance of documentation of water application method.

A batch of homogenous silicone hemi-spheres with different stiffness was manufactured to simulate finger pads. Some silicone hemi-spheres have similar frictional behaviours as the finger pads and the predominant friction mechanism was still adhesion.

Also, the dynamic coefficients of friction of the silicone hemi-spheres were directly proportional (with a negative gradient) to the stiffness of the silicone hemi-spheres. However, the silicone hemi-spheres experienced much higher surface strain than the finger pad during sliding, which is caused by the adhesion hysteresis effect. In addition, it could also be due to the homogenous properties, size and geometry, and the surface roughness of the silicone hemi-spheres. Furthermore, a theoretical strain model was used successfully to predict the strain distribution pattern of a silicone hemi-sphere.

A study on the forearm skin showed that the surface strain and morphological change of human skin are relatable even when performing simple movements.

A study on the porcine aorta tissue fibres found that the damage done on the porcine aorta might have permanently deformed the tissue fibres. It was unsure how the orientation of the tissue fibres changes during the damage application because the confocal microscopy was not able to monitor the tissue fibres orientation in real-time, hence, highlighting the importance of real-time imaging.

Keywords: biotribology, 3D-Digital Image Correlation, Optical Coherence Tomography, friction, surface strain, human skin, soft tissue simulant.

Acknowledgements

I am really happy and grateful that this research has eventually come to fruition after years of hard work and experiments. This journey had been filled with tough challenges. However, the joyful feeling of overcoming one obstacle after another had never been more rewarding, especially writing this final section of the thesis.

First and foremost, I want to express my deepest gratitude and appreciation to my outstanding supervisors, Professor Roger Lewis and Dr Matt Carré, because they have been supporting and guiding me with tremendous patience and encouragement throughout my PhD studies. At near end of my PhD research, it can be summarised that I have learnt a lot from their feedbacks and advice, which improved most of my research skills, for instance, academic writing and oral communication. I would also like to give my thanks to my industrial supervisor, Professor Steve Franklin, who had also been incredibly thoughtful during my time in Philips working on a research project.

Next, I want to give lots of thanks to my colleague and also as my friend, Dr Raman Maiti, who has been helping me with the research and experiments at multiple occasions. This thesis wouldn't be what it is today without his contribution into this research. I think he also served as a lovely guinea pig at some point. It should be noted that no animals were harmed in any way in this research.

I also have a wonderful time with my fellow PhD friends, Diyana, Daniel(s), Almaky, Victor, Rachel, Chris etc., all of whom occasionally get together on Friday night, to be distracted from experiments that had not been working out. Those are the good times!

Finally, I am forever sincerely grateful to my parents, Mr Kek Keong Lee and Mrs Sook Chin Tang, and my first Godparents, Dr Lai and Mrs Lai. Without their unconditional love, sacrifice and strict parenting, I wouldn't be who and where I am now. I also would like to extend my thanks to my mentor, Mr Poh Soon Cheong, who sparked my interests and somehow lured me into studying mechanical engineering.

On a special note, I would like to make thanks for the partial funding from the Mechanical Engineering Department, University of Sheffield for this research.

A BIG thank you for ALL!

List of figures

Figure 1-1, Workflow of the imaging techniques used on the experimental set-ups8

Figure 2-1, Structure of human skin (<http://histologyolm.stevegallik.org/node/353>) 14

Figure 2-2, The rearrangement of collagen fibres undergoing a tensile test (Holzapfel, 2000) 14

Figure 2-3, Roughness and thickness of the human skin at the front body site (Maiti, 2017) 15

Figure 2-4, Roughness and thickness of the human skin at the back body site (Maiti, 2017).16

Figure 2-5, Structure of porcine aorta (Tsamis et al., 2013)..... 18

Figure 2-6, Illustration of collagen and elastin fibres
(https://www.boundless.com/biology/textbooks/boundless-biology-textbook/the-animal-body-basic-form-and-function-33/animal-primary-tissues-193/connective-tissues-loose-fibrous-and-cartilage-738-11968/images/fig-ch33_02_06/) 20

Figure 2-7, Schematic of a single ridge in contact with the finger pad, which N is the applied normal force, θ is the angle of the ridge, t is the distance from the centre line of the ridge, a is the largest distance from the centre line to contact of the ridge with the skin, p is the pressure along the contact area of the ridge and skin, dl is the length of the contact area, W is the resultant force due to the applied pressure and $F_{hysteresis}$ is the deformation force (Tomlinson et al., 2011a).....25

Figure 2-8, Two-part relationship between friction force and normal load (Tomlinson et al., 2009) 27

Figure 2-9, 'Bell curve' behaviour of the coefficient of friction when water was added and removed from the human skin (Adams et al., 2007).....29

Figure 2-10, The ink stamping method (Liu et al., 2017).....31

Figure 2-11, Image of finger pad using OCT and the scanned skin region (Liu et al., 2017) .32

Figure 2-12, The relationship between contact area and normal force (Tomlinson, 2009).....32

Figure 2-13, Sliding of a spherical indenter along human skin– near point loading (Kwiatkowska et al., 2009) 35

Figure 2-14, Line loading of different bar width on human skin (Johnson & Phillips, 1981) 36

Figure 2-15, Experimental work (top) and theoretical model (bottom) of a finger pad partial slipped against flat smooth glass (Delhaye et al., 2016).....36

Figure 2-16, Shear strain data along the epidermal to dermal tissue, obtained from DIC (Gerhardt et al., 2012) 36

Figure 2-17, Tensile test on human skin - dead (Jacquomond et al., 2007)40

Figure 2-18, Full field strain of the elbow joint (Obropta & Newman, 2015)41

Figure 2-19, OCT image: finger pad skin in contact with smooth glass plate (Liu et al., 2013)41

Figure 3-1, Stereo DIC set-up.....48

Figure 3-2, Working principal of DIC - The tracking of the “blue box” subset (left), the region of subsets will eventually form a field of displacement vectors, “red arrows”, that will be used for strain computation (right)48

Figure 3-3, The size of the speckles using different speckle application methods (on a silicone hemi-sphere).....50

Figure 3-4, Stereo camera set-up terminology.....	51
Figure 3-5, Calibration grid (11*10 dots with 2mm space between each dots) with three distinctive hollow marker dots (left) Calibration score (right)	52
Figure 3-6, Area of interest selected	54
Figure 3-7, Selected subset size within the area of interest (a) 41×41 pixels (b) 81×81 pixels	54
Figure 3-8, The first principal strain of a silicone hemi-sphere (Chapter 6)	55
Figure 3-9, Working principal of an OCT system (Liu, 2013)	58
Figure 3-10, Illustration of A-scan, B-scan and C-scan (Kraus, et al., 2012).....	58
Figure 3-11, Vivosight OCT set-up	59
Figure 3-12, Removing the probe standoff	59
Figure 3-13, Procedure for determining the epidermis thickness (a) the boundary line detection for stratum corneum (yellow line) and dermal-epidermal junction (green line) (b) thickness determination of epidermis (in pixels) based on skin layers detection	60
Figure 3-14, Extracting the roughness (red lines) from topographical skin profiles (blue lines) of (a) stratum corneum and (b) dermal-epidermal junction	63
Figure 3-15, The structure of standard confocal microscopy (Rossetti et al., 2013).....	64
Figure 3-16, Outcome of Fiji – directionality image analysis of one image	66
Figure 3-17, Outcome of Fiji – directionality image analysis of a group of images (Z-stacked scan)	66
Figure 3-18, The orientation map of the outcomes.....	67
Figure 4-1, Illustration of the finger pad sliding experiment set-up	70
Figure 4-2, Finger holding rig.....	71
Figure 4-3, OCT images obtained for a finger in contact with different types of grooves.....	71
Figure 4-4, Timeline of the moisture measurement of (a) OCT and (b) DIC test	73
Figure 4-5, The stiffness experiment set-up	74
Figure 4-6, The relative position between the flat plate and finger pad	74
Figure 4-7, Illustration of friction experiment set-up with 3D-DIC	76
Figure 4-8, Finger pad with speckles	76
Figure 4-9, Illustration of (a) the deformed finger pad with slices and (b) a slice of position graph of deformed shape of the finger pad in contact with glass plate.....	77
Figure 4-10, The process of finding the boundary points from Z position graph (differentiations and filtration).....	77
Figure 4-11, The ellipse best fit of the boundary points of the contact area.....	78
Figure 4-12, Experimental set-up using OCT	79
Figure 4-13, Scanning positions of the OCT on the finger pad	79
Figure 4-14, Illustration of the finger pad loaded against a glass plate	80
Figure 4-15, (a) Force-displacement graph of the finger pads and (b) stiffness vs normal load graph using polynomial equation relationship	81
Figure 4-16, (a) Force-displacement graph of the finger pads and (b) stiffness vs normal force graph using power equation relationship	81
Figure 4-17, Force vs time graph of the finger pad in natural state loaded at 3N during the whole sliding interaction (3D-DIC)	82

Figure 4-18, The relationship between the dynamic apparent contact area, friction force and the moisture level of the soaked finger pad before the sliding test with DIC.....	86
Figure 4-19, The relationship between the dynamic apparent contact area, friction force and the moisture level of the soaked finger pad before the sliding test with OCT.....	86
Figure 4-20, (a) Friction force against normal load with the dynamic coefficient of friction (COF) against (b) normal load and (c) the stiffness of the finger pad.....	87
Figure 4-21, An illustration of the position reference axis (global) of the finger pad and the sliding direction of the plate.....	88
Figure 4-22, DIC result of the natural finger pad loaded at 0.5N with the respective strains 1 st principal strain E_1 , 2 nd principal strain E_2 and shear strain E_{xy}	89
Figure 4-23 Illustration of finger pad from top view.....	91
Figure 4-24, First principal strain E_1 of the natural finger pad obtained along y axis in the (a) static and (b) dynamic state, second principal strain E_2 of the natural finger pad obtained along y axis in the (c) static and (d) dynamic state, and the geometrical shape of the finger pad along y axis in the (e) static and (f) dynamic state.....	91
Figure 4-25, Average first principal strain E_1 strain within the contact area of the finger pad from (a) static to (b) dynamic state, and average second principal strain E_2 strain within the contact area of the finger pad from (c) static to (d) dynamic state when plotted against the normal load applied on the finger pads.....	92
Figure 4-26, Average first principal strain E_1 strain within the contact area of the finger pad from (a) static to (b) dynamic state, and average second principal strain E_2 strain within the contact area of the finger pad from (c) static to (d) dynamic state when plotted against the stiffness of the finger pads.....	93
Figure 4-27, The relationship between the apparent contact area, moisture level of the finger pad and the normal load applied in (a) the static state and (b) the dynamic state.....	94
Figure 4-28, The relationship between the shear force and the apparent contact area of the finger pads in the dynamic state.....	94
Figure 4-29, The change of the ratio of the real against apparent contact area of the finger pad from the static state to the dynamic state with the normal load.....	95
Figure 4-30, The mean roughness, Ra, and mean roughness depth, Rz, against the normal load.....	96
Figure 4-31, OCT images of position 2 of the natural finger pad.....	97
Figure 4-32, Sliding finger pad across different grooves.....	100
Figure 4-33, Dynamic coefficient of friction against normal load of the natural and soaked finger pad.....	102
Figure 4-34, Moisture changes of the finger pad.....	106
Figure 4-35, The force-displacement graphs of the finger pads in a natural state and soaked condition using (a) a polynomial equation fit and (b) a power equation fit, which includes the data points in high normal load application.....	107
Figure 4-36, Illustration of the roughness distribution within the contact area of the finger pad.....	112
Figure 4-37, The dynamic coefficient of friction against the mean roughness graph when the finger pad was sliding.....	112

Figure 5-1, Front view (top) and side view (bottom) of the sliding experiment set-up of the silicone hemi-sphere	117
Figure 5-2, Illustration of the stiffness experiment set-up on silicone hemi-sphere.....	118
Figure 5-3, Deformed shape of the silicone hemi-sphere in contact with glass plate from DIC position data and the cross section Z-position graph	120
Figure 5-4, The process of finding the boundary points (differentiations and filtration) from the 45 th cross section Z-position graph	120
Figure 5-5, Ellipse "best-fit" on the determined DIC position data from Matlab code	120
Figure 5-6, (a) Force-displacement graph of the silicone hemi-spheres and (b) stiffness vs normal load graph using polynomial equation relationship.....	122
Figure 5-7, Force-displacement graph of the silicone hemi-spheres using power equation fit	122
Figure 5-8, Illustration of the bending mechanism of the glass plate	124
Figure 5-9, Graph of dynamic coefficient of friction against (a) normal force and (b) stiffness of all 4 silicone hemi-spheres.....	125
Figure 5-10, DIC results of the silicone hemi-sphere of 0% deadener at 0.5N with the respective strains 1st principal strain E_1 , 2nd principal strain E_2 and shear strain E_{xy}	126
Figure 5-11, The top view of silicone hemi-sphere that illustrates the position reference axis x and y with the hint of sliding direction of the glass plate	129
Figure 5-12, First principal strain E_1 of a silicone hemi-sphere obtained along y axis in the (a) static and (b) dynamic state, second principal strain E_2 in the (c) static and (d) dynamic state, and the geometrical shape of a silicone hemi-sphere along y axis in the (e) static and (f) dynamic state	130
Figure 5-13, Average first principal strain E_1 strain within the contact area of all 4 silicone hemi-spheres from (a) static to (b) dynamic state, and average second principal strain E_2 strain within the contact area of the finger pad from (c) static to (d) dynamic state when plotted against the normal load applied of the silicone hemi-spheres.....	131
Figure 5-14, Average first principal strain E_1 strain within the contact area of all 4 silicone hemi-spheres from (a) static to (b) dynamic state, and average second principal strain E_2 strain within the contact area of the finger pad from (c) static to (d) dynamic state when plotted against the stiffness of the silicone hemi-spheres ..	132
Figure 5-15, The apparent contact area of silicone hemi-sphere in (a) static and (b) dynamic state	133
Figure 5-16, The relationship between the shear force and the apparent contact area of the silicone hemi-spheres	134
Figure 5-17, Dynamic coefficient of friction with respective to the normal load for of the silicone hemi-spheres and the finger pads	143
Figure 5-18, The stiffness profile and the respective frictional behaviour of the silicone hemi-spheres and the finger pads	143
Figure 5-19, The average E_1 strain with respective to the normal load for both the silicone hemi-spheres and the finger pads.....	143

Figure 5-20, Apparent contact area with respective to the normal load of the silicone hemispheres and the finger pads from the static state to the dynamic state.....	144
Figure 5-21, The shear force against the apparent contact area of the silicone hemispheres and the finger pads in the dynamic state (from DIC tests only)	144
Figure 6-1, The top view of silicone hemi-sphere that illustrates the position reference axis x and y with the hint of sliding direction of the glass plate	149
Figure 6-2, Comparison of strain distribution profile between DIC data and the numerical modelling	151
Figure 6-3, Sensitivity test of input parameters: normal force, Young's modulus and coefficient of friction of E_{xx}	152
Figure 6-4, Sensitivity test of input parameters: normal force, Young's modulus and coefficient of friction of E_{yy}	153
Figure 7-1, (a) The forearm with the spray pattern shown along with superimposed X-Y coordinate system defined for surface strain measurements, (b) 3D-DIC set-up showing the positioning of the cameras relative to the forearm position	159
Figure 7-2: (a) OCT set-up, (b) Schematic of volar forearm: regions of interest and scan dimensions	160
Figure 7-3: Contour plot of the skin surface strain field (E_{yy}) at (a) 90° (natural strain) and (b) induced strain through full extension at 180° arm angle	161
Figure 7-4: OCT images of unstretched skin (90 flexion - top) and stretched forearm skin (180 full extension - bottom), which the qualitatively smoothing of skin surface (stratum corneum) and flattening of dermal-epidermal junction can be observed.	162
Figure 7-5: Box plot of epidermal thickness measured before and after stretching at 90° and 180°. The boxplots are made out of thickness value of in total up to 600 images, each which contains 1342 individual thickness values.	163
Figure 8-1, Front view of the experimental set-up	171
Figure 8-2, Top view and front view of the experimental set-up	173
Figure 8-3, Timeline of 8 separate Z-stacked scanning.....	173
Figure 8-4, The actual experimental set-up	173
Figure 8-5, Outcome of Fiji – directionality image analysis of the Z-stacked images.....	173
Figure 8-6, Undamaged directionality histogram for Set 3 Experiment (0.5N, 1 pass)	175
Figure 8-7, Damaged directionality histogram for Set 3 Experiment at 1.88 minute after catheterisation process (0.5N, 1 pass).....	176
Figure 8-8, Damaged directionality histogram for Set 3 Experiment at 15 minutes after catheterisation process (0.5N, 1 pass).....	176
Figure 8-9, Undamaged directionality histogram for Set 1 Experiment (2.0N, 1 pass)	177
Figure 8-10, Damaged directionality histogram for Set 1 Experiment at 1.88 minutes after catheterisation process (2.0N, 1 pass).....	177
Figure 8-11, Damaged directionality histogram for Set 1 Experiment at 15 minutes after catheterisation process (2.0N, 1 pass).....	178
Figure 8-12, Undamaged directionality histogram for Set 1 Experiment (5.0N, 1 pass)	178
Figure 8-13, Damaged directionality histogram for Set 1 Experiment at 1.88 minutes after catheterisation process (5.0N, 1 pass).....	179

Figure 8-14, Damaged directionality histogram for Set 1 Experiment at 15 minutes after catheterisation process (5.0N, 1 pass).....	179
Figure 8-15, Comparison of mean directionality angle of 5 sets of experiments for case 1: 0.5N, 1 pass.....	180
Figure 8-16, The stained porcine aorta sample that is cut open to investigate the depth of Eosin B stain	183
Figure 8-17, The detailed structure of the layers of porcine aorta (Tsamis et al., 2013).....	184
Figure 8-18, (a) The endothelial cells stained with Eosin B imaged using standard confocal microscopy (b) The endothelial cells were magnified	184
Figure 9-1, OCT image of finger pad, plastic glass and water layer	190
Figure A-1, Illustration of tractions on the circular contact region (Johnson, 2004).....	216
Figure B-1, a “.txt” file that has the three axial coordinates for the shape of a silicone hemi-sphere	219
Figure B-2, Importing ".txt" file into Matlab.....	220
Figure B-3, The process of finding the 2 boundary points from the 33 th cross section of the silicone hemi-sphere	220
Figure C-1, Surface strains of the dry finger pad along x axis	223
Figure C-2, Surface strains of the dry finger pad along y axis	224
Figure C-3, Surface strains of the moist finger pad along x axis.....	225
Figure C-4, Surface strains of the moist finger pad along y axis.....	226
Figure E-1, OCT images of position 1 of the natural finger pad	230
Figure E-2, OCT images of position 1 of the natural finger pad	231
Figure E-3, OCT images of position 1 of the soaked finger pad	232
Figure E-4, OCT images of position 2 of the soaked finger pad	233
Figure F-1, Strain line profile of silicone hemi-sphere with 0% deadener along x axis.....	234
Figure F-2, Strain line profile of silicone hemi-sphere with 0% deadener along y axis.....	235
Figure F-3, Strain line profile of silicone hemi-sphere with 10% deadener along x axis.....	236
Figure F-4, Strain line profile of silicone hemi-sphere with 10% deadener along y axis.....	237
Figure F-5, Strain line profile of silicone hemi-sphere with 15% deadener along x axis.....	238
Figure F-6, Strain line profile of silicone hemi-sphere with 15% deadener along y axis.....	239
Figure F-7, Strain line profile of silicone hemi-sphere with 20% deadener along x axis.....	240
Figure F-8, Strain line profile of silicone hemi-sphere with 20% deadener along y axis.....	241
Figure G-1, Comparison of mean directionality angle of 5 sets of experiments for case 1: 0.5N, 1 pass.....	242
Figure G-2, Comparison of mean directionality angle of 5 sets of experiments for case 2: 0.5N, 5 passes.....	242
Figure G-3, Comparison of mean directionality angle of 5 sets of experiments for case 3: 0.5N, 10 passes.....	243
Figure G-4, Comparison of mean directionality angle of 5 sets of experiments for case 4: 2N, 1 pass.....	243
Figure G-5, Comparison of mean directionality angle of 5 sets of experiments for case 5: 2N, 5 passes	244

Figure G-6, Comparison of mean directionality angle of 5 sets of experiments for case 6: 2N, 10 passes	244
Figure G-7, Comparison of mean directionality angle of 4 sets of experiments for case 7: 5N, 1 pass.....	245
Figure G-8, Comparison of mean directionality angle of 4 sets of experiments for case 8: 5N, 5 passes	245
Figure G-9, Comparison of mean directionality angle of 3 sets of experiments for case 9: 5N, 10 passes	246

List of tables

Table 2-1, Young’s Modulus of elasticity for skin reported in literature	17
Table 2-2, Elastic modulus of human aorta reported in literature	19
Table 3-1, The amount of arginine, histidine and lysine in pig collagen, pig elastin and aortic wall represented as the number of residues per 1000 amino acids [n/1000] (Zeeman et al., 1998)	65
Table 4-1, Instantaneous normal force at state 1 (static) and state 2 (dynamic) of finger pad 83	
Table 4-2, Moisture level of the stratum corneum of the finger pads in natural state or soaked condition in stiffness, 3D-DIC and OCT tests	85
Table 5-1, The instantaneous normal force at state 1 (static) and state 2 (dynamic).....	124
Table 6-1, Input parameters for the numerical modelling	149
Table 6-2, Root mean square error (RMSE) of the numerical strain model.....	154
Table 7-1, Mean skin surface strains at full arm extension at 180. The values listed are mean values of 5 repeated experiments, in each of which 3 stationary images were analysed from which an average strain or area was calculated.....	161
Table 7-2, Roughness parameters of stratum corneum at 90° flexion and 180° full extension. Data determined from 30 images are shown as means ± 1S.D.....	163
Table 7-3, Roughness parameters of dermal-epidermal junction at 90° flexion and 180° full extension. Data determined from 30 images are shown as means ± 1S.D.	163
Table 8-1, Recovery progress based on the amount of mean directionality angle change	181
Table 8-2, Amount of mean directionality angle change at T ₀ with respect to T _{undamaged}	181
Table 8-3, Amount of mean directionality angle change at T ₄ with respect to T _{undamaged}	182
Table 8-4, Amount of mean directionality angle change at T ₇ with respect to T _{undamaged}	182
Table D-1, Moisture level of the natural finger pad during stiffness test	227
Table D-2, Moisture level of the soaked finger pad during stiffness test	227
Table D-3, Moisture level of the natural finger pad during 3D-DIC sliding experiment.....	227
Table D-4, Moisture level of the soaked finger pad during 3D-DIC sliding experiment.....	228
Table D-5, Moisture level of the natural finger pad during OCT sliding experiment	229
Table D-6, Moisture level of the soaked finger pad during OCT sliding experiment	229
Table E-1, The roughness of the position 1 and position 2 of natural finger pad.....	231
Table E-2, The roughness of the position 1 and 2 of soaked finger pad.....	233

Glossary

Collagen fibres	A type of protein fibre
Elastase	A pancreatic enzyme that digests elastin
Elastin fibres	A type of protein fibre
Endothelium	The tissue which forms a single layer of cells lining various organs and cavities of the body
Eosin B	A type of fluorescent dye for microscopy imaging
Pathogen	A bacterium, virus or other microorganism that can cause disease
Stratum corneum	The outermost layer of skin
Stratum lucidum	A thin, clear layer of dead skin cells in the epidermis
Stratum granulosum	A thin layer of cells in the epidermis
Stratum spinosum	A layer of epidermis
Stratum basale	Deepest layer of the five layers of epidermis
Squamous epithelium	A single layer of flat cells in contact with the epithelium
Tunica intima	The innermost layer of an artery or vein
Tunica media	The middle layer of an artery or vein
Tunica adventitia	The outermost layer of an artery or vein
Histidine	An α -amino acid that is used in the biosynthesis of proteins
Lysine	An α -amino acid that is used in the biosynthesis of proteins
Arginine	An α -amino acid that is used in the biosynthesis of proteins

Abbreviations

3D-DIC	3D-Digital Image Correlation
AU	Arbitrary Unites
CCD	Charge-Coupled Device
CM	Confocal Microscopy
COF	Coefficient of friction
DEj	Dermal-Epidermal Junction
DIC	Digital Image Correlation
JKR	Johnson-Kendall-Roberts
OCT	Optical Coherence Tomography
PMT	Photomultiplier Tube
RMSE	Root Mean Square Error
SC	Stratum Corneum
SD	Standard Deviation

Nomenclature

A	Apparent contact area [m ²]
A_{real}	Real contact area [m ²]
a	Radius of the circular contact area [m]
b	A contact area specific exponent
C_i	the right Cauchy-Green deformation tensor,
D	A unit distance
E	Reduced Young's modulus [Nm ⁻²]
E_{skin}	Young's modulus of skin [Nm ⁻²]
$E_{substance}$	Young's modulus of counter-face substance [Nm ⁻²]
E	Strain tensor
E_{xx}	Green-Lagrange strain in x direction
E_{yy}	Green-Lagrange strain in y direction
E_{xy}	Green-Lagrange shear strain
E_1	First principal strain
E_2	Second principal strain
E_i	Green-Lagrange strain tensor
F	Resultant friction force [N]
$F_{adhesion}$	Friction force caused by adhesion mechanism [N]
$F_{deformation}$	Friction force caused by deformation mechanism [N]
$F_{hysteresis}$	Friction force caused by deformation hysteresis mechanism [N]
$F_{interlocking}$	Friction force caused by interlocking mechanism [N]
G	The bulk modulus
h_{ridge}	The height of the ridge
I	the unit matrix
k	A contact area specific constant
m	A contact area specific constant
N	Normal load [N]
N_{max}	The normal load at which the deformation reaches a maximum
n	The number of ridges
n	A normal load specific exponent
n	The sample length (total image pixel number)
P	The normal load [N]
$p(\xi, \eta)$	The nominal pressure [Nm ⁻²]
q_0	The mean traction [N]
$q_x(r)$	The Hertzian surface tangential traction profile
R	Radius of the spherical probe [m]
r	The radial position on the contact area of the traction profile [m]
Ra	Mean surface roughness [μm]
Rz	Mean maximum height of the topographical profile [μm]

Rt	the maximum profile height [μm]
Rt_i	the maximum profile height Rt for the i^{th} sampling length [μm]
$R_{\text{real-to-apparent}}$	Real-to-apparent contact area ratio
S	A closed area in contact [m^2]
u_x	Displacement in x direction [m]
u_y	Displacement in y direction [m]
\bar{u}_x	Surface displacement in x direction [m]
\bar{u}_y	Surface displacement in y direction [m]
W	Elastic work done [W]
$W_{\text{lost per unit distance}}$	Work lost per unit distance [W]
y_i	the vertical pixel distance from the mean line to the i^{th} data or image pixel point
ν_{skin}	Poisson's ratio of the skin
$\nu_{\text{substance}}$	Poisson's ratio of the counter-face substance
β	The viscoelastic hysteresis loss fraction
τ	Interfacial shear stress [Nm^{-2}]
α	Constant fraction of the lost input elastic energy
α	The pressure coefficient
$\lambda_{1,2}$	The eigenvalues of matrix E that is called the principal strains
λ	Eigenvalues in the strain matrix
λ	The distance between each ridge [m]
μ	Dynamic coefficient of friction
μ_{adhesion}	Dynamic coefficient of friction caused by adhesion mechanism
θ	The angular position of the radial position r on the contact area
$\psi, \psi_1,$ F, G, H, F_1, G_1, H_1	The potential functions

Table of Contents

Towards real-time imaging of strain in soft tissue.....	1
Abstract.....	i
Acknowledgements.....	iii
List of figures.....	iv
List of tables.....	xi
Glossary.....	xii
Abbreviations.....	xiii
Nomenclature.....	xiv
Table of Contents.....	xvi
Chapter 1 Introduction.....	1
1.1 Introduction.....	1
1.2 Deformation, strain and damage on human body.....	2
1.3 Real-time imaging.....	3
1.4 Imaging in biomechanics.....	4
1.5 Imaging in biotribology.....	5
1.6 Motivation of research.....	5
1.7 Aim and objectives.....	5
1.8 Workflow.....	6
1.9 Research contribution and limitations.....	8
1.10 Structure of the thesis.....	8
Chapter 2 Literature Review.....	11
2.1 Introduction.....	11
2.2 Soft tissues and their morphology.....	12
2.2.1 Human skin.....	12
2.2.2 Aorta.....	17
2.2.3 Collagen and Elastin.....	19
2.3 Frictional behaviour of human skin.....	20
2.3.1 Adhesion.....	21
2.3.2 Hysteresis.....	22
2.3.3 Interlocking.....	23
2.4 Parameters affecting friction.....	25

2.4.1	Normal load	25
2.4.2	Skin hydration	27
2.4.3	Contact area	29
2.5	Strain behaviour of soft tissue	33
2.5.1	Non-contact type	33
2.5.2	Contact type	34
2.6	Strain assessment methods of soft tissues	37
2.6.1	Mechanical tests	37
2.6.2	Imaging techniques	38
2.6.3	Skin modelling	41
2.7	Soft tissue stimulants	42
2.8	Summary	43
Chapter 3	Imaging Equipment Set-up	46
3.1	Introduction	46
3.2	Three-Dimensional Digital Image Correlation (3D-DIC)	47
3.2.1	System Overview	47
3.2.2	Sample preparation	48
3.2.3	Camera set-up	50
3.2.4	Calibration	51
3.2.5	Data Collection	53
3.2.6	Image Correlation	53
3.2.7	Strain Analysis	55
3.2.8	Post-processing	56
3.3	Optical Coherence Tomography	57
3.3.1	System overview and set-up	57
3.3.2	OCT image analysis	59
3.4	Confocal microscopy	63
3.4.1	System overview	63
3.4.2	Eosin B and Amino Acid Composition of Porcine Aorta	64
3.4.3	Image Analysis Using Fiji (Directionality Plugin)	65
Chapter 4	Interaction between finger pad and transparent glass plate	68
4.1	Introduction	68
4.2	Aim and objectives	69

4.3	Methodology	69
4.3.1	Friction test set-up.....	69
4.3.2	Water application to make a soaked finger pad.....	72
4.3.3	Stiffness test.....	73
4.3.4	3D-DIC camera set-up, calibration and data acquisition.....	74
4.3.5	Apparent contact area	76
4.3.6	Optical Coherence Tomography	78
4.3.7	Real to apparent contact area ratio.....	79
4.4	Results	80
4.4.1	Stiffness of the a natural and a soaked finger pad	80
4.4.2	Force behaviour before, during and after sliding.....	81
4.4.3	Moisture level of the finger pad.....	83
4.4.4	The influence of normal force and stiffness on the dynamic coefficient of friction 86	
4.4.5	General strain and deformation behaviour.....	88
4.4.5.1	First principal strain, E_1	88
4.4.5.2	Second principal strain, E_2	88
4.4.5.3	Shear strain, E_{xy}	88
4.4.6	The effect of normal load and the stiffness of the finger pad on the strain behaviour	89
4.4.6.1	First principal strain, E_1	90
4.4.6.2	Second principal strain, E_2	90
4.4.7	Apparent contact area of the finger pad.....	93
4.4.8	Real to apparent contact area ratio of the finger pad	94
4.4.9	Roughness of the finger pad	95
4.4.10	Morphological change of finger pad against grooved plate during sliding	97
4.5	Discussion	100
4.5.1	Relationship between the frictional and the strain behaviour of finger pad	100
4.5.2	Moisture level in human skin.....	102
4.5.3	Force-displacement relationship of the finger pads	106
4.5.4	Effect of stiffness on dynamic coefficient of friction of finger pad	107
4.5.5	Contact area of the finger pad.....	108
4.5.6	Roughness of the finger pad ridges.....	110

4.5.7	Feasibility of OCT in studying finger pad – grooved plated interaction	112
4.6	Conclusions	113
Chapter 5	Interactions between silicone hemi-spheres and glass.....	115
5.1	Introduction	115
5.2	Aim and objectives.....	116
5.3	Methodology	116
5.3.1	Manufacture of silicone hemi-sphere specimens.....	116
5.3.2	Experimental set-up for the sliding interaction.....	116
5.3.3	Stiffness test.....	118
5.3.4	DIC camera set-up, calibration and data acquisition	118
5.3.5	Determining the apparent contact area	119
5.4	Results	121
5.4.1	Stiffness of the silicone hemi-spheres.....	121
5.4.2	Friction force behaviour before, during and after.....	122
5.4.3	The influence of normal force and stiffness on the dynamic coefficient of friction 125	
5.4.4	General strain and deformation behaviour.....	125
5.4.5	The effect of normal load and the stiffness of silicone hemi-sphere on the strain behaviour	127
5.4.5.1	First principal strain, E_1	127
5.4.5.2	Second principal strain, E_2	128
5.4.6	Contact area	132
5.5	Discussion	134
5.5.1	Relationship between the frictional and strain behaviour of silicone hemi-spheres 134	
5.5.2	Significance of stiffness test	137
5.5.3	Contact area of silicone hemi-sphere in both static and dynamic states.....	138
5.5.4	The comparison between the finger pads and silicone hemi-spheres	140
5.5.5	Robustness of using 3D DIC on highly deformable material interaction.....	144
5.6	Conclusions	145
Chapter 6	Theoretical model – surface strain on silicone hemi-spheres	146
6.1	Introduction	146
6.2	Aim and objectives.....	147
6.3	Methodology	147

6.4	Results	150
6.4.1	Strain field profile of the silicone hemi-sphere.....	150
6.5	Discussion	154
6.5.1	The feasibility of the theoretical strain model	154
6.6	Conclusions	156
Chapter 7	Natural strain of forearm skin at different postures.....	157
7.1	Introduction	157
7.2	Aim and objectives.....	158
7.3	Methodology and Experimental Set-up.....	158
7.3.1	Test subjects.....	158
7.3.2	Stereo Digital Image Correlation (DIC) set-up.....	158
7.3.3	Optical Coherence Tomography (OCT) set-up.....	159
7.4	Results	160
7.4.1	Surface strain behaviour of the forearm skin based on DIC data	160
7.4.2	The sub-surface change of the forearm skin based on OCT images.....	161
7.5	Discussion	163
7.5.1	Skin surface strains and epidermal thickness change	163
7.5.2	Skin topography and dermal epidermal junction geometry and undulation change	165
7.6	Conclusions	167
Chapter 8	Disorientation of aortic tissue fibres subjected to different loads.....	169
8.1	Introduction	169
8.2	Aim and objectives.....	170
8.3	Methodology and experimental set-up.....	170
8.3.1	Preparation of Porcine Aorta	170
8.3.2	Imaging using confocal microscopy	170
8.4	Results	174
8.4.1	Directionality histogram of Z-stacked scan	174
8.4.2	Unique pattern of directionality histogram of each case	174
8.4.3	Inability of aortic wall tissue fibre to recover to undamaged state	174
8.4.4	Comparison of mean directionality angle of each set.....	179
8.4.5	Recovery progress of tissue fibres based on the direction angle difference ($\theta_{\text{undamaged}} - \theta_{\text{Tn}}$) for each case	180
8.5	Discussion	182

8.5.1	Suitability of Eosin B in Imaging Surface or Subsurface of Porcine Aorta	182
8.5.2	Recovery of aortic wall tissue fibre	184
8.5.3	Real-time monitoring of porcine aorta tissue fibres	185
8.6	Conclusions	186
Chapter 9	Discussion	188
9.1	Introduction	188
9.2	A summary of real-time imaging techniques in studying the deformation of soft tissues 189	
9.2.1	3D-Digital Image Correlation (DIC)	190
9.2.2	Optical Coherence Tomography (OCT)	191
9.2.3	Confocal microscopy	191
9.3	From human skin to soft tissue simulant to theoretical model.....	192
9.4	Strain study of soft tissue	193
Chapter 10	Conclusions and Future work.....	196
10.1	Introduction	196
10.2	Conclusions	197
10.2.1	Real-time imaging techniques.....	197
10.2.1.1	3D-Digital Image Correlation.....	197
10.2.1.2	Optical Coherence Tomography.....	197
10.2.1.3	Confocal microscopy	197
10.2.2	Frictional behaviour, strain behaviour, morphological changes and surface moisture changes of finger pad with tribological interactions	198
10.2.3	Frictional behaviour and strain behaviour of silicone hemi-sphere with tribological interactions and its theoretical modelling	198
10.2.4	Strain behaviour and morphological changes of forearm movement without tribological interactions	200
10.2.5	Deformation of porcine aorta tissue fibres due to catheterisation damage	200
10.3	Future work	200
10.3.1	Real-time imaging techniques.....	200
10.3.1.1	3D-Digital Image Correlation.....	200
10.3.1.2	Optical Coherence Tomography.....	200
10.3.1.3	Confocal microscopy	201
10.3.2	Frictional and strain behaviours of finger pads and silicone hemi-spheres	201

10.3.3	Theoretical strain model of the silicone hemi-sphere	201
10.3.4	Morphological change of finger pad.....	202
10.3.5	Moisture level of the finger pad.....	202
10.3.6	Contact area measuring method.....	202
References.....		203
Appendix A:	Derivation of the theoretical strain model.....	215
Appendix B:	Measuring the apparent contact area from 3D-DIC data	219
Appendix C:	Strain line profile of the finger pads.....	223
Appendix D:	The moisture levels of the finger pads at different tests	227
Appendix E:	Roughness profiles of the finger pads	230
Appendix F:	Strain line profiles of the silicone hemi-spheres.....	234
Appendix G:	Temporal evolution of the orientation of the porcine aorta tissue fibres .	242

Chapter 1

Introduction

1.1 Introduction

There is almost nothing in the world that does not require human interaction. From common actions such as people interacting with electronic devices that have touch screen to surgeons handling surgical blades that require absolute precision. This study could help understand and improve humans' comfort and ease of use during interaction with various applications that require gripping, manipulation and holding. Human skin would deform to grip or hold objects. In order to visualise deformation and strain, various real-time imaging systems are explored, such as, confocal microscopy, Optical Coherence Tomography (OCT) and 3D-Digital image Correlation (DIC). These imaging techniques can help to understand the strain behaviour and potential damage of soft tissues in the human body.

1.2 Deformation, strain and damage on human body

By definition, deformation refers to the change in shape or size of an object due to the application of external force or environmental conditions. From the perspective of mechanical engineering, it is often represented by the term strain to show how an object deforms relatively to its un-deformed state.

Deformation could occur on a human body performing some simple movements. For example, when a person extends his/her arm, certain regions of the arm need to be in tension or compression in order to complete the movement. Small deformation also occurs on the surface of the skin when a person tries to grip or hold an object.

Human skin has a big role in people's everyday life because it has the most interaction with all kinds of materials from consumer products, gadgets, sporting equipment etc. In people's daily life, hands and fingers are often used for gripping and holding things. Smartphones with touch screens were introduced to the public approximately two decades ago. Nowadays, a significant number of electronics come with a touch screen and huge percentage of the human population has at least one electronic gadget that has a touch screen, which highlights the fact that finger interaction has become increasingly important since. Sports that require the handling of sporting equipment also raises the importance of strain study on human body because efficient handling of the sporting equipment often leads to better performance, increase in comfort or less sports injuries. There is also an abundance of human body interactions in the medical field as medical staff often needs to interact with the human body of the patients to perform diagnoses, examinations and/or treatment.

However, excessive strain on the human body (or any materials in this sense) will often lead to damage human body, such as, bruises, cuts, dislocations and sprains to name a few. For example, cuts from skin and blade interaction could happen from time to time during a shave. Also, people with dry skin over the finger pad often have annoying experiences with carrying out daily life activities that involves in gripping and touching with different materials because it hinders the normal operation of the human skin. Therefore, health services or organisations often recommend the use of ointment or moisturisers. However, the application of ointment or moisturisers often leads to new problems such as the hand or finger being too greasy or uncomfortable. In sports, cyclists could gain skin irritation and rash at the sensitive areas from chafing due to long periods on the saddle during cycling tours or long endurance rides. As an example in the medical field, cardiac catheterisation will

always have potential tribological complications as the catheter interacts with the blood vessels, which could be perforated when mishandling happens.

This research may not be able to create a cure all solution in the short term. In the long term, however, the basic understanding of the deformation and strain of human body may open up different possibilities in the future that could mitigate discomfort or potential damage on the human body effectively.

1.3 Real-time imaging

As medical imaging keeps on improving, the real-time aspect in imaging has been gaining a lot of interest. The definition of real-time has been summarised by Kehtarnavaz & Gamadia (2006) into three groups. The first group is the real-time in a perceptual sense, which describes the near instantaneous response of the computer device perceived by the human user after the input into the device. For example, the algorithm of the photo enhancement effect (in digital cameras or app in smart phones) only needs to operate approximately for 110ms on each photo frame to make the processing seem imperceptible to a human user.

The second group is real-time in a software engineering sense. It is similar to the perceptual sense in terms of the concept of a bounded response time, provided that the result of processing is logically correct. In other words, the issue of real-time is not entirely focused on fast processing, but also the performance of the device. Laplante (2008) has further classified this group into three subgroups, which are hard real-time imaging systems, firm real-time imaging systems and soft real-time imaging systems, based on the strictness attached to the maximum bounded response time, also known as the deadline. Hard real-time systems cannot miss even one deadline in task completion as the failure to do so will lead to a complete system failure. For example, a robot that is not able to detect an obstacle like a rock in time (deadline) will result in the robot being toppled over. Then, the toppled robot will not be able to continue to move forward (complete system failure). Firm real-time systems allow a few missed deadlines because it will not constitute to complete system failure. For example, weather reporting, in which the wind speed is recorded every minute, may have a few errors on an overall 1 hour data acquisition, but this does not affect the average wind speed for the weather report. However, frequent errors will lead to the miss-representation of the wind speed during the weather report. Lastly, soft real-time systems are systems that have missed deadlines, however, this does not lead to complete system failure, but instead this is reflected as performance degradation. For example, it will take a longer time (performance degradation)

to obtain desired measurements by post-processing the images after acquiring the images from an imaging system.

The third group is real-time in the signal processing sense. This is based on the concept of completing the processing of one input within the available time between two consecutive input samples.

The main advantage of having a real-time aspect in imaging is the visual results can show the condition or reaction of the biological samples instantaneously in response to the changes of external stimuli or the environmental conditions, if any. This is especially useful in biomechanics related research, for example, the strain behaviour of soft tissues. The imaging techniques that had been used in this research are real-time systems. However, when the imaging techniques were coupled with experimental set-ups, the processes in measuring deformation or strain of the soft tissues were not necessary real-time as the information was obtained through post-processing after the acquisition of the images.

1.4 Imaging in biomechanics

“Biomechanics is the study of the structure and function of biological systems by means of methods of mechanics (Hatze, 1974)”

Due to the fact that soft tissues such as aorta and skin are anisotropic, viscoelastic and non-linear materials, the strain behaviour of the soft tissues tends to be complex and unpredictable. As a start, several studies started investigating the strain behaviour of soft tissues from a simple tensile test set-up (Jacquemoud et al., 2007; Annaidh et al., 2012; Lanir & Fung, 1974). Currently, there is only one real-time imaging technique that can measure the strain of the biological samples, which is Digital Image Correlation (DIC). Further research successfully used DIC to look at the strain field of the in-vivo human skin at the region around the arm and joint experiencing deformation by performing basic exercise postures (Obropta & Newman, 2015; Wessendorf & Newman, 2012).

Other than DIC, optical coherence tomography (OCT) is another common real-time imaging technique that images the cross sections of biological samples and is able to show the composition layers of the soft tissues. However, the post-processing of the images from OCT cannot be done while the sample is being scanned.

Various other medical imaging systems, like Computed Tomography (CT) scans and Magnetic Resonance Imaging (MRI) etc., are not considered in this study because the imaging systems may not be able to provide strain measurements of a dynamic sample.

1.5 Imaging in biotribology

“Biotribology is defined as a scientific field that studies the friction, wear and lubrication of the biological systems (Dowson & Wright, 1973)”

Although imaging in biotribology is not as popular as in biomechanics, it definitely has started to attract more researchers to use imaging techniques like DIC, high speed cameras or OCT in biotribology experiments (Tomlinson et al., 2009; Liu, 2012; Liu et al., 2013; Delhaye et al., 2016). Liu et al. (2013) have used OCT to study the morphology of the finger pad when sliding against a glass while Delhaye et al. (2016) looked at the strain pattern within the contact area of the finger pad using a bespoke post-processing algorithm.

1.6 Motivation of research

A picture speaks a thousand words. As the imaging techniques have been advancing so much in the past decade, they are much more reliable, user friendly and commercially available. As such, it is interesting to explore biomechanics and, especially, biotribology problems with the current imaging techniques to discover what these imaging techniques can achieve and their limitations.

Biotribology is emphasised in this context because only very few and limited imaging technique options can be used to study the strain behaviour of biological material in contact with other material experimentally. Most studies used finite element modelling simulating different biotribology problems, where the modelling is based on a theoretical model of contact mechanics (Johnson & Phillips, 1981; Dandekar et al., 2003; Sripathi et al., 2006; Wang et al., 2012). The modelling often requires displacement inputs obtained in experimental studies.

1.7 Aim and objectives

The aim of this research was to develop a range of high-speed imaging techniques to move towards real-time imaging of deformation and strain in soft tissue. The project wanted to explore which imaging systems can be used to obtain strain measurements of a dynamic object in real-time. There are only a few imaging techniques where deformation or strain can be determined from the captured images of a moving object. These imaging techniques are

3D-DIC, OCT and confocal microscopy. An imaging technique is considered as high-speed if it can capture the deformation or strain response of a moving object due to external stimulation. For example, 3D-DIC can show how the strain distribution of the finger pad in contact evolves when a stationary glass plate in contact starts to move.

The research is mainly focused on *in-vivo* human skin. However, confocal microscopy is used to study a different soft tissue, porcine aorta, because this imaging technique can damage *in-vivo* human skin.

The objectives were to:

- Explore the available imaging techniques that can measure the deformation and strain of soft tissues and study what kind of information can be extracted from the visual results
- Investigate how confocal microscopy can be used to study the deformation damage of tissue fibres
- Investigate the frictional and strain behaviour of finger pad undergoing sliding interaction with a plate
- Investigate if a silicone hemi-sphere experimental model undergoing sliding interaction with a plate with similar experimental conditions would have a similar frictional and strain behaviour to a finger pad
- Investigate the morphological change of forearm skin from simple posture change
- Compare the experimental strain behaviour of the silicone hemi-sphere to an analytical model

1.8 Workflow

The workflow chart shows how the project advanced in using different imaging techniques on different soft tissue-related experiments as shown in Figure 1-1. The experiments were performed to study the morphology and strain behaviour of soft tissues in response to different external stimuli. It also shows how the real-time aspect is connected with the experiments.

The project first started out using confocal microscopy as a pilot test to study the deformation of soft tissue. Due to the possible risk of permanent injuries on living test subjects using confocal microscopy, the project shifted from studying human skin to another tribological situation. As such, the confocal microscopy was used to study the catheterisation

damage on porcine aorta because cardiac catheterisation could cause complications and often discomfort to patients. Confocal microscopy work is shown in Chapter 8.

Then, it was found that the Optical Coherence Tomography (OCT) and 3D-Digital Image Correlation (DIC) were suitable to study human skin (finger pad region) deformation during tribological interaction on living test subjects, which is in Chapter 4. Human interaction experiments on living test subjects are known to have a large pool of data with high standard deviations. Therefore, the next study used the same imaging techniques on soft tissue simulants, which is in Chapter 5. This study also aimed to be the first step in manufacturing an experimental model that simulates a finger pad tribological interaction, which is shown in Chapter 6. The next study was done to model the strain behaviour of the soft tissue simulant by starting from a simple analytical model.

OCT and 3D-DIC are traditionally designed for use in non-tribological tests such as tensile experiments, identification of different skin layers etc. So, non-tribological experiments were performed to investigate if the nature of the experiment or experiment type could affect the images quality. This work is shown in Chapter 7. High quality images are often easier to analyse and able to generate more accurate measurements.

The imaging techniques – 3D-DIC, OCT and confocal microscopy are all hard or firm real-time imaging devices. “Hard” or “firm” real-time images of the biomechanics and biotribology experiment were obtained using OCT and 3D-DIC. However, the whole deformation or strain measurement system was considered to be “soft” real-time because the post-processing of the images to obtain strain measurement and morphological changes were done by analysing the “hard” real-time images after the image acquisition process.

It should be noted that only 3D-DIC among the imaging systems is able to show the strain measurement during the image acquisition process, but this feature was not used as improving the strain result was a priority.

In the case of confocal microscopy, the whole deformation measurement system for the biotribology experiment was not considered as a real-time experiment, both soft and hard, because this imaging technique was not able to capture images of the porcine aorta from before loading to after loading.

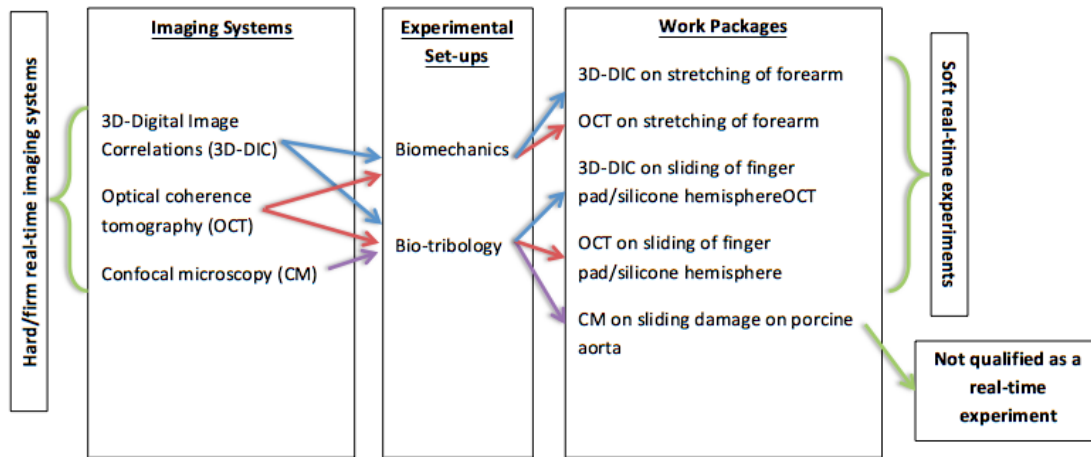


Figure 1-1, Workflow of the imaging techniques used on the experimental set-ups

1.9 Research contribution and limitations

This research hopes to offer novel methodologies for assessing deformation and strain in soft tissues using high speed imaging techniques. This research has also successfully documented the typical frictional and strain behaviour of the finger pad and silicone hemi-sphere. This will pave the way to studies researching more complicated experimental models such as silicone hemi-sphere with multiple layers or ridged silicone hemi-sphere and to see which experimental models has the most similar frictional and strain behaviour to the finger pad.

As this research is intended as a case study in developing methodologies for assessing deformation and strain in soft tissues, the size of the sample is not intended to produce normative data. Future work will contribute to the gathering of high-quality normative data for the methods developed.

1.10 Structure of the thesis

This thesis is organised into nine chapters that address the key aspects of this research:

Chapter 1 gives an overview, the background of this research study and the motivation driving this research.

Chapter 2 presents a review of the current knowledge on the frictional and strain behaviour of soft tissues. It further discuss' the strain assessment methods that have been used in the literature. The latter part of the chapter discuss' the potential of using soft tissue simulants in biotribological experiment.

Chapter 3 demonstrates how the 3D-DIC (Correlated Solutions), OCT (Vivosight) and confocal microscopy (Leica) were used and set-up for the experiments in this research. The post processing and the interpretation of the data from respective imaging techniques are also discussed in this chapter.

Chapter 4 presents one of the main research works that investigates the strain behaviour of human finger pad before, during and after the sliding interaction with a glass plate. 3D-DIC and OCT were used in this study to investigate the surface and sub-surface deformation respectively. In this chapter, there is also a very interesting pilot study that looks at how the ridges of the finger pad deform when slid against a grooved plastic plate. However, the sole purpose of this pilot study is to provide a visual result of the deformation of ridges of finger pad during sliding against grooved plate.

Chapter 5 is a follow up of chapter 4 that studies the deformation and the strain behaviour of the silicon hemi-sphere during the interaction with a glass plate. This chapter will investigate if a silicone hemi-sphere is suitable to simulate the frictional and strain behaviour of a real life finger pad, so the results in this chapter are compared with those from chapter 4.

Chapter 6 is a follow up from chapter 5 as this chapter compares the strain and displacement data of silicone hemi-sphere obtained from DIC to the theoretical model of hemi-sphere in contact mechanics. This can show if the experimental strain data is a good representative of the theoretical model.

Chapter 7 presents different research work that studies the morphological change of human forearm skin when performing a simple posture change without any interactive material. This work proves that the visual result of the soft tissues, using the same imaging techniques and set-up in chapter 4, is easier to obtain without an interactive material.

Chapter 8 presents research work done in Philips that studied the orientation of aortic tissue fibres subjected to different damaging loads using confocal microscopy. This work investigates the deformation behaviour of animal tissue at microscopic level.

Chapter 9 discuss' the main connections of all the work packages done in previous chapters.

Chapter 10 brings a closure to this research by listing the key findings and the future work needed.

Chapter 2

Literature Review

2.1 Introduction

This chapter starts by introducing the human soft tissues (human skin and aorta) and their morphology, and then the tissue fibres composition in the soft tissues. The next sections cover the frictional and strain behaviour of the soft tissues as described and documented in the literature. For example, the sliding mechanisms between human skin and other materials, and the strain distribution profile of the human skin when subjected to different types of loading. Next chapter shows how the strain behaviour of the soft tissues have been previously assessed, by means of mechanical tests, imaging techniques or finite element modelling. Then, it discuss' how soft tissue simulants have been used in attempts to imitate the human skin in biotribology experiments. The last section summarises and explains how each section in the literature is connected. It also outlines the gaps in the current literatures.

2.2 Soft tissues and their morphology

2.2.1 Human skin

Skin is the largest organ in a human body and it acts as the first line of defence of the human body to external damage. It is an anisotropic and viscoelastic material that is sensitive to environmental conditions. Skin is composed of three main layers: the epidermis, dermis and hypodermis (Gerhardt et al., 2012; Lamers et al., 2013; Weickenmeier & Jabareen, 2014).

The epidermis, the top layer of the skin, consists of stratum corneum, stratum lucidum, stratum granulosum, and stratum spinosum and stratum basale as shown in Figure 2-1. The stratum corneum acts as a barrier for pathogens entering the skin and prevents unregulated loss of water (Proksch et al., 2008). The roughness and the thickness of the human skin varies across different body sites. Some body sites, like the foot sole, have thicker skin to protect against due the prolong interaction with other materials, while the face skin is thinner because it does not have a lot of interactions with other materials. Maiti (2017) has measured and quantified the roughness and the thickness of the human skin from various body sites using OCT, which is shown in Figure 2-3 and Figure 2-4. The resolution of the OCT used was 7.5 μm lateral and 5 μm axial for an image of 1342 \times 460 pixels. The work studied the morphological change (surface roughness and skin thickness) of the human skin across different body sites. This could be important in the study of human skin friction because surface roughness of the human skin may also have an effect on human skin friction.

Mechanical properties of the skin are mostly dominated by the dermis, which is rich in collagen fibrils and other proteins like elastin. In addition, the tissue fibres are not unidirectional oriented. Although the stratum corneum is relatively stiff, it is thin and strongly influenced by the environmental conditions, such as temperature and humidity (Hendriks et al., 2006). Therefore, the stratum corneum does not have big contribution to the overall stiffness of the skin (Brown, 1973). The mechanical properties of human skin are also influenced by a number of additional factors such as age, gender, ethnicity, anatomic region, physiological conditions, hormonal status, skin diseases and the use of different skin care products (Rigal et al., 1989; Escoffier et al., 1989; Gorodetsky et al., 1999; Vexler et al., 1999; Serrat et al., 2007; Hendriks et al. 2006). Skin is nearly incompressible with very low shear stiffness in comparison to its bulk modulus. It also exhibits a highly nonlinear stress-strain curve. When the human skin was studied *in-vitro* using a uniaxial test, the stress-strain relationship of the human skin is often split into three stages as shown in Figure 2-2 (Daly

1982; Holzapfel, 2000; Silver et al., 2001). In the first phase, human skin would behave as an isotropic material with low stiffness. Most work is done on the elastin fibres and the stress-strain of the human skin follows a linear relationship. In the second phase, as the stress increases, the collagen fibres start to line up and stretch in the force direction. Then, the stress-strain relationship becomes non-linear. In the third phase, the collagen fibres are all lined up and stretched, which caused the stress-strain of the human skin to follow the linear relationship again. Holzapfel (2000) has presented a model suitable to predict the anisotropic elastic response of soft tissues in the last strain domain (phase 3) based on nonlinear continuum mechanics (Ogden, 1997). Also, Holzapfel & Gasser (2001) has presented a viscoelastic model for fibre reinforced material composite materials undergoing finite strains. This model could be more suitable for modelling human skin because human skin is made of mostly elastin and collagen fibres. In addition, human skin has also been modelled as a neo-Hookean material, often termed as hyperelastic material. Neo-Hookean model is normally used to predict the non-linear stress-strain behaviour of materials undergoing large deformations. Various studies have used neo-Hookean model to model the material behaviour of soft tissues (Delalleau et al., 2008; Luboz et al., 2014; Limbert & Kuhl, 2018). Delalleau (2008) showed that the standard linear elastic and neo-Hookean model could not be used to model an in vivo skin deflection from suction test.

The Young's modulus elasticity of the human skin was tabulated in Table 2-1. Even though at the same localised region – the forearm, the Young's modulus of the human skin varies between different human beings, which could be affected by the gender, age and ethnicity of the human being (Liu, 2013).

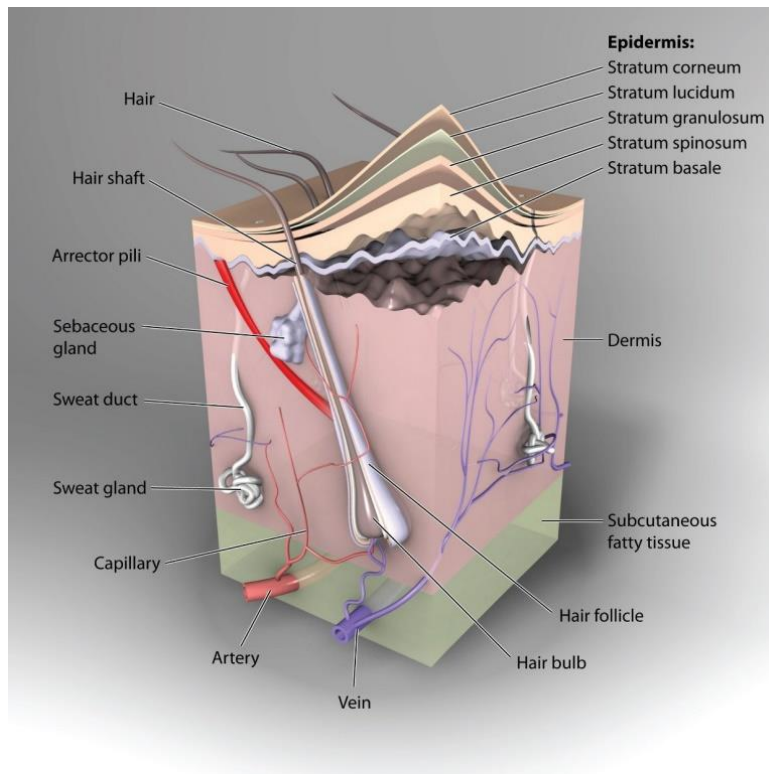


Figure 2-1, Structure of human skin (<http://histologyolm.stevegallik.org/node/353>)

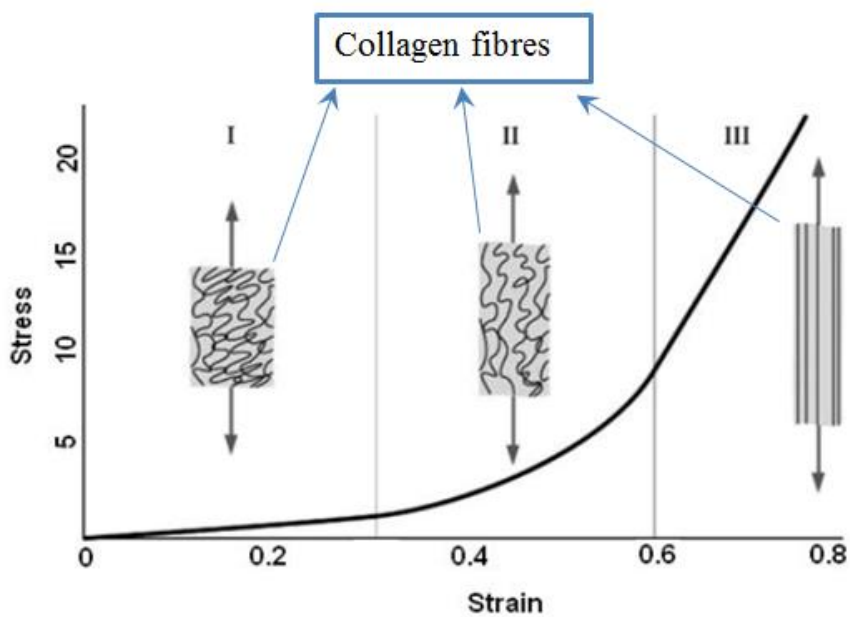
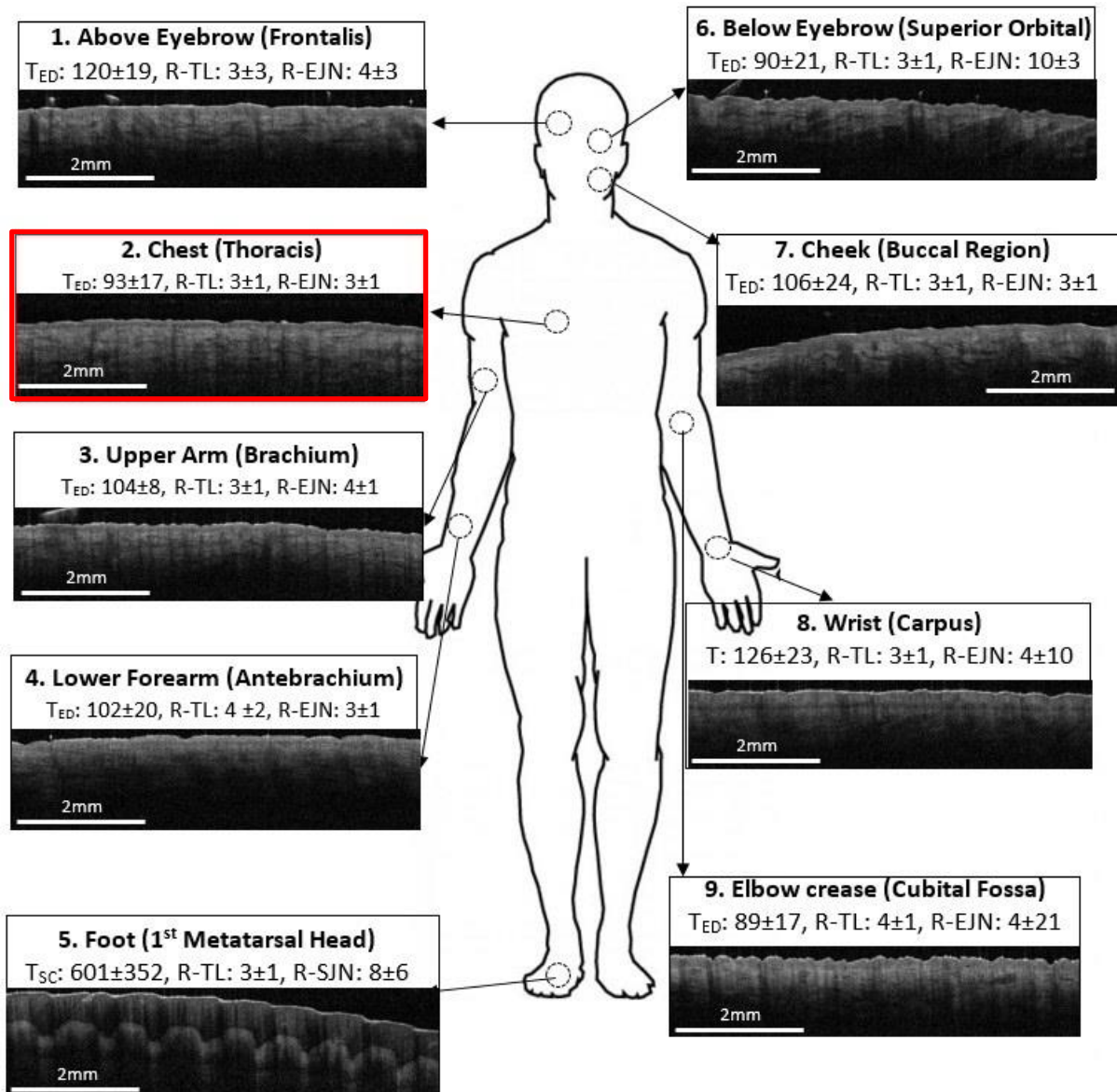


Figure 2-2, The rearrangement of collagen fibres undergoing a tensile test (Holzapfel, 2000)



Thickness (**T**) stated as Mean \pm SD μm ; $T_{\text{SC-SC}}$ thickness and $T_{\text{ED-ED}}$ Thickness

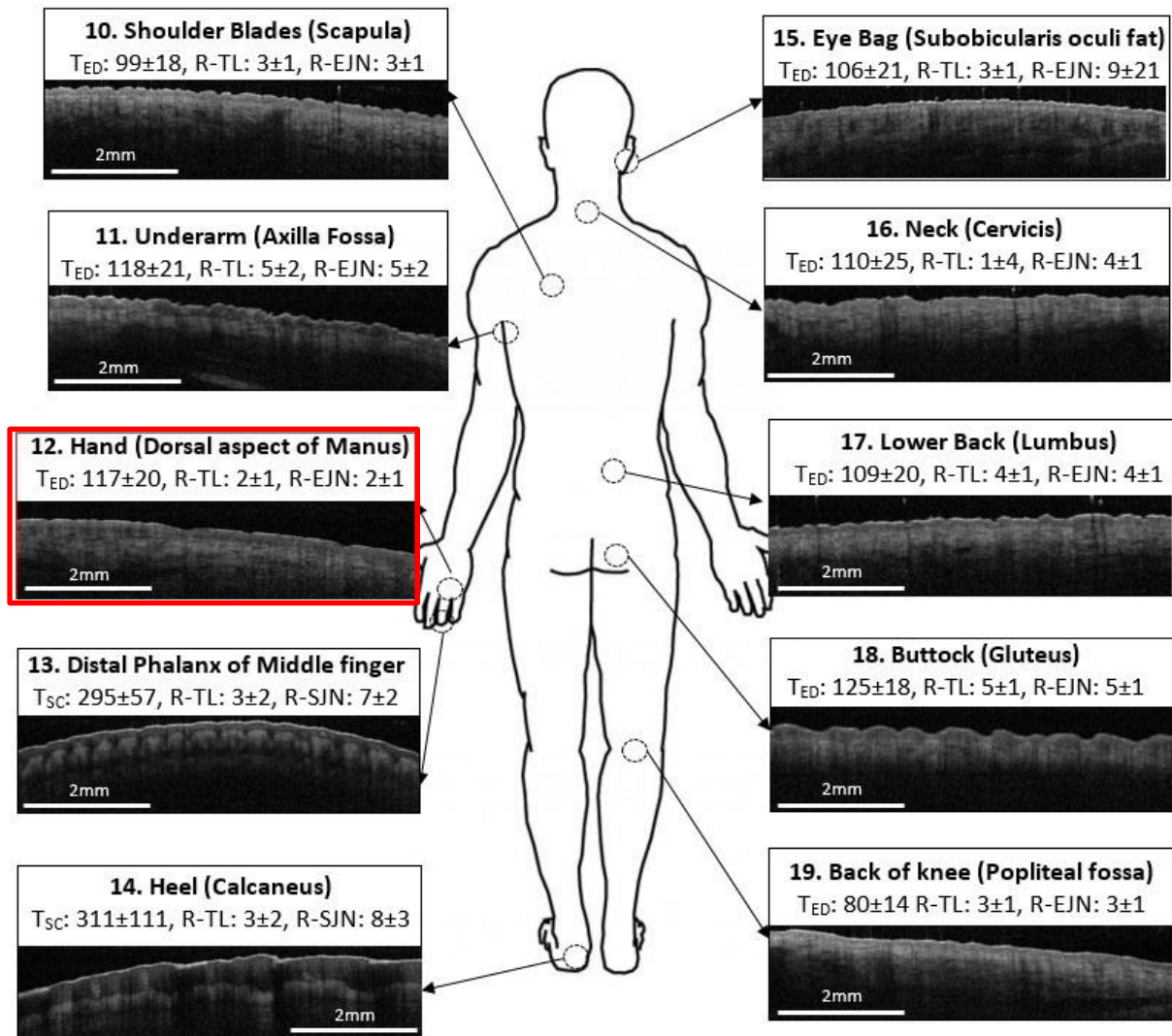
Average Roughness of SC-Epidermal Junction (**R-SJN**) stated as Mean \pm SD μm

Average Roughness of Epidermal-Dermal Junction (**R-EJN**) stated as Mean \pm SD μm

Average Roughness of Top Layer (**R-TL**) stated as Mean \pm SD μm

Red Box represents dorsal skin

Figure 2-3, Roughness and thickness of the human skin at the front body site (Maiti, 2017)



Thickness (**T**) stated as Mean \pm SD μm ; T_{SC} -SC thickness and T_{ED} -ED Thickness

Average Roughness of SC-Epidermal Junction (**R-SJN**) stated as Mean \pm SD μm

Average Roughness of Epidermal-Dermal Junction (**R-EJN**) stated as Mean \pm SD μm

Average Roughness of Top Layer (**R-TL**) stated as Mean \pm SD μm

Red Box represents dorsal skin

Figure 2-4, Roughness and thickness of the human skin at the back body site (Maiti, 2017)

Table 2-1, Young's Modulus of elasticity for skin reported in literature

Author	Skin region	Measurement technique	Young's Modulus (MPa)
Bader & Bowker (1983)	Forearm/thigh	Indenter (20mm)	0.011
Agache et al. (1980)	Forearm Back	Torsion (25mm)	Young: 0.42 Aged: 0.85 SC: 2.1
Barel et al. (1995)	Forearm Forehead	Suction (2mm)	0.13 - 0.17 0.20 - 0.32
Diridollou et al. (2000)	Volar forearm	Suction (6mm)	0.153
Hendriks et al. (2006)	Forearm (dermis)	Suction (6mm)	2100
Sanders (1973)	Doral side forearm	Torsion (8.7mm)	0.02 - 0.1
Grahame (1969)	Forearm	Suction	18 - 57
Escoffier et al. (1989)	Forearm (anterior)	Torsion	1.1 - 1.32

2.2.2 Aorta

The aorta is the largest artery in the body. Its main role is to deliver oxygenated blood to all body systems. It is usually divided into 5 sections: the ascending aorta, the aorta arch, the descending aorta, the thoracic aorta and the abdominal aorta (Van De Graaff, 1998).

There are 3 significant layers in the aorta, from innermost to outermost - tunica intima, tunica media and tunica adventitia, as shown in Figure 2-5. Firstly, the intima is made of a

layer of simple squamous epithelium known as the endothelium that is in direct contact with blood flow (Collins et al., 2014). The endothelium rests on a network of connective tissue membranes consisting of elastin and collagen fibres (Ross & Pawlina, 2006). The endothelium helps in prevention of blood clotting and may also help in regulating blood flow. It can also release nitric oxide to relax the smooth muscle of the vessel (Shier et al., 2010).

The tunica media layer makes up most of the arterial wall including smooth muscle fibres and a thick elastic connective tissue layer (Ross & Pawlina, 2006).

The tunica adventitia is thinner, in comparison to the tunica media layer, and is mostly made up of connective tissue with irregular fibres that are attached to the surrounding tissues (Ross & Pawlina, 2006).

Mechanical properties of the aorta are dependent on the amounts of the aortic wall main constituents, spatial organization and the mechanical interactions among these constituents. The most important mechanical property of the aortic wall is its non-linear elasticity. Studies that investigated the elastic modulus of the human aorta have been tabulated in Table 2-2 (Choudhury et al., 2009; Azadani et al., 2012; Kim et al., 2013; Ferrara et al., 2016). This table goes on to show that the Young modulus of the human aorta could be difference with different human volunteers.

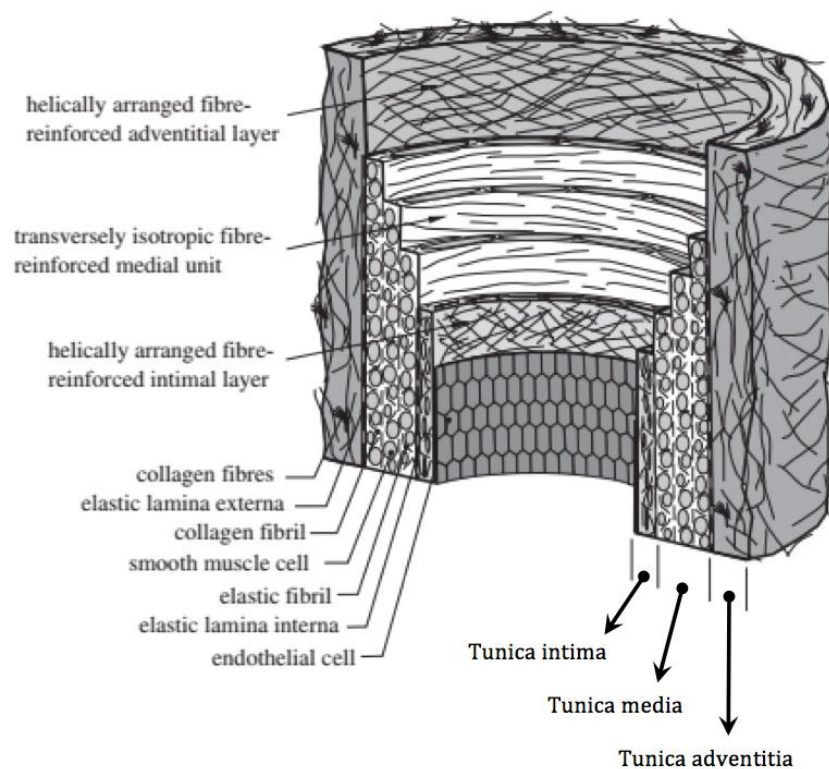


Figure 2-5, Structure of porcine aorta (Tsamis et al., 2013)

Table 2-2, Elastic modulus of human aorta reported in literature

Author	Location	Orientation	Type of Test	Elastic Modulus (MPa)
Kim et al. (2013)	Anterior, proximal thoracic aorta Posterior, proximal thoracic aorta Anterior, distal thoracic aorta Posterior, distal thoracic aorta	Tangential	Inflation test	0.5 0.75 0.4 1.0
Azadani et al. (2012)	Anterior, ascending aorta Posterior, ascending aorta Anterior, ascending aorta Posterior, ascending aorta	Circumferential Circumferential Longitudinal Longitudinal	Biaxial test	0.81-1.42 0.86-1.53 0.79-1.39 0.86-1.53
Ferrara et al. (2016)	Anterior, ascending aorta Posterior, ascending aorta Anterior, ascending aorta Posterior, ascending aorta	Circumferential Circumferential Longitudinal Longitudinal	Uniaxial test	18.3 ± 9.0 30.0 ± 13.9 8.4 ± 4.2 6.4 ± 2.6
Choudhury et al. (2009)	Anterior, ascending aorta Posterior, ascending aorta	Circumferential	Biaxial test	0.45 0.45

2.2.3 Collagen and Elastin

Collagen, made up of long and fibrous structural proteins, is the main protein of the connective tissue and represents about one-quarter of the total protein content in many animals (Berillis, 2013). The collagen network provides the overall tensile strength thus creating a strong construct that can withstand implantation and high burst pressures in vivo.

Elastin is shown to be responsible for the initially compliant behaviour at lower strains and that collagen is responsible for stiffening behaviour at higher strains (Weisbecker et al., 2013). Figure 2-6 shows the network of collagen and elastin fibres. Experiments conducted by v wall in its original shape (Gundiah et al., 2007). Gundiah et al. (2007) reported that elastic fibres of porcine arteries are oriented axially in the intima and the adventitia, and circumferentially in the media.

In human skin, collagen fibres are the main component of the dermis layer, about 77% of the fat-free dry weight, and form an irregular network of wavy coiled fibres oriented almost parallel with the skin surface. This component has a high stiffness and a low extensibility. Elastin fibres are the second main component of the dermis, represent about 4% of the fat-free dry weight, are less stiff than the collagen and show reversible strains of more than 100% (Hendriks et al., 2006).

In aorta, elastin and collagen are the principal components to determine the passive mechanical properties of the aortic wall while smooth muscle cells are responsible for the active mechanical properties and the production of extracellular matrix.

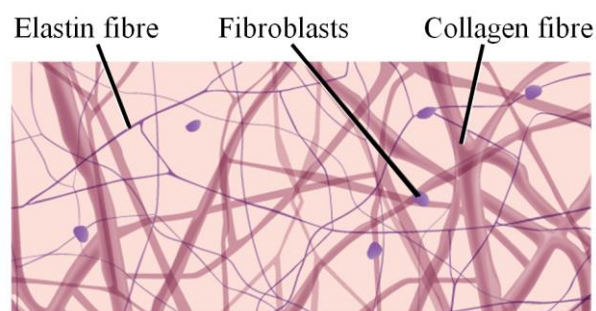


Figure 2-6, Illustration of collagen and elastin fibres

(https://www.boundless.com/biology/textbooks/boundless-biology-textbook/the-animal-body-basic-form-and-function-33/animal-primary-tissues-193/connective-tissues-loose-fibrous-and-cartilage-738-11968/images/fig-ch33_02_06/)

2.3 Frictional behaviour of human skin

Skin friction is a complex mechanism that involves several factors and conditions, especially due to the non-linear, viscoelastic material properties of human skin. An overview of recent papers shows that the coefficient of friction of human skin is affected by various factors including the skin condition, skin structural properties, surface properties, and the contacting material, as well as skin hydration, lipid film and intermediate layers of trapped substances (Adams et al., 20017; Derler et al., 2009; Tomlinson et al., 2011a; Tomlinson et al., 2011b; Adams et al., 2012; Derler Gerhardt, 2013; Conttenden & Cottenden, 2013; Kuilenburg et al., 2013; Tomlinson et al., 2013; Liu et al., 2015).

The classical two-term non-interacting model can be used to describe the skin friction (Bowden & Tabor, 1954). This model assumes an additive decomposition of an adhesion and a deformation term, as shown in the equation 2-1, where F is the skin friction; $F_{adhesion}$ is

the adhesive force of the skin and counter-face material interface and $F_{deformation}$ is the friction due to incomplete recovery of the energy dissipated by skin deformation.

$$F = F_{adhesion} + F_{deformation} \quad \text{Equation 2-1}$$

The measurement of friction between skin and counter-face material can be classified into two experimental types. Firstly, a spherical probe is used to slide against the skin (Kwiatkowska et al., 2009). The second experimental type is one in which the skin is slid against a flat plate. For instance, previous studies have investigated the frictional behaviour and the mechanisms of a finger pad sliding against a plate (Liu et al., 2013; Tomlinson et al., 2009; Tomlinson & Lewis et al., 2011).

It is also worth mentioning that human skin also exhibits stick-slip behaviour under certain conditions (Derler & Rotaru, 2013; Adams et al., 2012; Carré et al., 2017). Adams et al. (2012) mentioned that stick-slip occurs when the friction decreases with increasing velocity provided that the system is not subcritically damped. Generally, the coefficient of friction varied more than $\pm 25\%$ of the mean value during stick-slip (Derler & Rotaru, 2013). However, major stick-slip behaviour may not occur in this project because the relative sliding speed is low (0.25mm/s).

2.3.1 Adhesion

During interaction with dry and smooth solid surfaces, the skin friction is normally assumed to associate only with the adhesion part of the friction mechanism while the deformation part is ignored (Wolfram, 1983; Johnson et al., 1993; Adams et al., 2007; Tomlinson & Lewis et al., 2011). However, the adhesion friction mechanism may be replaced by hydrodynamic effect when human skin is wet as the excess water accumulates on the surface (Adams et al., 2007; Derler et al., 2009).

The skin friction is suggested to follow a linear relationship with the normal load when dry human skin interacts with a dry and smooth counter-face. Therefore, it can be described using equation 2-2, where A_{real} is the real contact area of the skin and τ is the interfacial shear stress (Johnson et al., 1993; Han et al., 1996; Adams et al., 2007).

$$F = F_{adhesion} = \tau \cdot A_{real} \quad \text{Equation 2-2}$$

The adhesive mechanism is governed by two factors. One of them is the surface energy of the counter-faces, which is the molecular nature of adhesive bonds like the Van der

Waals forces, electrostatic forces, hydrogen bonds etc. The second factor is the area of contact over which such adhesive bonds are formed (Tomlinson et al., 2009; Mossel & Roosen, 1994; Tang et al., 2008).

Based on the Hertzian theory, the contact area between a hemispherical probe sliding on deformable materials (skin or rubber) is proportional to 2/3 power of the load as shown in equation 2-3, where R is the radius of the sphere, N is the applied normal load and E is the reduced Young's modulus. The description of reduced Young's modulus is shown in equation 2-4, where ν_{skin} and ν_{sub} are the Poisson Ratios with respect to skin and a substance in contact with the skin. E_{skin} and $E_{substance}$ are Young's modulus of the skin and substance in contact respectively. A more detailed explanation of how contact area affects skin friction is discussed in section 2.4.3. This section also introduces alternative contact models.

$$A = \pi \cdot \left(\frac{9RN}{16E}\right)^{\frac{2}{3}} \quad \text{Equation 2-3}$$

$$E = \left(\frac{1-\nu_{skin}^2}{E_{skin}} + \frac{1-\nu_{substance}^2}{E_{substance}}\right)^{-1} \quad \text{Equation 2-4}$$

In general, the second part of the equation 2-4 $\left(\frac{1-\nu_{substance}^2}{E_{substance}}\right)$ can be neglected when a soft surface material is in contact with a hard counter-face material because $E_{substance}$ is much larger than E_{skin} .

Then equation 2-3 can be rewritten as equation 2-5:

$$A = \pi \cdot \left(\frac{9RN}{16(E_{skin}/(1-\nu_{skin}^2))}\right)^{\frac{2}{3}} \quad \text{Equation 2-5}$$

As such, friction coefficient due to adhesion, $\mu_{adhesion}$, is expressed in equation 2-6 by combining equation 2-2 and equation 2-5.

$$\mu_{adhesion} = \frac{\tau A_{real}}{N} = \tau \cdot \frac{\pi 9R}{16 \left(\frac{E_{skin}}{1-\nu_{skin}^2}\right)^{\frac{2}{3}}} \cdot N^{\frac{2}{3}-1}; \quad (\mu \propto E_{skin}^{-\frac{2}{3}} \cdot N^{-\frac{1}{3}}) \quad \text{Equation 2-6}$$

2.3.2 Hysteresis

When the human skin is sliding against a counter-face material with spherical asperities of high roughness, skin friction is reported to depend on the adhesive mechanism and hysteresis.

In contrast with smooth surfaces, the influence of hysteresis in the friction significantly increases, resulting from the deformation of the skin due to the surface asperities sliding over the skin surface (Derler et al., 2009). The deformation friction can be expressed as shown in equation 2-7 (Greenwood & Tabor, 1958), where a is the radius of the circle of contact (equation 2-8) under a normal load, N .

$$F_{deformation} = \frac{3Na}{16R} \quad \text{Equation 2-7}$$

$$a = \frac{3NR}{4a^2} \cdot \frac{1-\nu_{skin}^2}{E_{skin}} \quad \text{Equation 2-8}$$

In moving forward a unit distance ($D=1$), the elastic work done (W) in horizontal direction is expressed in equation 2-9 (Greenwood & Tabor, 1958) based on the work done formula, $W = F_{deformation} * D$.

$$W = \left(\frac{3N}{16R}\right) \cdot \frac{3NR}{4a^2} \cdot \frac{1-\nu_{skin}^2}{E_{skin}} = \frac{9N^2}{64a^2} \cdot \frac{1-\nu_{skin}^2}{E_{skin}} \quad \text{Equation 2-9}$$

Equation 2-9 helps to visualise that the spherical indenter expends the elastic energy on the skin with the amount of W for every unit distance it moved. If the skin is ideally elastic, then the skin behind the sphere would yield up to the same amount of elastic energy. Therefore, no net energy is lost in this case. However, in the case of hysteresis in the skin, it is assumed that a constant fraction α of the input elastic energy is lost. Parameter α is also called viscoelastic hysteresis loss fraction. As such, the work lost per unit sliding distance, is expressed in Equation 2-10 and the respective friction coefficient due to the deformation, $\mu_{deformation}$, is expressed in Equation 2-11.

$$W_{lost \text{ per unit distance}} = \alpha W \quad \text{Equation 2-10}$$

$$\mu_{deformation} = \frac{\alpha W}{N} = \frac{9\alpha N}{64a^2} \cdot \frac{1-\nu_{skin}^2}{E_{skin}}; \left(\mu \propto E_{skin}^{-\frac{1}{3}} \cdot N^{\frac{1}{3}} \right) \quad \text{Equation 2-11}$$

2.3.3 Interlocking

When the asperities of a high roughness counter-face are triangular shaped instead of spherical, the friction could be dominated by interlocking effect. The interlocking condition happens when the increase in friction that is caused by the asperities of the two materials interlocking with each other. Simply put, the ridges of the finger pad will interlock with the

uneven surface texture of the counter-face material, which will contribute to the friction that resists the sliding of finger pad. It is especially significant when both materials have passed through a certain level of roughness (Jerrams, 2004; Tomlinson et al., 2011a).

A study done by Tomlinson et al. (2011a) has suggested that the skin friction can be analysed in terms of adhesive mechanism ($F_{adhesive}$) and hysteresis mechanism ($F_{hysteresis}$) and interlocking mechanism ($F_{interlocking}$), described in equation 2-12, when the finger pad is sliding against materials with triangular ridged surface. The adhesive mechanism is related to the attractive forces at the skin-material interfacial region. The adhesion friction model of the human skin is the same regardless of the geometry of the asperities – spherical or triangular shaped. However, the hysteresis friction mechanism is affected by the geometry of the asperities. Therefore, the hysteresis coefficient of friction model in section 2.3.2 cannot be applied for the interaction between human skin and triangular ridges. Greenwood & Tabor (1958) derived a hysteresis coefficient of friction model for the interaction between human skin and triangular ridges. Tomlinson et al. (2011a) further expanded the coefficient of friction model to a friction model, which is shown in equation 2-15. Tomlinson et al. (2011a) found that the added friction model predicted that the friction mechanism was dominated by adhesion if the height of the ridges was less than 42.5 μ m. On the other hand, the interlocking effect started to dominate when the height of the ridge was higher than 42.5 μ m.

Figure 2-7 illustrates the interlocking mechanism, which the skin surface ridges move over contact surface asperities.

$$F = F_{adhesion} + F_{interlocking} + F_{hysteresis} \quad \text{Equation 2-12}$$

$$F_{adhesion} = \tau \cdot A_{real} \quad \text{Equation 2-13}$$

Where τ is the interfacial shear strength, A_{real} is the real contact area, α is the pressure coefficient and N is the applied normal force.

$$F_{interlocking} = N \cdot \tan(90^\circ - \theta) \quad \text{Equation 2-14}$$

Where N is the applied normal force and θ is the angle of the ridge.

$$F_{hysteresis} = \begin{cases} \alpha \cdot n \cdot \frac{N}{2n} \cdot \frac{\lambda \cdot \cos\theta}{2h_{ridge}} \cdot \cot\theta, & \frac{N}{n} < N_{max} \\ \alpha \cdot n \cdot \frac{N_{max}}{2} \cdot \cot\theta, & \frac{N}{n} \geq N_{max} \end{cases} \quad \text{Equation 2-15}$$

Where α is the viscoelastic hysteresis loss fraction, n is the number of ridges, λ is the distance between each ridge, h_{ridge} is the height of the ridge and N_{max} is the normal load at which the deformation reaches a maximum.

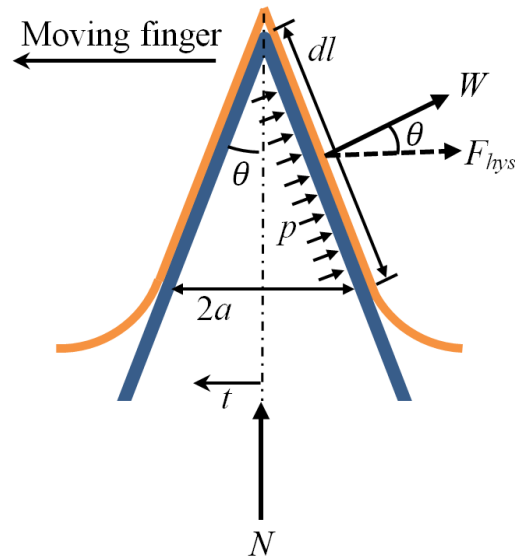


Figure 2-7, Schematic of a single ridge in contact with the finger pad, which N is the applied normal force, θ is the angle of the ridge, t is the distance from the centre line of the ridge, a is the largest distance from the centre line to contact of the ridge with the skin, p is the pressure along the contact area of the ridge and skin, dl is the length of the contact area, W is the resultant force due to the applied pressure and $F_{hysteresis}$ is the deformation force (Tomlinson et al., 2011a)

2.4 Parameters affecting friction

2.4.1 Normal load

Amontons' law of friction proposes that the ratio of friction force to normal force, known as coefficient of friction, was assumed to remain constant regardless of the applied normal load and it is independent of the apparent contact area of the material under dry contact conditions (Sivamani et al., 2003). However, Amontons' law of friction is not applicable to skin friction because human skin is categorised as a nonlinear, viscoelastic material (soft tissue). Therefore, the theoretical concepts of friction of elastomers are applied on human skin instead (Moore, 1972; Dowson, 1997). Several studies have performed sliding experiments and found that the static coefficient of friction of the human skin decreased initially as the normal load increased and would reach a plateau once the load reached a threshold value, which is approximate to be 3N (Comaish & Bottoms, 1971; Han et al., 1996). The studies

suggested that the decrease in coefficient of friction was due to the viscoelastic properties of the human skin that allows a non-linear deformation of the skin with increased normal load.

A model that describes the relationship between coefficient of friction and normal load has been developed, shown in equation 2-16, where μ is the coefficient of friction, N is the normal load and n is the exponent of the normal load ($n < 1$). Several studies have suggested that the n value of skin is 0.3 (Comaish & Bottoms, 1971; Asserin et al., 2000; Sivamani et al., 2003).

$$\mu \propto N^{-n} \qquad \text{Equation 2-16}$$

Some studies also show the type of counter-face material also plays a role in skin friction and found out that the coefficient of friction (between skin and all other materials) decreased with increasing normal load except for polypropylene (Tomlinson, 2009; Tang et al. 2008).

Tomlinson et al. (2009) described a detailed relationship between friction force and applied normal load, which was achieved by sliding the finger pad over different types of materials at various normal loads. It was observed that for a low normal load region, which ranges from 0N to 10 N, a two part linear relationship was observed as shown in Figure 2-8. The figure showed that the relationship between the normal load and friction force is linear from 0N to 2N normal load. Although the relationship between normal load and friction force is still linear when the normal load is higher than 2N (high normal load region), but the gradient of the relationship is smaller than the relationship in low normal load region. Ramalho et al., (2005) investigated the skin frictional behaviour at various anatomical sites of the body and had a similar finding that showed a double stage Amontons-Coulomb linear model at the forearm area.

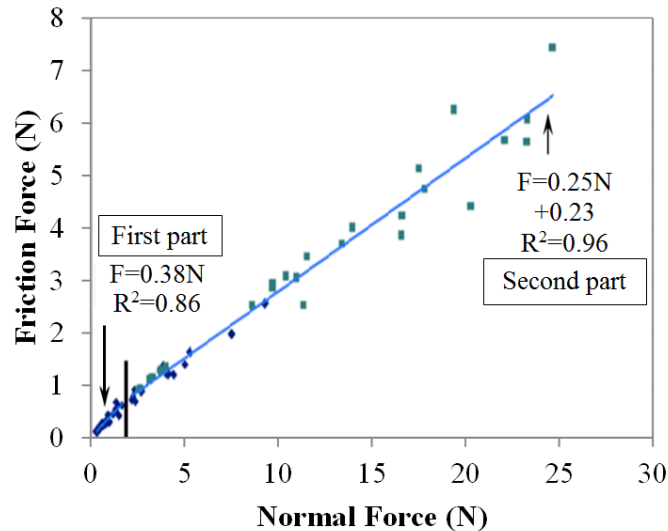


Figure 2-8, Two-part relationship between friction force and normal load (Tomlinson et al., 2009)

2.4.2 Skin hydration

The hydration of skin plays an important role in skin friction. The moisture of the human skin is highly dependent on environmental factors, the perspiration secreted by sweat glands, sebum layer, dust, food (after touch) and cosmetics. Therefore, a lot of studies investigated how hydration or moisture affects the skin friction (Comaish & Bottoms, 1971; Dinç et al., 1991; Adams et al., 2007; Persson, 2008; Nonomura et al., 2009; Tomlinson et al., 2011b; Veijgen et al., 2013; Derler et al., 2015).

When excess water was added on the contact between human skin and counter-face material, studies found that there was an increase in friction on the human skin (Comaish & Bottoms, 1971; Nonomura et al., 2009; Veijgen et al., 2013). Some studies suggested a linear correlation between finger pad moisture and friction (Cua et al., 1990; Gerhardt et al., 2008; Veijgen et al., 2012; Liu et al., 2015). On the other hand, Kwiatkowska et al. (2009) fitted an exponential relationship between the human skin moisture and coefficient of friction. Although linear correlation is more commonly used, both curve-fitting methods show positive relationship between human skin moisture and friction. Next, some studies also found a ‘bell curve’ response in the coefficient of friction of the human skin against the skin hydration or the amount of water (Adams et al., 2007; André et al., 2009; Tomlinson et al., 2011b). The coefficient of friction of the skin was gradually after a certain amount of water level was reached because the excess water would serve as a thin lubrication on the contact.

In order to explain the increase in friction when the water was added to the contact region, past studies suggested several different friction mechanisms. The first friction mechanism is the water absorption (Adams et al., 2007; Gerhardt et al., 2008; Liu, 2012). The human skin swells as the water absorption occurs. The contact area increases as a result, which will lead to the increase of friction on human skin. Secondly, a study by Dinç et al. (1991) suggests that viscous shearing of the liquid bridges could be a friction mechanism. A liquid bridge is formed when there is water that accumulates between the finger pad ridges (human skin) and the counter-face material. The liquid bridge will have some resistance against the sliding material due to the viscosity of the liquid. So, the viscous shear resistance will contribute towards the friction of human skin. Thirdly, Persson (2008) suggested the capillary adhesion as a friction mechanism. Capillary adhesion only occurs at narrow space. Persson (2008) found that the real contact area between two elastically hard materials when the narrow space is filled with just enough water. As for the interaction between an elastically soft material and a hard material, the capillary adhesion brings the two materials closer (increase in contact area) when the water level in the narrow space decreases. Many experiments have been carried out with respect to each mechanism, individually. In particular, Tomlinson et al. (2011b) designed various tests to investigate the relative contribution of each mechanism on the skin friction in moist conditions. After being fully examined, the water absorption was believed to be the major cause of the friction coefficient increase, followed by capillary adhesion. The viscous shear was found unlikely to affect friction due to the low water film thickness. Under low water film thickness, it is inferred that the capillary adhesion effect outweighs the viscous shear of the liquid bridge.

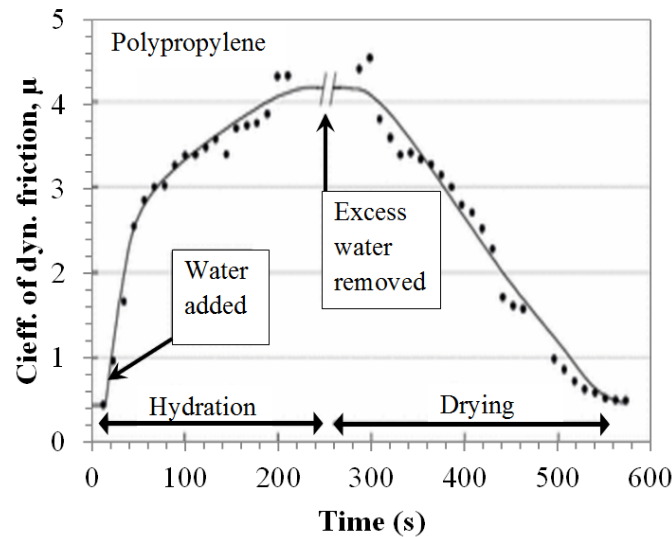


Figure 2-9, 'Bell curve' behaviour of the coefficient of friction when water was added and removed from the human skin (Adams et al., 2007)

2.4.3 Contact area

In section 2.3.1, equation 2-2 has shown that the adhesive friction force is proportional to the real contact area. This is why adhesive friction is the most dominant friction mechanism especially when skin is interacting with smooth surface materials. As such, it is essential to study the contact area between the materials during sliding interactions.

According to Herzian theory, the contact area between the materials is proportional to the 2/3 power of the normal load when a hemispherical probe was slid against deformable materials such as rubber or skin (Johnson, 1985; Adams et al., 2007). However, this model is only applicable if the deformation of the material falls in the elastic region and, it is mentioned and shown in section 2.3.1 as equation 2-3. The contact area, in most experiments that involved in sliding a relatively high Young's modulus probe against the human skin, can be described by Herzian theory.

However, this model is not suitable to describe the interaction of a finger pad sliding against a flat surface. Firstly, the finger pads are not made up of smooth surfaces but the finger pad ridges. Therefore, the finger pad will not experience a smooth spherical contact. Secondly, the finger pad is a nonlinear material due to its viscoelasticity. As such, Han et al. (1996) proposed that the contact area of the finger pad should be expressed as equation 2-17, where A is the contact area, N is the normal load, k and b are experimental constants.

$$A = kN^b \quad \text{Equation 2-17}$$

Exponent constant b is often compared between studies. Han et al. (1996) reported it was between 0.2 and 0.4 for apparent contact between a human finger pad and a transparent acrylic board (Han et al., 1996). Soneda & Nakono (2010) presented the b value in terms of apparent contact area and real contact area, which is 0.54 and 0.66 respectively. Next, Liu et al. (2017) further classified the b value into apparent contact area in low normal load region, apparent contact area in high normal load region, real contact area in low normal load region and real contact area in high normal load region, which are 0.42, 0.14, 0.5 and 0.28 respectively. Xydas & Kao (1999) has also reached a similar power law contact model as in Equation 2-17 that described the contact radius instead of the contact area. Both models are essentially the same because the spherical contact area is the product of π and the square of contact radius. Xydas & Kao (1999) mentioned that the b value should be between 0 and $2/3$. When b value is $2/3$, then it is essentially the Hertz model. When b is 0, then the model corresponds to the case of an ideal soft finger pad because the full contact area is reached. Therefore, the increase in normal load will not further increase the contact area. This could be the reason why Liu et al. (2017) reported the b values from low normal load region and high normal load region separately.

Several contact area measuring methods have been developed so far, such as the ink stamping method (Childs & Henson, 2007; Warman & Ennos, 2009; Tomlinson et al., 2011b; Liu et al., 2017), optical methods (like high speed cameras and Optical Coherence Tomography technique) (André et al., 2009; Tomlinson et al., 2009; Soneda & Nakano, 2010; Liu et al., 2013; Liu et al., 2015) etc.

Among the methods, the ink stamping and the optical methods are able to show the morphology of the finger pad because these methods are able to produce the fingerprint of the finger pad in contact. By using the ink-stamping method, the black regions of the fingerprint, as shown in Figure 2-10, are the regions where the finger pad is actually in contact with the paper. However, the drawbacks of this method are the errors (due to the spreading of the ink), the noise level, and the threshold value to be set during image processing (Liu, 2013). One of the optical methods known as Optical Coherence Tomography, which works like ultrasound except it uses light as a medium, is able to capture the cross section of the finger pad in contact, as shown in Figure 2-11. However, this method is limited to the field of scan that is smaller than the apparent contact area of the finger pad, as shown in Figure 2-11 as well. It should also be noted that both methods (ink stamp and OCT) could only currently measure the area in contact when the finger pad is not in motion (dynamic state).

Tomlinson (2009) has tried to predict the contact area of the finger pad, based on Hertz Theory and JKR theory, and made a comparison with the experimental contact area obtained from the optical method, which is shown in Figure 2-12. The main difference between the two theories is that Hertz theory states that the contact area is proportional to the normal force with the power of 0.67 while JKR theory states that there is an attractive force acting between the finger pad and counter-face material, therefore having a contact area due to the surface energies of the contact surface. However, both theories have been built on the assumption that the Young's modulus of the finger pad remained constant, which is arguably wrong. So, Tomlinson (2009) plotted the contact area against normal force graph with varied Young's modulus that were obtained and post computed from using high-speed camera images of a finger pad compressed at different normal loads.



Figure 2-10, The ink stamping method (Liu et al., 2017)

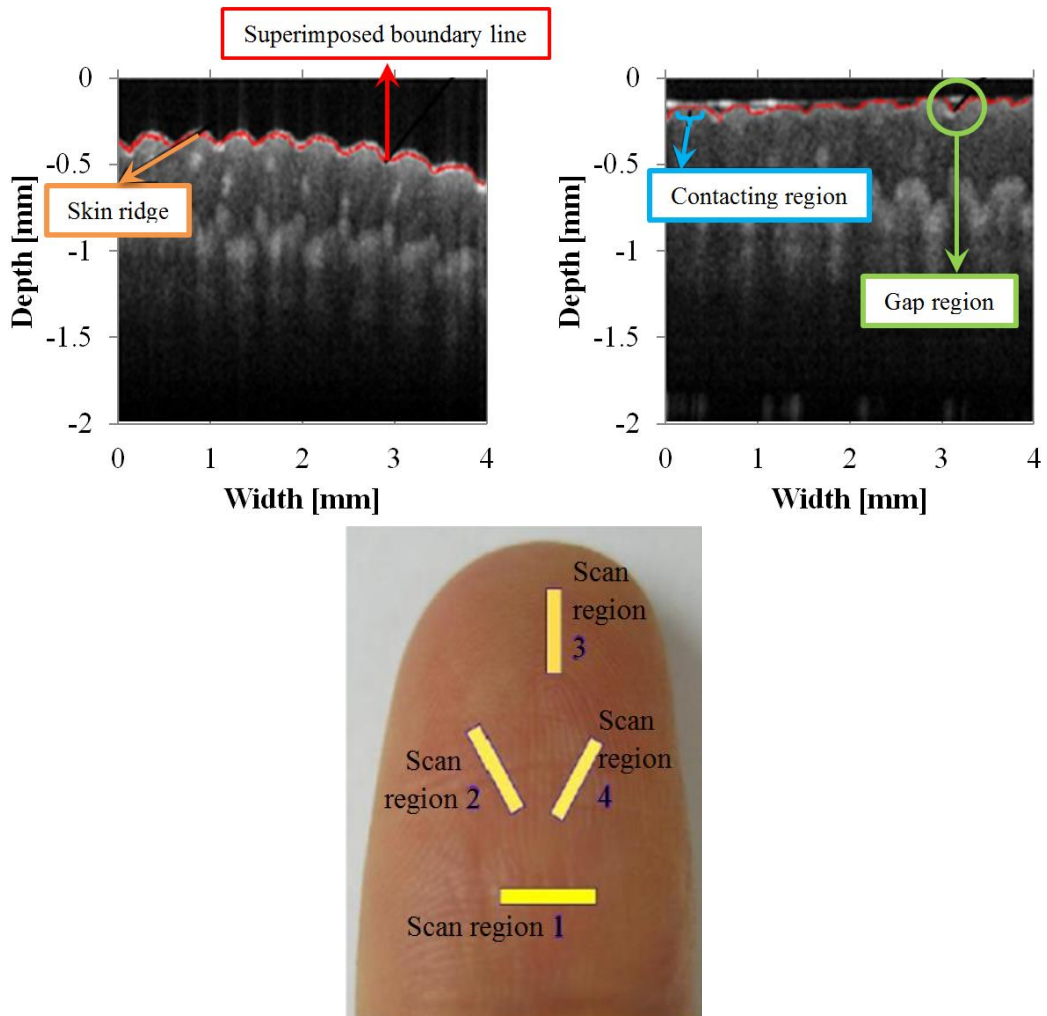


Figure 2-11, Image of finger pad using OCT and the scanned skin region (Liu et al., 2017)

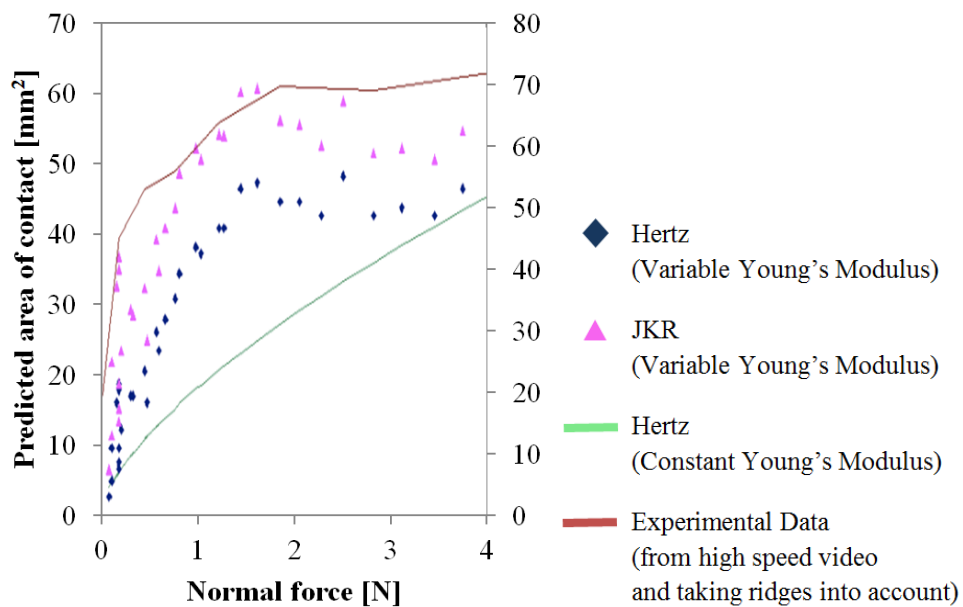


Figure 2-12, The relationship between contact area and normal force (Tomlinson, 2009)

2.5 Strain behaviour of soft tissue

Strain behaviour of soft tissue is important in the study of biomechanics because whenever a human body moves, changes postures, or interacts with consumer products, medical applications, and sports equipment, the soft tissues (human skin, muscles, blood vessels etc.) will experience deformation and hence introducing strain in the soft tissues. Extreme deformation may lead to skin irritation or damage. In terms of human skin friction (biotribology), strain distribution may help in identifying deformation friction mechanism because strain is a measurement of deformation. Delhaye et al. (2016) has mentioned that the interactions between human skin and external objects are translated into complex tactile information, which is connected to the spatial-temporal patterns of strain in the skin and subjacent soft tissues. However, no studies have looked into quantifying the relationship between strain and human skin damage to the author's knowledge because a reliable method for measuring and quantifying damage is required.

The strain study of human skin can be categorised based on the two circumstances, which are the strain that occurs on human skin without the interaction with a counter-face material (non-contact type), like movement and exercise, and the strain that occurs on human skin due to the interaction with a counter-face material (contact type), like touching, gripping etc.

2.5.1 Non-contact type

This case focuses on the strain behaviour of the human skin when it is not in contact with another solid body, for instance, the study of localisation of strain of an excised human skin during uniaxial tensile test (Jacquemoud et al., 2007). From the literature, the non-contact strain behaviour of human skin can be summarised into (i) excise human skin (in vitro) and (ii) human skin as a whole (in vivo).

Firstly, several studies investigated the strain of specimens under tensile loading until failure using conventional tensile machines (Jacquemoud et al., 2007; Annaidh et al., 2012; Lanir and Fung, 1974; Marcellier et al., 2001). In vitro tests can easily provide the stress-strain relationship of human skin (or any other soft tissues). Brown (1973) demonstrated that a typical stress-strain graph of a skin is non-linear and the response can be described as a three-phase deformation as shown in Figure 2-2. The first phase of the deformation shows that the skin experiences high strain even at low load, which the fibres are largely unaligned at this state. The second phase shows a non-linear relationship between stress and strain as

the fibres are aligning themselves in the direction of the load applied. The third phase shows that the stress increases dramatically with increasing strain because the collagen fibres are mostly aligned at this state and the overall stress-strain response becomes dependant on the mechanical properties of the collagen fibres (Silver et al., 2001; Hendriks et al., 2006; Holzapfel, 2001). Jacquemoud et al. (2007) found a distinctive difference between ultimate global longitudinal strain (Green-Lagrange strain, 9.5%) and the ultimate local longitudinal strain (Green Lagrange strain, 24%), which were obtained from the LVDT of the tensile machine and the DIC respectively.

Wan Abas & Barbenel, (1982) has performed a uniaxial tensile test on human skin as a whole by attaching two rectangular tabs on the human skin surface using double sided taped. The tabs were connected to a load application device that pulled the human skin. This study found that the strain distribution is non-homogenous with most high strains concentrated near area of load application. Was Abas & Barbenel (1982) also plotted a load-intensity against strain graph that has similar response to stress-strain relationship of excised human skin.

The strain behaviour of the human skin as a whole can also be studied without performing tensile tests. A few studies have investigated how the strain changes in the human skin when adapting different postures by measuring the full strain field of the elbow joint and knee joint, which showed that the high strains are more concentrated at the joint region (Obropta & Newman, 2015; Wessendorf & Newman, 2012). Obropta & Newman (2015) found out that the first principal strain (E_1) of a volunteer is 60% while the second principal strain (E_2) was 44%.

2.5.2 Contact type

Several studies have tried measuring the stresses and strains in human skin with different loading profiles - point, load or flat surface loading (Johnson & Phillips, 1981; Sripathi et al., 2006; Srinivasan , 1989; Dandekar et al., 2003; Serina et al., 1998; Wu et al., 2004; Wang, 2012). These studies predicted the skin deflection under different indentation profiles using theoretical continuum models like Timoshenko & Goodier (1970) or a revised version Johnson (1985). Some predictions were done using finite-element model simulations (FEM) based on additional conditions such as the skin is made of multi-layered materials or the finger pad is a structure of membranes filled with incompressible fluid.

In terms of point loading, Kwiatkowska et al. (2009) has shown that the skin facing the direction of a sliding ball is compressed and forms a “bow wave” shape whereas the skin

behind the sliding ball is in high tension as shown in Figure 2-13. Although this study did not measure the strain in human skin, it can give an idea of how the strain is distributed in human skin during sliding interaction with a spherical ball indenter.

In terms of line loading, Johnson & Phillips (1981) has studied how the strains in human skin changed when indented by a rectangular bar (line loading) and demonstrated that the strain in human skin is highest at the edges of the contact. This is especially obvious with a bar of longer width (Figure 2-14) where the strain profile computed shows two peak strains at either edges of contact between the rectangular bar and the human skin. It should be noted that the interaction between human skin and the indenter in this experiment was static.

In terms of flat surface loading, Delhaye et al. (2015) has compared the surface strain of a finger pad in contact with a flat smooth glass plate at partial slip phase (the phenomenon when a region of the area in contact between finger pad and glass is stick while the other region is slipped) obtained from experimental data and a theoretical strain prediction. This study concluded that the theoretical model was in qualitative agreement with the experimental work at low strain, but not in high strain region as shown in Figure 2-15.

Due to the fact that human skin is composed of multiple layers, the layers may experience different shear strain when the sample is subjected to shear load. As such, a study visualised the full field shear strain of a porcine skin under shear load to investigate how the shear strain changes by using 2D-digital image correlation (Gerhardt et al., 2012). This study found that the surface epidermal layer experienced approximately 4% shear strain, which decreased until the region between epidermal and dermal layer (3% shear strain). At the dermal layer, the shear strain increased again until middle region of the dermis layer where the highest strain (approximate 7-8%) was reached as shown in Figure 2-16.

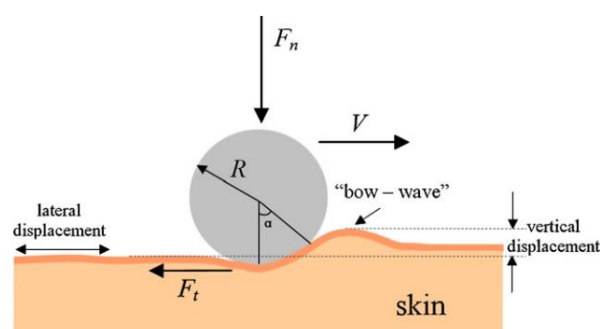


Figure 2-13, Sliding of a spherical indenter along human skin– near point loading (Kwiatkowska et al., 2009)

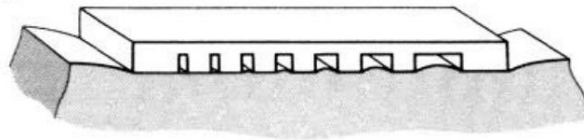


Figure 2-14, Line loading of different bar width on human skin (Johnson & Phillips, 1981)

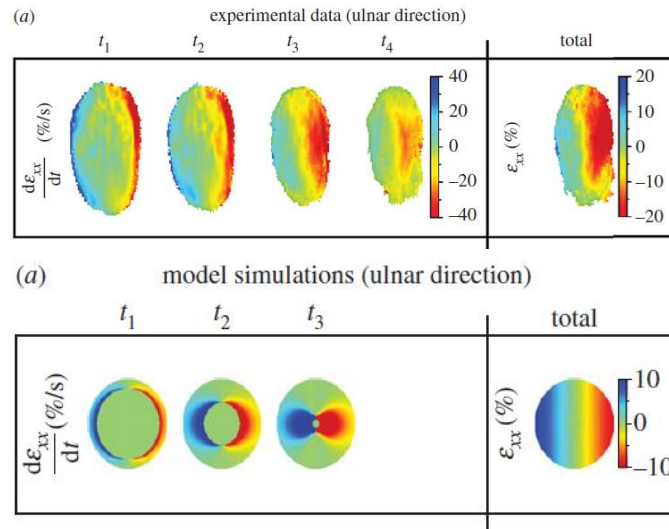


Figure 2-15, Experimental work (top) and theoretical model (bottom) of a finger pad partial slipped against flat smooth glass (Delhaye et al., 2016)

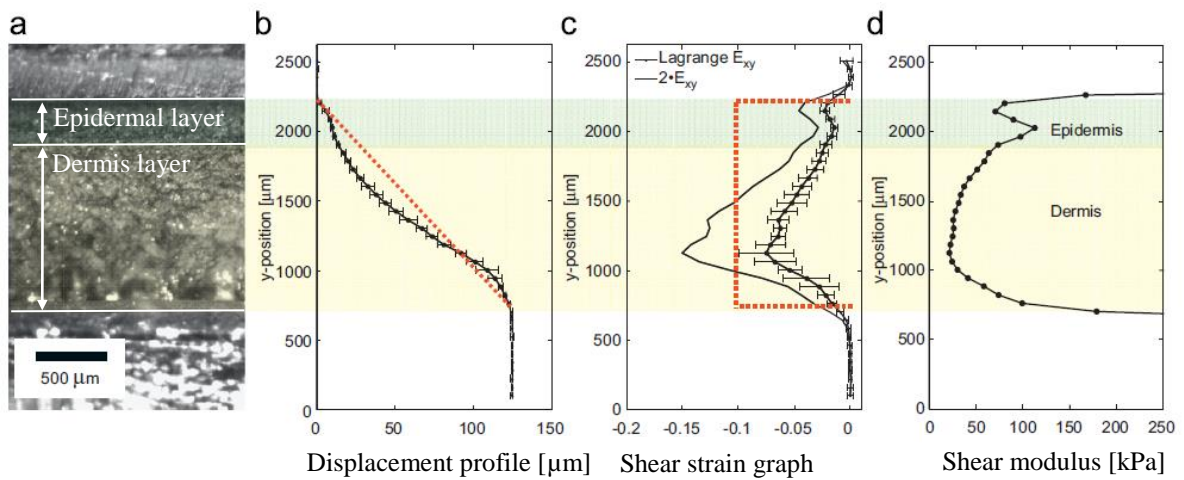


Figure 2-16, Shear strain data along the epidermal to dermal tissue, obtained from DIC (Gerhardt et al., 2012)

2.6 Strain assessment methods of soft tissues

In general, strain has been associated with stress of a body. In non-contact mechanics, strain assessment is easier with measuring techniques readily available. For example, the strain behaviour of soft tissue can be studied from a simple tensile test to strain visualisation of human skin while certain body parts are performing different postures.

On the other hand, strain study in contact mechanics is more complex and difficult. Unlike non-contact mechanics, very few studies have investigated the strain in soft tissue experimentally (Delhaye et al., 2016; Liu, 2013), although there are a lot studies that have investigated, developed and improved the theoretical models of soft tissue strain (Johnson & Phillips, 1981; Sripathi, 2006; Dandekar, 2003; Wang, 2012).

As such, this section by first introduces the common mechanical test set-ups that are possible for strain measurement. Then, it shows how the imaging techniques were used for respective mechanical tests. This part introduces other useful imaging techniques that have been widely used with soft tissue that can be related to the deformation of the soft tissue using different benchmarks such as the change in skin roughness when extending the forearm and also the orientation of tissue fibres after being slid with an indenter probe. The final part of this section will go through how the theoretical models of strain are applied to soft tissue.

2.6.1 Mechanical tests

The most direct approach for studying strain behaviour of soft tissue in non-contact mechanics is the tensile test. Most studies used tensile tests on excised soft tissue samples using conventional tensile machines (Jacquemoud et al., 2007; Annaidh et al., 2012). However, there is also one study that performed a tensile test on soft tissue (human skin) *in vivo* by pulling rectangular tabs attached on human skin (Wan Abas & Berbenel, 1982). In addition, a tensile test machine was also used in studying the shear strain behaviour of soft tissue (Gerhardt et al., 2012).

In contact mechanics, the most standard tests in strain studies are indentation tests and sliding tests. Originally, indentation tests were to define mechanical properties of soft tissue such as Young's Modulus (Pailler-Mattei et al., 2008; Zahouani et al., 2009; Genovese et al., 2015; Kao et al., 2016). In strain studies, indentation tests can be used to measure the surface deflection under a variety of indentation profiles (point, line, or flat surface loading), which will be used in theoretical modelling of strain and stress (Johnson, 2003; Sripathi, 2006). It

should be noted that indentation tests mentioned in this part are limited only to normal load application and there is no tangential force interaction between the two bodies.

Next, the sliding tests are used to study the frictional behaviour of the soft tissue with another solid body. The whole sliding process comprises of both static and dynamic states. During the static state, there are normal and tangential forces acting between the two interacting bodies, but the tangential force is not sufficient to cause sliding. By increasing the magnitude of the tangential force, it will reach a threshold value where the force holding the two bodies together preventing slip will be exceeded and sliding will occur. This is known as the dynamic state.

Sliding tests on soft tissues can be generalised into two types, the first type utilises a probe (mostly spherical) to slide across the soft tissue (Bostan et al., 2016; Nachman & Franklin, 2016; Kiwiatkowska et al., 2009). This test type normally uses a tribometer. The second test type requires a flat plate (smooth or ridged) during sliding interaction with soft tissue. For instance, the sliding of a finger pad across a ridged plate was investigated to study the hyperlocking effect of human skin in human skin friction (Tomlinson, 2009). Other studies that can be categorised as second types are Liu (2012), Derler (2010) and Adams (2006). The main difference between first and second testing types is the relative shape and size of the solid body interacting with soft tissue. In addition to the sliding tests mentioned above, which require both normal and tangential loading, there was a study that focused solely on the effect of shear loading on soft tissue (Gerhardt et al., 2012).

2.6.2 *Imaging techniques*

Digital image correlation (DIC) is the most popular imaging technique in measuring and visualising the full strain field of soft tissues by tracking the position of the speckles applied on the soft tissues. The visualisation of full strain field of human skin has been gathering interests from biomedical researchers because this technique can show the location of the strain concentration and the changes strain patterns when subjected to different loading types (Jacquemoud et al., 2007; Obropta & Newman, 2015). This is especially useful because soft tissue is an anisotropic and inhomogeneous material, for which the strain behaviour is asymmetric and dependent on a variety of factors such as the body location of where excised skin is obtained, the moisture of human skin etc.

There are two types of DIC: 2D-DIC and 3D-DIC. The first DIC system uses only one camera. 2D-DIC can only capture planar strain and insensitive to of plane measurement. The

latter uses two cameras. Therefore, a 3D-DIC system can capture the surface topography and the surface curvature of the objects.

Several studies have taken the advantage of full field strain on soft tissues (muscle, skin and organ parts) to determine the mechanical properties of the soft tissues (Jacqumond et al., 2007; Annaidh et al., 2012). For instance, Jacquamond et al. (2007) used image correlation technique on dead human skin undergoing tensile tests to investigate the failure mechanism of the human skin as Figure 2-17 shows.

In addition to tensile tests, DIC was used to map the surface strain field from different parts of body (Obropta & Newman, 2015). Some optical methods can also capture the 3D surface strain field from parts of the body. Obropta & Newman (2015) used 3D DIC to visualise the natural strain of the elbow joint of a volunteer that changed his arm posture without using external loading on the elbow or hand, as Figure 2-18 shows.

It should be noted that DIC is only able to visualise the strain distribution of the surface of the specimen and cannot determine the strain behaviour of the sub-surface of the specimen. This is unless the DIC is used to map the strain field of the specimen from the side of the specimen that can clearly show how strain changes across different layers of soft tissues (Gerhardt et al., 2012).

Optical coherence tomography (OCT) is more popular in studying the morphology of human skin. OCT has a similar function like ultrasound except OCT uses light as a medium, therefore the penetration depth is limited and OCT is normally used on human skin. It has been used for study of vascular morphology using correlation mapping (Enfield et al., 2011; Zafar et al., 2014; Zhang, et al., 2014; Byers et al., 2016) and measuring epidermal thickness of various body skin sites (Barton et al., 2003; Neerken et al., 2004; Gambichler et al., 2006; Josse et al., 2011; Tsugita et al., 2013; Trojahn et al., 2015). In addition to the epidermal thickness, Egawa et al. (2002), Li et al. (2006), and Trojahn et al. (2015) measured the arithmetic mean roughness, Ra, and mean depth roughness, Rz, of the top skin surface (stratum corneum). Most of the forearm studies using OCT have never considered angular variations of the volar forearm relative to the biceps/upper arm, variations of the angle of the elbow joint. Although OCT cannot directly provide any results on strain behaviour of soft tissues, but the morphology of soft tissue can give some important information on deformation of soft tissue when deformed or strained.

In addition, OCT can also be used in a biotribological experiment. Liu et al. (2013) demonstrated this by investigating the morphology of finger pad ridges in contact with a counter-face material - a smooth glass plate as Figure 2-19 shows. OCT was able to show clearly how finger pad ridges morph in contact with the smooth glass plate, which the images were then used to estimate the real in-contact area of the finger pad.

Confocal microscopy is an imaging technique that can image the fibres of soft tissues. It scans the samples with a focused beam of a specific wavelength, required to excite the fluorophore, which is the fluorescent chemical compound in fluorescent dye, and the fluorophore will re-emit the light signals with longer wavelength. The re-emit light signals are then collected by light detector and used to build up the image of porcine aortic tissue fibres point by point (Minsky, 1988). However, the main characterization of confocal microscopy is that there is a pinhole in front of the detector (a photomultiplier tube or PMT). Due to the small pinhole, only laser is able to give enough light energy into the small spot. Also, multiple lasers of different wavelengths can be used to give a range of wavelengths for multiple fluorescence. The main advantage of the pinhole is to smear out out-of-focus light from going through the PMT. Therefore a confocal image only contains in-focus information, increasing the resolution and quality of the images (Schatten & Pawley, 1988; White et al., 1987). In addition, by collecting a series of images, a full three-dimensional representation of the specimen can be collected. By using respective software of the confocal microscopy, the 3D images can be manipulated, controlled and provide different views on the specimen (Lichtman, 1994).

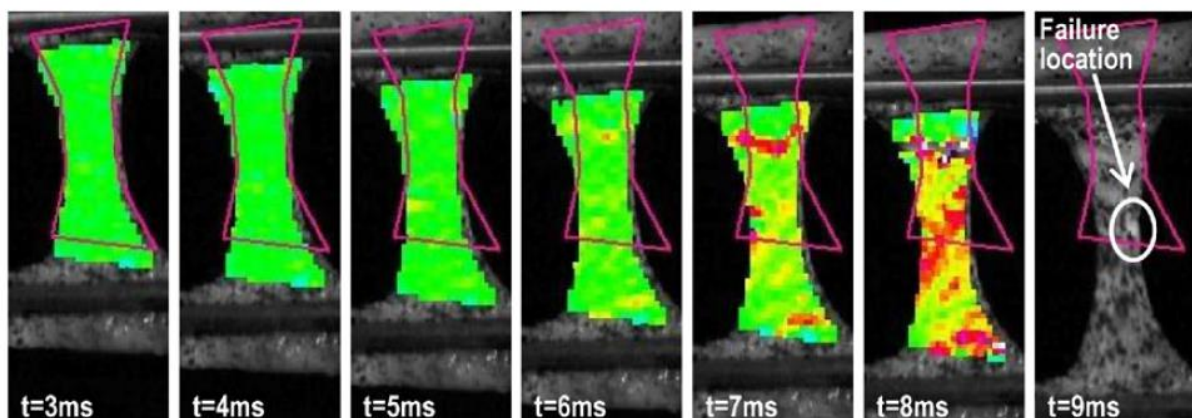


Figure 2-17, Tensile test on human skin - dead (Jacquomond et al., 2007)

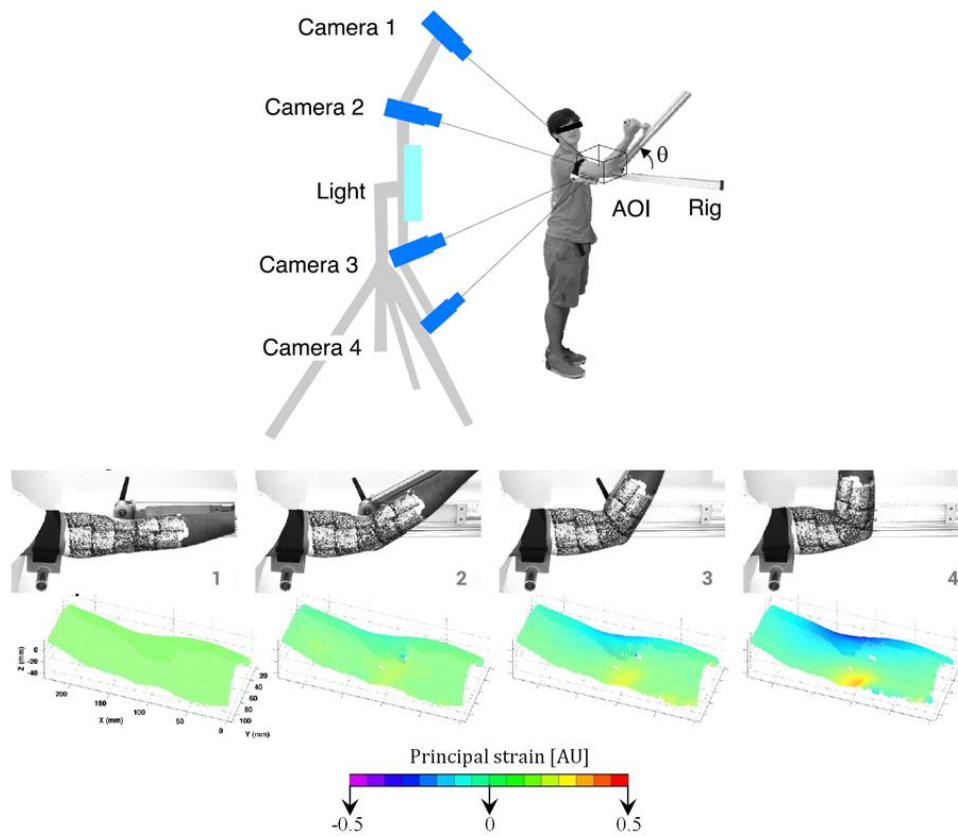


Figure 2-18, Full field strain of the elbow joint (Obropta & Newman, 2015)

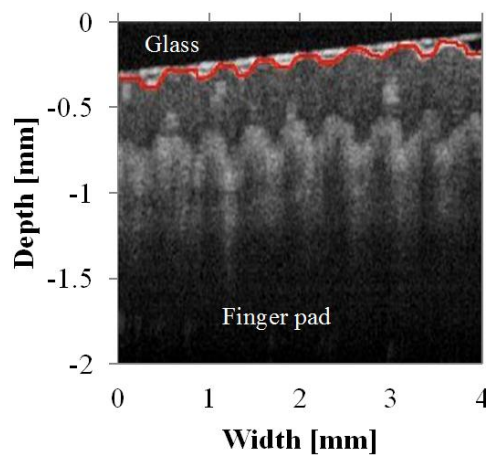


Figure 2-19, OCT image: finger pad skin in contact with smooth glass plate (Liu et al., 2013)

2.6.3 Skin modelling

Strain modelling is essential in contact mechanics of soft tissues due to the difficulties in strain measurement and visualisation in experimental studies. The stress and strain in numerical modelling and FE modelling required the surface deflection profile to start and compute (Johnson & Phillips, 1981; Sripathi, 2006; Dandekar et al., 2003; Wang et al., 2012).

Delhaye et al. (2016) used the approach (details of the formula derivation of the approach is attached in the Appendix A) explained in Johnson (1985) that uses the Boussinesq-Cerruti Equation presented by Love (1952) and the Hertzian surface tangential traction profile as described in equation 2-18, in which q_0 is the mean traction, a is the radius of the circular contact area and r is the radial position on the contact area of the traction profile. The traction profile is actually the shear stress distribution across a contact area.

$$q_x(r) = q_0 \left[1 - \left(\frac{r}{a} \right)^2 \right]^{1/2} \quad \text{Equation 2-18}$$

Delhaye (2015) modelled the finger pad as an isotropic elastic sphere and the glass plate was modelled as a rigid surface. The contact area of the finger pad is assumed to be circular. As the study focused only on the surface strain, a simplified surface displacement model based on Hertzian traction model is obtained (within the circular contact area, $0 \leq r \leq a$) and showed as equations 2-19 and 2-20, where ν is the Poisson's ratio of human skin and θ is the angular position of the radial position r on the contact area.

$$u_x(r, \theta) = \frac{\pi q_0}{32Ga} [2 \cdot (2 - \nu) \cdot (2a^2 - r^2) + \nu \cdot r^2 \cdot \cos(2\theta)] \quad \text{Equation 2-19}$$

$$u_y(r, \theta) = \frac{\pi q_0}{32Ga} [\nu \cdot r^2 \cdot \sin(2\theta)] \quad \text{Equation 2-20}$$

The displacement models are then applied to Green-Lagrange strain as displacement gradients in the contact area as shown in equations 2-21, 2-22 and 2-23.

$$E_{xx} = \frac{\partial u_x}{\partial x} + 0.5 \cdot \left[\left(\frac{\partial u_x}{\partial x} \right)^2 + \left(\frac{\partial u_y}{\partial x} \right)^2 \right] \quad \text{Equation 2-21}$$

$$E_{yy} = \frac{\partial u_y}{\partial y} + 0.5 \cdot \left[\left(\frac{\partial u_x}{\partial y} \right)^2 + \left(\frac{\partial u_y}{\partial y} \right)^2 \right] \quad \text{Equation 2-22}$$

$$E_{xy} = 0.5 \cdot \left[\frac{\partial u_x}{\partial y} + \frac{\partial u_y}{\partial x} \right] + 0.5 \cdot \left[\frac{\partial u_x}{\partial x} \cdot \frac{\partial u_x}{\partial y} + \frac{\partial u_y}{\partial x} \cdot \frac{\partial u_y}{\partial y} \right] \quad \text{Equation 2-23}$$

2.7 Soft tissue stimulants

Studying soft tissue is difficult due to its complex nature, as soft tissue comprises of several layers of materials that have different mechanical properties. There are a number of factors that could influence the friction and strain behaviour of soft tissues such as age, ethnicity, the skin condition etc. (Liu, 2012). Experiments on human subjects have also proven to be a

difficult and lengthy process because human experiments require ethical approval and need to give extra care in designing experiments to not cause discomfort to volunteers. In addition, resourcefulness is required to get a group of volunteers for more accurate experimental results.

As such, there has been increasing demand for developing tissue simulants to serve as an alternative for soft tissues in experimental studies. Some of the tissue simulants that are available commercially, like EpiDermTM, EpiSkinTM etc., are used in cosmetic industry for the application of cosmetic products or treatment of skin wounds. These tissue simulants are designed to imitate the biological properties of the human soft tissue but not the mechanical properties.

In terms of mechanical properties, silicone rubbers and polyurethanes are the most popular materials of choice in imitating human soft tissues. However, these materials do not have the same biological properties as human soft tissues especially human skin. For instance, silicone rubber cannot absorb water like human skin due to its hydrophobic material properties.

Two recent studies have investigated the frictional behaviour between tissue simulants and soft tissues. Nachman & Franklin (2016) found that the frictional behaviour of a multiple layer tissue simulant (top layer: silicone rubber; bottom layer: polyurethane gel) was similar to the human skin. Likewise, Boston et al. (2016) concluded that a reliable test platform could be achieved by using a tissue engineered skin as the top layer and a synthetic skin (SynDaver) as the bottom layer.

2.8 Summary

From the perspective of a mechanical engineer, soft tissue is a very complex material. Unlike other materials, it has mechanical properties that are very difficult to predict accurately due to the large amount of influential parameters. Yet, it is very important to our daily life because soft tissue is one of the most common materials as most multicellular organisms will be comprised of soft tissues.

Imaging techniques are important in the study of soft tissues because imaging techniques are the common tools in measuring to obtain information regarding the mechanical properties of the materials. For example, DIC was generally used to investigate the tensile strength of the soft tissues or the natural strain of the human skin while performing

simple movements in several studies but seldom used to study the strain of soft tissues while interacting with a counter-face material. On the other hand, OCT and confocal microscopy are generally used to study the sub-surface morphology of the biological samples. Only very few studies have actually used OCT to study the roughness of the soft tissues during tribological interactions. It is similar for confocal microscopy as well. There are few studies that have investigated the structure of the soft tissue before and after damaging the soft tissue using friction (Barros et al., 2015; Bostan et al., 2017). The main disadvantage of this method is it cannot capture the soft tissue behaviour when damage is being applied in real-time.

A lot of past literature has studied the frictional properties of human skin. These studies provided detailed information on the friction mechanism of a human skin and have quantified various parameters affecting the frictional behaviour of the human skin. As the research on human skin tribology advances and becomes more complex, the friction on the human skin is often caused by adhesion, deformation or both. At the same time, recent studies have identified more and more parameters affecting the human skin friction (Adam et al., 2007; Derler & Gerhardt, 2012; Tomlinson et al., 2011a; Tomlinson et al., 2011b; Liu). The frictional behaviours of the human skin showed in section 2.3 are the most general and popular friction mechanisms. Only these frictional behaviours are listed because these could potentially occur in this study. One of the main objectives of this project was to find the link between the strain behaviour and the frictional behaviour of the human skin. So, it is important to understand the strain behaviour of the human skin. There have been a lot of previous studies done on the human skin strain as mentioned in section 2.5 (Wan; Gerhardt, holzapfel etc.). However, very few researchers have measured the strain and friction of the human skin in the same experiment because it is difficult to acquire the strain field profile of human skin in contact with a counter-face material experimentally. As such, many studies used the numerical modelling method to determine the strain field of human skin instead.

The literature on the tactile of human skin is not focused because this study focuses more on studying the friction and strain behaviour of the human skin using imaging techniques. Also, unlike other studies that used counter-face material with a complex geometry, this study mostly focuses on a flat counter-face material during the imaging of the human skin sliding interaction (Tomlinson et al., 2011a; Kuilenburg et al., 2013).

Most contact models discussed in this chapter assume a linear elastic material because this model is used to test the feasibility of the imaging techniques. However, it should be

noted that the human skin is a viscoelastic material. This is important when the human skin is undergoing sliding interaction. After sliding has stopped, the contact area of the human skin would experience a slow recovery phase due to its viscoelasticity. Therefore, more in-depth work can be done in the future if the imaging methodologies can give useful measurements.

In this study, the imaging techniques are particularly used to work towards studying the strain of soft tissue in real-time, especially when interacting with a counter-face material. Firstly, this study attempts to determine the strain field of human skin undergoing tribological interaction using 3D-DIC and combine with the OCT that studies the morphological changes of the human skin during sliding. Based on the previous studies, the mechanical properties and the condition of the human skin vary significantly depending on the internal and external parameters such as the gender, age, surrounding temperature, humidity etc. Therefore, a human skin simulant is manufactured and studied to minimise the gap between a human skin and a skin simulant. The next stage of this study will test the feasibility of a theoretical strain modelling by modelling the skin simulant used in this study.

In addition, 3D-DIC and OCT are also used to study the natural strain of the forearm skin while performing simple movements to show that identical methodology can also be used on non-tribological experiments.

The main reason 3D-DIC and OCT are used to study the strain of soft tissues because these imaging techniques can compute and visualise deformation and strain of the soft tissue. Although this research focuses mainly on 3D-DIC and OCT, confocal microscopy is also used to study the structural changes of a different soft tissue, which is the porcine aorta. Porcine aorta is used instead of human skin with the confocal microscopy because this imaging technique is detrimental to perform *in-vivo* human skin experiment. Total internal reflection imaging is not used in this study because this project is not focused on strain study at a cellular level.

Chapter 3

Imaging Equipment Set-up

3.1 Introduction

Different work packages in this research have used different imaging techniques and each of these had different testing procedures, data and post-processing. So, this chapter will outline the principal, equipment and set-up used and the post-test analysis for the imaging techniques used in this research.

It first describes the approach used for the 3D-Digital Image Correlation (DIC) system that is able to measure the 3 dimensional shape, displacement and strain of a specimen. This section also includes the post-process analysis used on the DIC data in this research. Next, the chapter introduces the medical Optical Coherence Tomography (OCT) used to investigate the human skin structure. This section also describes the image analysis technique used to determine the roughness of the surface of the human skin and the thickness of the epidermal layer. Finally, confocal microscopy is introduced. This imaging technique can show the micron scale structure of the soft tissues such as elastin and collagen fibres. The final section demonstrates how the imaging software, ImageJ, is used to analyse and determine the orientation of the tissue fibres in the images.

3.2 Three-Dimensional Digital Image Correlation (3D-DIC)

3.2.1 System Overview

The principal of DIC relies on tracking the random and unique speckle pattern on the material surface by using DIC software. The speckle pattern will be assigned a series of subsets, as in Figure 3-2. Then, Figure 3-1 shows how DIC tracks the speckles via the deformed subset, where the displacement vector and displacement gradient can be extracted from the deformed subset. The displacement gradient will then be used to compute the strain field of the subject.

A DIC system that uses two cameras is known as 3D-DIC. As a 3D-DIC system, it is able to give the three axial of the position of the speckles and the respective three axial displacement vectors. However, 3D-DIC cannot compute the tri-axial strain in three axes, it can only give the local surface strain, which the strain direction is tangential to the surface of the subject. This is due to the fact that the third axis strain computation, along z-axis for example, requires a displacement gradient along the z-axis, which the 3D-DIC algorithms is unable to compute because the 3D-DIC algorithm is built on the assumption of plane strain.

In order to collect strain data using 3D-DIC, the user must have a sample that has speckles and a set-up with calibrated cameras. Images that are captured during the test will be analysed using a DIC software. These can be classified into 5 steps, which are sample preparation, camera set-up, calibration, data collection and post-processing.

The surface strain measurement of the specimens (Chapter 4, 5 and 7) were performed using a 3D-DIC system, VIC-3DTM, from Correlated Solutions, Inc., which the set-up is shown in Figure 3-1. This system includes two Pike F505B cameras (Allied Vision Technologies GmbH, Germany) equipped with monochromatic CCD sensor (Sony ICX625; 2/3"; 2452×2054 pixels) and 50mm lens objectives (XENOPLAN2.8/50-0902, Schneider, Kreuznach). There are two softwares available. The first, 'Vic-Snap' is mainly used as a trigger to capture the images of the samples. Second, 'VIC-3D' (version 7.2.4) is a commercially available software with the DIC algorithm.

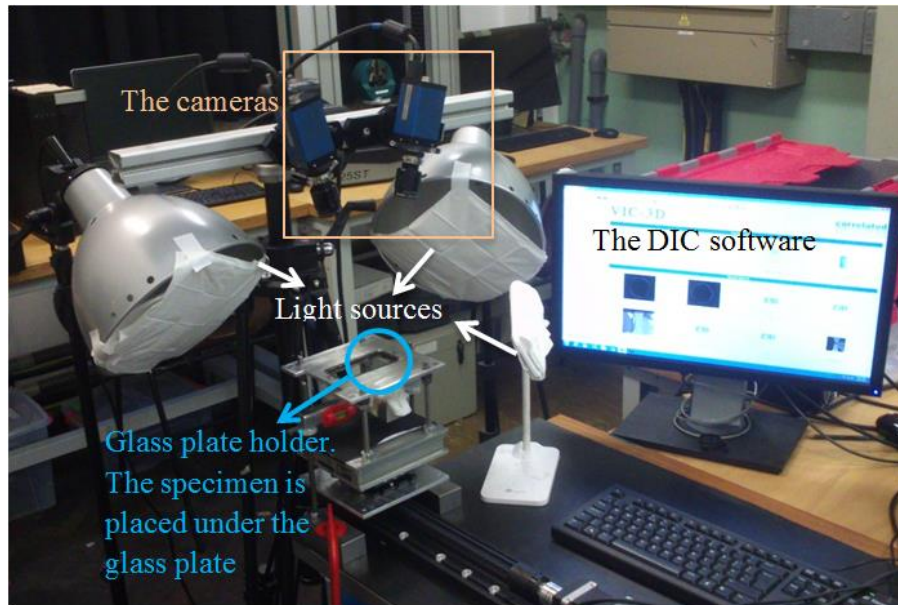


Figure 3-1, Stereo DIC set-up

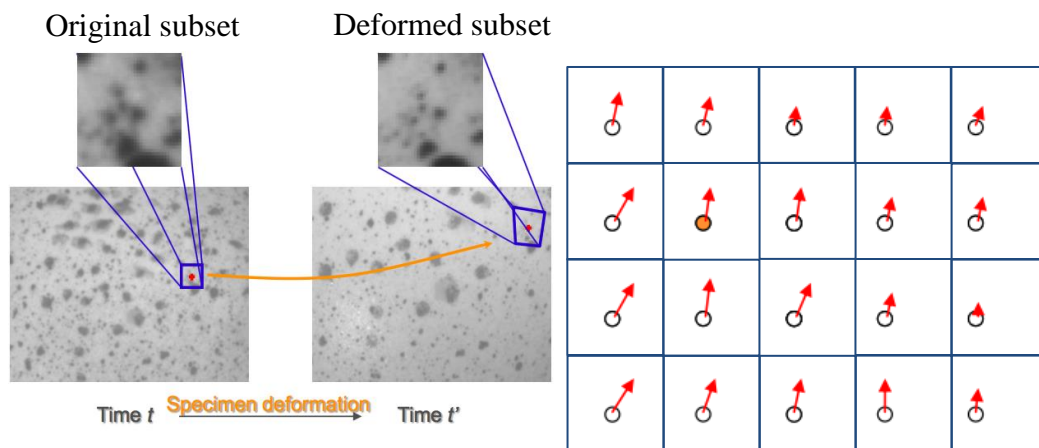


Figure 3-2, Working principal of DIC - The tracking of the “blue box” subset (left), the region of subsets will eventually form a field of displacement vectors, “red arrows”, that will be used for strain computation (right)

3.2.2 Sample preparation

The first step in using stereo DIC system is to know how to apply speckles pattern on the specimens. There are several methods to apply speckles pattern on the experimental sample. The speckles pattern should be random and have good contrast against the background (Reu, 2015). Some application methods are able to produce fine speckles with a size of less 1mm^2 , while some are only able to produce a large speckle pattern.

In this study, three methods were trialled, as shown in Figure 3-3. One of the methods is the airbrush method. An airbrush can produce very fine speckles, even on small specimens. Fine speckles on small specimens will improve the spatial resolution of the DIC data. The second method was to use an aerosol paint spray (black ink), which is commercially available. The aerosol paint spray method is able to produce very fine speckles for small specimens as well. The third method was the toothbrush method, in which the speckle pattern is applied through flicking the bristles of the toothbrush after dipping in ink. The size of the speckles is slightly larger using this method.

The airbrush and toothbrush method require the preparation of the ink. The colour of the ink is essential, as the speckles on the specimen should form a good contrast during image correlation stage. In this study, the finger pad and forearm (Chapter 4 and 7) and silicone hemi-spheres (Chapter 5) have a light-coloured background. Therefore, a black water-based ink (crafters acrylic paint, DecoArt Inc., Stanford) was used, mixed with a paint thinner at a ratio of 1:3. Then, the paint was to first applied on a piece of paper from a distance, approximately 20-30cm and 3-5cm for the airbrush method and toothbrush method respectively. This was to test out if the speckles sizes were suitable for the sample. When the speckles sizes were satisfactory and consistent on the paper, the speckles could then be applied on the sample as Figure 3-3 shows.

In summary, every speckles application method will be acceptable as long as the speckles applied form a good contrast with the background (Reu, 2015).

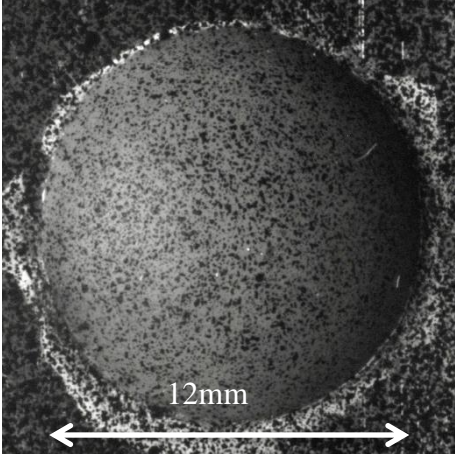
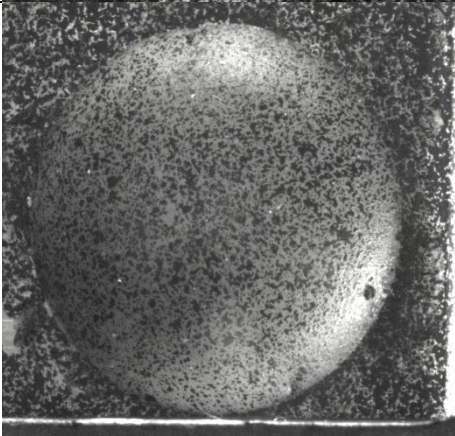
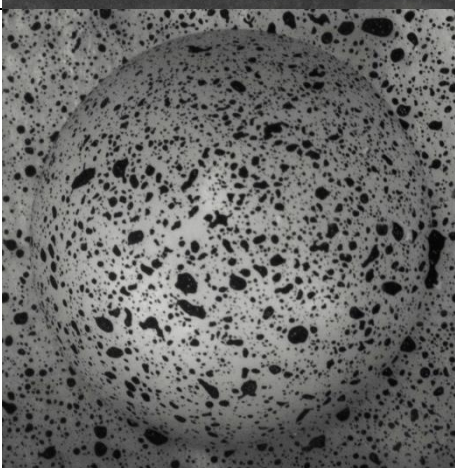
Speckles application method	Outcome (Topview)	Speckles relative size
Airbrush		Very Fine
Aerosol paint spray		Fine
Toothbrush		Least fine

Figure 3-3, The size of the speckles using different speckle application methods (on a silicone hemi-sphere)

3.2.3 Camera set-up

To start using the stereo DIC system, the cameras should be correctly set-up based on the experiment set-up. Throughout the set-up, VIC-Snap (Columbia, Correlated Solution), an image acquisition software, was used to monitor the live image set captured by the cameras. There are a few set-up parameters that need to be considered before setting up the cameras.

Firstly, the stereo angle between the cameras, illustrated in Figure 3-4. The stereo angle should be chosen between 20° and 60° (Reu, 2012). The out-of-plane measurement is more accurate with a wider stereo angle while a narrower stereo angle gives less projection errors.

The next set-up parameter to be considered is the distance between the cameras and the specimen. Ideally, the specimen should roughly fill up the field of view of the cameras. If the distance between the cameras and the specimen is too short, then the specimen will be larger than the field of view of the cameras. This will cause the DIC data to be localised on a small region of the specimen. On the other hand, if the distance between the cameras and the specimen is too far, then the specimen will be smaller in the field of view of the cameras. In this case, the spatial resolution of the DIC data will be reduced. In addition, the deformation of the specimen should also be taken into account because the deformed specimen must remain in the field of view of the cameras. For instance, the silicone hemi-spheres (Chapter 5) with low Young's modulus will be more susceptible to high deformation. Therefore, the silicone hemi-sphere should only fill up roughly half of the field of view of the cameras.

Before adjusting the focus of the cameras, the aperture of the lens should be turned to the largest possible. This will help in finding a good focus more easily. After the focal length has been fixed, then the aperture of the lens can be adjusted to the appropriate setting. This is illustrated in Figure 3-4.

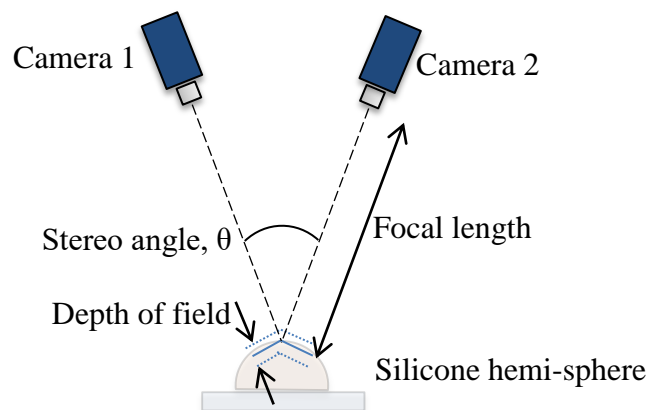


Figure 3-4, Stereo camera set-up terminology

3.2.4 Calibration

After the cameras are set-up, the next step is to perform the calibration for the cameras. Unlike the 2D-DIC, where the calibration only requires measuring the ratio of the actual

distance to the pixels dimension in the image, 3D-DIC requires a more sophisticated calibration. A calibration grid is required for the calibration of the stereo DIC. The calibration grid consists of an array of dots with fixed distance between each dot. Among the dots, there are three distinctive hollow marker dots (highlight using red circles), which the Vic-3D software will track during the calibration process, as shown in Figure 3-5. The calibration grid should also roughly fill up the field of view of the cameras at the same focal plane as the specimen that consist of all three hollow maker dots because the calibration algorithm is designed to track the three hollow marker dots before tracking other dots. Therefore, if the tracker dots are too small, then the Vic-3D software will not able to find the dots while if the tracker dots are too big then calibration will be unsuccessful.

In the acquisition stage of the grid images, it is typical to acquire 15 to 20 sets of grid images. But, it is better to acquire abundant grid images because this allows poor images of high calibration score (red) to be discarded as shown in Figure 3-5. The grid images captured should consist of the grid in various poses that include significant grid rotation about all 3 axes and moving closer and further away from the cameras. These will help in estimating the perspective information, aspect ratio and distortion accurately.

The Vic-3D will give a calibration score, which is the standard deviation of residuals for all views (Vic-3D Testing guide v7). If the final calibration score is green, then the calibration can be accepted and the user can proceed with acquiring images of the specimen that under consideration.

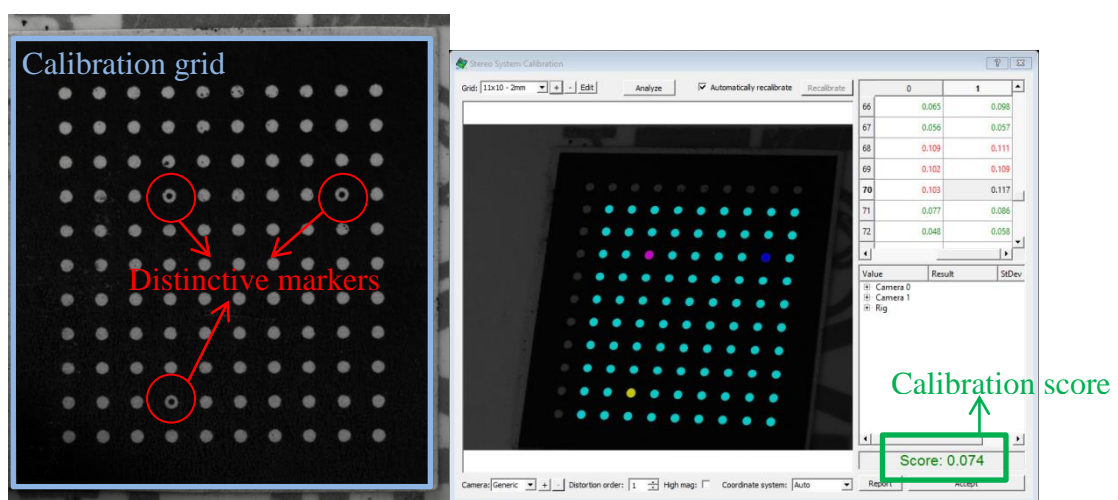


Figure 3-5, Calibration grid (11*10 dots with 2mm space between each dots) with three distinctive hollow marker dots (left) Calibration score (right)

3.2.5 Data Collection

The next stage involves image acquisition of the specimen undergoing deformation in an undeformed state. For the Vic-3D system, the image acquisition of the specimen is achieved using Vic-Snap, which is an image acquisition software developed by Correlated Solutions. The only setting that required attention is the image acquisition rate or the frame rate. This is highly dependent on the type of camera. The maximum frame rate of the 3D-DIC system in this study is 8 frames per second.

3.2.6 Image Correlation

A 3D-DIC system gives two pair of images showing an undeformed and a deformed specimen. The image correlation algorithm will compute the position/displacement field of the specimen for each pair of images, which is similar to 2D-DIC. Then, the 3D-DIC algorithm could generate the 3D position/displacement data by triangulating the two pairs of images using the calibration that has been set-up previously. The 3D displacement field can then be used to compute the surface strain of the specimen.

In order to correlate images using VIC-3D, an area of interest must be defined, as shown in the transparent red box in Figure 3-6. Then, the appropriate subset size and step size can be selected. The subset size controls the partial region of the image that is used to track the displacement between the images (Vic-3D reference manual, 2010). As such, the subset size has to be large enough to contain some distinctive speckles pattern. In addition, the subset size also directly affects the spatial resolution of the DIC data, which is shown in Figure 3-7.

The step size controls the spacing of the points that are analysed during correlation (Vic-3D reference manual, 2010). If a step size of 1 is selected, then the correlation analysis will be performed at every pixel inside the area of interest. However, a lower step size has a very high correlation analysis time because the analysis time varies inversely with the square of the step size. As a trade-off, the step size selected is either half of the subset size selected or less.

For the strain computation, the settings that require attention are the filter size and the strain tensor type. Filter size is required for smoothening of the strain data, which the total smoothening area is the multiplication of filter size and step size. The smoothened area is also known as the virtual strain gauge size. If the virtual strain gauge size is too small, the DIC data will become noisier. On the other hand, oversized virtual strain gauge will produce

erroneous strains for specimen with complicated geometries, for instance, a curved surface specimen such as silicone hemi-spheres. In this study, the Green-Lagrange strain tensor was chosen throughout the study because the spatial coordinates of the specimen change with time. If the correlation is successful, a full field displacement/strain DIC data can be presented, as shown in Figure 3-8.



Figure 3-6, Area of interest selected

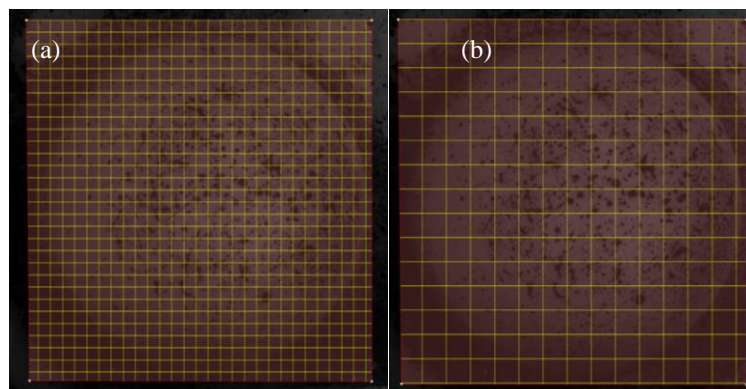


Figure 3-7, Selected subset size within the area of interest (a) 41×41 pixels (b) 81×81 pixels

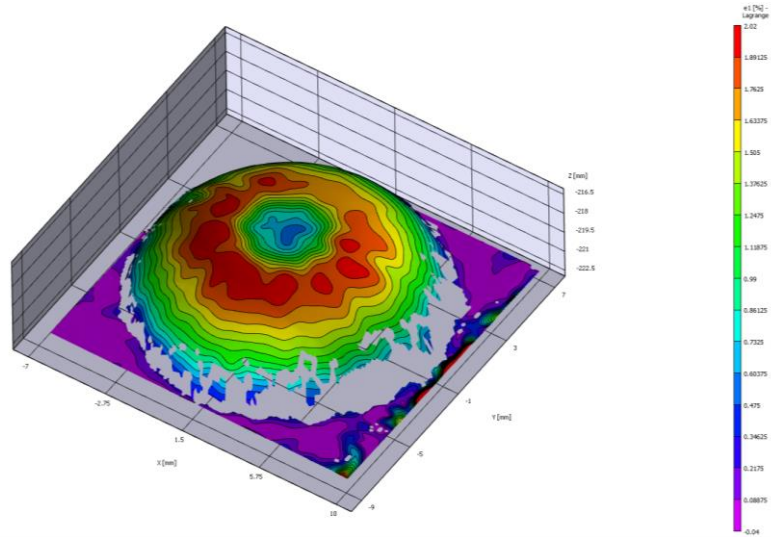


Figure 3-8, The first principal strain of a silicone hemi-sphere (Chapter 6)

3.2.7 Strain Analysis

There are generally two types of strain measure for hyperelastic material, which are Euler Almansi strain and Green-Lagrange strain. The first strain measure is Eulerian based while the latter is Lagrangian based. Eulerian based strain measure tracks a spatial point across at different time points while the Lagrangian based strain measure tracks a material point at different time points. Therefore, a Green-Lagrange strain tensor is chosen because the DIC software tracks the material points (speckles) on the specimen.

The Green-Lagrange strain tensor, E , was calculated based on a deformation gradient tensor formulation for motion kinematics mapping from a reference to a deformed configuration (Parsons et al., 2004; Sutton et al., 2009).

$$E_i = \frac{1}{2} (F_i^T \cdot F_i - I) = \frac{1}{2} (C_i - I) \quad \text{Equation 3-1}$$

where E_i is the Green-Lagrange strain tensor of point i of the random pattern, F_i is the corresponding deformation gradient based on the reference frame, C_i is the right Cauchy-Green deformation tensor, I is the unit matrix.

The matrix components of tensor E are given by:

$$[E] = \begin{bmatrix} E_{xx} & E_{xy} \\ E_{yx} & E_{yy} \end{bmatrix} \quad \text{Equation 3-2}$$

Note that tensor components in the Equation above are referred to pattern surface and hence evaluated on two-orthonormal local axis X, Y tangent at each point of the pattern. Out-of-surface strains are considered to be negligible versus computed membrane (surface) strains, according to the classical hypothesis of thin layer surface kinematics (Timoshenko & Woinowsky-Krieger, 1959).

As the matrix $[E]$ is symmetrical, by definition $E_{yx}=E_{xy}$. By introducing eigenvalues λ in the strain matrix, which by mathematical definition are principal strains when the determinant of the matrix becomes zero, which is in associated principal strain directions, the shear components E_{xy} are null.

$$\begin{bmatrix} E_{xx} - \lambda & E_{xy} \\ E_{yx} & E_{yy} - \lambda \end{bmatrix} = 0 \quad \text{Equation 3-3}$$

The principal strains E_1 and E_2 were computed from the characteristic polynomial, as shown in Equation 3-4.

$$(E_{xx} - \lambda) \cdot (E_{yy} - \lambda) - E_{xy}^2 = 0 \quad \text{Equation 3-4}$$

Solving the characteristic polynomial of Equation 3-4 will give:

$$\lambda_{1,2} = E_{1,2} = \frac{E_{xx}+E_{yy}}{2} \pm \sqrt{\left(\frac{E_{xx}-E_{yy}}{2}\right)^2 + E_{xy}^2} \quad \text{Equation 3-5}$$

$\lambda_{1,2}$ are eigenvalues of matrix E and called principal strains.

3.2.8 Post-processing

Successful correlation can give the full field displacement data U , V and W of the specimen. Full field strain data E_{xx} , E_{yy} , E_{xy} , E_1 and E_2 can be presented in contour terms as well. However, due to the complex shape geometry of the specimen (curved surface) in this study, the 1st principal strain and 2nd principal strain are often used to describe the strain behaviour of the specimen. This is also due to the fact that the reference axes of the full field strain data are localised. The X, Y and Z-axes in Figure 3-8 are used only to plot the shape of the specimen.

As the 3D-DIC system captures images at real-time with a frame rate at 5fps, so this means that the strain behaviour of the specimen is registered every 0.2s. This could help

visualising the viscoelastic property of the soft material specimen especially when the soft material recovers from deformation.

3.3 Optical Coherence Tomography

3.3.1 System overview and set-up

Optical Coherence Tomography (OCT) is a non-invasive imaging technique that can take images that show the surface and subsurface morphology of biological tissues. The working principle of the OCT technique is dominated by interferometric methods. Infrared light is split into two paths as shown in Figure 3-9. The first path launches into the sample and the second path goes to a reference mirror. The combination of lights scattering in the sample and the reference generates a two dimensional image (Fercher, 2010). Normally the OCT has a penetration depth of 1 - 2 mm in a sample with varying path length.

The morphology and the structure of the human skin (Chapter 5 and 7) were imaged using clinically approved Vivosight from Michelson Diagnostics (Kent). The Vivosight system is a Fourier domain OCT with a 20kHz swept source diode laser at 1300 nm centre wavelength. OCT is able to present different image results depends on the types of scanning, which are known as A-scan, B-scan and C-scan. A-scan is the abbreviation for axial scan that shows the intensity of the reflected optical amplitude (described as gray value) along the distance (pixels) on the axis of the light propagation, as shown in Figure 3-10. A B-scan gives the cross-sectional images of the specimen whereas C-scan is a volumetric scan that uses multiple B scans to form a 3-dimensional scanned specimen, as shown in Figure 3-10.

The Vivosight OCT has a 7.5 μ m lateral and 5 μ m axial resolutions with an A scan image capture rate of 20 frames per second with each image of 1342 \times 460 pixels. The hand held probe of the Vivosight OCT system has a visible red spot that is used to position the scan on the required area of the skin. In addition, the live imaging of the OCT software can be used to further pin point the region for imaging. The probe was fixed in a microscope holder to improve the stability through the scanning process, as shown in Figure 3-11. There is a method to make sure that the resolution of the image is a correct representation of actual magnitude of the measurement. The user can first capture an image by aligning the scanning region to a small rectangular piece of paper with a set length of less than 6mm. Then, ImageJ can then be used to measure the length of the paper that had been scanned.

The hand held probe “standoff”, as shown in Figure 3-12, is removed to prevent a physical contact with the human skin (Chapter 4) as the contact will affect the natural stretching of the human skin at different postures. The probe standoff was removed in the finger pad glass interaction experiment (Chapter 7) because the physical contact between the standoff and the glass will affect the force behaviour and the surface strain of the finger pad. Therefore, the working distance between the probe and the specimen is adjusted using a microscope holder to get an optimum B-scanned OCT image.

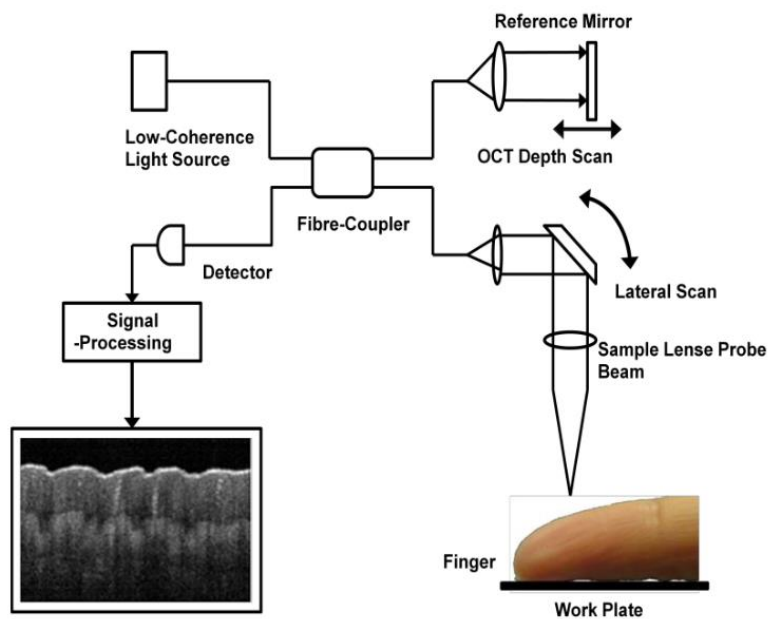


Figure 3-9, Working principal of an OCT system (Liu, 2013)

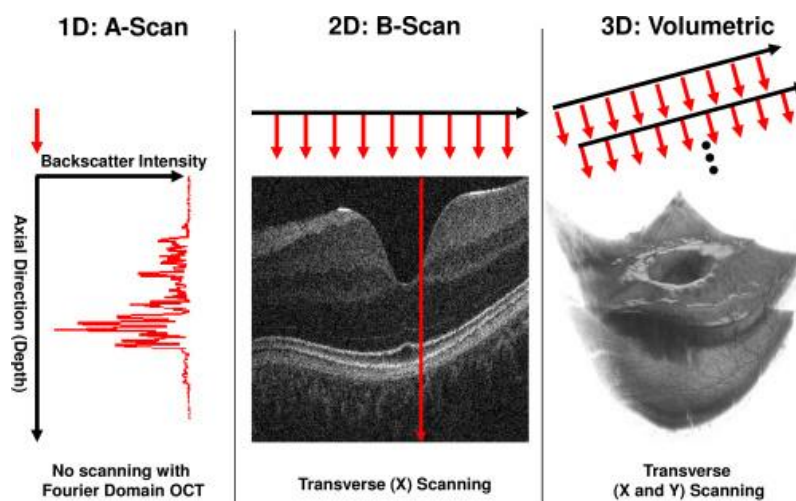


Figure 3-10, Illustration of A-scan, B-scan and C-scan (Kraus, et al., 2012)

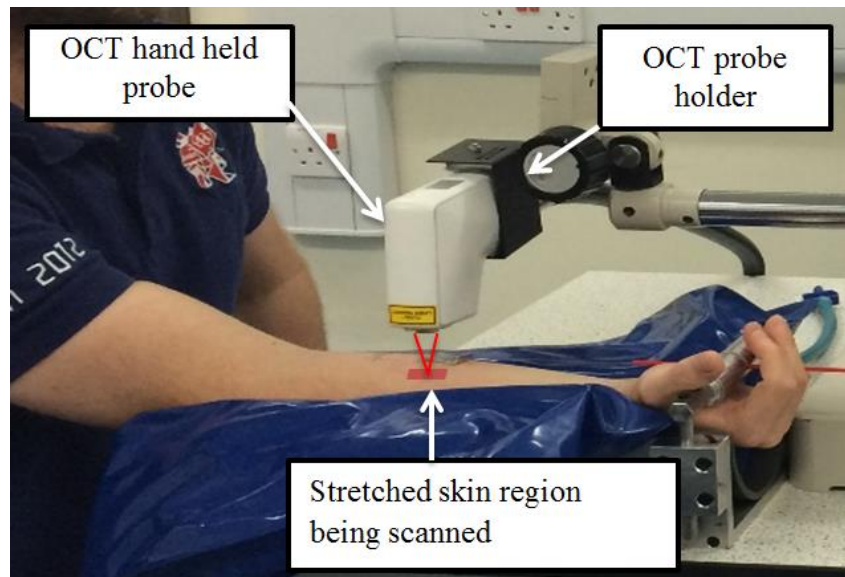


Figure 3-11, Vivosight OCT set-up



Figure 3-12, Removing the probe standoff

3.3.2 OCT image analysis

B-scan images obtained from OCT measurements were first converted to single tag image file format (tiff) file by using an image-processing-software ImageJ from ImageJ Developers. Next, a Matlab algorithm (Matlab version R2015a) was used to identify the boundary lines of the skin layer. The Matlab algorithm was developed by a post-doctoral researcher and a Ph.D. student (Maiti et al., 2016).

The surface is identified in each image (yellow line in Figure 3-13(a)) and the dermal-epidermal junction (DEj) (green line in Figure 3-13(a)). However, it should be noted that the layer between the surface boundary line and dermal-epidermal junction (DEj) is still under debate as to whether this layer is stratum corneum or epidermal layer. The boundary lines

identified are used to determine the roughness of the skin or the dermal-epidermal junction (DEj). It is then used to study the morphological change of the skin. This identification method is based on the change in the gray value in the light intensity profile from the A scan (Kraus et al., 2012).

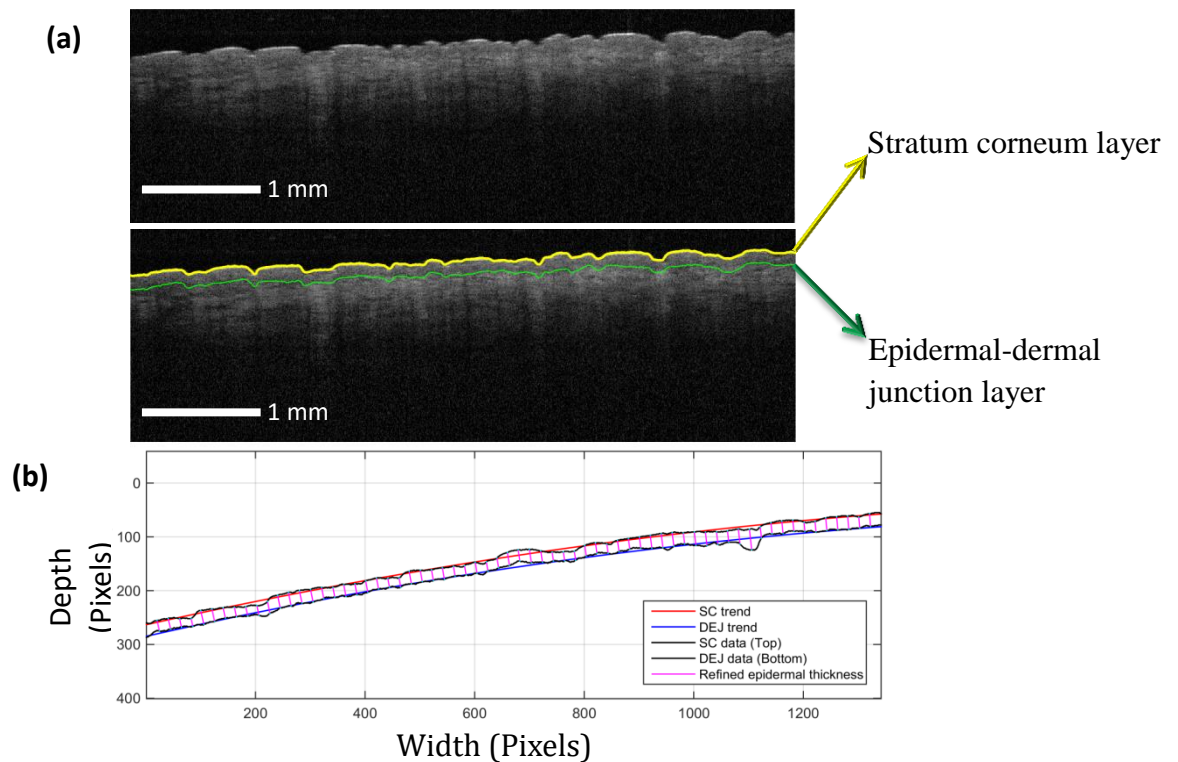


Figure 3-13, Procedure for determining the epidermis thickness (a) the boundary line detection for stratum corneum (yellow line) and dermal-epidermal junction (green line) (b) thickness determination of epidermis (in pixels) based on skin layers detection

The Matlab algorithm uses anisotropic filtering to remove the speckle noises from the images, using priory knowledge of the multiple channel foci in the multi-beam OCT. A first mean filter is used to remove speckle noise from the images. First, a proprietary filter is used to blend the four multi-beam OCT channels, which maximises speckle suppression while maintaining resolution and contrast. A second mean filter is then used (chosen for simplicity and speed) which is not uniform in shape, having a greater size in and giving greater weight to pixels in the X and Y dimensions (i.e., laterally). This filter has been chosen to preserve resolution in the axial dimension and therefore minimise blurring of the interface between the epidermis and dermis.

The image is then processed using two separate algorithms, in which the first of these uses an edge filter designed to identify the boundary line between the air and the stratum corneum by targeting the edge spike combination caused by the sharp change in refractive index. Candidate edges exceeding a threshold (greater than 30 pixels in size) are recursively used to calculate a confidence value for each measurement based on surface smoothness and edge-fit. This confidence is used to negate the effect of surface artefacts caused by overlaying hairs or surface “flare” or reject measurements if no satisfactory solution can be found. Finally, the point in each image column with the greatest confidence factor is chosen.

The second algorithm was designed to detect the contrast change at the dermal-epidermal junction (DEj), where the image changes in character from the grainy keratinocytes of the spinosum to the smoother, mottled and brighter papillary dermis (Abignano et al., 2013). At the position of the meeting of these two skin layers, a hyporeflective region (typically visible as only a line in OCT images of this resolution) is present, due to the relatively high nuclear-cytoplasmic ratio within the basal membrane (Coleman et al., 2013). Detection of the candidates for this surface is selected in a similar manner to the algorithm used to detect the skin surface.

No direct validation exists confirming the selection of the correct morphological feature in this step, but widespread consensus of its identity is present in literature, based on histology correlation (Coleman et al., 2013) and, in the case of pathological morphology, modification of the DEj in a manner predicted by knowledge of the condition as investigated by Pomerantz et al. (2011), Sattler et al. (2013), Alawi et al. (2015) and Ulrich et al. (2015).

In addition to boundary segmentation of stratum corneum and DEj, the algorithms were programmed to determine epidermal thickness, skin surface roughness and geometrical parameters of the dermal-epidermal junction roughness. To account for any possible skin curvature in the OCT images, the epidermal thickness was calculated by measuring the perpendicular lines (approximately 224 lines per mm) between the 3rd order polynomial fitted stratum corneum and fitted dermal-epidermal layer, as shown in Figure 3-13(b), on the basis of a locally weighted fit and a 5-point moving average filter (Matlab command `loose` with smoothing parameter of 0.1). Epidermal thickness distribution is shown in boxplots and data reported as mean thickness \pm 1 SD.

To remove the natural curvature from the surface topography, discriminate between waviness and true surface roughness (topography profile decomposition in waviness and

roughness) and be able to reliably determine the geometry change of DEj, the skin line profiles of SC and DEj layers were trend removed by subtracting a 3rd order polynomial curve fit of the topographical profile from the full profile as shown in Figure 3-13. The 3rd order polynomial curve fits were selected based on sensitivity analysis of a close match to the trend, and removal of unnecessary undulation in the skin, not required for the trend calculation. A third polynomial fit was found to describe best the natural curvature of the OCT images. Higher order fits did not further improve the fitting.

Then, after converting image pixels into distances by dividing the pixel numbers by the image resolution (230 pixels/mm), the skin surface roughness and geometry parameters were determined using DIN ISO 1302 standard definitions for arithmetic mean roughness Ra and 10 point roughness depth Rz as shown in Equation 6 and 7.

The average surface roughness is defined as:

$$Ra = \frac{1}{n} \sum_{i=1}^n |y_i| \quad \text{Equation 3-6}$$

where n is the sample length (total image pixel number), y_i is the vertical pixel distance from the mean line to the i^{th} data or image pixel point

Rz represents the average maximum height of the topographical profile over five equal and consecutive sample length periods, into which the full profile as shown in figure 32 was divided per following definition. The roughness parameters are presented as mean \pm 1sd.

$$Rz = \frac{1}{5} \sum_{i=1}^5 Rt_i \quad \text{Equation 3-7}$$

$$Rt_i = \max_i(y_i) - \min_i(y_i) \quad \text{Equation 3-8}$$

where Rt_i is the maximum profile height Rt for the i^{th} sampling length

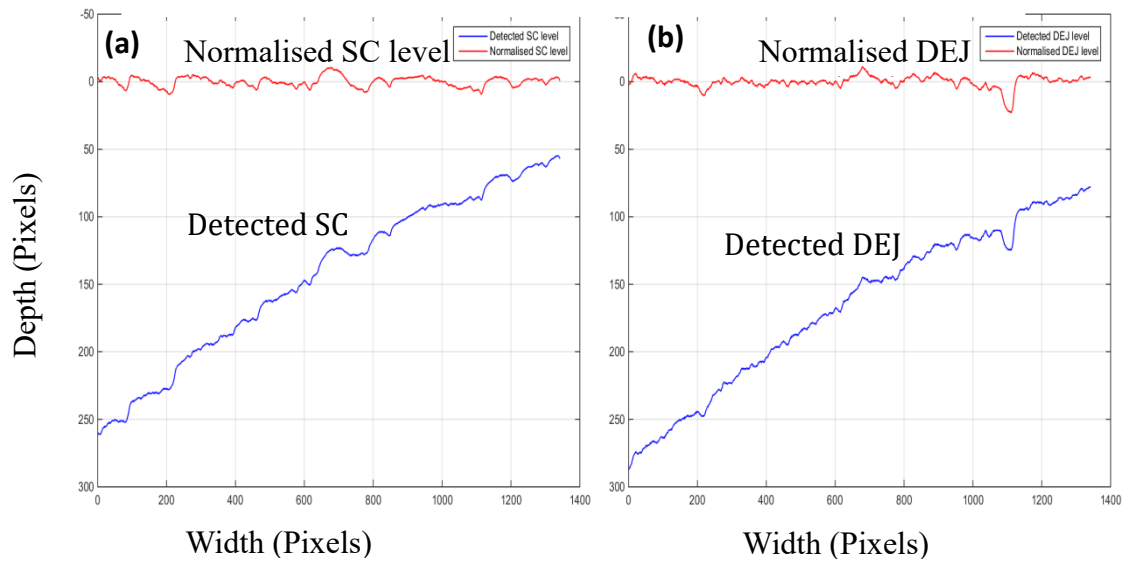


Figure 3-14, Extracting the roughness (red lines) from topographical skin profiles (blue lines) of (a) stratum corneum and (b) dermal-epidermal junction

3.4 Confocal microscopy

3.4.1 System overview

A confocal microscope is a scanning microscope, similar to a scanning electron microscope, which scans the samples with a focused beam and builds up the image point by point as Figure 3-15 shows. However, the main characterization of confocal microscopy is that there is a pinhole in front of the detector (a photomultiplier tube or PMT). Due to the small pinhole, only laser is able to give enough light energy into the small spot. Also, multiple lasers of different wavelengths can be used to give a range of wavelengths for multiple fluorescence.

The main advantage of the pinhole is to smear out out-of-focus light from going through PMT. Therefore confocal image only contains in-focus information, increasing the resolution and quality of the images. In addition, by collecting a series of images, a full three-dimensional representation of the specimen can be collected. By using respective software of the confocal microscopy, the 3D images can be manipulated, controlled and provide different views on the specimen. However, samples preparation is required before using the confocal microscope, which is the dyeing of the biological samples with fluorescent dyes. This can be done by immersing the biological samples in a fluorescent dye solution.

In this study, a fluorescent dye named Eosin B was used to dye the porcine aorta samples and the confocal microscopy used in this research is Spectral Confocal & Multiphoton System Leica TCS SP2.

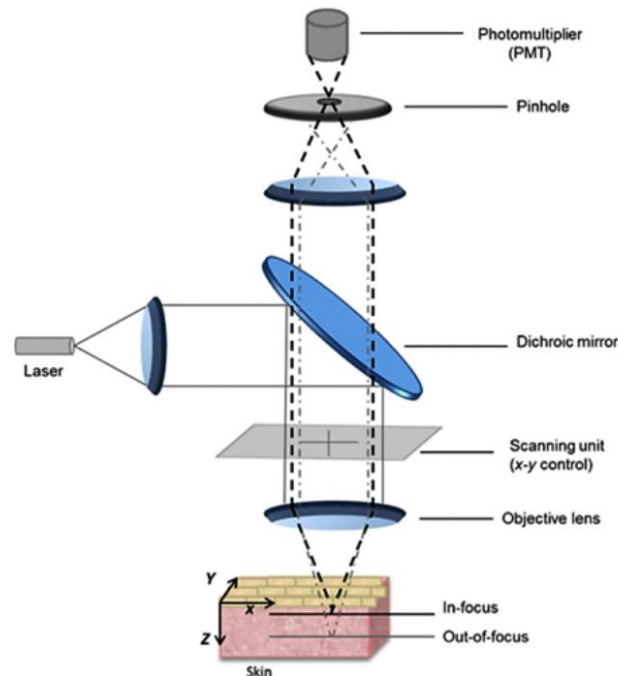


Figure 3-15, The structure of standard confocal microscopy (Rossetti et al., 2013)

3.4.2 Eosin B and Amino Acid Composition of Porcine Aorta

Eosin B is one of the derivatives of Eosin fluorescent dye. Although Eosin was used previously in a study to stain elastin fibres, however it was not mentioned which Eosin derivative was used (Megens et al., 2007). Moreover, Eosin B is used to stain cytoplasm and proteins like collagen, which contradicts the previous study. Therefore, it is important to know which type of fibre Eosin B stains.

Based on Waheed's study, it is identified that Eosin B is able to target three types of amino acids, which are histidine, arginine and lysine (Waheed et al., 2000).

Multiple studies show that collagen has a small portion of histidine, arginine and lysine across a range of amino acids tested while elastin on the other hand has less or none of the amino acids mentioned above. In addition, a porcine aorta wall has a sufficient amount of histidine, arginine and lysine as Table 3-1 shows (Stein & Miller, 1938; Zeeman et al., 1998; Grant, 1966).

It can be assumed that Eosin B is able to stain porcine aortic wall, which could comprise both collagen and elastin fibres. This would be further discussed in section 8.4.1.

Eosin B was chosen for this study because it is commercially available and easy to get. There are more specific fluorescent dyes that targets collagen fibres. However, the supply was highly limited at the time of the experiment.

Table 3-1, The amount of arginine, histidine and lysine in pig collagen, pig elastin and aortic wall represented as the number of residues per 1000 amino acids [n/1000] (Zeeman et al., 1998)

	Arginine	Histidine	Lysine
Pig collagen (average)	49	5	33
Pig elastin (average)	8	0	4
Aortic wall	28	7	27

3.4.3 Image Analysis Using Fiji (Directionality Plugin)

In this study, Fiji software was used for image analysis. The area of interest from the images (tissue fibres) was the preferred direction of the tissue fibres, which serves to indicate the ability of the tissue fibres to recover to their undamaged state. As such, the directionality plugin was used at this stage to infer the preferred orientation of structures present in the input images. This plugin is able to compute a histogram indicating the amount of the structure in a given direction for one image, which is called “Directionality Histogram”, as shown in Figure 3-16.

The software can also analyse the tissue fibres orientation in batch, as shown in Figure 3-17. This is especially useful when Z-stack scan is used where images are taken with very small increment in z-axis. The plotted directionality histogram should represent the whole Z-stacked scan, as shown in Figure 3-17. The blue lines represent the images at or near surface section of the specimen, green lines are from the images in the middle section of the Z-stack scan and brown lines represent the lowest part of the Z-stack scan.

There are two useful outcomes of the directionality plugin process for the later stage of analysis. First, the directionality histogram that shows the dominant orientation across the range of directionality angle of -90° to 90° under “direction” tab as shown in Figure 3-18. Second, a table that shows the peak directionality angle of the image, dispersion, amount and

goodness of the image as shown in Figure 3-16 and Figure 3-17. The particular sections of interest are peak directionality and the quality of the image. The quality of the image implies the quality of the fit, in other words, it shows how credible the result is. The highest quality value is “1” (highest credibility) and “0” for the lowest credibility.

The main concept of using Fiji to analyse the confocal images in this project (Chapter 8) was to determine the orientation of the tissue fibres before and after the friction induced damages were applied on the porcine aorta. The orientation of the fibres can be analysed as a whole value before and after damages and also how the orientation of tissue fibres changes at different layers of the porcine aorta specimen.

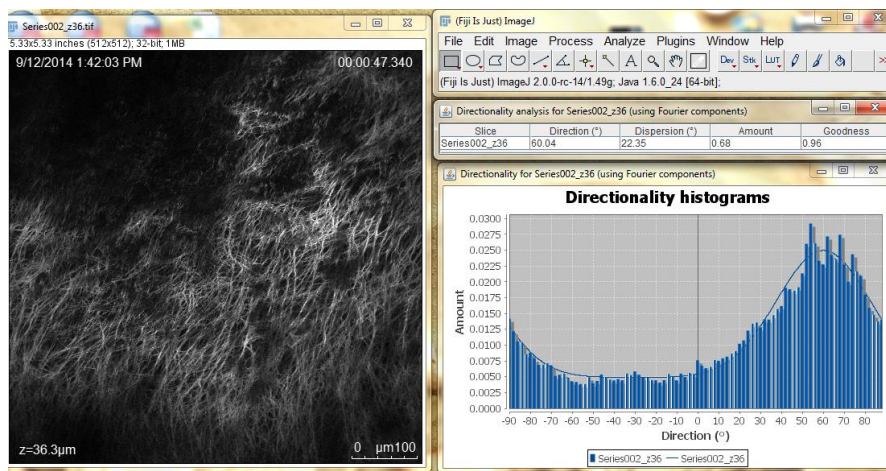


Figure 3-16, Outcome of Fiji – directionality image analysis of one image

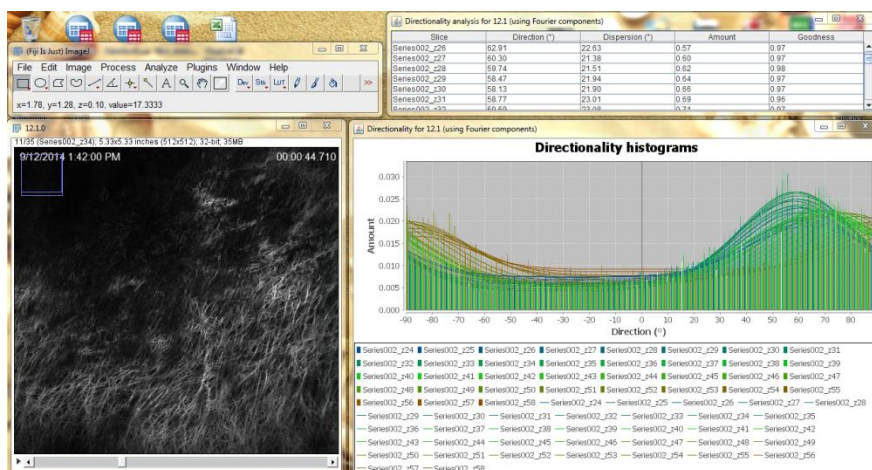


Figure 3-17, Outcome of Fiji – directionality image analysis of a group of images (Z-stacked scan)

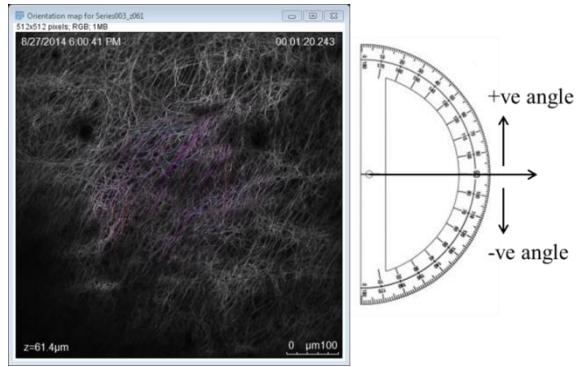


Figure 3-18, The orientation map of the outcomes

Chapter 4

Interaction between finger pad and transparent glass plate

4.1 Introduction

To date, there have been very few studies that look into investigating biotribology problems using multiple imaging techniques. Additionally, even less studies have focused on obtaining the strain distribution profile of a finger pad in contact with another material experimentally. This work used two imaging techniques that give different visual results to study the finger pad sliding interaction with a glass plate. Firstly, Digital Image Correlation (DIC) is able to show the strain field on the finger pad throughout the sliding interaction while Optical Coherence Tomography (OCT) shows the subsurface morphology of the finger pad. This work will give some new insights on how the finger pad deforms and is strained in response to the sliding glass.

4.2 Aim and objectives

The aim of this work was to determine if there is any correlation between the frictional behaviour and the strain behaviour of the finger pad during sliding interaction with a smooth glass plate.

The main objective of this work was to investigate the feasibility of using 3D-DIC on sliding interactions. Other objectives include obtaining the coefficient of friction of the finger pad in response to the stiffness of the finger pad or the normal load applied, monitoring the change in moisture level of the finger pad of each experiment, obtaining the visual result of the strain on the finger pad while sliding and obtaining the visual result of the morphology of the sliding finger pad using OCT.

Additionally, in order to understand the differences between a smooth and a grooved plate, a pilot study was done to investigate the morphological change of the finger pad when slid across a grooved plastic plate.

4.3 Methodology

4.3.1 Friction test set-up

The friction test was done with 3D-DIC and OCT separately. In other words, the same friction test was repeated using different imaging techniques. The friction tests were carried out to study the frictional behaviour of the finger pad by means of coefficient of friction. Each friction test was done to determine how normal load, finger pad stiffness and moisture level would affect the coefficient of friction and other dependant variables. Other dependant variables were measured, such as the strain profile or distribution, surface roughness and contact area, using imaging techniques.

The left index finger pad of a volunteer (age 25, male) was loaded against the glass plate from the experiment set-up (Figure 4-1) through a finger holding rig (Figure 4-2). The interaction forces between the finger pad and the glass plate (average thickness of 396 μ m) were recorded through a force plate (AMTI), which is shown in Figure 4-1. The normal loads applied on the glass plate were 0.5N, 1N, 2N and 3N, which were within the low normal load region (Liu, 2013). After the desired load had been achieved and stabilised, the glass plate was slid against the finger pad. The movement and the speed of the glass plate were controlled through the dynamic rig. The average speed of the sliding plate was 0.5mm/s. After the sliding had stopped, the set-up was left for more than 3 seconds or until there was

no significant change in force between the finger pad and the glass plate. The load would only be taken off after that.

The finger pad sliding experiments were done for two types of finger condition: a finger pad in a natural state that was not treated with any water, ointment, hand cream etc. before the test and a soaked finger pad that was treated by immersion in a cup of water for 20 minutes and left to acclimatise for 8 minutes.

A thin glass plate was used in this finger pad sliding experiment so that the OCT could show scanned images of the finger pad interacting with the glass plate with higher quality. This is due to the properties of light that reflect and refract when passing through a transparent medium. As the glass material is highly reflective, thicker glasses will cause reflection of the glass or both glass and finger pad to overlay on the original image, which causes a drop in the quality of the images.

In addition to the smooth glass plates, grooved plastic plates (made of polypropylene) were also investigated in this study. Different shape and size grooves were made to study its effect on the performance of the OCT and to see how the skin deformed around the grooves, which will be reflected on the quality of the images captured. The grooves were made by applying a certain amount of force on a cutting knife and sliding against the plastic plate. Sharp grooves were made by facing the edge of the cutting blade on the plate while facing the backside of the cutting blade on the plate made non-sharp grooves, which is summarised in Figure 4-3. The normal force and the friction force were not measured and investigated in the study of the interaction between the finger pad and the grooved plastic plate.

The study protocol was approved by The University of Sheffield (Ethics Number 002074).

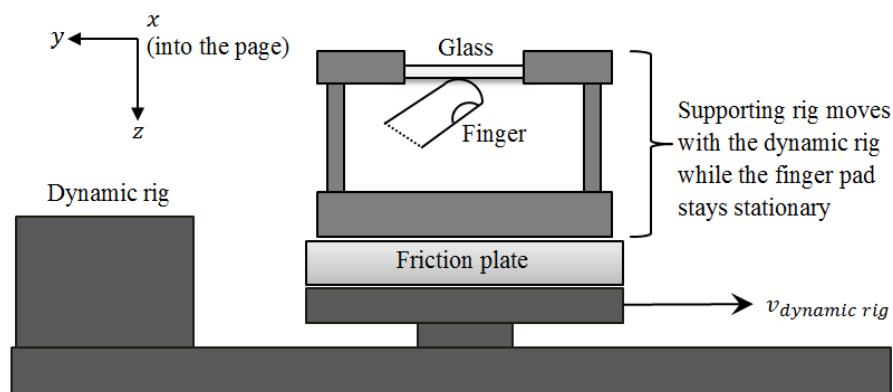


Figure 4-1, Illustration of the finger pad sliding experiment set-up

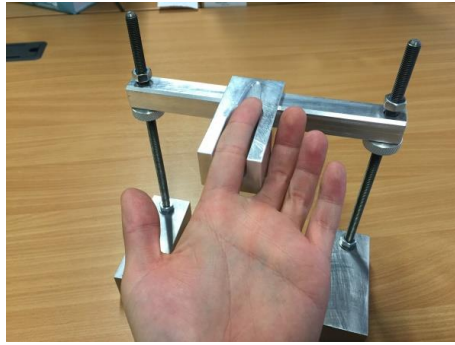


Figure 4-2, Finger holding rig

Groove type	OCT image
Sharp groove	
Broken sharp groove	
Shallow groove 1	
Shallow groove 2	
Big groove	

Figure 4-3, OCT images obtained for a finger in contact with different types of grooves

4.3.2 Water application to make a soaked finger pad

In this study, the frictional behaviour of soaked finger pad was also investigated because skin hydration is one of the main interests in the biotribology study. It is important to know how the water was applied because different water application methods may yield different expectations on the skin moisture.

The method of water application on the finger pad for the 3D-DIC test was slightly different to the other tests because 3D-DIC requires the application of speckles (black ink) on the finger pad to be able to track the displacement field of the finger pad. The moisture level of the finger pad was measured using a corneometer (Courage + Khazaka electronic GmbH).

The illustration of the timeline of the water application during OCT and stiffness tests is shown in Figure 4-4 (a). The left index finger pad was first immersed into a glass of water for 20 minutes. The moisture level of the finger pad before and after the immersion was recorded. Then, dry and clean tissue was used to wipe off the excess water by dabbing on the finger pad. Next, the finger pad was left to acclimatise for 8 minutes and moisture level was measured. Finally, the soaked finger pad was ready for the OCT or the stiffness tests. After the tests, the moisture level of the finger pad was recorded again.

The illustration of the timeline of the water application during 3D-DIC tests is shown in Figure 4-4 (b). The left index finger pad was similarly immersed into a glass of water for 30 minutes. The moisture level of the finger pad before and after the immersion was obtained before using dry and clean tissue to wipe of the excess water. The speckles were applied immediately after the excess water had been removed. Then, the finger pad was left to acclimatise for 8 minutes. The moisture level of the finger pad before and after the speckles application was recorded. Finally, the soaked finger pad was ready for the OCT or the stiffness tests. After the tests, the moisture level of the finger pad was recorded again.

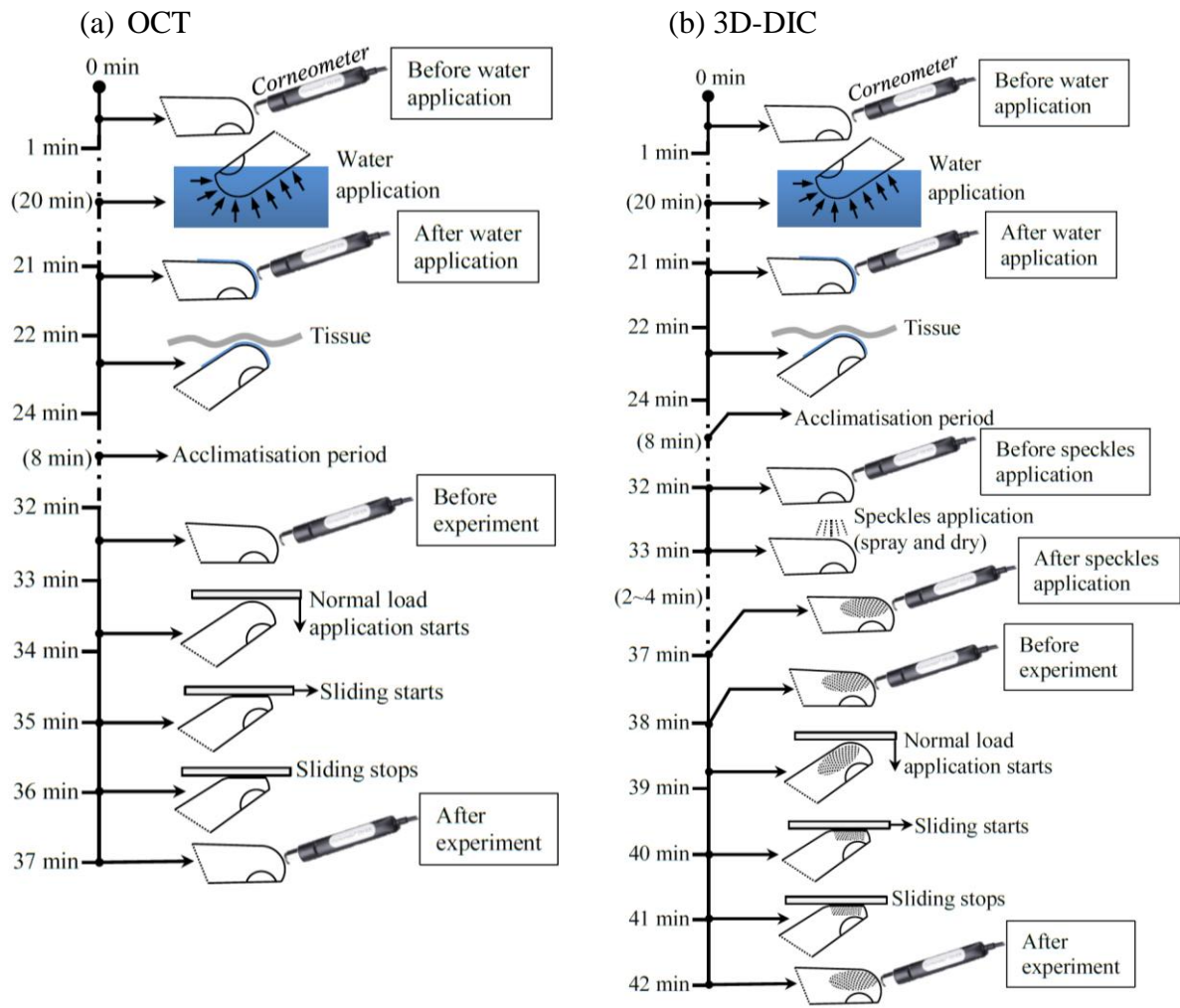


Figure 4-4, Timeline of the moisture measurement of (a) OCT and (b) DIC test

4.3.3 Stiffness test

The stiffness test was performed to measure the finger pad stiffness under a normal load. The current stiffness test set-up is meant to be convenient, portable and flexible to different experiments. The stiffness test set-up in this study is similar to an indentation test. However, the stiffness test uses a flat plate instead of an indenter probe in order to simulate the actual condition of the friction test as much as possible.

The left index finger was located in the finger holder located and fixed on the MDD Manual Test Stand. A flat stainless steel plate was attached to a Mesmechin force gauge (500N) and the MDD Manual Test Stand (Figure 4-5). The face of the stainless steel plate was adjusted to be as close as possible to the tip of the finger pad without touching it, as shown in Figure 4-6. The force gauge and the displacement transducer were zeroed before acquiring the force magnitude every 0.10mm displacement increment. The stiffness of the finger pad was computed from the force-displacement graph obtained from the stiffness test. The first

test was done on a natural finger pad (temperature: 22.8°C, relative humidity: 47.5%) and the second test was done on a soaked finger pad (temperature: 22.8°C, relative humidity: 48.3%).

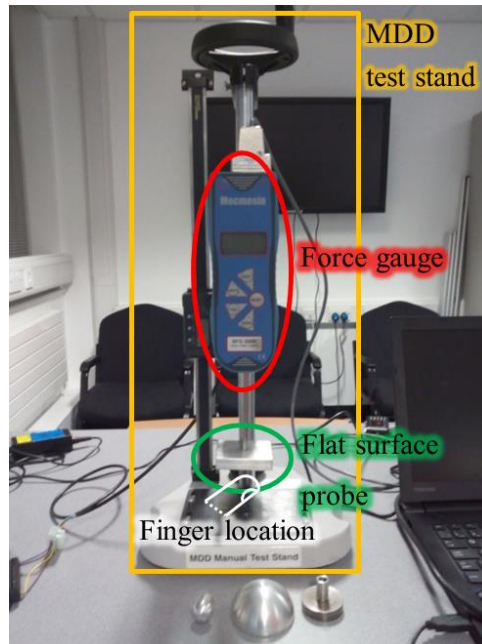


Figure 4-5, The stiffness experiment set-up

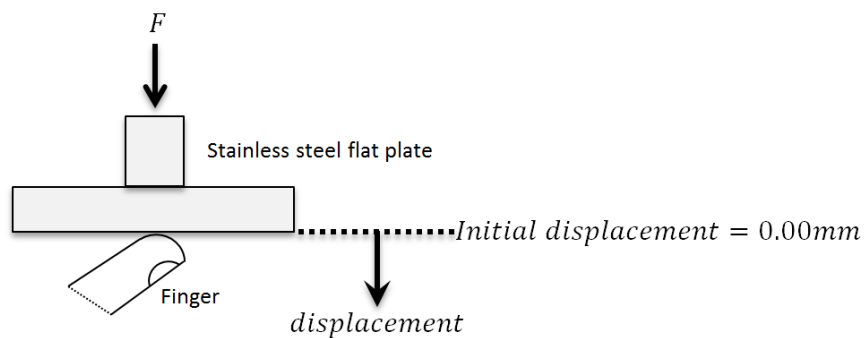


Figure 4-6, The relative position between the flat plate and finger pad

4.3.4 3D-DIC camera set-up, calibration and data acquisition

Detailed information regarding 3D-DIC set-ups and the development of the image analysis has been introduced in section 3.2.

In the speckles preparation stage for the finger pad, droplets of black water-based ink (crafters acrylic paint, DecoArt Inc., Stanford) were distributed randomly on the finger pad through the flickering the bristles of an unused toothbrush as shown in Figure 4-8. The paint was left for approximately 1~2 minutes to dry.

Next, the camera set-up included choosing the stereo angle of the cameras and the distance between the cameras and the object, which in this study, were 30° and 150mm

respectively (Figure 4-7). The details of the camera set-up can be referred to section 3.2.3 in this thesis. The distance was set between camera and the glass plate to ensure that the interaction between the finger pad and glass plate would not go out of focus.

After the cameras were set, the next step is to calibrate the cameras to the DIC software. A grid size of 11×10 with 2mm spatial distance was selected in this study. The calibration score was 0.062 pixels which is in the green region. The calibration of 3D-DIC is done by placing the grid at the same focal plane of the material.

The friction experiment was ready to start after the calibration. The acquisition rate was set to 5 frames per second. The acquisition was started before the finger pad came in contact with the glass and stopped after the finger pad was fully lifted from the glass. Then, the images were input into VIC 3D DIC software in which subset size, step size and filter size must be set (61×61, 7, and 15 respectively in this study) before running the software. The strain calculated was based on Lagrange.

The DIC software correlates the deformed image and reference image that is undeformed and give the surface contour of the samples in terms of displacement and strain. During the post analysis, the strain along the X-axis or Y-axis can be extracted using the DIC software as well.

It needs to be noted that using ink may have an effect on the surface properties of the human skin because ink can be treated as a third body layer or lubricant. Therefore, the ink applied in this study was minimised so that the ink has a lesser effect on the frictional and moisture data.

The measurements were carried out at 26.6°C and 36-37% relative humidity.

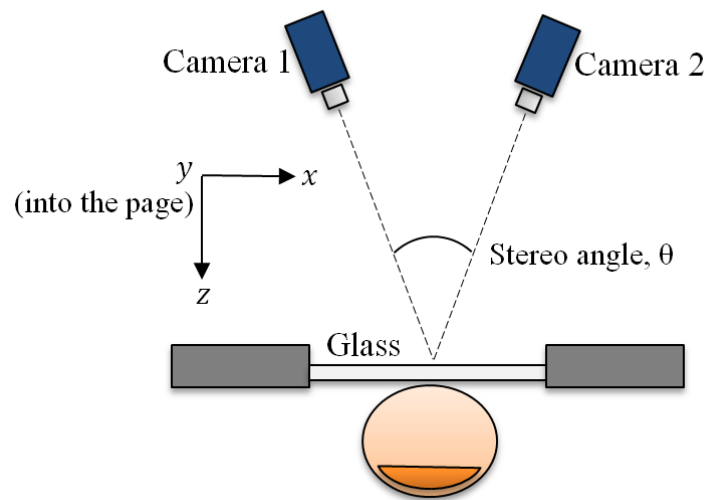


Figure 4-7, Illustration of friction experiment set-up with 3D-DIC

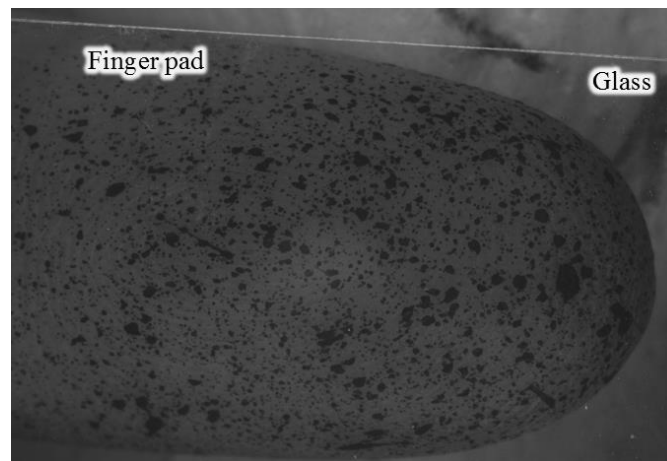


Figure 4-8, Finger pad with speckles

4.3.5 Apparent contact area

3D-DIC data gives a cloud of coordinates that represent the shape of the finger pad. When the finger pad is in contact with the plate, some coordinates change due to the deformation. So, the main concept of this measuring method is to find the coordinates at the boundary of the deformation. The collection of the coordinates will give us the shape and the apparent contact area of the finger pad. As the previous studies found, the real contact area of the finger pad is much smaller than the apparent contact area due to the finger pad ridges. The real contact area of the finger pad cannot be determined because the resolution of the coordinates is not fine enough to re-construct the geometry of the finger pad ridges.

The apparent contact area can be found using 3D-DIC imaging technique. It was determined by using a series of Matlab coding (attached in Appendix B) that is able to find the boundary line from the deformed shaped of the finger pad when in contact with the glass plate. The deformed shaped of the finger pad in contact with the glass plate is presented as Figure 4-9. The Matlab coding performs multiple differentiations and filtration to determine the two boundary points (the first and the last), for which the result is shown in Figure 4-10. Then the ellipse best-fit Matlab function can be used to determine the size of the contact of the finger pad in Figure 4-11.

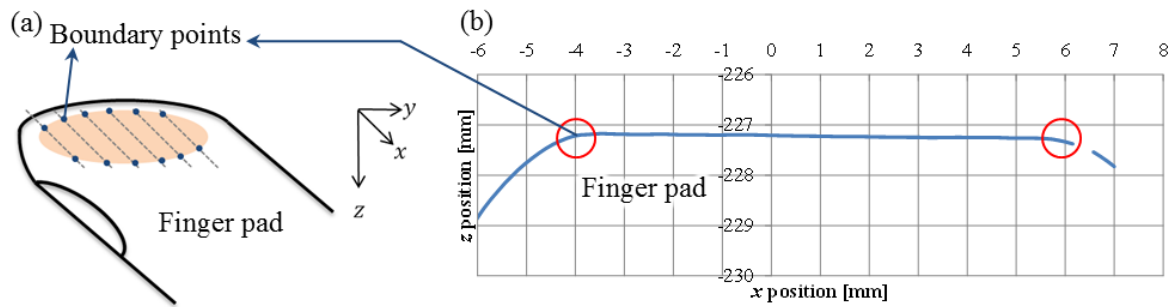


Figure 4-9, Illustration of (a) the deformed finger pad with slices and (b) a slice of position graph of deformed shape of the finger pad in contact with glass plate

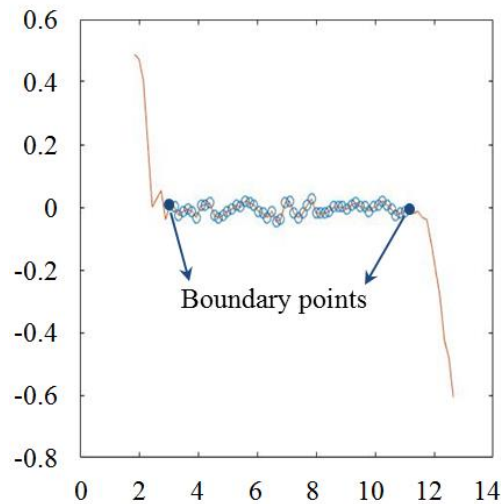


Figure 4-10, The process of finding the boundary points from Z position graph (differentiations and filtration)

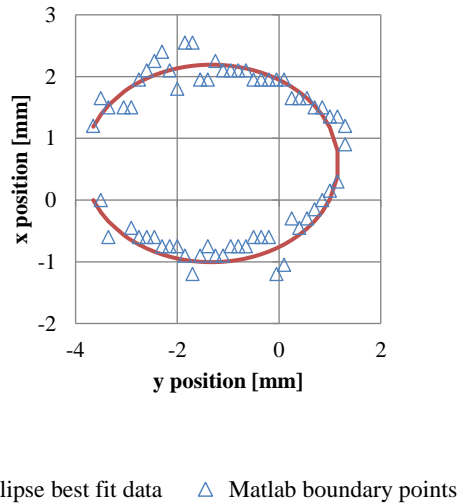


Figure 4-11, The ellipse best fit of the boundary points of the contact area

4.3.6 *Optical Coherence Tomography*

Detailed information regarding OCT system and the development of the image analysis has been introduced in section 3.3.

The OCT system used in this study was a Vivosight (Michelson Diagnostics, Kent) and it was set-up as shown in Figure 4-12. In the data acquisition stage, A-scan (reflectivity) was used and the frame rate was set to 20 images per second. The images captured have a resolution of 1342×460 pixels. For stability, the hand held probe was fixed on the microscope holder.

In the OCT experiment, the images were taken at two positions of the finger pad (Figure 4-13). The B-scan of the OCT was first used to scan the finger pad before it touched the finger pad. Then, the B-scan of the OCT was used continuously from the loading of the finger pad under the plate (no sliding at this point) to sliding and until the sliding stopped.

The measurements were carried out at 20°C and 45-50% relative humidity.

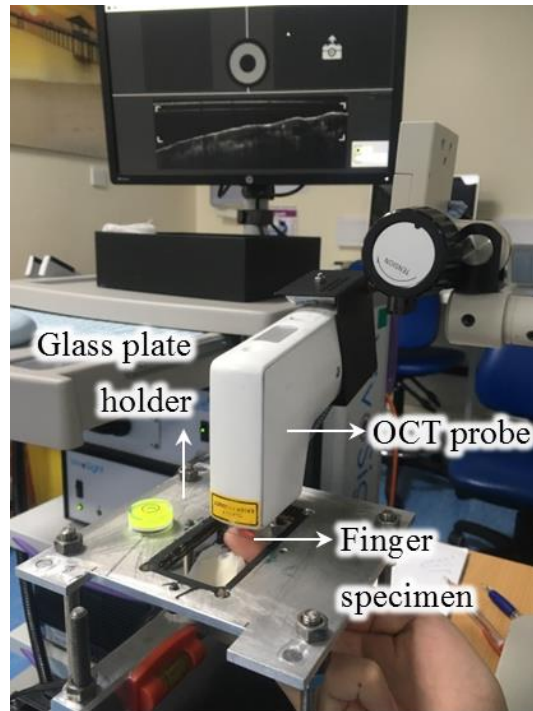


Figure 4-12, Experimental set-up using OCT

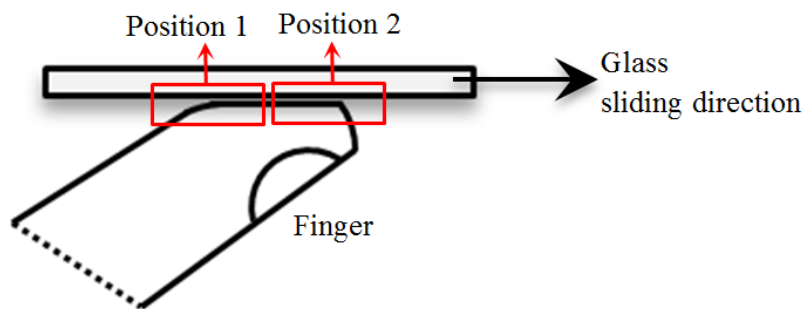


Figure 4-13, Scanning positions of the OCT on the finger pad

4.3.7 *Real to apparent contact area ratio*

By definition, the real contact area should always be smaller than the apparent contact area. Due to the limitation of the scanning range of the OCT, it cannot be used to determine the whole real contact area of the finger pad. Instead, Liu (2013) used OCT to determine the real-to-apparent contact area ratio of the finger pad, as shown in Figure 4-14. The real-to-apparent contact area ratio is calculated by dividing d_{real} , which is the summation of d_1 , d_2 and d_3 in Figure 4-14, by d_{apparent} .

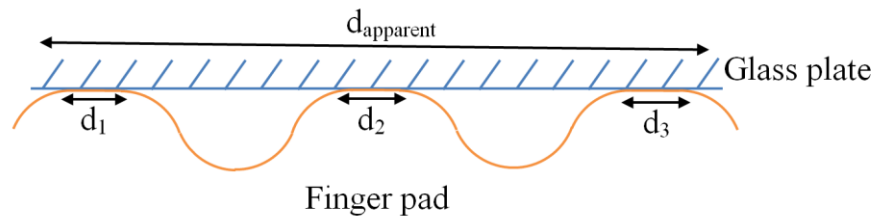


Figure 4-14, Illustration of the finger pad loaded against a glass plate

4.4 Results

4.4.1 Stiffness of the a natural and a soaked finger pad

The force-displacement graph of the finger pads shows a non-linear relationship as shown in Figure 4-15 (b) due to the viscoelasticity of the finger pads. The equation of best fit was applied as a polynomial function with a maximum power of 4. The condition of the finger pad has a direct effect on the force-displacement graph as the soaked finger pad requires a lower normal force to reach the same displacement as the natural finger pad. Additionally, a power equation of best fit was also applied on the normal load vs displacement data, as shown in Figure 4-16 (a). The differences between the polynomial equation relationship and the power equation relationship are discussed in section 4.5.3.

It should be noted that the stiffness values of the finger pads used in the remaining result sections are obtained from the polynomial equation relationship in Figure 4-15 (a).

The stiffness of the finger pad, which is the gradient of a force-displacement graph, can be plotted against the change in normal load on the finger pad, as shown in Figure 4-15 (b). The figure shows that there is a difference between the stiffness of a natural state finger pad and a soaked finger pad at the same normal load. However, this difference becomes smaller as the normal load increases. Both the natural and soaked finger pads have the same stiffness value when they are loaded at 5N. As this study only focused on the low normal load region (0N - 3N), it can be safely assumed that the stiffness of the natural finger pad is higher than the soaked finger pad throughout the experiments in this study.

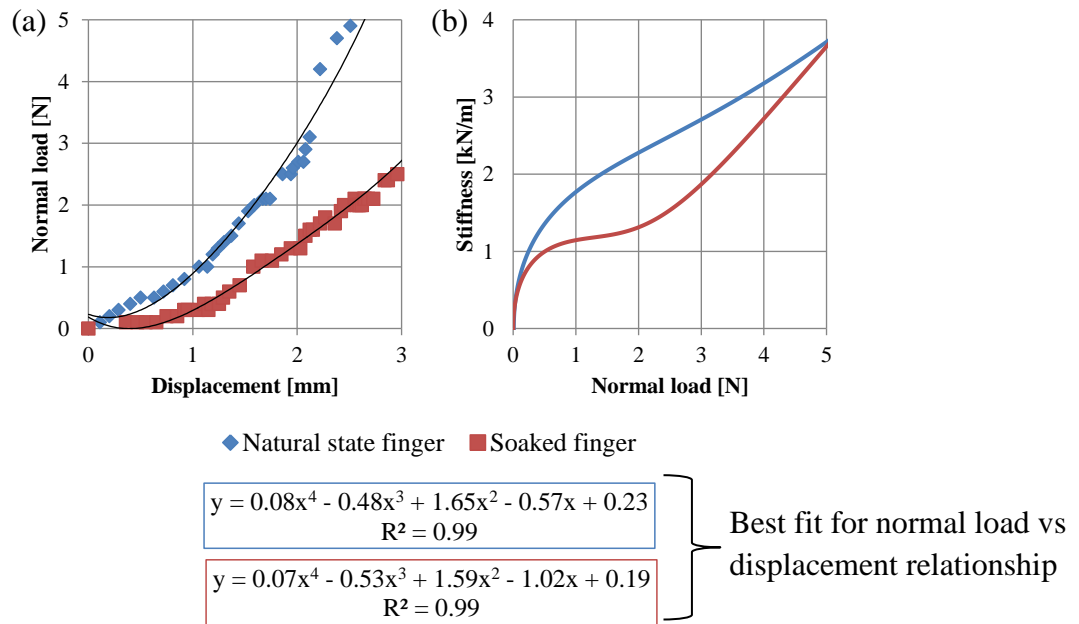


Figure 4-15, (a) Force-displacement graph of the finger pads and (b) stiffness vs normal load graph using polynomial equation relationship

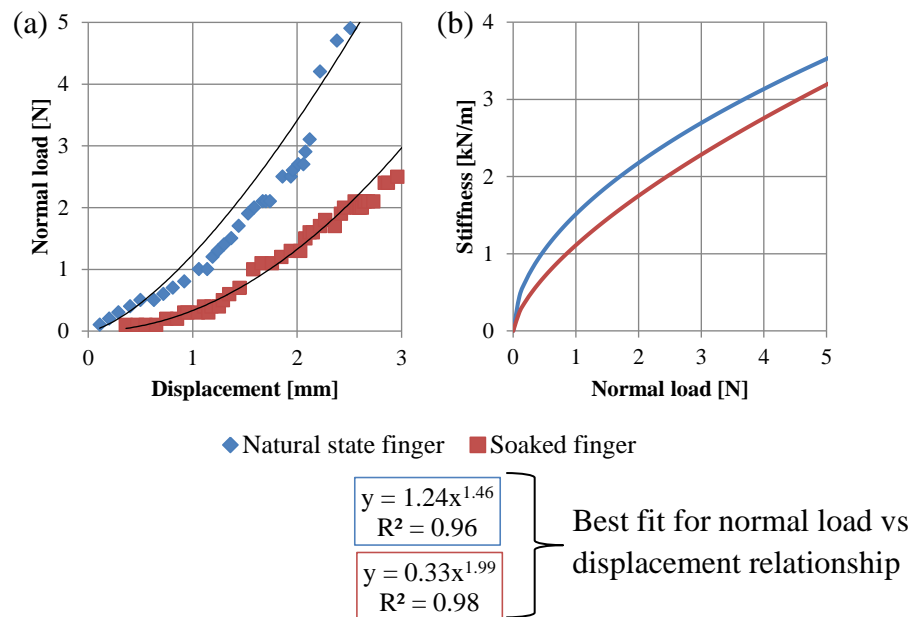


Figure 4-16, (a) Force-displacement graph of the finger pads and (b) stiffness vs normal force graph using power equation relationship

4.4.2 Force behaviour before, during and after sliding

Figure 4-17 shows the changes in the behaviour of the normal forces applied and the frictional forces on the finger pad before, during and after being slid against a glass plate. The origin of the graph (when $t=0s$) was set at the time point when the glass was about to slide because the duration of the slide was the same for all finger pad experiments as the sliding distance and speed of sliding were fixed.

Three different states have been highlighted in Figure 4-17. The first state was set at the point where only normal load was applied and before the friction increased substantially due to sliding. The normal load was applied on the finger pad for a period of time to be stabilised. At this state, there should be minimal or no friction acting on the finger pad. There are some friction fluctuations before the state 1 due to involuntary finger pad movement. The second state is known as the steady sliding state, which only happens when the finger pad is fully slipped against the sliding glass. Before reaching the steady state, the friction increased sharply. After the whole contact has fully slipped, the friction would reach a steady friction value. The time used to achieve this state varies with the normal load applied, which ranges from 3s to 5s in DIC sliding experiments and 3s to 8s in the OCT sliding experiments. State 3 is when the sliding stopped. When the sliding stopped, the friction tended to decrease because the finger pad was recovering from the sliding deformation due to its viscoelastic property.

The normal load applied on the finger pad decreased initially after the sliding started and increased after a period of time. The main factor is due to the bending of the glass plate during sliding interaction. This curved parabolic normal load behaviour during sliding was not found in Liu’s study (2013) and the normal loading in Liu’s study was more consistent during sliding. As such, state 2 in the later sections was taken at $t=19.5s$, which was half of the sliding duration. The respective normal load at state 2 was recorded in Table 4-1.

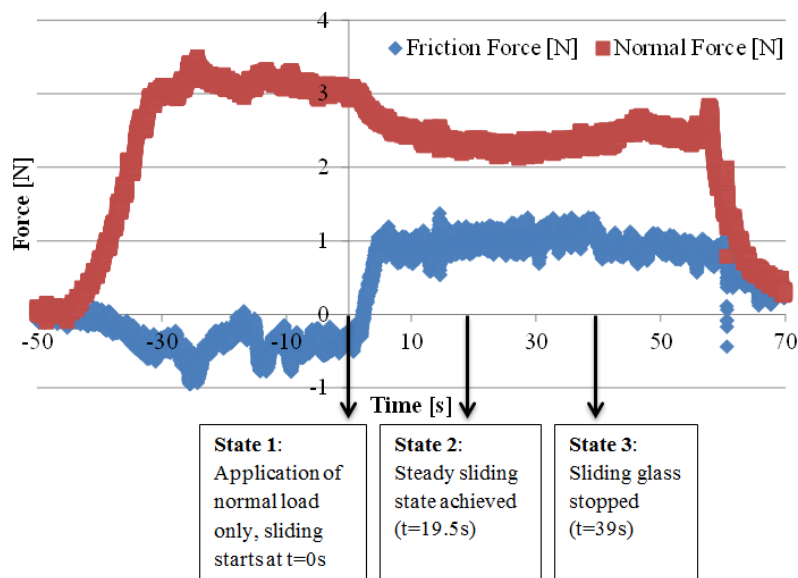


Figure 4-17, Force vs time graph of the finger pad in natural state loaded at 3N during the whole sliding interaction (3D-DIC)

Table 4-1, Instantaneous normal force at state 1 (static) and state 2 (dynamic) of finger pad

	State 1: Static (t=0s)	State 2: Dynamic (t=19.5s)
Natural finger DIC	0.5 N	0.5 N
	1.0 N	0.9 N
	2.0 N	1.7 N
	3.0 N	2.3 N
Soaked finger DIC	0.5 N	0.6 N
	1.0 N	1.1 N
	2.0 N	1.7 N
	3.0 N	2.3 N
Natural finger (Position 1) OCT	0.5 N	0.6 N
	1.0 N	0.8 N
	2.0 N	1.6 N
	3.0 N	2.0 N
Natural finger (Position 2) OCT	0.5 N	0.4 N
	1.0 N	0.8 N
	2.0 N	1.4 N
	3.0 N	2.5 N
Soaked finger (Position 1) OCT	0.5 N	0.5 N
	1.0 N	0.7 N
	2.0 N	1.1 N
	3.0 N	2.0 N
Soaked finger (Position 2) OCT	0.5 N	0.4 N
	1.0 N	0.8 N
	2.0 N	1.6 N
	3.0 N	2.5 N

4.4.3 Moisture level of the finger pad

This section shows the overall change of the moisture level of the finger pad before and after of each test under a natural state or a soaked condition. For the soaked finger pad, Table 4-2 also shows the moisture level before the application of water on the finger pad. The specific moisture levels of the finger pad are tabulated in Appendix D, like the moisture level of the

finger pad before and after the water application, and before and after the speckle application for a DIC test.

Table 4-2 summarises the moisture levels of the finger pads throughout the test, which are the moisture level of the finger pad before water application, before the sliding experiment (after acclimatisation) and after the sliding experiment. The purpose of this table is to show how the moisture level of the soaked finger pad changed before the sliding experiment in comparison to a finger pad in natural state. This table shows that there is not much difference in the moisture level between the natural finger pad and the soaked finger pad. Even though the soaked finger pad had been immersed into a glass of water for 20 minutes, the moisture level of the soaked finger pad before the experiment decreased after the acclimatisation of the finger pad. Then, the moisture level of the finger pad increased after the experiment regardless of the experiment type and the moisture state of the finger pad, which demonstrates the occlusion phenomenon of the finger pad (Adams, 2012). Occlusion occurs whenever the finger pad is pressed against a counter-face material and the water under the skin is forced onto the surface or sub-surface of the finger pad.

It should be noted that the moisture level of the finger pad did become higher after the water application as the measurement was taken before the excess water was wiped off, which is shown in Appendix D. There was also a very small amount of wrinkling in the finger pad.

It was expected previously that the natural finger pad and soaked finger pad would represent the dry and moist finger pads respectively. However, Table 4-2 shows that it is difficult to identify the dry and moist finger pads based on the moisture level measured before the experiment itself. Even though the moisture measurement was not able to properly distinguish a dry finger pad and a moist finger pad, the moisture level of the finger pad measured before the experiment could still be used as a benchmark in the post-analysis. Therefore, the moisture level of the finger pad was used to plot with the apparent contact area (measured from DIC data), real to apparent contact area ratio (measured from OCT data) and the shear force on the finger pad as shown in Figure 4-18 and Figure 4-19.

Overall, the moisture level of the finger pad during the DIC test has a lower moisture values than the finger pad during the OCT test, where the natural finger pad has the most notable difference. On the other hand, the shear force on the finger pad seems to increase

with the increase of the moisture level of the finger pad if the shear data from both the Figure 4-18 and Figure 4-19 are combined, although there are fluctuations in the shear data.

In Figure 4-18, the apparent contact area of the finger pad decreases when a certain moisture level is reached. In Figure 4-19, the real-apparent contact area ratio might have an increasing correlation with the moisture level of the finger pad although the fluctuation or noise is quite obvious. Although it is difficult to draw a conclusion with certainty based on the dataset, this could be achieved by repeating the test with a wider population.

Table 4-2, Moisture level of the stratum corneum of the finger pads in natural state or soaked condition in stiffness, 3D-DIC and OCT tests

Test type	Moisture state	Static normal load [N]	Moisture level of stratum corneum [AU]		
			Before water application	(After acclimatisation) Before experiment	After experiment
Stiffness test	Natural	-	-	38.2±5.7	46±8.7
	Soaked	-	46.8±7.3	30.6±3.1	42.6±3.3
3D-DIC	Natural	0.5	-	17.4±1.7	18.2±3.1
		1	-	15.6±1.5	16.2±3.2
		2	-	14.8±1.3	17.8±2.2
		3	-	17.8±1.8	17.6±3.4
	Soaked	0.5	44.8±4.3	25.0±4.9	28.0±6.4
		1	34.4±6.2	22.8±4.6	25.2±5.9
		2	38.4±1.8	16.4±4.8	16.0±2.5
		3	31.8±5.3	15.2±3.3	18.8±4.6
OCT	Natural	0.5	-	35.8±4.2	42.4±6.4
		1	-	36.4±4.7	42.9±9
		2	-	36.7±5.3	44.3±8.3
		3	-	41.6±6.1	46.5±9.8
	Soaked	0.5	34.9±3.8	23.7±4.7	27.6±5.3
		1	29.2±5.2	24.5±3.6	27.4±3.5
		2	29.2±3.8	26.5±2.4	32±5.2
		3	28.1±3.3	26±3.9	31±6

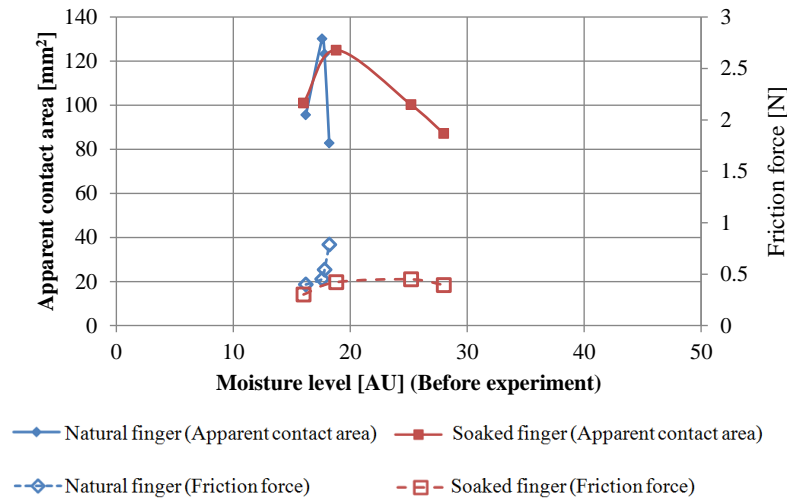


Figure 4-18, The relationship between the dynamic apparent contact area, friction force and the moisture level of the soaked finger pad before the sliding test with DIC

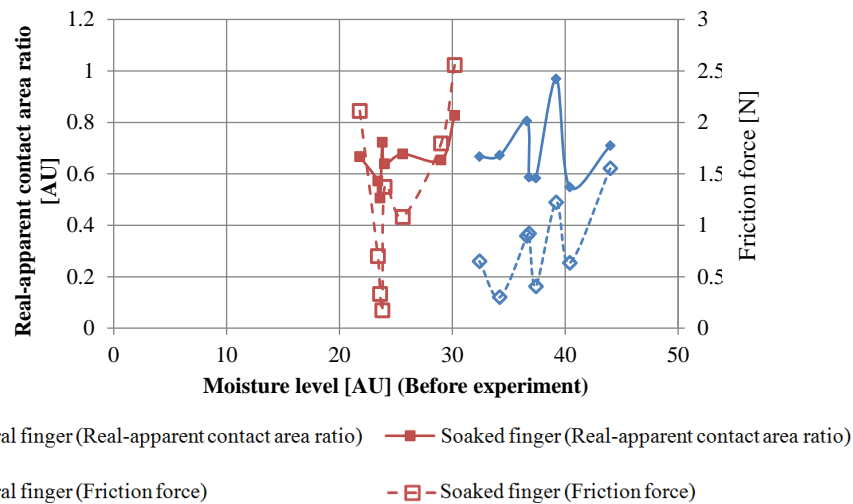


Figure 4-19, The relationship between the dynamic apparent contact area, friction force and the moisture level of the soaked finger pad before the sliding test with OCT

4.4.4 The influence of normal force and stiffness on the dynamic coefficient of friction

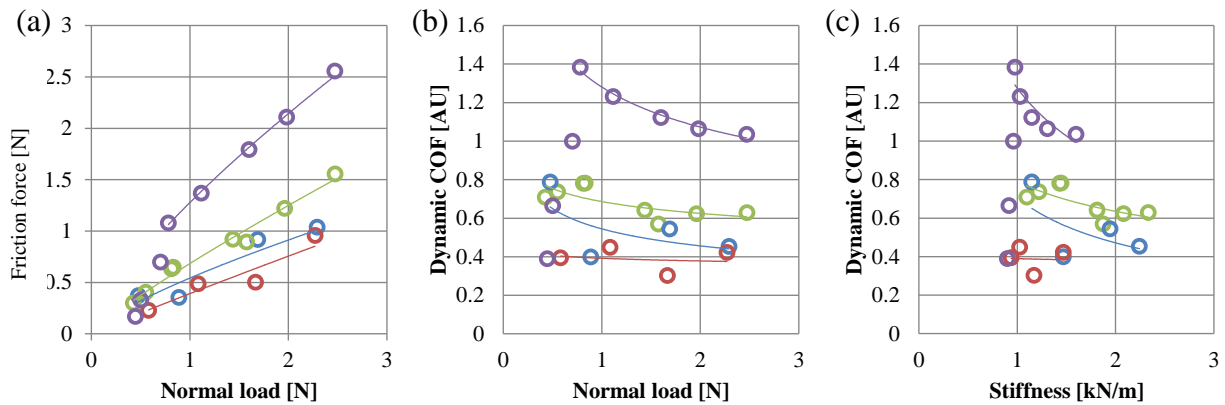
Figure 4-20 (a) shows the relationship between the dynamic coefficient of friction and the normal load of the finger pad in both natural and soaked conditions using both imaging techniques (OCT and 3D-DIC). The overall pattern of the graph is similar to Derler & Gerhardt (2012), where there is a pool of coefficient of friction data that decreases with the normal load applied.

In general, both the shear force and dynamic coefficient of friction of the soaked finger pads from the OCT test is higher than the natural finger pads although there a few data points have fallen into the natural finger pad region. However, the dynamic coefficient of friction from all the soaked finger pad data points in 3D-DIC tests behaves like a natural

finger pad, as shown in Figure 4-20 (a) and (b). The moisture level of the finger pad could be the main cause of this behaviour because the soaked finger pad was drying out during the DIC test (see the moisture results in section 4.4.3) and the application of the speckle pattern applied on the finger pad during the sample preparation stage before the 3D-DIC test. This behaviour is further discussed in section 4.5.2.

In terms of the curve fitting, as the normal load is getting nearer to zero, the coefficient of friction increases. So, a power law equation is used for the curve fitting in this study. The curve fitting pattern also looks similar to Derler & Gerhardt (2012) even though they expressed the coefficient of friction with the pressure applied. It is found that the exponent constant in the Figure 4-20 (b) is the subtraction of value 1 from the exponent constant in the Figure 4-20 (a).

Next, the dynamic coefficient of friction was also plotted against the stiffness of the finger pads, as shown in Figure 4-20 (c). Similarly, this figure shows that the dynamic coefficient of friction decreases with the increase of the stiffness of the finger pads. In the case of the soaked finger during OCT test, the dynamic coefficient of friction decreases only after a certain stiffness value.



Best fit for (a): $y = 0.54x^{0.74}$ $y = 0.39x^{0.95}$ $y = 0.69x^{0.86}$ $y = 1.28x^{0.74}$

Best fit for (b): $y = 0.54x^{-0.26}$ $y = 0.39x^{-0.05}$ $y = 0.69x^{-0.14}$ $y = 1.28x^{-0.26}$

Best fit for (c): $y = 0.70x^{-0.58}$ $y = 0.39x^{-0.04}$ $y = 0.79x^{-0.32}$ $y = 1.27x^{-0.53}$

○ DIC, natural finger ○ DIC, soaked finger ○ OCT, natural finger ○ OCT, soaked finger

Figure 4-20, (a) Friction force against normal load with the dynamic coefficient of friction (COF) against (b) normal load and (c) the stiffness of the finger pad

4.4.5 General strain and deformation behaviour

Figure 4-22 show the 1st principal strain E_1 (tensile), 2nd principal strain E_2 (compressive) and shear strain E_{xy} on the surface of the finger pad when loaded at 0.5N in static state. Figure 4-21 is added to illustrate the global position axis of the finger pad and also the sliding direction of the glass plate while the finger pad was stationary. The irregular strain patterns or fluctuations in the strain distributions are caused by the involuntary or subconscious human motion during the experiment. The strain profile in the static and dynamic state were taken when $t=0s$ and $t=19.5s$ in the force vs time graph in section 4.4.2. They are state 1 and state 2 of the force temporal evolution behaviour respectively.

4.4.5.1 First principal strain, E_1

The strain distribution pattern shows that there is a pool of low 1st principal strain field within the contact area that is near to the fingertip region, as shown in Figure 4-22. From the static state to the dynamic state, the size of the low strain field is smaller and nearer to the fingertip region.

4.4.5.2 Second principal strain, E_2

Similarly, low 2nd principal strain was more concentrated within the contact area, which is surrounded by high strain field in both the static and the dynamic states. The size of the low strain region increases from the static to the dynamic state.

4.4.5.3 Shear strain, E_{xy}

In both the static and dynamic states, a shear strain pattern was formed by the negative and positive shear strain with each occupying one side of the finger pad. The negative and positive notions of the shear strain means that the surface of the finger pad was sheared in a clockwise and counter clockwise direction when viewed in the “+z” direction.

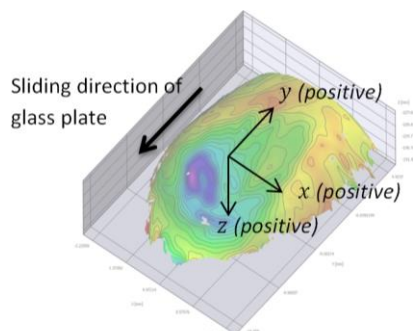


Figure 4-21, An illustration of the position reference axis (global) of the finger pad and the sliding direction of the plate

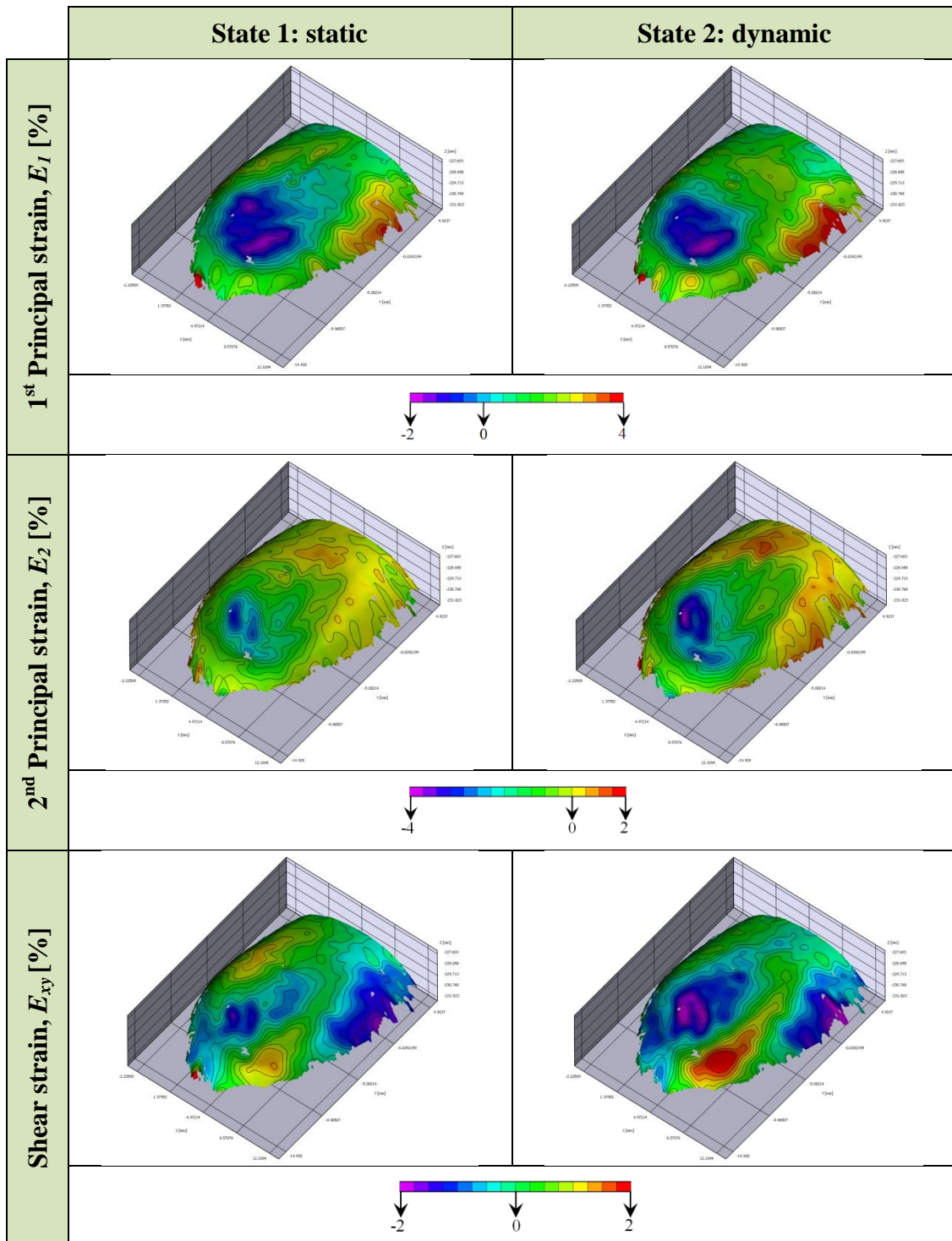


Figure 4-22, DIC result of the natural finger pad loaded at 0.5N with the respective strains 1st principal strain E_1 , 2nd principal strain E_2 and shear strain E_{xy}

4.4.6 The effect of normal load and the stiffness of the finger pad on the strain behaviour

This section presents the strain line profile from a cross-section of the natural finger pad, along the y axis, to show how the normal load changes the surface strain behaviour of the finger pad, as shown in Figure 4-24. The remaining strain line profiles are shown in

Appendix C. The main advantage of the strain line profile is that it makes it easier to identify which region has a higher tendency to deform based on the change in strain values. The cross section of the finger pad is shown in Figure 4-23 and illustrates the top view of a finger pad in contact with a glass plate. The outermost boundary line (dark blue in colour) is the selected region of interest before the 3D-DIC correlation process. The area of the inner circle (pink region covered by dotted lines) is the area in contact between the finger pad and the glass plate. X, X', Y and Y' are the respective position points located at the intersections between the edge of the area in contact and x or y axes. In Figure 4-24, the most obvious change in strain distribution from static to dynamic state is the 2nd principal strain.

Figure 4-26 presents the averaged strain values within the contact area of the finger pad that are plotted against the normal load and the stiffness of the finger pad. This figure can show the big picture in strain values between the natural and the moist finger pad. A linear equation with an intercept at $y = 0$ when $x = 0$ is used in describing the relationship between the average contact surface strain and the normal or the stiffness of the finger pad.

4.4.6.1 First principal strain, E_1

The first principal strain, E_1 , is the maximum possible strain at a position point on a structural specimen. In the static state, there is a peak 1st principal strain at the edge of the contact area near to the palm, as shown in Figure 4-24 (a). The peak strain value increases with the increase of normal load. In the dynamic state shown in Figure 4-24 (b), there is also a peak 1st principal strain at the edge of the contact area near to the palm but there are no considerable changes from the static state, which is also reflected in the change in average contact strain from a static state to a dynamic state, as shown in Figure 4-25 (a) and (b). The peak strain value still increases with higher normal load.

4.4.6.2 Second principal strain, E_2

The second principal strain, E_2 , is the minimum possible strain at a point position on a structural specimen. In the static state, there is no obvious strain pattern in the 2nd principal strain line profile of the finger pad Figure 4-24 (c). However, in the dynamic state, there is a negative peak strain value at the edge of the contact area near the fingertip. The peak strain value decreases with higher normal load, as shown in Figure 4-24 (d).

On the other hand, it is very difficult to see the average E_2 has a straightforward relationship with the normal load or the stiffness of the finger pad in the static state and dynamic state, as shown in Figure 4-25 (c) and (d), and Figure 4-26 (c) and (d).

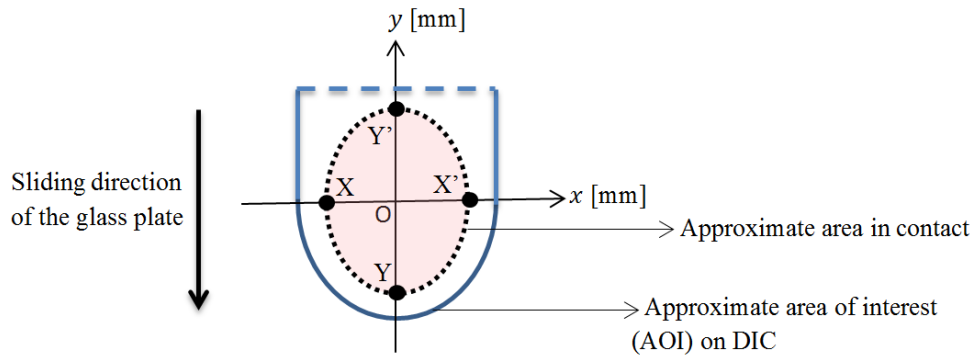


Figure 4-23 Illustration of finger pad from top view

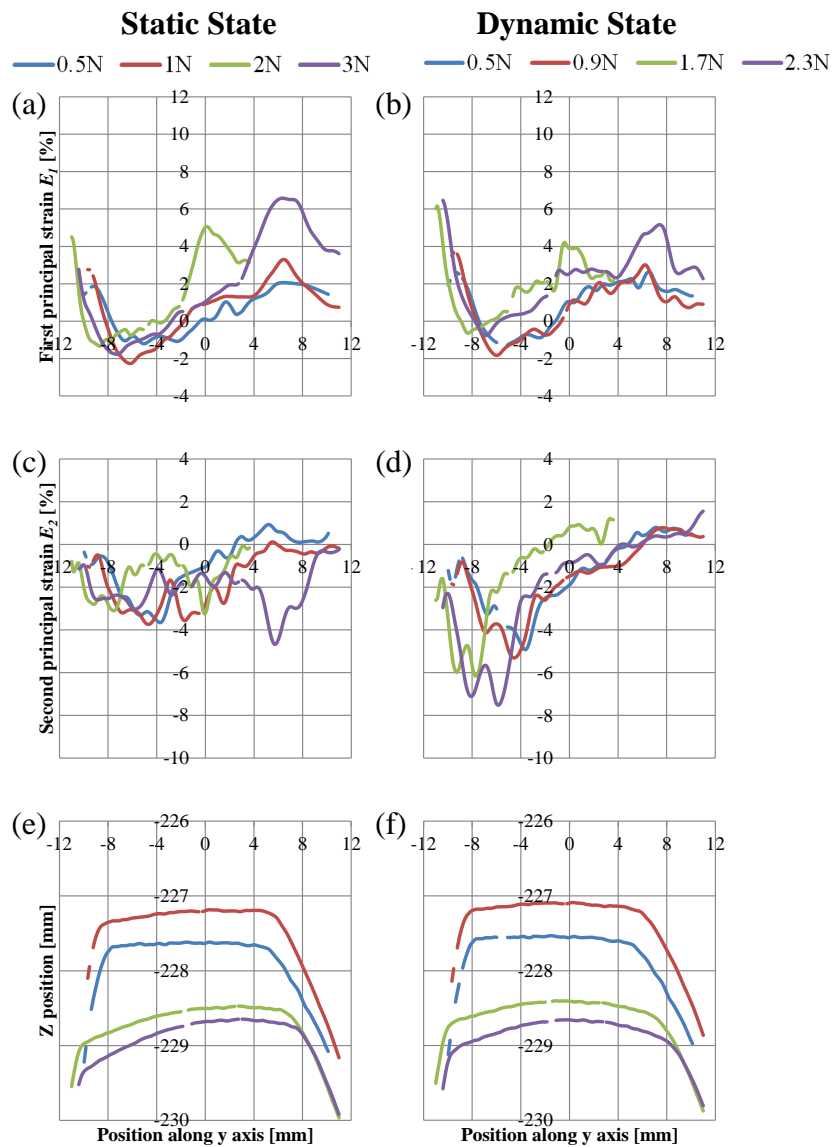


Figure 4-24, First principal strain E_1 of the natural finger pad obtained along y axis in the (a) static and (b) dynamic state, second principal strain E_2 of the natural finger pad obtained along y axis in the (c) static and (d) dynamic state, and the geometrical shape of the finger pad along y axis in the (e) static and (f) dynamic state

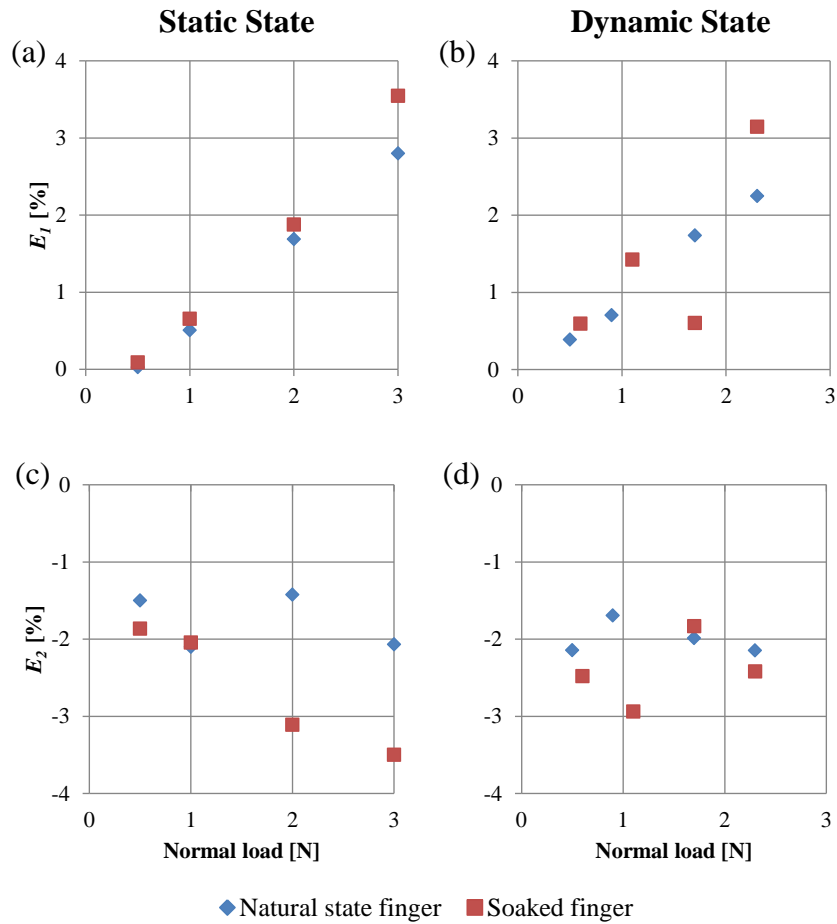


Figure 4-25, Average first principal strain E_1 strain within the contact area of the finger pad from (a) static to (b) dynamic state, and average second principal strain E_2 strain within the contact area of the finger pad from (c) static to (d) dynamic state when plotted against the normal load applied on the finger pads

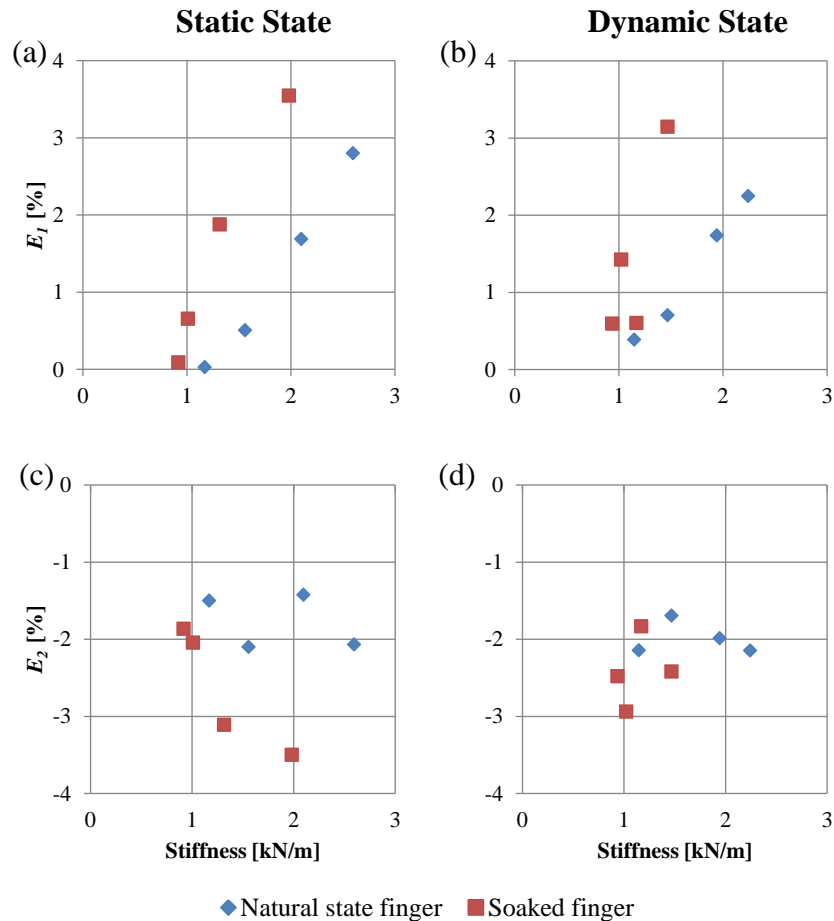


Figure 4-26, Average first principal strain E_1 strain within the contact area of the finger pad from (a) static to (b) dynamic state, and average second principal strain E_2 strain within the contact area of the finger pad from (c) static to (d) dynamic state when plotted against the stiffness of the finger pads

4.4.7 Apparent contact area of the finger pad

It should be noted that the apparent contact area of the finger pad can only be measured from the 3D-DIC data. The apparent contact areas of the finger pad measured in both the static and the dynamic states are shown in Figure 4-27 (a) and (b) respectively. This figure also shows the respective moisture level of the finger pad taken before and after the sliding tests, however, the moisture level does not seem to have a direct relationship with the apparent contact area in this experiment. Based on Archard (1957), the contact area of the finger pad can be described by $A = kN^b$. In this study, the k values range from 95.1 to 102.2mm² and the b values range from 0.2 to 0.3.

By using the curve fitting equation in Figure 4-28 (b), the apparent contact area of the finger pad (both natural and soaked) increases from the static state to the dynamic state if the

magnitude of the normal load remains the same. On the other hand, the moisture level of the finger pad has increased after the sliding tests.

Additionally, Figure 4-28 was plotted to show the linear relationship between the apparent contact area of the finger pad and the shear force acted on the finger pads.

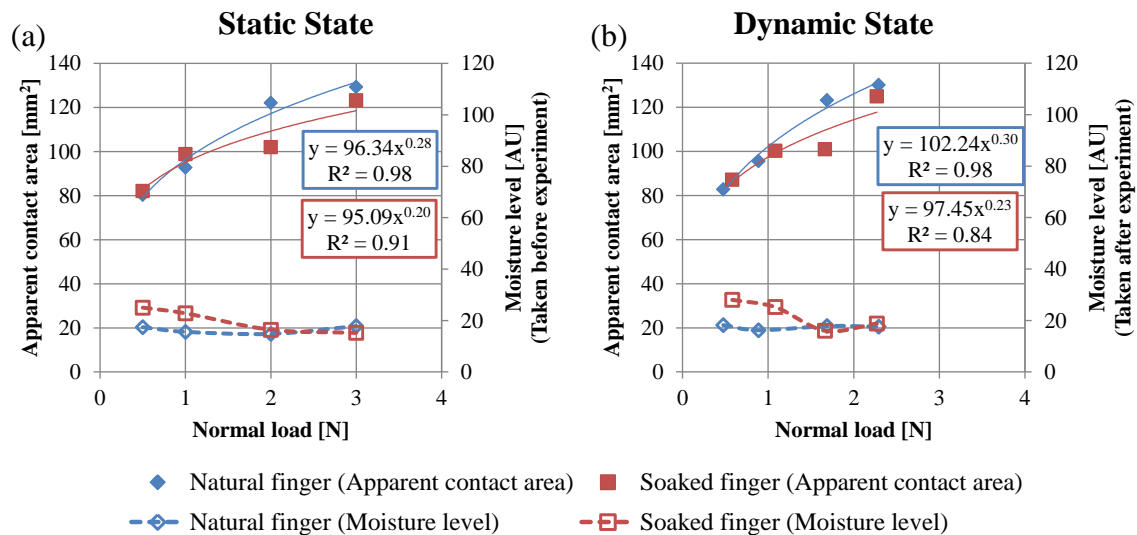


Figure 4-27, The relationship between the apparent contact area, moisture level of the finger pad and the normal load applied in (a) the static state and (b) the dynamic state

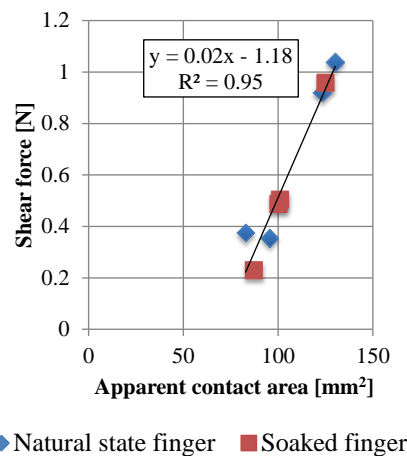


Figure 4-28, The relationship between the shear force and the apparent contact area of the finger pads in the dynamic state

4.4.8 Real to apparent contact area ratio of the finger pad

It should be noted that the real-apparent contact area ratio of the finger pad can only be measured from the OCT data. A power-law equation can be used to describe the relationship between the real-to-apparent contact area ratio of the finger pad and the normal load, as shown in equation 4-1 (Liu, 2013).

$$R = mN^n$$

Equation 4-1

where R is the real-to-apparent contact area ratio, N is the normal load, m is a constant and b is an exponent.

Figure 4-29 (a) and (b) show the change in real-apparent contact area ratio against the increase of the normal load applied on the finger pad in the static state and dynamic state respectively. In both states, the contact area ratios seem to increase with the normal load applied. Figure 4-29 also shows that the moisture level of the soaked finger pad was lower than the moisture level of the natural finger pad. Even though the moisture level of the finger pad whether “natural” or “soaked” is different, it is difficult to say for certain if the moisture level is affected by the sliding conditions. Therefore, more data is needed by performing tests on wider population.

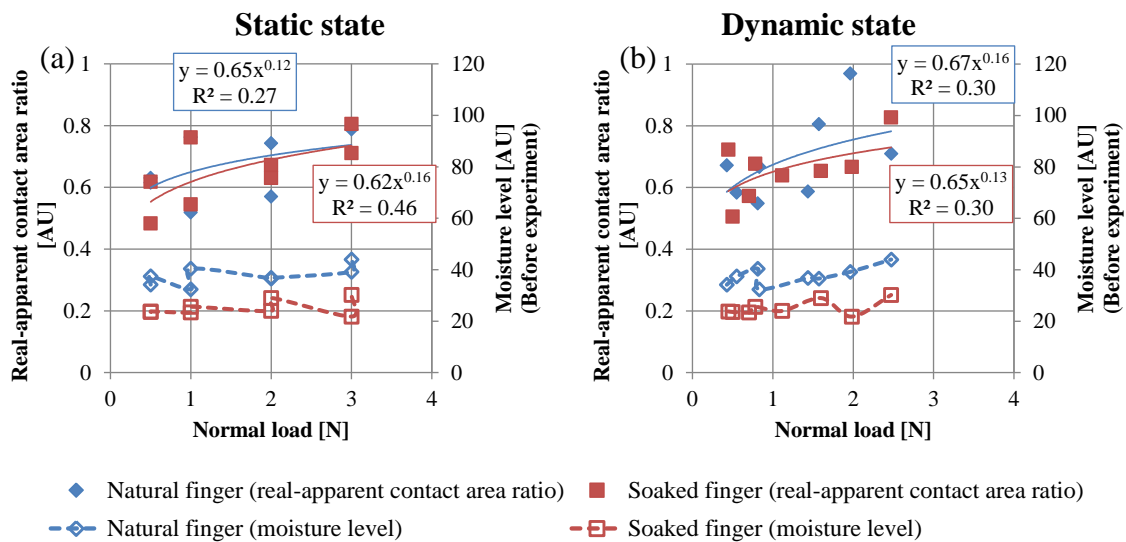


Figure 4-29, The change of the ratio of the real against apparent contact area of the finger pad from the static state to the dynamic state with the normal load

4.4.9 Roughness of the finger pad

This section shows how the morphology of the finger pad changed from the static state to the dynamic sliding state, as shown in Figure 4-31 from the position 2 of the natural finger pad.

The morphological changes are reflected in the Table E-1 and Table E-2 (in Appendix E) that give the mean roughness (R_a) and the mean roughness depth (R_z) of the finger ridges at the position 1 and position 2 of the finger pad, which were averaged from 5 continuous static or dynamic sliding images. The roughness is then plotted against the normal load applied, as shown in Figure 4-30. The figure shows that the roughness of the finger pad

decreases with the increase in normal load. Figure 4-30 (b) also shows that the roughness data is more concentrated at the low roughness region when the finger pad was at the dynamic state. This demonstrates that the sliding has made the finger pad flatter in the process. Finally, the figure goes on to show that the soaked finger pad has a higher roughness profile than the natural finger pad. This might mean that the water application has an effect that results in the change in roughness of the finger pad.

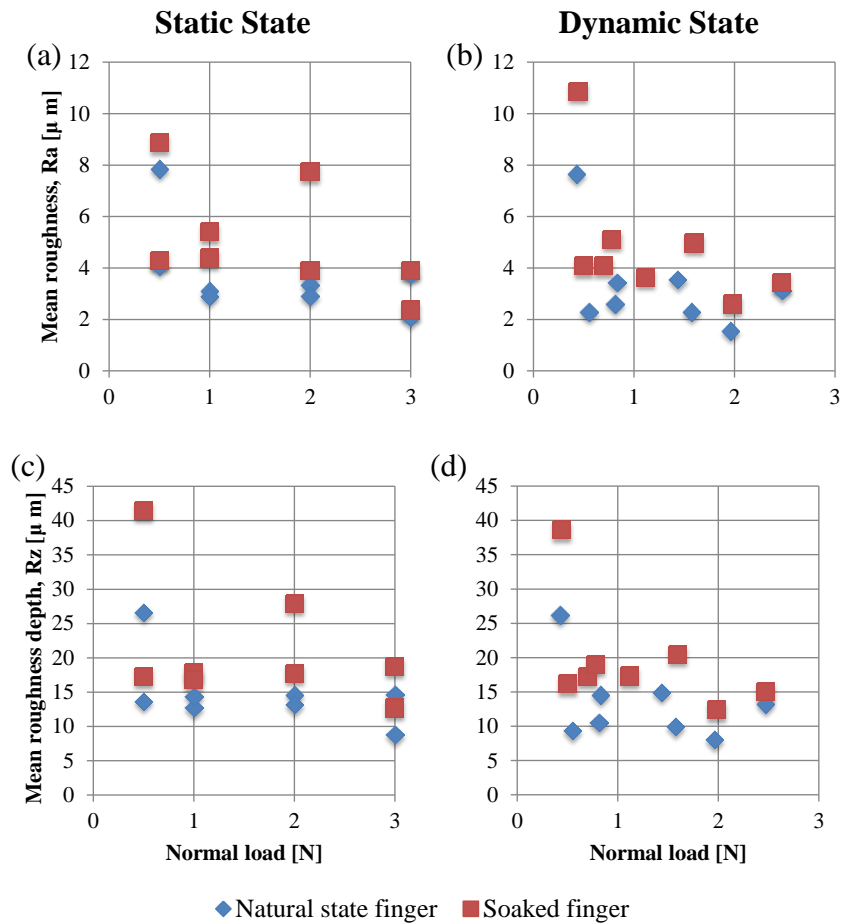


Figure 4-30, The mean roughness, Ra, and mean roughness depth, Rz, against the normal load

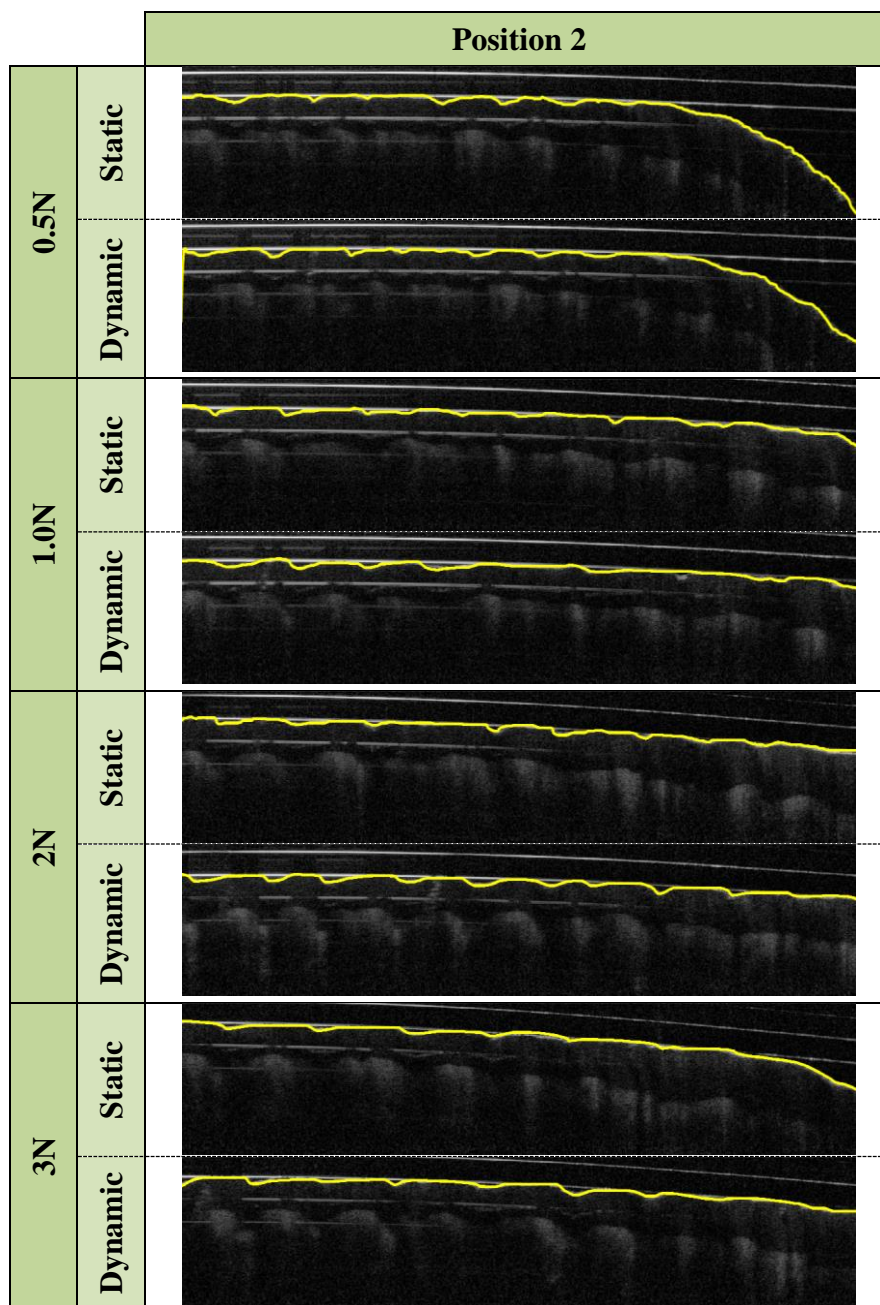


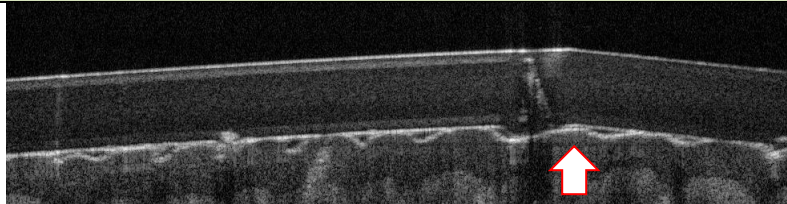
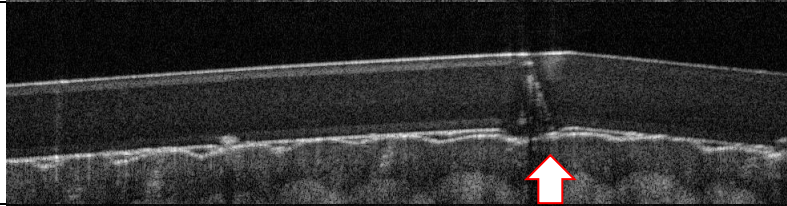

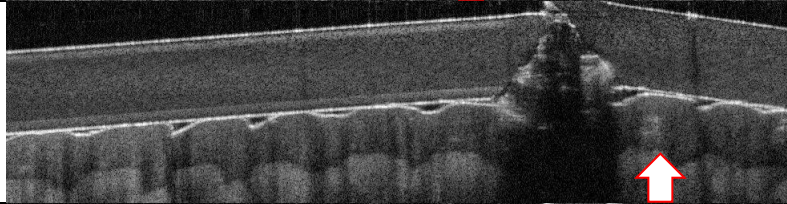
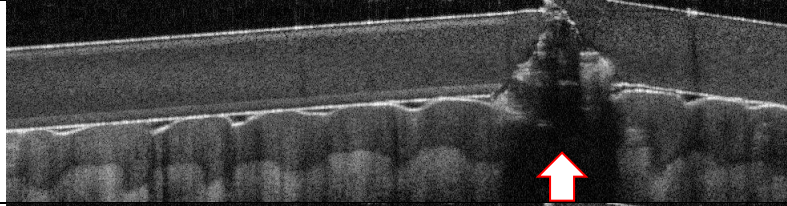

Figure 4-31, OCT images of position 2 of the natural finger pad

4.4.10 Morphological change of finger pad against grooved plate during sliding

Figure 4-32 shows the morphological changes of the finger pad when the finger pad was slid against different types of grooved plastic plate. The white arrows are to show how the specific finger pad ridges move across the groove. It has shown that there was distinctive loss of visualisation of OCT images under the grooves for the “sharp groove”, “broken sharp groove”, “shallow groove 1” and “shallow groove 2”. The “broken sharp groove” OCT

images suffered the most loss of visualisation while the “big groove” suffered the least or no loss of visualisation.

From the “big groove” OCT images, it can be seen how the ridge of the finger pad climbed up the groove before changing its morphology to suit the change of the geometry of the plate. Some OCT images from other grooves typed plates can somewhat show how the ridge of the finger pad get across the groove although the image quality is not as good as the “big groove”.

Grooves type	Frame number	Deformation of the finger pad		
Sharp groove	99			
	102			
	103			
Broken sharp groove	80			
	83			
	87			



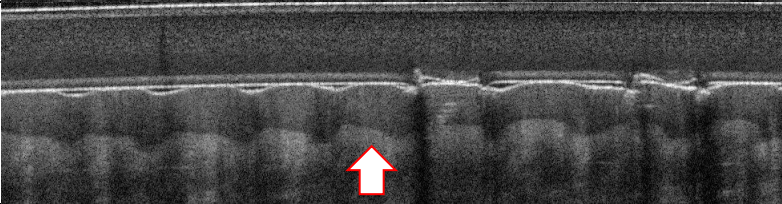
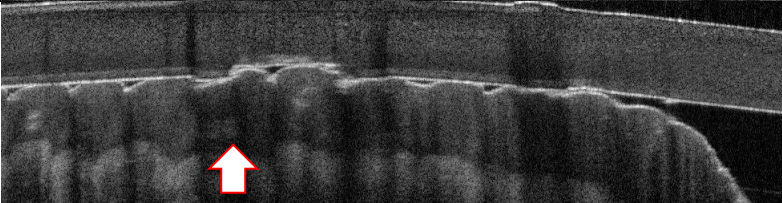
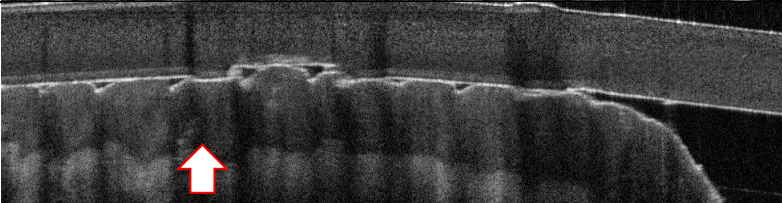
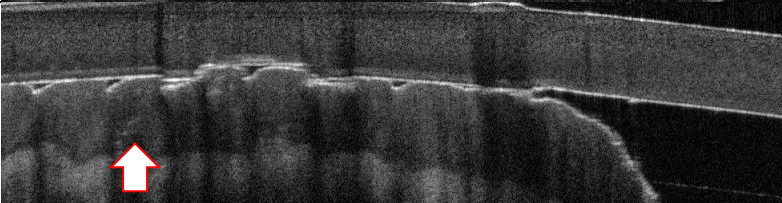
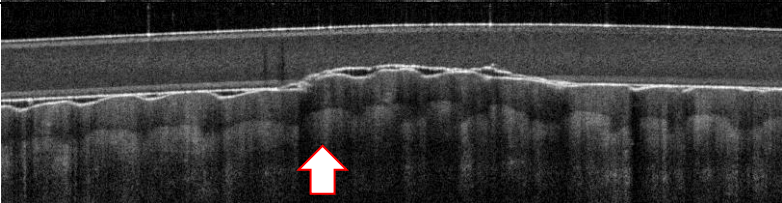
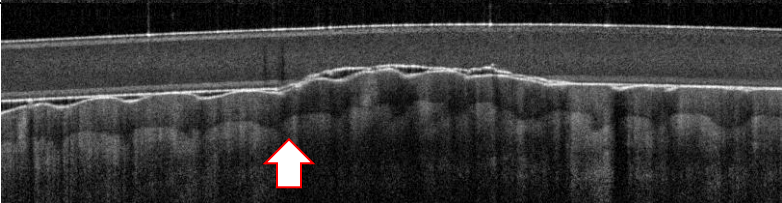
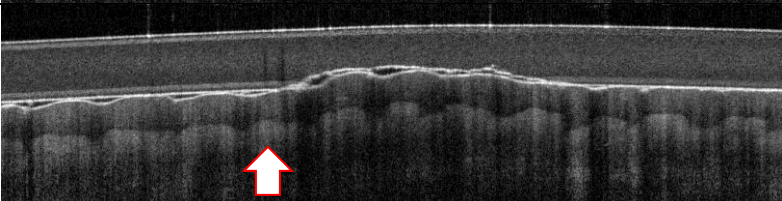
Shallow groove 1	117	
	119	
	121	
Shallow groove 2	73	
	75	
	78	
Big groove	33	
	39	
	43	

Figure 4-32, Sliding finger pad across different grooves

4.5 Discussion

4.5.1 *Relationship between the frictional and the strain behaviour of finger pad*

In studying the friction interaction between a human skin and a counter-face material, various studies (Wolfram, 1983; Johnson et al., 1993; Adams et al., 2007) have suggested that the friction mechanism during the interaction of the two materials could be dominated by an adhesive mechanism (through shear stress) and/or deformation mechanism (through work lost or hysteresis). Adhesive mechanism that contributes towards the friction force is caused by the rupture of the interfacial junctions while the deformation mechanism is due to the hysteretic or interlocking effect that results from the deformation of the interacting material (Greenwood and Tabor, 1958; Adams et al., 2007; Derler et al., 2009; Tomlinson et al., 2011a).

In the case of the sliding a smooth plate across a finger pad, multiple studies concluded that the predominant friction mechanism is adhesion while the deformation friction is relatively small in comparison (Adams et al., 2007; Derler et al., 2009; Kwiatkowska et al., 2009; Tomlinson et al., 2011b; Liu, 2013). There are different methods in assessing the predominant friction mechanism. Firstly, Tomlinson (2009) had listed out the three conditions that will cause the deformation mechanism to be excluded as the predominant friction mechanism – low counter-face roughness, low normal load application (<3N) and no cyclic movements (backwards and forwards) during sliding, in which the current study has fulfilled all three of them. Alternatively, Derler et al. (2009) suggested a graphical method in assessing the predominant friction mechanism, which was to identify the exponents of the power-law relationship in the dynamic coefficient of friction against normal load graphs. Derler et al. (2009) found that the exponents of the adhesion mechanisms and deformation mechanism are $-1/3$ and $1/3$ respectively. The range of the exponents in this study is -0.05 to -0.25 as shown in Figure 4-33, which could mean that the adhesion mechanism is the more dominant friction mechanism.

In the study of the strain behaviour of the human skin during sliding interactions, it is important to know which type of sliding test has been conducted. First testing type uses a rigid probe to slide across a human skin, forearm skin for instances, while the second type requires the human skin to slide across a rigid plate, for example, a finger pad, the side of the

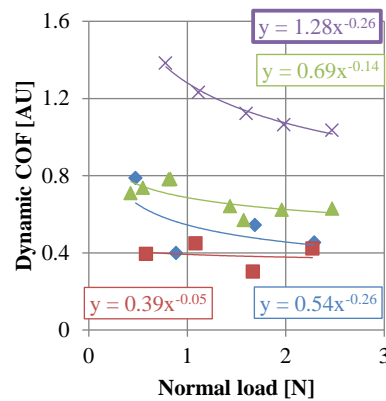
hand etc. (Adams et al., 2007; Kwiatkowska et al., 2009; Tomlinson et al., 2011a; Liu, 2013; Derler et al., 2009; Delhaye et al., 2016).

In the case of the sliding a smooth plate across a finger pad in the direction away from the body, this study showed that the in contact region of the finger pad nearer to the palm has higher 1st principal strain value while the opposite far end contact region near the finger tip has a higher 2nd principal strain value, which corresponds to the finger pad in tension and in compression along the sliding direction. Delhaye et al. (2016) found that both strain amplitudes increased with the increase in normal force during sliding. Similarly, this study has found that the mean 1st principal strain of the finger pad within the contact area (Figure 4-26) increased with the magnitude of the normal load in both the static and the dynamic states. The mean 2nd principal strain, however, only increased in the static state. In the dynamic state, the mean 2nd principal strain remains at the same constant range regardless of the magnitude of the normal load. This is probably due to the increase of the 2nd principal strain value at the edge of the contact area, which cancelled out the decrease of the 2nd principal peak strain values (Figure 4-24) in the dynamic state as the mean 2nd principal strain averages the strain values within the contact area. From the static state to the dynamic state, the inputted shear load has a lesser influence on the strain behaviour of the finger pad than the normal load applied, which is evidenced from the small changes between the mean principal strain graphs in Figure 4-26. This might be caused by the surface condition of the finger pad, which will be further explained in the next section. For example, the speckles application and the moisture level of the finger pad.

As such, this goes on to show that there are connections between the frictional and the strain behaviour of the finger pad as the normal load affects the strain behaviour of the finger pad whereas the shear load that caused sliding has a less notable effect on the change in the strain behaviour. However, more work is required to further understand the strain behaviour of the finger pad in response to a large range of normal loads during sliding as the current work only focuses on the low load region.

Delhaye et al. (2016) also reported both the mean principal strain values (ranges from 25% - 45% which the 2nd mean principal strain values have been absolute) of the sliding finger pad, which are much higher than both the mean principal strain values in this study (ranges from 0.39% - 3.15%). This can be explained by the difference in the contact area in both studies as the finger pad contact area in Delhaye et al. (2016) study ranges from 100mm²

to 200 mm² whereas the finger pad contact area in this study ranges from 80mm² to 120mm². As the adhesive friction force is proportional to the contact area of the finger pad (Liu, 2013), the finger pad will then have to undergo higher strain in order to gain enough horizontal force to break free from the adhesive friction force. Moreover, the finger pad in this study was applied with speckles whereas the finger pad in Delhaye et al. (2016) study did not. The next section will explain how the finger pad moisture and the speckles affect the frictional behaviour of the finger pad during sliding. Also, during the strain computation of the sliding finger pad in Delhaye et al.'s study (2016), the un-deformed state of the finger pad was likely set as when the finger pad was in full contact with the plate before sliding, which is equivalent to the state 1 (Figure 4-17) of the finger pad in this study. It is important to know which finger pad state is set as the un-deformed state for the strain computation because the strain calculations are relative to the un-deformed state.



◆ DIC, Dry finger ■ DIC, Moist finger ▲ OCT, Dry finger × OCT, Moist finger

Figure 4-33, Dynamic coefficient of friction against normal load of the natural and soaked finger pad

4.5.2 Moisture level in human skin

The moisture state of the finger pad plays a vital role in the sliding interaction between the finger pad and the glass plate because the frictional and the strain behaviour of the finger pad are influenced by the surface condition of the finger pad.

This study shows that the soaked skin has higher dynamic COF than natural skin in OCT test. An outcome that is similar to the previous studies (Tomlinson, 2009; Adams et al., 2012; Liu, 2013). However, the soaked skin behaves like a natural skin in 3D-DIC sliding test. The main reason could be that the bulk moisture level of the soaked finger pad has returned to the moisture level of a natural finger pad before the sliding experiment during the DIC test.

Although Table 4-2 has shown that the measured moisture level of the soaked finger pad before the experiment during the DIC test was somewhat similar to that of the OCT test. However, the measured moisture level only represents the moisture of the stratum corneum (the outermost layer of the human skin). This is further discussed later in this section. The time taken to prepare a soaked finger pad for the DIC test was longer (approximately 5 minutes) than the OCT test because the soaked finger pad needed the speckles application. This period of time could be sufficient enough to increase the amount of water loss from the surface and sub-surface of the finger pad to the environment through evaporation. When a certain level of water loss amount is achieved, the soaked finger pad would behave like a natural finger pad during the sliding interaction. Also, the environmental conditions of the DIC test and the OCT test were different as well. The environmental temperature, where the DIC test was held, was 6.6°C higher and the difference in relative humidity was at least 8%. Therefore, the environmental conditions could have escalated the water loss rate of the soaked finger pad where the DIC test was held.

Additionally, the frictional behaviour of the soaked finger pad during DIC test could be due to the effect of the speckles pattern applied on the finger pad, which caused the surface condition of the soaked finger pad in 3D-DIC tests to be different from the soaked finger in OCT tests. The application of speckles pattern has acted as a barrier between the finger pad and the glass plate. The region of the finger pad, where the speckles were applied, would behave like a natural finger pad because the black ink was hydrophobic. Therefore, this would prevent friction mechanisms, such as the capillary adhesion or the occlusion of the finger pad, from occurring during sliding (Dinç et al., 1991; Adams et al., 2012).

The monitoring of the moisture level of the finger pad throughout the sample preparation and the experiment has proven to be helpful as it shows how susceptible the moisture level of the stratum corneum layer is to the external and probably internal environment of the human skin, for example, the difference in the environmental temperature and the relative humidity when the tests were conducted and the period of acclimatisation that caused different amount of water lost from the finger pad in each test.

This study also shows that the moisture level of a finger pad can be plotted with various variables that might influence the sliding interaction of the finger pad. Even though the moisture level of the finger pad cannot be measured in real time, using the measured moisture level before the experiment started has proven to be useful as a benchmark. The

main issue with the moisture level of the finger pad is nonetheless the methodology of the water application to control the moisture level of the finger pad because different methodologies may result in different frictional and strain behaviour. Past studies have had slight different approaches in applying water on the human skin. For example, Tomlinson et al. (2011b) used wet towels to achieve the moisture level desired before performing the friction test. On the other hand, Liu (2013) soaked the finger pads and performed the friction test without any acclimatisation period. Adams et al., (2007) also studied the effect of the soaked condition of the finger pad by dropping a few water droplets on the forearm skin while the spherical probe was still sliding across.

In this study, the methodology of the water application focuses on the effect of long period of water soaking (20 minutes) in making a soaked finger pad and acclimatisation period (3 minutes) was included in the water application process to allow the surface condition of the finger pad to reach a steady state before the sliding tests. This study has found that the moisture level of the human skin after the acclimatisation would be lower than the initial state before the water application. The moisture measurements were measured using a corneometer (C+K, Germany) that has low measuring depth. Even so, both the stiffness and sliding test went on to show that this finger pad still behaved as a soaked finger pad, with the soaked finger pad from 3D-DIC tests being an exception. This means that the long water soaking process may have changed the bulk properties of the finger pad. So, the low moisture reading after the acclimatisation period may show that the water at the surface level of the finger pad evaporated during the acclimatisation period, without having a big effect on the bulk properties of the finger pad. Hence, this shows that the acclimatisation period is important in the study of the frictional behaviour of the soaked finger pad and this requires more work to further understand how the water evaporation during the acclimatisation period can affect the dynamic coefficient of friction to what extent.

Figure 4-34 illustrates the main concept how the water is being transferred into/from the finger pad during the water application and the sliding test. This should explain the notable changes in the moisture level of the finger pad discussed previously. The current concept assumes the possibility of water being able to diffuse into deeper skin epidermal layer. Firstly, before the water soaking process, the finger pad is assumed to be a natural finger when a moisture reading is taken. Then the finger pad is soaked in the water for 20 minutes and another moisture level is taken right after the finger pad was taken out from the water bath, which shows an increase in the moisture reading. However, the moisture level of

the human skin decreases after the acclimatisation period, and normally become lower than the moisture reading taken before the water application process. This has demonstrated that the water in the surface of the human skin is either evaporated into the atmosphere or further absorbed into deeper skin epidermal layer. Next, when the soaked finger pad was pressed down against the glass plate, the water in deep skin epidermal layer is being squeezed into the surface of the finger pad. Therefore, it will cause the increase of the friction on the finger pad through capillary adhesion or occlusion and the moisture reading at this point will be higher than the moisture level taken before the sliding test.

There are also other studies that investigated the mechanisms of a wrinkly finger pad (Changizi et al., 2011; Kareklas et al., 2013; Lin et al., 2015, Sáez & Zöllner, 2017). Even though the current study used the term “soaked finger”, the state of the finger was similar to that of a wrinkly finger because it was soaked for a long period of time. It is unknown why the finger pad of the current study did not exhibit a lot of wrinkles after a soaking period of 20 minutes. So, this could belong to an individual case. By means of computational model, Sáez & Zöllner (2017) concluded that the wrinkly finger is potentially caused by both contraction of the deeper layer of the skin and also the swelling of the upper layer of the skin. Contraction of the deeper skin layer is often caused by the shrinking of the blood vessels while the swelling of the upper skin layer is often associated with the osmosis effect. Sáez & Zöllner (2017) justified the mechanisms of forming a wrinkly finger, it is not mentioned if it is possible for the water might diffuse into deeper skin layer.

In the study of moisture of wrinkled skin, Lin et al. (2015) has measured the moisture of the finger pad before and after the soaking. It was found that the moisture level of the finger pad did not have much change from the soaking. However, the coefficient of friction of a soaked finger pad was higher than a dry finger pad. The study did not mention if the skin hydration was measured straight from the soaking or after the excess water was wiped off. Even if it is assumed that the excess water was wiped off, the moisture level of the finger pad in the current study still decreased by a considerable range in comparison to Lin et al. (2015). The only possible explanation could be the acclimatisation period in the current study because the finger pad was left to acclimatised for 8 minutes before performing the friction test.

This study does not investigate a wet sliding condition because the DIC software is not able to track the movement of the speckles when there is a water film between the

interacting counter-faces. The images acquired would show a region of magnified speckles, normally at the edges of the contact, due to the properties of light travelling into a different medium. In addition, the speckles are very easy to fall off during the wet sliding.

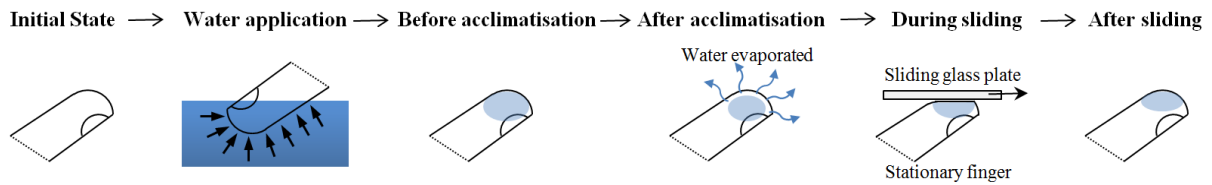


Figure 4-34, Moisture changes of the finger pad

4.5.3 Force-displacement relationship of the finger pads

Section 4.4.1 has shown that the force-displacement relationship of the finger pads can be described using either polynomial equation or power equation as shown in Figure 4-15 (a) and Figure 4-16 (a) respectively.

From the perspective of the whole data set of the force-displacement graph of the finger pads, the polynomial equation can fit into the whole data nicely while the power equation can fit into the most part of the data as shown in Figure 4-35 (a) and (b) respectively. This is reflected in their respective R-squared values as well. The R-squared values of the polynomial equation fit are 0.99 for both types of finger pads and the R-squared values of the power equation fit are 0.96 and 0.98 for the natural finger pad and soaked finger pad relatively.

When only low normal load region is investigated, both polynomial and power equation fits give similar stiffness prediction in response to the normal load applied on the natural finger pad. In the case of a soaked finger pad, the pattern of the stiffness prediction of the power equation is similar to that of a natural finger pad. On the other hand, by using polynomial equation fit, there is a region in the stiffness vs normal load graph where the stiffness of the soaked finger pad has a slow increase in response to the increase of the normal load, as shown in Figure 4-15 (b). The stiffness of the finger pad increases substantially if the normal load is increased further.

The main advantage of using a polynomial equation fit is that it can fit the whole force-displacement data set, which the same reasoning was used in a study by Liu (2013) although the polynomial equation with the power of 2 was used. On the other hand, the power equation may have a better representation of the stiffness prediction in the low load region

because the pattern of the finger pad stiffness prediction is more consistent with the finger pads under different conditions (natural state or soaked condition). However, as discussed in section 4.5.2, the water application affects the bulk properties of the finger pad and the water loss starts from the surface of the finger pad, which is illustrated in Figure 4-34. Therefore, the region of the finger pad where the water is still trapped could have different stiffness from the region of the finger pad where the water is evaporated. If the soaked finger pad is further pressed during the stiffness test, the region of the finger pad where the water is still trapped will not further influence the overall stiffness of the finger pad. Therefore, the stiffness of the finger pad increases substantially again after a certain normal load value is achieved.

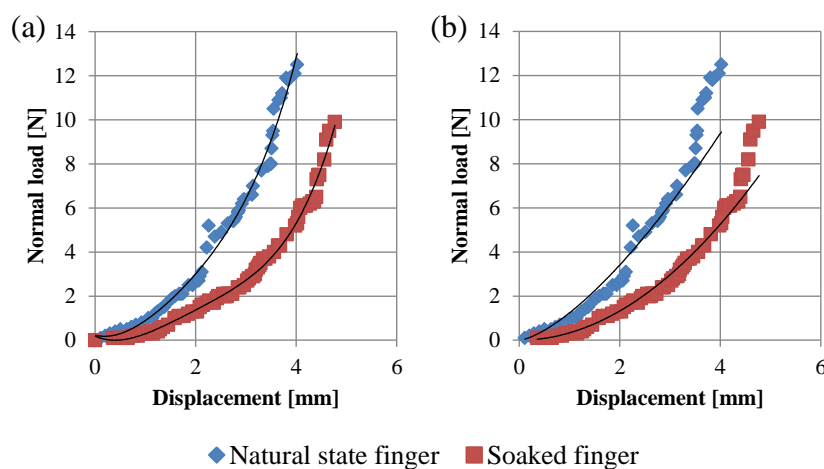


Figure 4-35, The force-displacement graphs of the finger pads in a natural state and soaked condition using (a) a polynomial equation fit and (b) a power equation fit, which includes the data points in high normal load application

4.5.4 Effect of stiffness on dynamic coefficient of friction of finger pad

Previous studies have found that human skin friction is associated with the mechanical properties of the human skin itself (Johnson et al., 1993; Adams et al., 2007; Paillet-Mattei et al., 2007; Kwiatkowska et al., 2009; Liu, 2013). Most importantly, various studies showed that the stiffness of the finger pad decreased with the increase of water in the human skin (Jemec & Serup, 1990; Hendriks et al. 2004; Boyer et al., 2009; Hendriks & Franklin, 2009). Therefore, a stiffness test was performed in this study to investigate how the stiffness would influence the dynamic coefficient of frictions of a finger pad.

When the dynamic coefficients of friction were plotted against the stiffness, Figure 4-20 (c) shows that the range of the dynamic coefficient of friction seems to converge to a certain value as the stiffness of the finger pad increases, which agrees with the results of

previous studies (Tomlinson, 2009; Liu, 2013; Derler & Gerhardt, 2012). However, in the case of soaked finger pad during OCT test, this study has found that the graphical pattern of the relationship between the dynamic coefficient of friction and the stiffness (and the normal load as well) was somewhat different, which the dynamic coefficient of friction increased sharply to a certain point at first. Then, it decreased similarly with other data sets (OCT natural finger, DIC natural and soaked finger), which the suggested a “power” relationship between the coefficient and the stiffness or normal load can be upheld. As shown in Figure 4-20 (b) and (c), the dynamic coefficient of friction data points of the soaked finger pad during the OCT test fell below the natural finger pad region. Therefore, it could be an indication of severe water loss from the finger pad before or during the test, which caused the soaked finger pad to revert back as a natural finger pad.

Undeniably, the dynamic coefficient of friction of the finger pad is not only influenced by the stiffness of the finger pad. So far, section 4.5.2 has shown that the water application method plays an important role where severe water loss during acclimatisation period could cause a soaked finger pad to behave as a natural finger pad in a matter of minutes. There are other potential factors as well, for instance, the environmental temperature, the relative humidity, the contact area (real or apparent) and the roughness of the finger pad, which will be discussed in later sections (4.5.5 and 4.5.6).

It is also important to discuss the robustness of the stiffness test set-up. The system is easy and convenient to set-up and obtains a force-displacement graph. Then, the stiffness of the specimen can be extracted from the force-displacement graph. However, the current set-up is limited because it is very difficult to determine the Young’s modulus of the specimen. The results may not be repeatable due to the geometry of the sample, unless a very thin indenter is used. Currently, it is difficult to say if the stiffness data may vary against the direction of sliding. Therefore, a more comprehensive work is needed in the future to improve the current stiffness test set-up.

4.5.5 Contact area of the finger pad

It should be noted that, in this study, the apparent contact area of the finger pad could only be measured from the DIC data while the real-apparent contact area ration was measured from the OCT images. Although it is desirable to measure the real contact area of the finger pad, the limitation of the scanning range of the OCT only allows giving the real-apparent contact area of the finger pad throughout the sliding interaction in real time. However, there are also

other on going projects that aim to develop OCT systems with high scanning speed and wider scanning range. These bespoke OCT systems could potentially be used to determine real contact area of the finger pad in the future.

The results showed that the apparent contact area of finger pad (both natural and soaked) in a dynamic state was very similar to the apparent contact area in a static state, with only a small increase. This outcome is in contrast with the findings from Liu (2012) and André et al. (2011) where the apparent contact area of the finger pad decreased from a static state to a dynamic state.

Various studies also showed that the real contact area of the finger pad increased when the finger pad was wetted, therefore having higher coefficient of friction (Adams et al., 2007; André et al., 2008; Derler et al., 2009; Tomlinson et al., 2010). This study, however, found that there is an insignificant difference between the apparent contact area of the natural finger pad and the soaked finger pad. Similar findings were observed in the real-to-apparent contact area ratio calculated from OCT images.

It is irrefutable that the contact area plays an important role in the frictional behaviour of the finger pad. Therefore, it is essential to know which parameters that are influencing the contact area during the sliding interaction. This study showed that both the apparent contact area and the real-apparent contact area ratio have a strong correlation with the normal load. However, there is not enough experimental data to determine if the apparent contact area has a strong relationship with the moisture condition of the finger pad because the finger pad with larger apparent contact area did not have higher moisture level (measured before experiment). On the other hand, the moisture level of the finger pad in the OCT test shows increasing signs as the real-apparent contact area increases. This might mean that although the moisture level of the finger pad prior to the experiment has an insignificant effect on the apparent area. However, it may affect the real contact area of the finger pad, which is in good agreement with the findings by Liu et al. (2017), through the water absorption mechanism (Tomlinson et al., 2011b; Liu et al., 2017). Water absorption might cause the human skin to expand and therefore increase the real contact area of the finger pad.

In terms of the sliding state of the finger pad (from static to dynamic state), more data is required to prove if the change of sliding state has a notable effect on the contact area because the change observed in Figure 4-27 and Figure 4-29 is minimal. As the results from this study were obtained from one volunteer, therefore it is not suitable to be used to

represent the whole human population. Even so, the contact area assessing methods developed in this study has shown that it is possible to measure the contact area of the finger pad in a real-time manner.

4.5.6 Roughness of the finger pad ridges

Finger pads are a very special human skin material because the finger pad skin has ridges that help people with gripping and holding objects with their daily life. Studying the roughness of these ridges can help in understanding the frictional behaviour because the ridge roughness could affect the contact area of the finger pad. Finger friction has always been associated with the contact area (Tomlinson et al., 2011b; Liu et al., 2015). The finger pad ridge roughness could also be linked with the strain behaviour because surface deformation always results in the change in surface roughness.

There are only few studies that investigated the effect of the roughness of the finger pad on the sliding interaction (Nakajima & Nakasama, 1993; Egawa et al., 2002). This study has provided evidences that the roughness of the finger pad decrease with the increase in normal load. This supports the fact that when the high normal load pushes down the finger pad ridges, it deforms the finger pad ridge and makes the skin flatter that will result in the increase of the contact area as shown in Figure 4-31.

Next, it seems that the overall roughness of the finger pad decreases from the static state to the dynamic state when sliding against a smooth flat plate in Figure 4-30. This may possibly due to the nature of the interaction between the finger pad and the smooth glass plate. As the surface roughness of the glass is very smooth ($\approx 0\mu\text{m}$), it will not cause interlocking effect on the finger pad that might further increase the roughness of the finger pad ridges. However, more work is required to validate the mechanism of this observation. Also, it should be noted that the term “overall roughness” is used in this context because there was a clear difference between the mean roughness measured in position 1 and position 2 of the finger pad, illustrated in Figure 4-13. Figure 4-36 is used to illustrate the change in roughness of a finger pad when it slid against the glass plate from the static state to the dynamic state. The mean roughness measured at each position of the finger pad at different conditions are tabulated in Appendix E.

It is also found that the soaked finger pad has higher overall roughness than the natural finger pad. It may be possible that the water absorption through the finger pad skin has expanded the stratum corneum layer of the skin, which caused the increase in the

roughness of the skin. Figure 4-37 is shown in order to investigate the effect of the mean roughness of the finger pad on the real-apparent contact area of the finger pad. It shows that the ratio of the real-apparent contact area of the finger pad decreases as the mean roughness increases. In other words, the real contact area of the finger pad decreases as the roughness of the finger pad ridges increase due to the water absorption of the human skin.

In terms of the sliding state of the finger pad, Liu et al. (2017) concluded that the apparent contact area in the dynamic state are always smaller than in the static state. However, Figure 4-27 has shown that the apparent contact area of the finger pad did not considerably decrease as observed in Liu et al.'s (2017) study, where the apparent contact area of the finger pad decreased by approximately 20 mm^2 . The main reason of this conflict is that the material is held stationary during sliding. The finger pad in Liu et al.'s (2017) study was moving along the glass plate while the finger pad in this study was held stationary throughout the sliding interaction. The main advantage of having a stationary finger pad during friction interaction is to minimise the uncontrolled vibration of the finger pad that could affect the force interaction measurement. It also helps to achieve and control the pre-decided normal load magnitude during the sliding tests. It was previously thought that the Matlab algorithm used to determine the apparent contact area from the DIC data (explained in section 4.3.5) could have overestimated the apparent contact area of the finger pad. However, this is ruled out because the overestimation could happen to the apparent contact in both the static and the dynamic states, so it should still be possible to reflect the decrease in apparent contact area in the post-analysis.

On the other hand, the relationship between the roughness profile and the stiffness of the finger pad is much easier to be explained. It is known that the stiffness of the soaked finger pad is lower than the natural finger pad. Therefore, it could be that the water application the expanded epidermal layer of the skin. This in turn resulted in the decrease of the density of the top skin layer and the increase in roughness profiles. Then, after the stiffness measurement has taken place, it will show the decrease in the measured stiffness of the skin because the roughness of the skin will not affect the stiffness measurement.

It is difficult to determine if the dynamic coefficient of friction of the soaked finger pad is decreasing with the increase of the mean roughness of the finger pad, as shown in Figure 4-37. Assuming the dynamic coefficient of friction decreases when the mean roughness of the finger pad increases is true. This means that the real contact area decreased

because the finger pad ridges did not flatten out during sliding. This could fit well to the frictional behaviour of the soaked finger pad in Figure 4-20 where the coefficient of friction decreases when the normal is near to “0”. On the other hand, Derler & Gerhardt (2012) mentioned that Egawa et al., (2012) found that the friction coefficient of females did not significantly correlate with the mean roughness of the forearm skin using a single regression analysis, similar to this study. Still, this study still requires more data input from the human population to validate this result.

In the future study, it would be useful to make a comprehensive study in measuring skin roughness using various materials texture analysis.

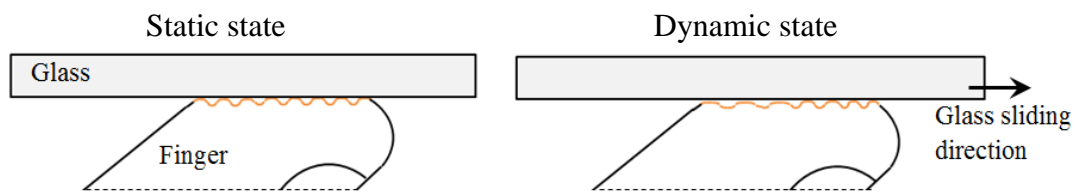


Figure 4-36, Illustration of the roughness distribution within the contact area of the finger pad

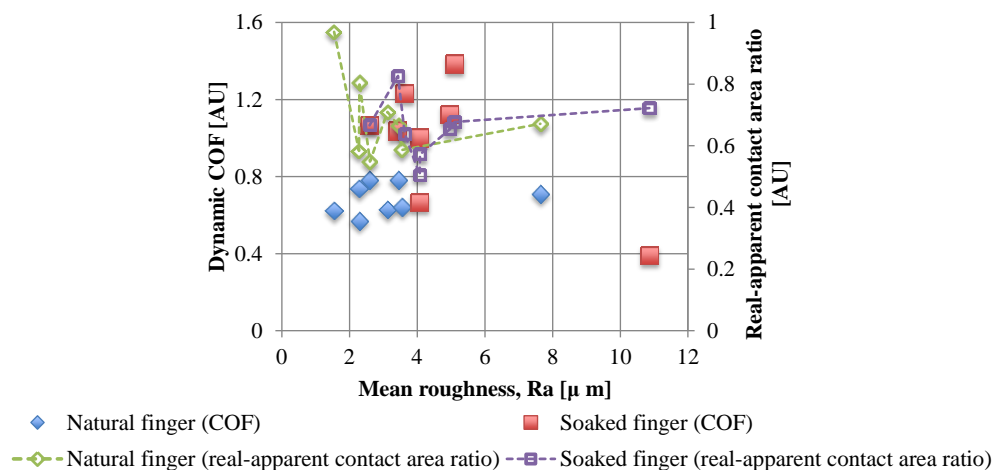


Figure 4-37, The dynamic coefficient of friction against the mean roughness graph when the finger pad was sliding

4.5.7 Feasibility of OCT in studying finger pad – grooved plated interaction

Although this pilot study only looks at the visual results of the experiments, it has successfully shown that OCT can be used to study how the ridges of the finger pad move across the grooves of the plate. The video (approximately 300 of continuous real-time OCT images) is able to show the transition of the morphology of the finger pad from the static state to dynamic state as well.

The images have shown that there were black out regions under the grooves (except for the “big groove”), with the “broken sharp groove” type plastic plate the most obvious.

These black regions were caused by the light diffraction phenomenon as OCT relies on the light reflection signal to produce the OCT images. It is also observed that the black regions normally occurred at the grooves that have a sharp change of plate thickness. In the case of the “big groove”, there are no black regions due to the fact that the thickness did not decrease as dramatically as other grooves that gave severe light diffraction.

As the methodology in making the grooves is very crude, the future work will involve in testing different manufacturing methods because this directly affects the image quality of the OCT images. Only when the image quality of the OCT images is consistent and acceptable, the roughness of the groove and the finger pad can be accurately measured and post-processed.

4.6 Conclusions

This study investigated the frictional and strain behaviour of the finger pad in a natural state and soaked condition, which shows that there are connections between the frictional and the strain behaviour of the finger pad as the normal load affects the strain behaviour of the finger pad whereas the shear load that caused the sliding has less effect to change the strain behaviour of the finger pad.

In terms of the water application of the finger pad, the acclimatisation period has an influence on the moisture reading of the finger pad even though the finger pad had been exposed to long period of water soaking. Therefore, various water application methods should be further researched and documented in the future.

This study supports the relationship between the contact area and the normal load as a power-law equation for both the apparent contact area and the real-apparent contact area ratio of the finger pads. The moisture in the finger pad skin may not have direct influence on the apparent contact area, however, it reflects on the real-apparent contact area ratio instead.

The roughness profile can also be used as a parameter in the sliding interaction between finger pad and the smooth glass plate because it has a relationship with the real-apparent contact area ratio that affects the frictional behaviour of the finger pad. It was found that the roughness profile decreases with the increase of the normal load, the roughness profile also decreases when the finger pad was in a dynamic state and the soaked finger pad has a higher roughness profile than a natural finger pad.

The pilot study that investigates the sliding interaction between a finger pad and a grooved plate has proven that the study of sliding interaction between finger pad and a grooved plate to be feasible and it opens up possibilities to further investigate the sliding mechanism of human skin with other material textures to study interlocking

It should also be noted that the tests in this study were conducted on one single volunteer. This can be solved either through the repeat of the testing on a wider human population. Based on the observation of previous studies on human related experiments, the correlation of results often exhibited a big pool of data. So, it should be expected that the results would have much higher standard deviation when using the same methodologies in the current study on a wider population. The main reason for only one subject was because this study aimed to develop a methodology that uses OCT and 3D-DIC on tribological experiment and to show which measurements can be measured during the test. When the methodology is ready, it can be used on a wider population.

For a more controllable experiment, the utilisation of the silicone hemi-spheres to replace finger pad as the experimental samples.

Chapter 5

Interactions between silicone hemi-spheres and glass

5.1 Introduction

This chapter investigated the frictional and strain behaviour of silicone hemi-spheres with different amount of deadener, which will vary the stiffness, when sliding against a glass plate. There are quite a few limitations when using volunteers in a study or research, which is why researchers have been trying to make or develop a material or a design that can simulate the human skin mechanical properties, physiology etc. This research work is aimed at further understanding and minimising the difference between human skin and a soft tissue simulant.

5.2 Aim and objectives

The aim of this work was to determine if a homogenous silicone hemi-sphere is a suitable soft tissue simulant to simulate a finger pad in terms of friction and strain behaviour.

One of the objectives was to obtain the frictional behaviour of the silicone hemi-sphere using friction tests and strain behaviour using the same methodology for 3D-DIC tests, as in Chapter 4. The OCT was not used in this study because the silicone hemi-spheres do not have ridges on the surface. The friction and strain profiles of both finger pad and silicone hemi-sphere were compared and discussed.

5.3 Methodology

5.3.1 *Manufacture of silicone hemi-sphere specimens*

The silicone hemi-spheres were developed using Room Temperature Vulcanizing (RTV) silicone rubber. Base and catalyst are required to make the silicone rubber with the ratio of 1:1. “Deadener” is only added to soften RTV silicone rubber, and give different stiffness, in this study, the proportions of the deadener in the silicone fluid mixture were 0%, 10%, 15% and 20%.

First, three syringes were used to measure the correct amount of silicone base, silicone catalyst and deadener required. The required volume of each was squeezed into a clean uncontaminated cup, as contamination in the silicone mixture will most likely have an effect on the stiffness of the final product. The base and deadener were added into the cup before the catalyst because the curing process will start when the catalyst is mixed with base. Then, a spatula was used to stir the mixture for 1 minute until all three liquid materials were mixed thoroughly. Then, the mixture was placed into a degassing chamber to remove the air bubbles in the mixture. When there were no more air bubbles in the mixture, it was poured into a spherical shaped mould of 6mm radius. It should be noted that the duration from mixing to pouring should not be longer than 15 minutes to prevent the mixture fully cured before pouring into the mould. After the pouring, flat plates were lightly put on top of the mould and the samples were left for one day to cure.

5.3.2 *Experimental set-up for the sliding interaction*

Figure 5-1 shows the set-up of the friction test for silicone hemi-spheres. Normal and shear forces between the silicone hemi-spheres and the glass plate with a thickness of $396 \pm 6\mu\text{m}$ were recorded through a force plate (AMTI). The normal loads were applied at +z direction

before the sliding. The normal loads used were 0.5N, 1N, 2N and 3N. After the desired load was achieved and stabilised, the glass plate would move at $-y$ direction and slid against the silicone hemi-sphere. The movement and the speed of the glass plate were controlled through Labview control software on the test-rig. The average speed of the sliding plate was 0.5mm/s because the cameras used in 3D-Digital Image Correlation (DIC) system were not high-speed cameras. Therefore, any higher speed than 0.5mm/s will result in capturing blurred images.

After the sliding had stopped, the set-up was left for more than 3 seconds or until there were no significant changes in forces between the silicone hemi-sphere and the glass plate. Then, the normal load was removed.

A thin glass plate was used in this study because the aim of this work was to replicate the exact experimental set-up as the finger pad-glass sliding experiment in chapter 4. The main reason the thin plate was used in the finger pad work was because thicker glasses will lead to overlay reflection of the glass plate and finger pad on the original OCT images.

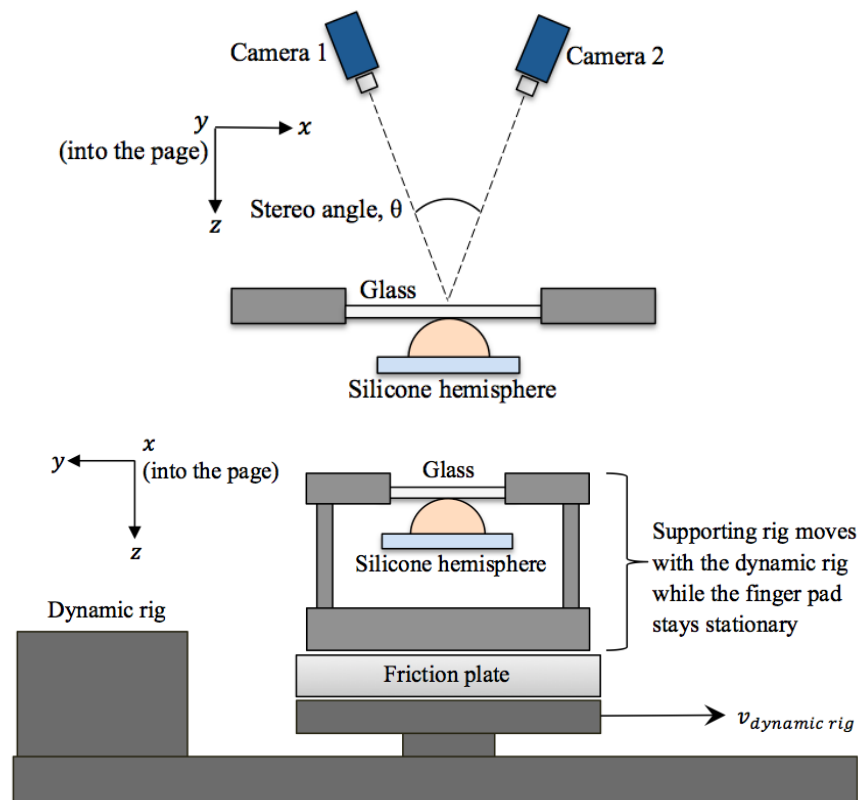


Figure 5-1, Front view (top) and side view (bottom) of the sliding experiment set-up of the silicone hemi-sphere

5.3.3 Stiffness test

The stiffness of various silicone hemi-sphere samples was obtained from the force-displacement graphs from a compression test as shown in Figure 5-2. The samples were placed and fixed under a flat stainless steel plate that was attached to the Mesmecin force gauge (500N). The force gauge, in turn, was attached to the Mecmesin MDD Manual Test Stand. The position of the stainless steel plate was placed as close as possible to the tip of the silicone hemi-sphere without touching it. The force gauge and the displacement transducer were zeroed before acquiring the force magnitude with every 0.1mm displacement increment, which were used to plot a force-displacement graph.

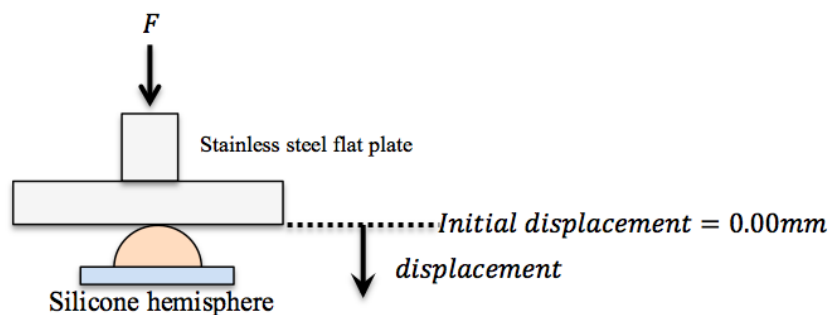


Figure 5-2, Illustration of the stiffness experiment set-up on silicone hemi-sphere

5.3.4 DIC camera set-up, calibration and data acquisition

Detailed information regarding 3D-DIC set-ups and the development of the image analysis has been introduced in section 3.2.

DIC is an optical numerical full field measuring technique that is able to compute displacement and deformation fields of the surface of the experimental object from the images of deformed and un-deformed specimen. Currently, increasing researchers used DIC in biomedical and experimental biomechanics field because it allows the characterisation of the deformation of biological tissues when subjected to different loading conditions.

The working principal of DIC relies on the tracking the random and unique speckles pattern on the material surface by using complex computer algorithms, which some are available commercially. The main characteristic of the DIC system is the amount of cameras used. The DIC system that uses only one camera is identified as the 2D-DIC while the DIC system that uses two cameras is more commonly known as 3D-DIC. The working principal of both systems is the same. The only difference between the two systems is that the 3D-DIC is more insensitive to out-of-plane motions of the experimental object [28]. Therefore, 3D-

DIC system is able to give more accurate strain results for a non-flat specimen such as the silicone hemi-sphere. VIC-3D Digital Image Correlation software (version 7.2.1, Correlated Solutions, USA) was used in the current study.

There are a few steps required to use the 3D-DIC system: sample preparation, camera set-up, calibration, data collection and analysis. Firstly, droplets of black water-based ink (crafters acrylic paint, DecoArt Inc., Stanford) were distributed randomly on the silicone hemi-sphere through the flicking the bristles of an unused toothbrush. It was left for more than 1 hour before friction and DIC testing. Next, the camera set-up section required the adjustment of the stereo angle of the cameras and the distance between the cameras and the object, which in this study, were 30° and 150mm respectively [29]. Two Pike F505B cameras (Allied Vision Technologies GmbH, Germany) equipped with monochromatic CCD sensor (Sony ICX625; 2/3"; 2452×2054 pixels) and 50mm lens objectives (XENOPLAN2.8/50-0902, Schneider, Kreuznach) were used in this study. After the cameras were set, the next step is to calibrate the cameras to the DIC software. A grid size of 11×10 with 2mm spatial distance was selected in this study. The calibration score was 0.064 pixels. The calibration of 3D DIC is done by placing the grid at the same focal plane of the material. Different positions and angles of the calibration grid were placed relatively to give the DIC software a good volume sense.

The sliding experiment was ready to start after the calibration. The acquisition rate was set to 5 frames per second. The image acquisition started before the silicone hemisphere came in contact with the glass and stopped after the glass plate was fully lifted from the silicone hemi-sphere. Then, the images were inputted into VIC 3D DIC software in which subset size, step size and filter size must be set (61×61, 7, and 15 respectively) before running the software. The strain calculated was based on Green-Lagrange strain because the silicone hemi-sphere sample as a whole rigid body. In the Lagrangian description, the strain evolution of the silicone sample with time is studied. The post-processing showed the surface contours of the samples in terms of displacement and strain.

5.3.5 Determining the apparent contact area

The contact area was determined by using Matlab codes. It was able to find the two boundary points, highlighted in red circles, from the deformed shape of the silicone hemi-sphere when in contact with the glass plate, as shown in Figure 5-3. The Matlab code performs multiple differentiations and filtration to determine the two boundary points. The result of this is

shown in Figure 5-4. The code was used to perform on multiple slices of the position graphs of the deformed silicone hemi-sphere as shown in Figure 5-3 (b) and the boundary points obtained are shown in Figure 5-5. Then the “ellipse best-fit” Matlab function can be used to determine the size of the contact, which is shown in Figure 5-5.

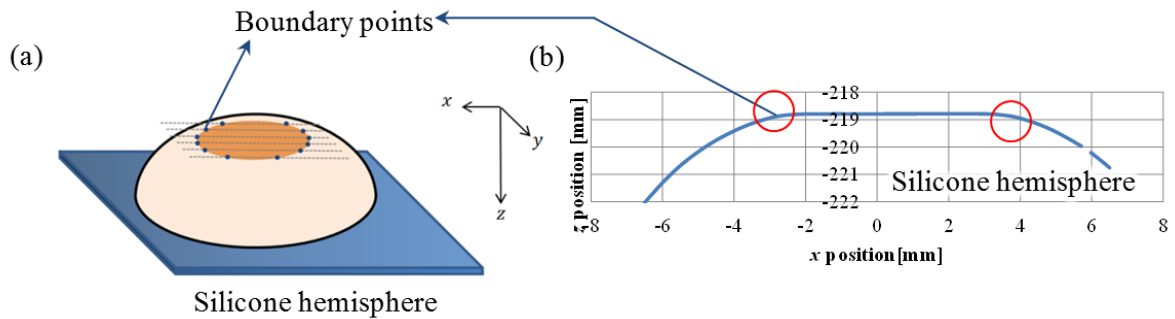


Figure 5-3, Deformed shape of the silicone hemi-sphere in contact with glass plate from DIC position data and the cross section Z-position graph

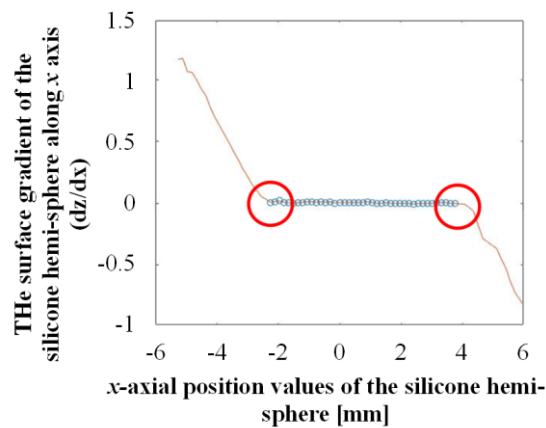


Figure 5-4, The process of finding the boundary points (differentiations and filtration) from the 45th cross section Z-position graph

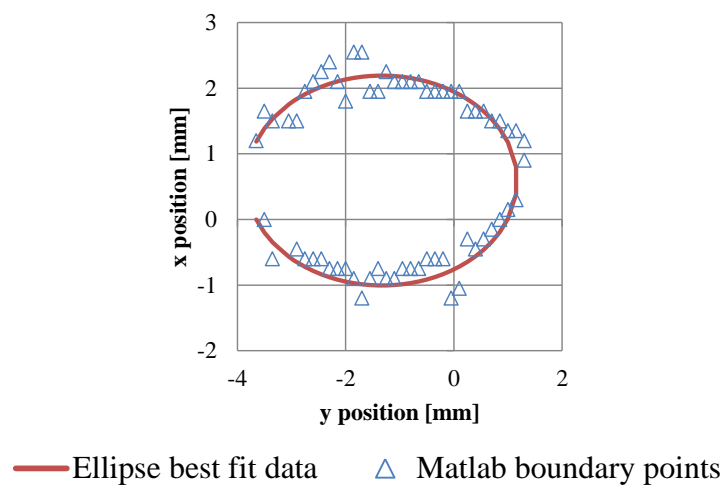


Figure 5-5, Ellipse "best-fit" on the determined DIC position data from Matlab code

5.4 Results

5.4.1 Stiffness of the silicone hemi-spheres

Due to the viscoelasticity of the silicone hemi-spheres, the force-displacement graph of the silicone hemi-spheres is a non-linear relationship. The equation of best fit applied is a polynomial function with a maximum power of 4. The main reason polynomial equation fit is chosen because it can fit into the whole force-displacement data nicely while the power equation deviates from the data set when a certain displacement value is achieved, as shown in Figure 5-7. The amount of deadener in the silicone hemi-spheres has a direct effect on the stiffness of the silicone hemisphere as the compressive force to displace 1mm of the silicone hemisphere drops with the increasing amount of deadener as shown in Figure 5-6 (a).

The specimen stiffness is defined as the gradient of a force-displacement graph and the relationship between the stiffness of a material and the normal force is shown in Figure 5-6 (b). It is more convenient for determining the respective stiffness at different time points with different applied normal load during sliding. However, when the stiffness was plotted against normal force, it can be observed that the difference in stiffness between the silicone hemi-sphere with 0% deadener and the silicone hemi-sphere with 20% deadener steadily decreased with increasing normal force. As the normal force increases, the silicone hemi-spheres will reach a critical point (approximately 4N) where the four silicone hemi-spheres will have the same stiffness. The critical loading point can be neglected because the normal loads used in this study were less than the critical normal load.

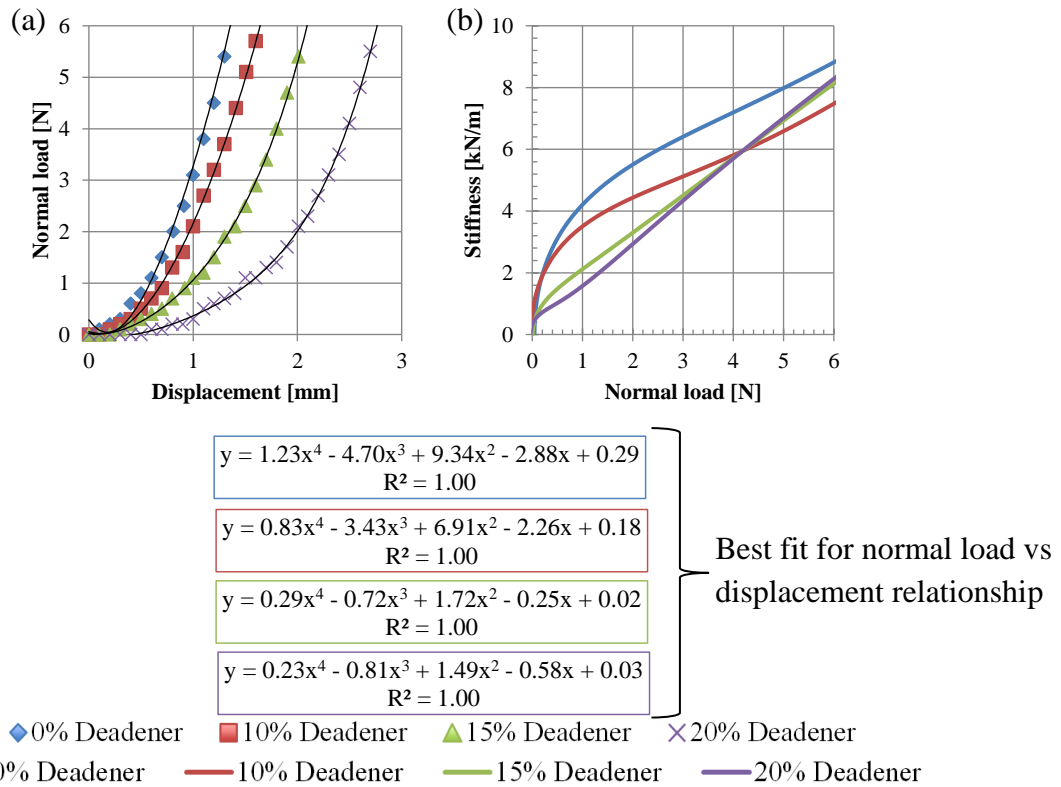


Figure 5-6, (a) Force-displacement graph of the silicone hemi-spheres and (b) stiffness vs normal load graph using polynomial equation relationship

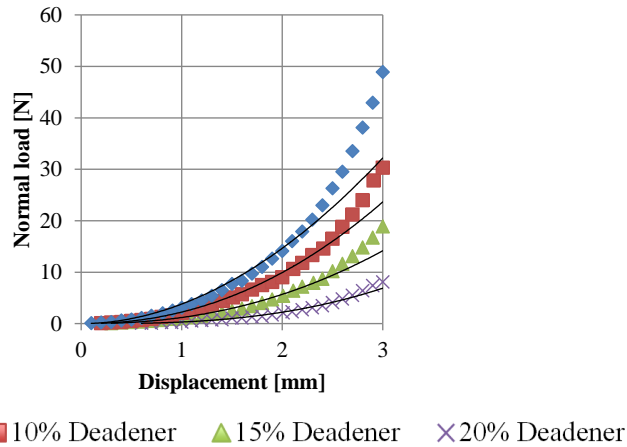


Figure 5-7, Force-displacement graph of the silicone hemi-spheres using power equation fit

5.4.2 Friction force behaviour before, during and after

Figure 5-8 shows the behaviour of the applied normal forces and the friction forces on a silicone hemi-sphere before, during and after being slid against a glass plate. The origin of the graph (when $t=0s$) was set at the time point when the glass was about to slide because the sliding duration was the same for all silicone hemi-spheres as the sliding distance and speed of sliding were constant.

Three different states have been highlighted in Figure 5-8. The first state was when the normal force applied on the silicone hemi-sphere was stabilised after a period of time. In this state, there should be minimal or no friction force acting on the silicone hemi-spheres. The second state is known as the steady sliding state, which only happens when the silicone hemi-sphere fully slips against the sliding glass. In this state, the friction force would have reached a steady state. The time used to achieve this state varied among the 4 silicone hemi-spheres. The silicone hemi-sphere with 0% deadener took around 13s to achieve the steady state (normal load applied was 3N) while silicone hemi-sphere with 20% deadener took approximately 5s at the same load. Lastly, the third state was when the plate stopped sliding against the silicone hemi-sphere. After this state, the friction force on the silicone hemi-sphere would decrease until it reached a steady value.

The normal forces applied on the silicone hemi-sphere decreased initially after the sliding started and increased after a period of time. This is due to the bending of the glass plate during sliding interaction. As such, state 2 in the later sections was taken at $t=37.5s$, which was half of the sliding duration. The respective normal load at state 2 was recorded in Table 5-1.

The bending stiffness of the glass plate is higher when the silicone hemi-sphere is in contact at the side of glass at state 1 and state 3 as the illustration in Figure 5-8 shows, which leads to higher normal force being applied on the glass. At state 2, the bending stiffness is lower and hence the applied normal force drops at state 2. This drop of applied normal force occurred because the relative position between silicone hemi-sphere and the support rig was fixed. Therefore, during the sliding interaction, the thin plate allows bending deformation that contributes to some relief in deformation of the silicone hemi-sphere. As result, the normal force between the two materials dropped.

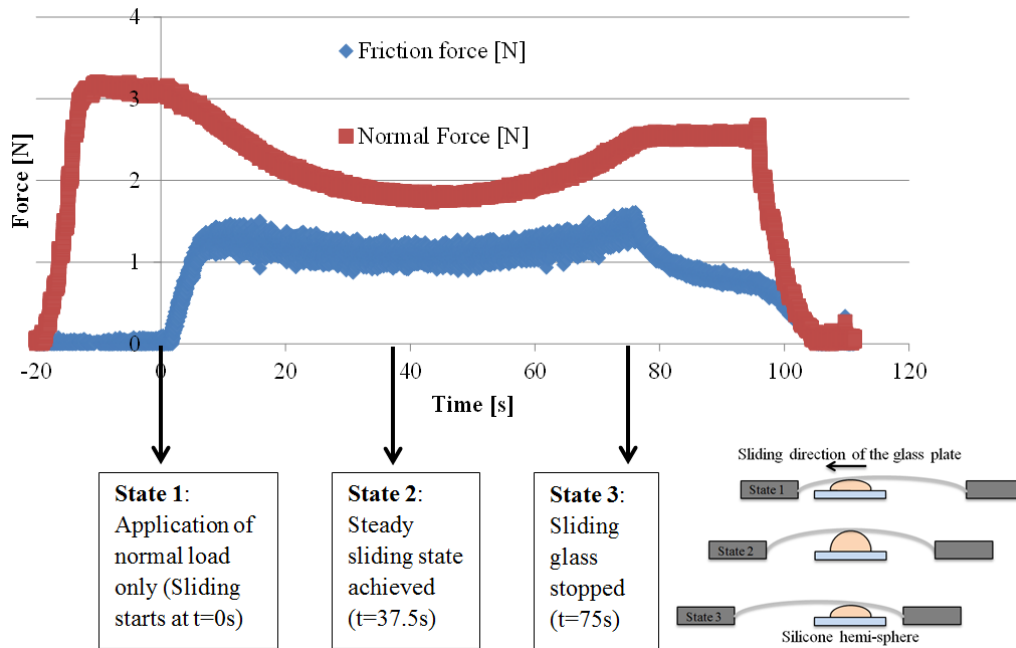


Figure 5-8, Illustration of the bending mechanism of the glass plate

Table 5-1, The instantaneous normal force at state 1 (static) and state 2 (dynamic)

	State 1: Static (t=0s)	State 2: Dynamic (t=37.5s)
Silicone Hemi-sphere with 0% Deadener	0.5N	0.4N
	1.0N	0.7N
	2.0N	1.3N
	3.0N	1.8N
Silicone Hemi-sphere with 10% Deadener	0.5N	0.4N
	1.0N	0.8N
	2.0N	1.3N
	3.0N	2.0N
Silicone Hemi-sphere with 15% Deadener	0.5N	0.4N
	1.0N	0.8N
	2.0N	1.4N
	3.0N	2.1N
Silicone Hemi-sphere with 20% Deadener	0.5N	0.5N
	1.0N	0.9N
	2.0N	1.6N
	3.0N	2.4N

5.4.3 The influence of normal force and stiffness on the dynamic coefficient of friction

The dynamic coefficient of friction of the silicone hemi-spheres decreased with increasing normal load as shown in Figure 5-9 (a). The figure also shows that the silicone hemi-sphere with higher deadener amount has higher dynamic coefficient of friction if the same normal force magnitude is applied. In addition, a common empirical approach is used to study the relationship between the dynamic coefficient of friction, μ , and the normal force N as shown in Equation 5-1, where k corresponds to the conventional friction coefficient at unit normal, $n-1$ is known as the exponent and n is termed the load index (Derler et al., 2009). The exponents of all four silicone hemisphere samples seem to average at -0.21 with a standard deviation of 0.02.

$$\mu = kN^{n-1} \quad \text{Equation 5-1}$$

This dynamic coefficient of friction is plotted against the stiffness of the silicone hemi-spheres that shows a much more direct relationship between the mechanical properties and the tribological properties of the silicone hemisphere as shown in Figure 5-9 (b). Figure 5-9 (right) shows a linear correlation between dynamic coefficient of friction and the stiffness of the silicone hemi-spheres with various deadeners, which can be described as $y = -0.175x + 1.505$.

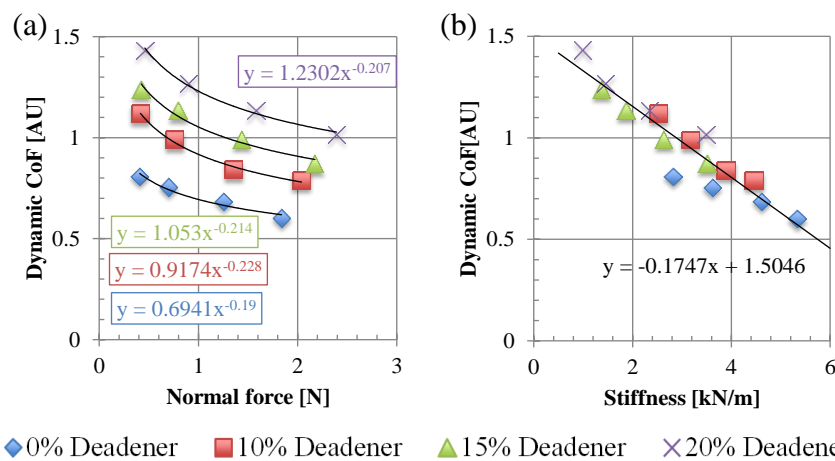


Figure 5-9, Graph of dynamic coefficient of friction against (a) normal force and (b) stiffness of all 4 silicone hemi-spheres

5.4.4 General strain and deformation behaviour

Figure 5-10 shows the 1st principal strain E_1 (tensile) and the 2nd principal strain E_2 (compressive) on the surface of the silicone hemi-sphere with 0% deadener. In both the static and dynamic states, the strain contour profile has shown that the edge of the contact area was

subjected to higher principal strain value while the principal strain in the middle region of the contact area is lower. As the glass plate slid in “-y” direction, high 1st principal strain value is more concentrated at the “+y” side of the contact while the high 2nd principal strain value is concentrated at the opposite side of the contact region.

In both the static and dynamic states, the shear strain does not seem to concentrate along the edge of the contact. However, in the dynamic state, the negative and positive shear strains are concentrated at both “-x” and “+x” side of the contact respectively, which shows that the surface of the silicone hemi-sphere was shearing at clockwise and counter clockwise direction when viewed in “+z” direction.

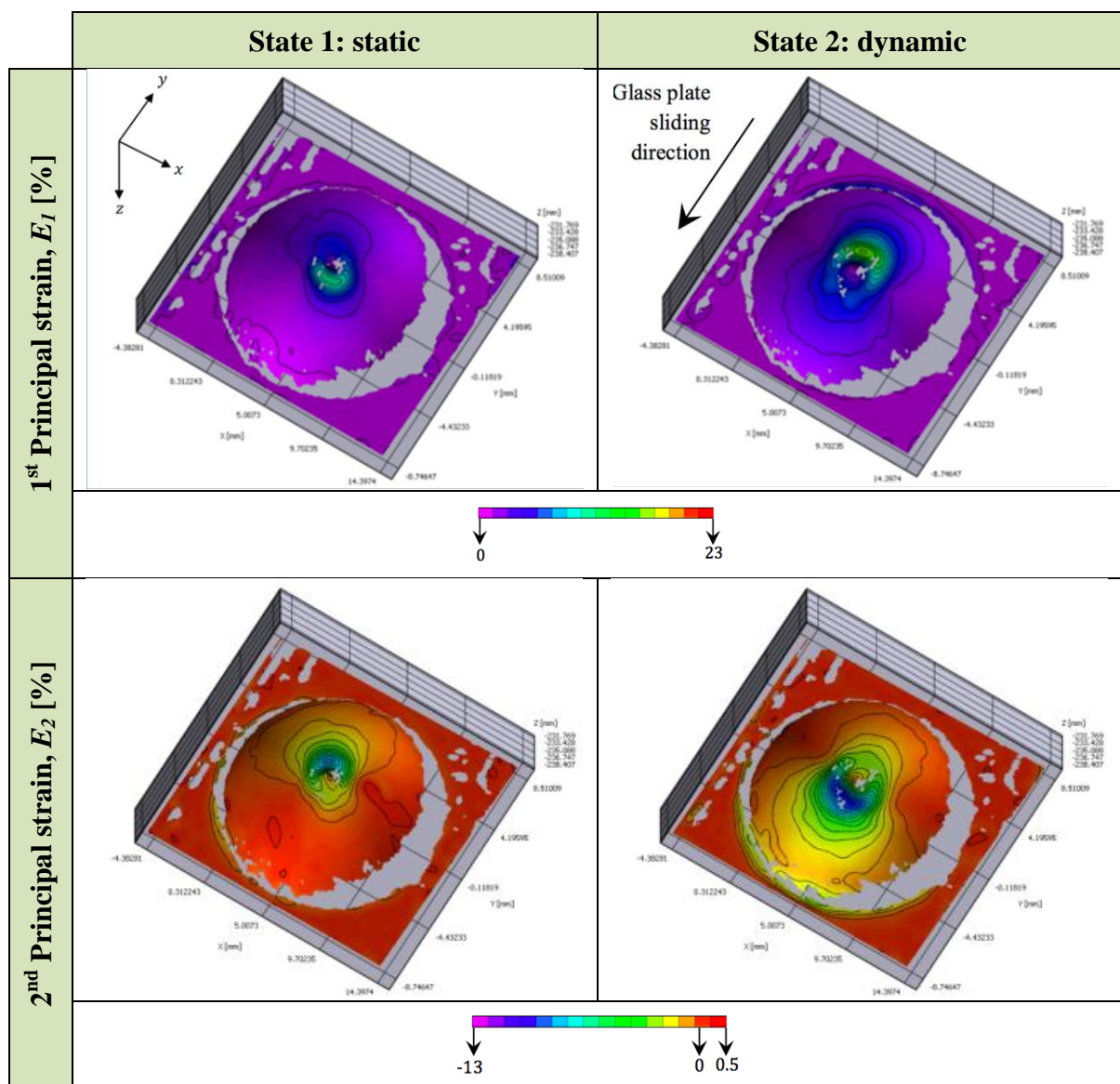


Figure 5-10, DIC results of the silicone hemi-sphere of 0% deadener at 0.5N with the respective strains 1st principal strain E_1 , 2nd principal strain E_2 and shear strain E_{xy}

5.4.5 The effect of normal load and the stiffness of silicone hemi-sphere on the strain behaviour

This section presents the strain line profile from a cross-section of the silicone hemi-sphere to show how normal force changes the strain behaviour and a graph that plots the average strain within the contact area to show how strain behaviour changes with different silicone hemi-spheres. To note, this section shows only the strain line profiles of the hemi-sphere with 10% deadener along y axis, the remaining strain line profiles are attached in Appendix F.

The main purpose of the strain line profile is to show the strain values across a certain region, which is a straight line in this case, and also to identify which region has a higher tendency to deform based on the change in strain values. The strain line profile in Figure 5-12 was obtained along the x position axis as shown in Figure 5-11. Figure 5-11 shows the selected region for image correlation (outermost blue solid circle line) and the contact area region (innermost dotted circle line). The “O” point ($x = 0$, $y = 0$ and $z = 0$) of the position axes x , y and z is set at the middle point of the contact area and lying on the surface of the silicone hemi-sphere. X , X' , Y and Y' are the respective position points located at the intersections between the edge of the contact and x or y axes. The respective Z -positions (plotted against x or y axes) of the silicone hemi-sphere with 10% deadener are shown under the strain graphs to give a good visualisation which part of the surface strain profile lies within the contact region.

Strain line profile is useful in identifying the changes in localised strain. However, it is difficult to show the difference in strain values from different silicone hemi-sphere samples as the line profiles mingled together. Therefore, the strain values within the contact area of each silicone hemi-sphere samples was averaged and plotted against the normal load applied or their own respective stiffness, as shown in Figure 5-13 and Figure 5-14 respectively.

It should be noted that both the 1st and 2nd principal strain values of the silicone hemisphere with 20% deadener at the dynamic state in Figure 5-13 (b) and (d), and Figure 5-14 (b) and (d) are invalid and misrepresented due to the severe data loss from unsuccessful image correlation process. In other words, the strain values obtained were not from a complete contact area.

5.4.5.1 First principal strain, E_1

The first principal strain, E_1 , is the maximum possible strain at a position point on a structural specimen.

In the case of a silicone hemi-sphere sample with 10% deadener, Figure 5-12 shows that there are two peak strain values lying at the edge of the contact area in the static state. The increase in the normal force results in the increase of the peak strain values whereas the strain values in the middle region of the contact area do not have notable changes. Similar strain behaviour patterns have been observed with other silicone hemi-spheres. In the comparison with other silicone hemi-sphere samples in terms of stiffness with no regards on the amount of deadener in Figure 5-14 (a), there seems to be no direct correlation between the average strain values from within the contact area and the stiffness of the silicone hemi-spheres. However, the higher the amount of deadener in the silicone hemi-sphere, the steeper the strain-to-stiffness gradient. Therefore, even at the same stiffness level, the silicone hemispheres do not necessarily experience the same average strain level. There could be other factors that effect the strain level like the size of the contact area. It should also be noted that the stiffness of the silicone hemispheres is dependent on the normal load, as shown in results in section 5.4.1.

In the dynamic state, the 1st principal strain distribution changes with one peak strain values considerably higher than the other peak strain by more than three times. Even so, the strain values in the middle region remain unaffected. Similar to the static state, the increase in the normal force increases both the peak strain values as well in the dynamic state. In terms of the stiffness of the silicone hemi-sphere samples, there is no direct correlation between the average strain values from within the contact area and the stiffness. However, the strain-to-stiffness gradient in the dynamic state is considerably higher than the static state.

5.4.5.2 *Second principal strain, E_2*

The second principal strain, E_2 , is the minimum possible strain at a point position on a structural specimen.

In the static state, Figure 5-12 shows that there are also two peaks of 2nd principal strain values near or at the edge of the contact area although one peak tends to be positive while the other is negative. The two peak strain values have shown to be increase in magnitude with the increasing normal force while the strain values in the middle region remain unaffected from the normal force. When the average strain values are plotted against the stiffness of the silicone hemi-sphere samples in Figure 5-14 (c), the graph shows that there are no direct correlations between the strain values and the stiffness. However, the

strain-to-stiffness gradient increases with the amount of deadener in the silicone hemi-sphere samples.

In the dynamic state, the distribution of the two peak strain values have shifted to the negative strain region with one of the peak strains is higher in magnitude than the other peak. Increase of the normal force also increases the magnitude of the two peak strains but the strain values in the middle region are unaffected. Unlike the 1st principal strain, the strain-to-stiffness gradient of the silicone hemi-spheres decreases and is nearer to zero gradients from static state to dynamic state. In other words, the averaged 2nd principal strain from the contact area may become constant after a certain stiffness has achieved a certain 2nd principal strain magnitude.

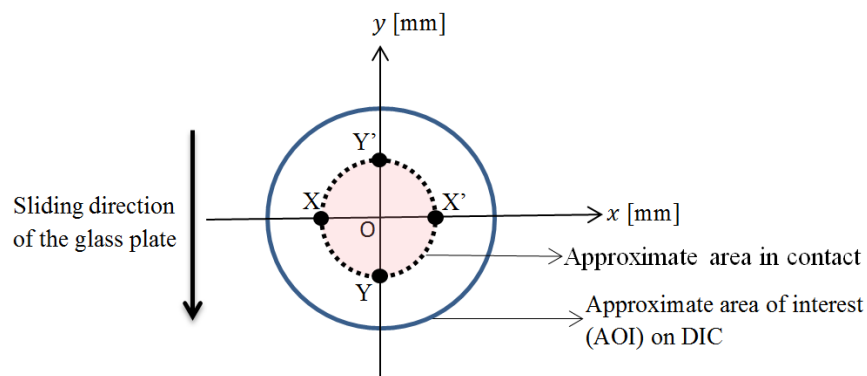


Figure 5-11, The top view of silicone hemi-sphere that illustrates the position reference axis x and y with the hint of sliding direction of the glass plate

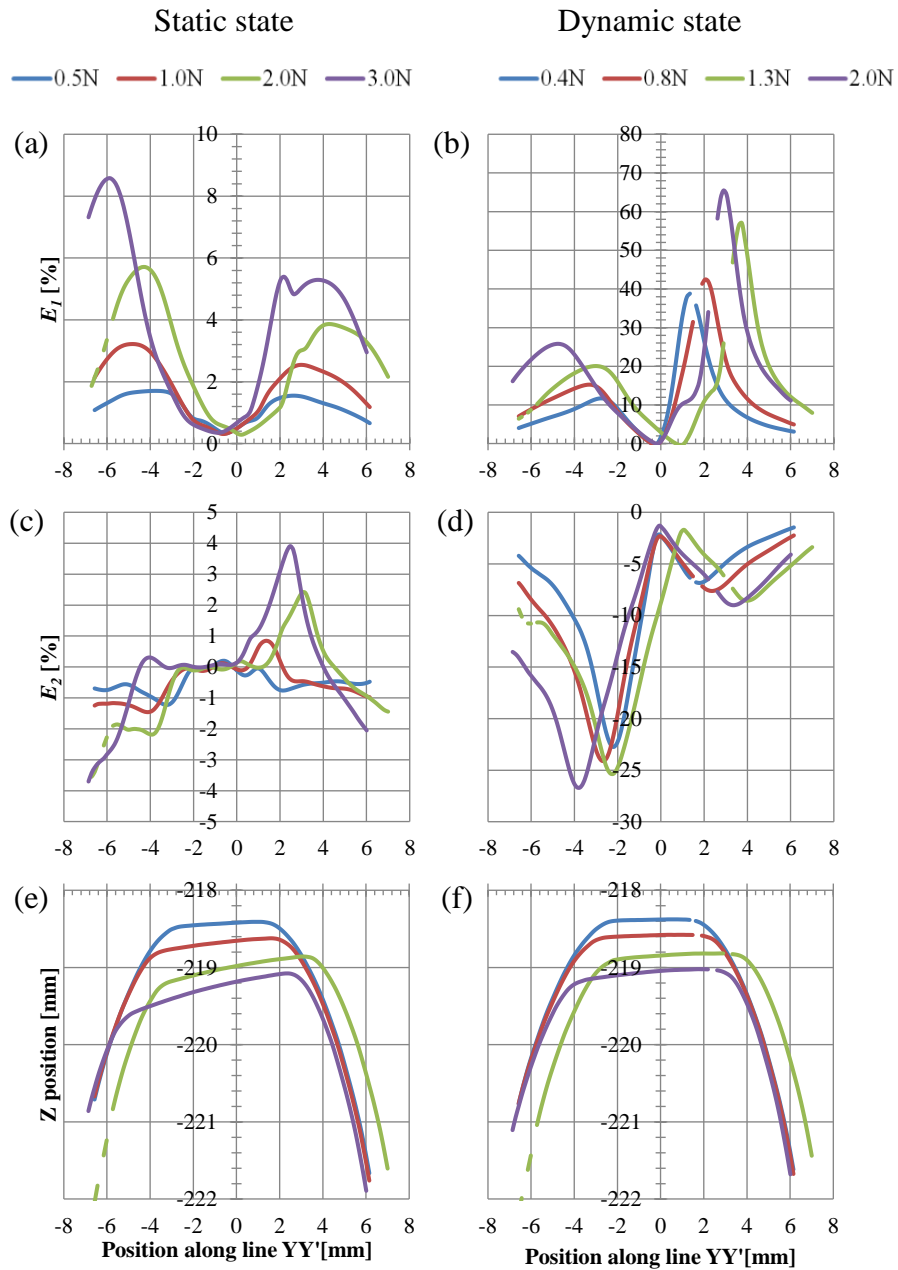


Figure 5-12, First principal strain E_1 of a silicone hemi-sphere obtained along y axis in the (a) static and (b) dynamic state, second principal strain E_2 in the (c) static and (d) dynamic state, and the geometrical shape of a silicone hemi-sphere along y axis in the (e) static and (f) dynamic state

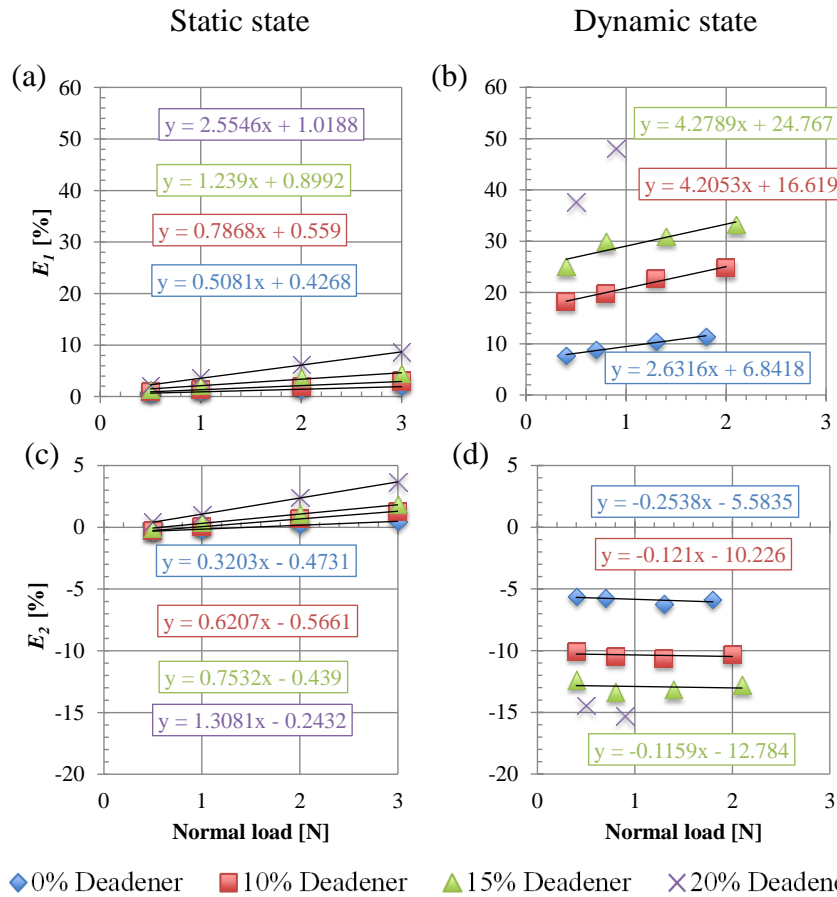


Figure 5-13, Average first principal strain E_1 strain within the contact area of all 4 silicone hemi-spheres from (a) static to (b) dynamic state, and average second principal strain E_2 strain within the contact area of the finger pad from (c) static to (d) dynamic state when plotted against the normal load applied of the silicone hemi-spheres

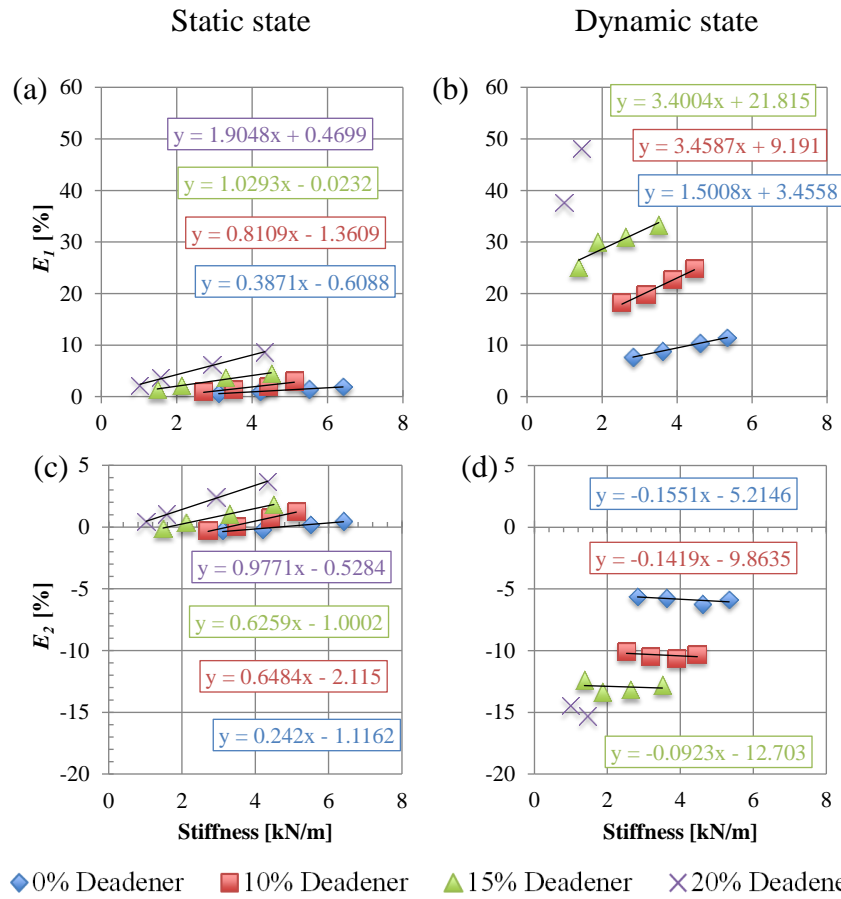


Figure 5-14, Average first principal strain E_1 strain within the contact area of all 4 silicone hemi-spheres from (a) static to (b) dynamic state, and average second principal strain E_2 strain within the contact area of the finger pad from (c) static to (d) dynamic state when plotted against the stiffness of the silicone hemi-spheres

5.4.6 Contact area

The apparent contact area of the silicone hemi-sphere samples in both static and dynamic states was measured from DIC data as shown in Figure 5-15. The apparent contact area at both states increases exponentially, which is similar to Han et al. (2008). Therefore, the contact area of the silicone hemi-spheres can be described by Equation 5-2, where A is the contact area, N is the normal load, k is an experimental constant that depends upon the assumed form of the surfaces and the elastic constants of the materials and b is also an experimental constant depends upon the form of the surfaces that ranges from 0.67 to 1.0 (Archard, 1957).

$$A = kN^b \quad \text{Equation 5-2}$$

In the static state, the k value (range: 12.5 – 32.9 mm²) increases while the b value (range: 0.52 – 0.65) decreases with the increase in the deadener amount in the silicone hemi-sphere samples. The ranges are taken from 4 silicone hemi-sphere samples of varied stiffness.

In the dynamic state, similarly, the k value (range: 12.4 – 32.9 mm²) increases while the b value (range: 0.54 – 0.74) decreases with the increase in the deadener amount in the silicone hemi-sphere samples. The ranges are taken from 3 silicone hemi-sphere samples of varied stiffness because the contact area of the silicone hemi-sphere sample with 20% deadener is incomputable due to incomplete DIC data.

From the static to the dynamic state, both the k and b values of all silicone hemi-sphere samples increased with the silicone hemi-sphere with 0% deadener sample the only exception. Therefore, the apparent contact area increases if the normal load does not change during sliding. For example, when the normal force is 2N, the contact areas of the silicone hemi-sphere with 10% deadener sample in static and dynamic states are 30.6mm² and 34.8mm² respectively. In the case of the silicone hemi-sphere with 0% deadener sample, the value decreases and the b value increased from the static to the dynamic state. So initially the apparent contact area of this sample at the dynamic state is smaller than the contact area at static state. When the normal load is higher than 1.03N, then the apparent contact area of this sample in the dynamic state will be larger than the contact in the static state.

Additionally, Figure 5-16 was plotted to show the linear relationship between the apparent contact area and the shear force on the silicone hemi-spheres.

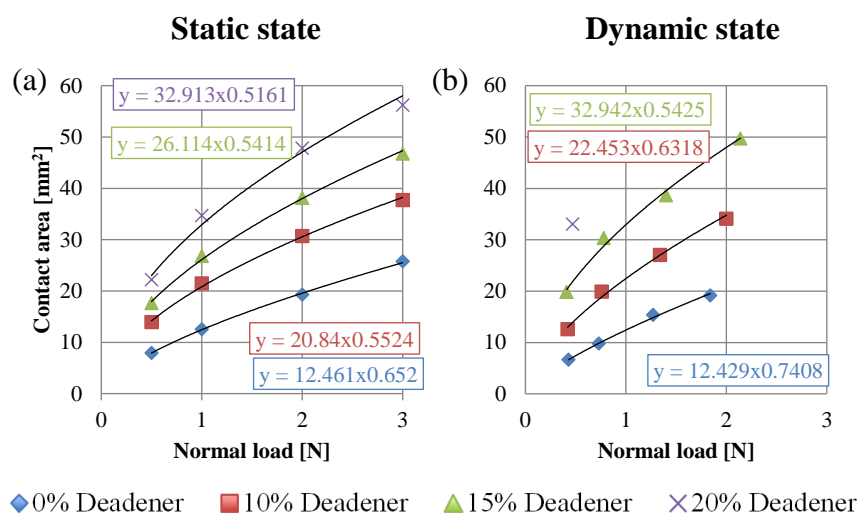


Figure 5-15, The apparent contact area of silicone hemi-sphere in (a) static and (b) dynamic state

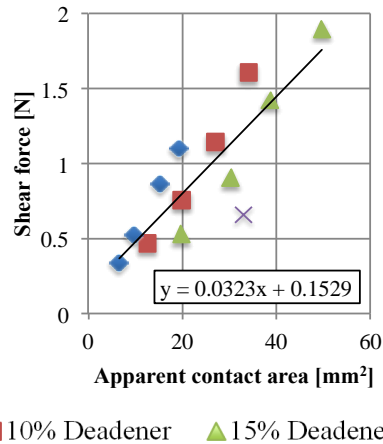


Figure 5-16, The relationship between the shear force and the apparent contact area of the silicone hemi-spheres

5.5 Discussion

5.5.1 Relationship between the frictional and strain behaviour of silicone hemi-spheres

Friction mechanism is normally consisted of two mechanisms, which are the adhesion mechanism and the deformation mechanism (Bowden & Tabor, 1954). The adhesive mechanism that contributes towards the friction force is caused by the rupture of the interfacial junctions while the deformation mechanism is due to the hysteresis or interlocking effect that results from the deformation of the interacting material (Greenwood & Tabor, 1958; Adams et al., 2007; Tomlinson et al., 2011a, Derler et al., 2009). Hysteretic effect is caused by the incomplete recovery of the viscoelastic material during sliding that causes a skewed shift of the pressure distribution at the contact, hence, resulting in a resistance to the sliding. On the other hand, interlocking is caused by the softer material changing its shape substantially or having a geometrical shape that sits perfectly on the asperities of the stiffer counter-face material.

In the case of sliding interactions between human skin and a counter-face material, multiple studies concluded that the predominant friction mechanism is adhesion while the deformation friction is relatively small in comparison (Adams et al., 2007; Tomlinson et al., 2011b, Derler et al., 2009; Kwiatkowska, 2009). Tomlinson et al. (2011a) has found that the deformation hysteresis effect only becomes influential when the roughness of the counter-face material is higher than 250µm while the influence of the interlocking effect increases when the roughness is higher than 42.5µm. Next, when a rigid plate is sliding on a human finger pad in the direction away from the body, one region in contact nearer to the palm is in tension and the opposite far end contact region at the finger tip is in compression, which

corresponds to the first principal strain, E_1 , and second principal strain, E_2 , respectively (Delhaye et al., 2016). Furthermore, Delhaye et al. (2016) found that both strain amplitudes increased with the increase in normal force. However, it should be noted that the undeformed state of the finger pad was likely when the finger pad in full contact with the plate before sliding in Delhaye et al.'s study (2016). It is important to know which finger pad position is set as the initial or undeformed state before strain measurement because the strain calculations are relative. Therefore, different strain results will most likely happen from setting different initial state, for example, the initial state of the current study was set as the position where the silicone hemi-sphere samples are not touching the plate.

In the case of the sliding interaction between the silicone hemi-sphere samples and a smooth glass plate at low normal load region, the predominant friction mechanism is likely to be adhesion because the exponent (refer to Equation 5-1) of the silicone hemi-sphere samples (-0.2) is similar to that of adhesion mechanism. It was suggested that the exponents of the friction mechanisms by adhesion and deformation should be $-1/3$ and $1/3$ respectively (Derler et al., 2009). Moreover, it is not difficult to imagine that dynamic coefficient of friction increases with the normal load because higher normal load increases the contact area of silicone hemi-spheres in contact with the glass plate and, therefore, require a higher friction force to rupture the additional interfacial junction adhered together. Despite the fact that the deformation hysteresis effect is not the predominant friction mechanism, it is still possible to contribute towards the total friction force although is relatively less influential. Hence, the strain of the silicone samples was measured during the tribological interaction because the deformation state of the samples is closely related to the deformation hysteresis effect. Both Figure 5-12 and Figure 5-14 have shown that there is a large change in surface strain of the silicone hemi-sphere samples from the static state to the dynamic state, which suggests there could be a large hysteresis loss for silicone hemi-sphere samples even though adhesion is probably the predominant friction mechanism. An additional issue Tomlinson et al. (2011b) mentioned is that the deformation of the finger pad during sliding does not contribute towards friction due to following three conditions – low counter-face roughness, low normal load application ($<3\text{N}$) and no cyclic movements during sliding, which the current study has fulfilled. Therefore, by expectations, the strain in the dynamic state should not have a considerable increase in value from the static state. Hence, assuming that there is little to no deformation occurred based on the friction mechanisms, interlocking for instance, then the considerable strain increase is probably due to the adhesive properties of the material or the

adhesion hysteresis. Adhesive hysteresis is defined as the phenomenon where taking apart two contact surfaces dissipates more energy than bringing both together (Qian & Yu, 2013), which is reasonable because the silicone material manufactured in this study is “stickier” than a finger pad. Therefore, more empirical and numerical works are required to find a clear relationship between the strain, the deformation hysteresis and the adhesion hysteresis. In addition, the future work should also explain the differences between deformation hysteresis and adhesion hysteresis. Detailed discussion on the E_1 and E_2 strain behaviour of the silicone samples at each static and dynamic state is discussed in the next paragraph. On the other hand, the interlocking effect is not considered in this study because the roughness of the glass plate is approximately $20\mu\text{m}$ (measured using optical coherence tomography).

In the static state, the E_1 strain line profile of the silicone hemi-sphere samples should theoretically show symmetric distribution where there are two peak E_1 strains at the peripheral of the contact area. Although initially the two peak strains appear to be similar in magnitude when the normal load is 0.5N, but the difference between the two peaks started to manifest itself when the normal load increased. Similarly, it is observed for the E_2 strain line profile. Firstly, the main cause could be the low bending stiffness of the glass plate, as higher normal load will further bend the thin glass plate. So, this has resulted in certain parts of the silicone hemi-sphere sample further deforming to accommodate the change and eventually lead to the uneven strain distribution. Secondly, it could be also due to the introduction of the static friction during normal loading phase even though it is assumed that there is no friction force acting at the contact region at static state. If the latter is held true, then this shows the potential of DIC in tracking where the hysteresis effect is occurring in the silicone hemi-sphere samples or whether the hysteresis effect is caused by deformation or the adhesion. Then, in the dynamic state, there is a clear shift in both the E_1 and E_2 strain distribution where the magnitude of the peak strain at one side of the contact is considerably higher than the other. Moreover, the magnitude of the E_1 and E_2 strain increased considerably from static state. So, in order to have a comparison in strain values between different silicone hemi-sphere samples, the strain value of each sample is quantified and averaged within the contact area, which the results are shown in Figure 5-14. The range of the E_1 strain values of the silicone samples at static and dynamic state is 0 to 10% and 8 to 52% respectively while the range difference of the E_2 strain at static and dynamic state is 0 to 4% and -6 to -16% respectively. These average strains within the contact increase proportionally with the normal force at the low normal load region, which can be described using a linear relationship. In the

static state, the linear gradient of both the E_1 and E_2 strains increases with silicone hemisphere samples of lower Young's modulus. In the dynamic state, however, only the linear gradient of the E_1 strain increases with lower Young's modulus samples whereas the gradient of the E_2 strain remains the same low values. This could suggest that the compressive side of the contact region has been compressed to a point in which further compression makes no difference, which also shows the potential of 3D-DIC in the study of tribological interactions.

5.5.2 Significance of stiffness test

In order to study the effect of the Young's modulus on the friction and the strain behaviour of the silicone hemisphere samples, deadener was added in the silicone mixture to vary the mechanical properties of the silicone samples. The greater the amount of deadener in the silicone mixture, the less stiff the silicone hemisphere sample is. As such, the degree of stiffness is often labelled as silicone hemisphere sample with "n%" amount of deadener.

However, there are also various external factors that could affect the softness of the silicone hemisphere samples. One of the factors is the uneven mixing of the silicone base, catalyst and deadener in the process of the manufacture of the silicone samples. This normally occurs when the chemical reaction (silicone solidifying) has started in some parts of mixtures without properly mixed with the designated ratio. Secondly, contamination may occur before or during the mixture process where there are unwanted particles or contaminants that became mixed with the silicone mixture. Depending on the amount of contaminants, the stiffness of the silicone hemisphere samples may change substantially or having no effects at all. The third factor is the "curing" time of the silicone hemispheres. When the silicone hemisphere sample is left for a long period of time, it will become stiffer because it will continue to be cured.

As such, a stiffness test is designed, the main purpose of which is to measure and label the stiffness of the silicone hemisphere samples. In order to simulate the actual normal loading condition with a glass plate, a flat plate indenter, larger than the size of the silicone samples, was used to carry out the stiffness test. The limitation of this test method is that the geometrical shape of the silicone hemisphere samples will influence the measured stiffness. Unless the geometrical shape is similar in the repeated experiments, the measure stiffness of the current study might not be comparable to the future experiments.

Friction is often associated with the contact area due to adhesion mechanism. The lower the stiffness (or the higher compliance) of the silicone hemispheres, the easier the

silicone hemi-spheres deform at contact. Larger contact area results in higher friction upon sliding. Therefore, the current stiffness test able to show that the dynamic coefficient of friction of the silicone samples is directly proportional with the stiffness with a negative gradient as shown in Figure 5-9 (b). This result is obtained despite of the amount of deadener in the silicone samples. So, one could suggest that the silicone samples should have similar dynamic coefficient of friction under the same sliding conditions if the silicone hemi-spheres reach the same stiffness level while in contact and have the same shape.

On the other hand, the strain behaviour (average strain within the contact area) of the silicone samples in Figure 5-14 is still dependent on the amount of deadener instead of the measured stiffness. This could mean that there could be other parameters that may affect the average strain of the silicone samples.

5.5.3 Contact area of silicone hemi-sphere in both static and dynamic states

Based on the Hertz theory, the contact area of a smooth elastic sphere pressed against a rigid plate can be related to the normal load with the experimental constant b value as $2/3$ (please refer to Equation 5-2) while the experimental constant k value is dependent on the local radius of curvature and the elastic constant of the material, assuming that the deformation is truly elastic (Archard, 1957). He instead suggested a more general contact area equation using a power-law model as described in Equation 5-2 because the Hertz model is only limited to linear elastic material with a constant and homogeneous Young's modulus (Xydas & Kao, 1999; Tomlinson, 2009; Liu et al., 2017; Han et al., 2008).

In a static state, Xydas & Kao (1999) have found that the corresponding exponent values of their experiments were found to be 0.51 for silicone fingers, which seems not far off for the silicone hemi-sphere samples (0.57 ± 0.06) in this study. In terms of the real finger pads, Liu et al. (2017) has compared the exponent values of the real contact area measured using OCT and an ink printing method, which are 0.16 ± 0.03 and 0.29 ± 0.11 respectively. It should be noted that the measured exponents of real contact area by Liu et al. (2017) were sampled from 4 smaller regions within the apparent contact area, due to the limited the scanning area of the OCT ($4 \times 0.8 \text{ mm}^2$). Additionally, Liu et al. (2017) also measured the full contact area of the finger pad using ink printing method, which gives an exponent value of 0.42 and 0.5 for apparent and real contact area respectively. Thus, the silicone hemi-sphere sample is more comparable to the finger pad when the contact area is sampled as a whole.

In a dynamic state, Liu et al. (2017) and Delhaye et al. (2014) found that the contact area of the finger pad decreases from a static state to a dynamic state. This is in good agreement with the silicone hemi-sphere samples with higher amount of deadener as the contact area of the silicone samples during the test also decreased from a static to dynamic state, disregarding the change of the normal force during the sliding. The only exception is the silicone hemi-sphere sample with 15% deadener as it's contact area increased during sliding. However, the contact area of the silicone hemi-sphere samples actually increases from the static to the dynamic state if the normal force remains constant, which contradicts to the findings for the finger pad (Liu et al., 2017; Delhaye et al., 2014). The main reason the initial analysis shows a decrease in the contact area is due to the bending of the glass plate during sliding. As the silicone hemi-sphere sample travelled to the middle point of the whole glass plate where the bending stiffness is the lowest, the silicone samples were allowed to have some amount of recovery due to its higher stiffness. The recovery would then reduce the contact area between the glass plate and the silicone samples. In the case of the silicone hemi-sphere sample with 15% deadener, the increase in the contact area is likely due to the slow recovery of the silicone sample because the slow recovery of the silicone sample allows the region in contact with the glass plate to stay in contact even when the bending of the glass allows the recovery of the silicone sample, provided the sliding speed is high enough. At the same time, the "in tension" part of the silicone hemi-sphere came into contact with the glass during sliding, hence, increasing the contact area. This situation is very similar to the definition of adhesive hysteresis, which more energy is required to separate the adhered material than adhering the material to the counter-face material. It is known that the silicone hemi-spheres with higher percentage of deadener are stickier than the silicone hemi-spheres with low or no deadener.

It is not clear if the contact area of the silicone hemi-sphere samples will decrease if the normal force is remained constant, as such, future work may investigate the difference in sliding interaction with a thick, rigid glass plate and a thin, flexible glass plate. Meanwhile, additional work should also focus on improving the Matlab coding because the Matlab coding is unable to accurately determine the boundary points of the contact area when the cross-sectional slice is nearer to the edge of the contact. As the cross-sectional slices get nearer to the edge of contact, the gradient change at the boundary point decreases as well. The gradient change is vital because the Matlab coding determines the boundary points by tracking the most substantial change in gradient throughout the shape profile of the cross-

section slice. As such, it is possible that the contact area is overestimated. However, this problem could be improved if the boundary points identification process is performed on the shape profile along both x and y axes.

5.5.4 The comparison between the finger pads and silicone hemi-spheres

This section will discuss the main aim of this study, which is to justify if a homogeneous silicone hemi-sphere is suitable to be simulate a human finger pad in tribological experiments. It should be noted that the silicone hemi-spheres with varied stiffness are specifically studied to simulate the mechanical behaviour of the finger pad. The biological and chemical behaviour of the skin are not studied.

In the study of these two materials, identical friction experiment had been set-up and the same 3D-DIC imaging technique was used. This experiment had been designed so that the silicone hemi-spheres were tested under the same conditions as the finger pads. The only difference is that the OCT imaging technique was opted out from the silicone hemi-sphere study because the silicone hemi-spheres do not have ridges. Therefore, it is not useful to use OCT imaging technique because both the roughness profiles, R_a and R_z , of the silicone hemi-sphere will be zero.

Firstly, it appears that the frictional behaviour of the silicone hemi-sphere is quite similar to the finger pads, which the soaked finger pad fits with the silicone hemi-sphere with 20% deadener and the natural finger pad fits with the silicone hemi-sphere with 0% deadener, as shown in Figure 5-17. Therefore, the homogeneous silicone hemi-spheres can be used to simulate the frictional properties of the finger pads, if the dynamic coefficient of friction is plotted against the respective normal load.

In terms of stiffness, however, Figure 5-18 (a) shows that the stiffness of the silicone hemi-spheres is substantially higher than the stiffness of the finger pads when the normal load is higher than 1.4N. On top of that, Figure 5-18 (b) shows the dynamic coefficient of friction and the stiffness relationship for both materials, which there is still a gap to be shortened between the two data pools. Therefore, the silicone hemi-spheres are not suitable to be used to predict the finger pads in this study if the dynamic coefficients of friction of the materials are to be plotted against the stiffness of the materials. It should be noted that there are extra data points for silicone hemi-spheres plotted in Figure 5-18 (b). These extra data points were obtained from different silicone hemi-spheres that were used in this chapter. However, the

testing conditions, such as the friction test and the stiffness test, for these extra silicone hemi-spheres were the same as the main silicone hemi-spheres used in this chapter.

In the case of the comparison of the strain behavior between the finger pads and the silicone hemi-spheres, it is also difficult to find the common ground between the finger pads and the silicone hemi-spheres, especially in the dynamic state. In the static state, the strain of the finger pad is still within the range of the strain values of the silicone hemi-spheres. However, when the materials are in the dynamic state, the silicone hemi-spheres were shown to endure a much higher strain than the finger pads. This demonstrates that the silicone hemi-sphere was much more flexible and stretchable than the finger pad.

In terms of the contact area, the apparent contact area of the finger pad is much larger than the apparent contact area of the silicone hemi-spheres, as shown in Figure 5-20 (a) and (b). However, it should be noted that the real contact area of the finger pad is much smaller than the apparent contact area of the finger pad while the real contact area of the silicone hemi-spheres is the same with its apparent contact area. This is due to the fact that the finger pad has ridges that produce air gaps within the apparent contact area while the smooth surface silicone hemi-sphere does not have air gaps within the apparent contact area based on the OCT images. When the real-to-apparent contact area ratio is applied on the apparent contact area of the finger pad, the range of the real contact area of the finger pads is from 39.7mm^2 to 126mm^2 whereas the range of the apparent contact area of the finger pads is from 80.3mm^2 to 130mm^2 . Although the range of the real contact area of the finger pad is still not the same with the range of the real contact area of the hemi-spheres ($6.6\text{mm}^2 - 56.1\text{mm}^2$), but the difference is much smaller. Additionally, Figure 5-21 shows the relationship between the shear force and the apparent contact area for both materials is linear even though the two pools of data are separated.

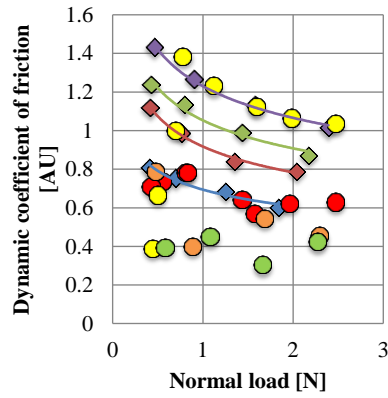
To summarise, the current silicone hemi-spheres used in this study can be used to simulate a finger pad, especially in terms of frictional behaviour, which the silicone hemi-sphere with 20% deadener is more suitable for soaked finger pad while the silicone hemi-sphere with 0% deadener for the natural finger pad. As for the strain behaviour, the stiffness profile and the apparent contact area, there are still rooms for improvement. In the case of the stiffness profile, the silicone hemi-spheres were homogeneous in this study while the finger pad skin is made of multi-layers of tissues with different mechanical properties. Silicone hemi-spheres can have the same stiffness profile as the finger pad in Figure 5-18 (a). This

would however jeopardise the simulation of the strain behaviour of the finger pad because silicone hemi-sphere with high deadener will experience high strain during sliding interaction, as shown in Figure 5-19 (b). Manufacturing a multi-layered silicone hemisphere can probably solve this issue. In order to manufacture a multi-layered silicone hemi-sphere, a glass or metal plate is still used as the innermost layer to imitate a bone structure. Then, the middle layer will be made of a silicone material with high percentage of the deadener to imitate the overall stiffness profile of the finger pad. Next, the outermost layer will be made of a stiffer silicone material that prevents the silicone hemi-sphere from over-stretching, in order to imitate the strain profile of the finger pad. A simple approach is to first make a few silicone layers independently. Then the layers are clamped down under a plate with a hole of pre-set diameter.

On top of that, the geometry and size of the silicone hemi-sphere should be considered as well. The strain profile of the silicone hemi-spheres may be much more similar to the strain profile of a finger pad if the silicone sample is made to be identical to a finger because the size of the silicone hemi-spheres is made to imitate the finger pad only. So, the smaller silicone hemi-sphere would have to experience higher strain than the finger pad even though the work input during the sliding process is the same for both material samples.

The third improvement is to manufacture a ridged silicone hemi-sphere. It does not require a sophisticated finger pad ridge but a controllable ridge size will be a good first step. This could probably be achieved by having a custom made hemi-sphere mould with integrated ridges shape. This issue arises due to the difference in surface roughness between the silicone hemi-spheres and the finger pad as the silicone hemi-spheres had a smoother surface in comparison to the finger pad ridges. The finger pad ridges are very important to human finger pads as it improves the gripping and handling of everyday objects.

This study is achieved its first step towards making a better version of the silicone hemi-spheres that may able to simulate finger pads with different mechanical properties in the future.



◆ 0% Deadener ◆ 10% Deadener ◆ 15% Deadener ◆ 20% Deadener
 ● OCT, Natural finger ● OCT, Soaked finger ● DIC, Natural finger ● DIC, Soaked finger

Figure 5-17, Dynamic coefficient of friction with respect to the normal load for of the silicone hemi-spheres and the finger pads

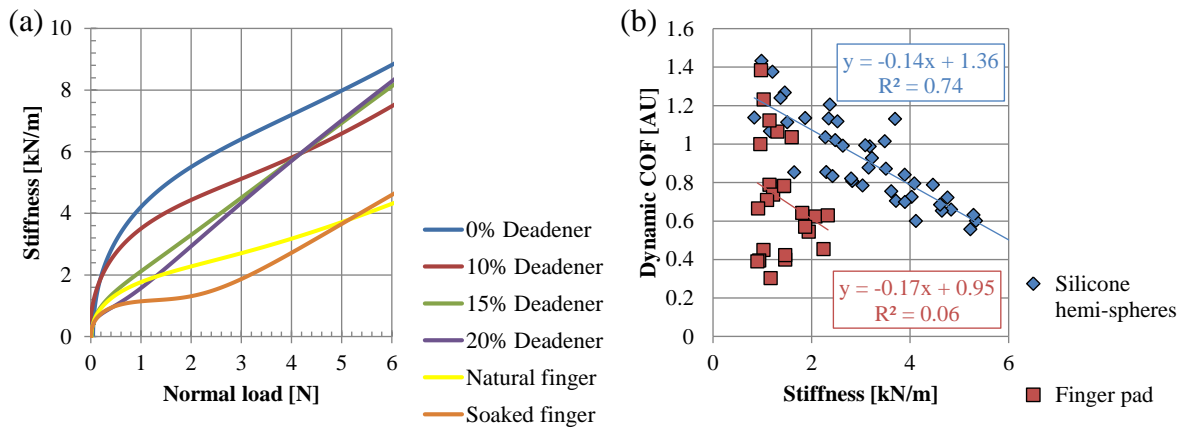


Figure 5-18, The stiffness profile and the respective frictional behaviour of the silicone hemi-spheres and the finger pads

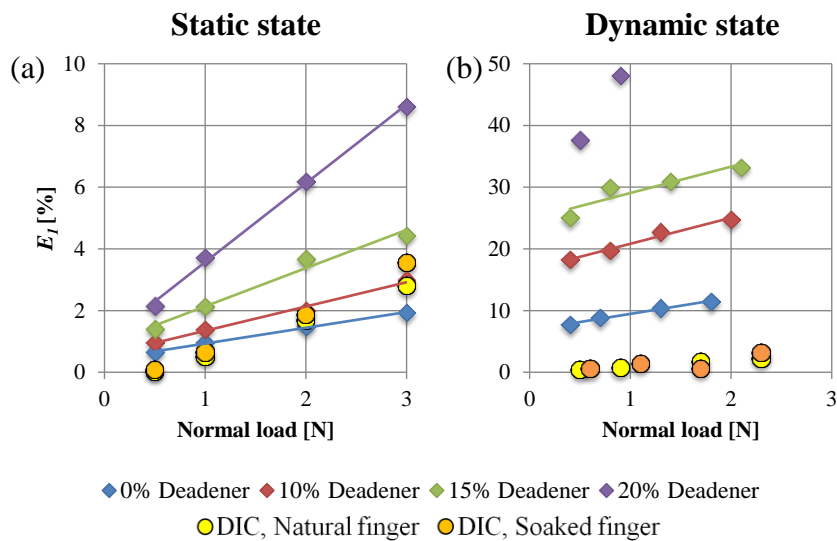


Figure 5-19, The average E_I strain with respect to the normal load for both the silicone hemi-spheres and the finger pads

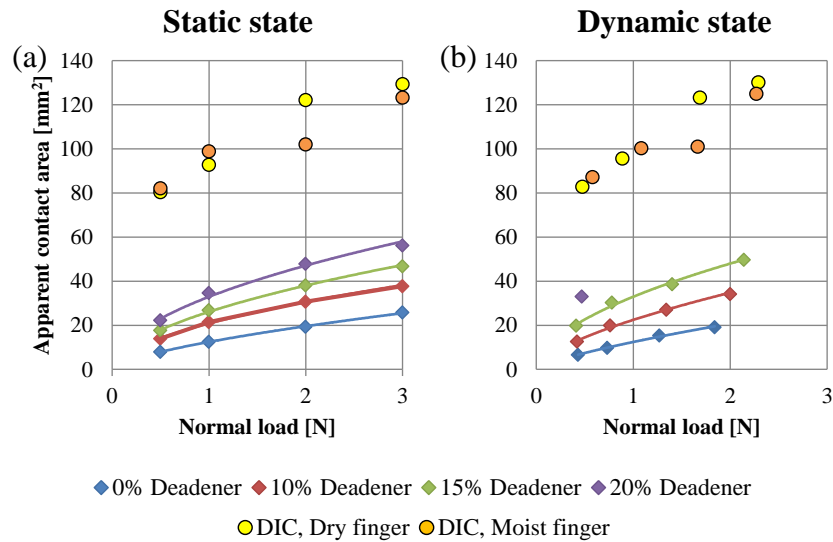


Figure 5-20, Apparent contact area with respect to the normal load of the silicone hemispheres and the finger pads from the static state to the dynamic state

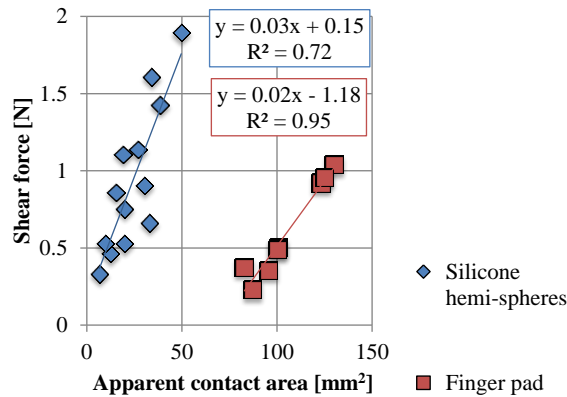


Figure 5-21, The shear force against the apparent contact area of the silicone hemispheres and the finger pads in the dynamic state (from DIC tests only)

5.5.5 Robustness of using 3D DIC on highly deformable material interaction

The 3D-DIC system is very useful in measuring the surface strain of the silicone hemi-sphere samples. However, some data loss aroused when the system was used to study the dynamic state of highly elastic silicone hemi-sphere samples (those with high amount of deadener) undergoing sliding interaction. The data loss manifests itself in the strain distribution profile as “holes” and often occurs at the edge of the contact area. The most severe case, however, will result in a complete failure in image correlation where no strain profile can be shown. The main cause of the data loss is due to the intense deformation that leads to the speckles either being too far apart or tightly squeezed together. It will reach a point when the 3D-DIC algorithms are not able to find and track the original speckles in the deformed images. So far,

failed image correlation only occurred for the silicone hemi-sphere sample with 20% deadener.

5.6 Conclusions

This study had investigated both the frictional and strain behaviour of the silicone hemi-sphere samples with different stiffness. The frictional behaviour of the silicone hemi-sphere with a smooth glass plate is dominated by the adhesion mechanism based on the exponent (-0.2) from a power-law relationship between the coefficient of friction and the normal force. Deformation mechanism (hysteresis effect) may have a notable contribution in the friction force based on the high average surface strain values (E_1 strain: 8 to 52%, E_2 strain: -6 to -16%) on the silicone hemi-sphere samples. However, more work is needed to determine the relationship between strain and hysteresis loss during sliding. Lastly, the deformation mechanism due to the interlocking effect is insignificant.

The silicone hemi-sphere samples can be labelled using the stiffness instead of the amount of deadener. It is found that the coefficient of friction is directly proportional to the stiffness of the silicone samples with a negative gradient regardless of the amount of deadener in the mixture. However, there is no direct relationship between the average strain and the stiffness of the silicone samples without the consideration of the amount of deadener although the relationship between the strain and the stiffness can still be described as a linear relationship.

The contact area of the silicone hemi-spheres and the normal load applied can be related by using power-law relationship. In addition, the shear force is shown to have a linear relationship with the contact area in the dynamic state. The contact area of the silicone hemi-sphere samples with higher stiffness decreases during sliding is due to the recovery of the silicone sample, as the bending stiffness of the glass decreases. On the other hand, the silicone sample with 15% deadener increases is likely due to the slow recovery of the silicone hemi-sphere at the compression part of the contact while the “in tension” part of the silicone hemi-sphere got into contact with the glass during sliding.

The silicone hemi-spheres used in this study can imitate the frictional behaviour of the finger pads. However, improvements are required to imitate the strain behaviour of a finger pad due to the homogeneous properties of the silicone hemi-spheres used in this study, the size and geometry of the silicone hemi-spheres and the surface roughness of the silicone hemi-spheres. Therefore, a multi-layer silicone hemi-sphere is suggested.

Chapter 6

Theoretical model – surface strain on silicone hemispheres

6.1 Introduction

The experimental model of the finger pad, which was a silicone hemi-sphere, has shown consistent strain profiles when in contact with a flat glass plate. Although the silicone hemi-sphere does not fully simulate the strain profile of a finger pad, it has been served as a starting point to further understand the gap between a soft tissue simulant and finger pad. Therefore, this chapter looks into developing a strain theoretical model to estimate the strain profile of the silicone hemi-sphere to be used as a comparison with the experimental strain profiles of a silicone hemi-sphere in Chapter 5.

6.2 Aim and objectives

The aim of this work was to investigate if a theoretical strain model can accurately estimate the strain profile and strain values within the contact region between the silicone hemi-sphere with 10% deadener and a glass plate.

The objectives of this work include derivation of the theoretical strain model; a comparison between the DIC experimental strain data and the theoretical strain model, and performing sensitivity tests on the theoretical strain modelling.

6.3 Methodology

The numerical strain model is obtained and derived from contact mechanics by Johnson (1985). The strain model is dependant on the traction profile at the contact because part of the displacement model is modelled from the traction profile. The strain model is modelled specifically to the surface strain from the 3D-DIC data. Therefore, DIC strain data will not have components from other directions that are not present in the numerical model.

The traction profile equation, as shown in Equation 6-1, is modelled from Hertz contact by assuming the silicone hemi-sphere as an isotropic elastic sphere and the glass plate as a rigid surface. In addition, the contact surface is assumed to be circular. Equation 6-2 is the traction coefficient that is modelled as the sliding case. Next, the traction profile equation is then used to derive the surface displacement field with respect to the x and y axes, as Equations 6-3 and 6-4, where G is the bulk modulus of the silicone hemi-sphere, a is the radius of the area is contact between silicone hemi-sphere and the glass plate, ν is the Poisson's ratio of the silicone hemi-sphere, μ is the dynamic coefficient of friction and P is the normal force applied. The bulk modulus (G) is relatable to Young's modulus (E) by the following equation, $E = 3(1-2\nu)G$.

$$q_y(x, y) = q_0 \left(1 - \frac{x^2 + y^2}{a^2}\right)^{1/2} \quad \text{Equation 6-1}$$

$$q_0 = \frac{3\mu P}{2\pi a^2} \quad \text{Equation 6-2}$$

$$\bar{u}_x = \frac{\pi q_0}{32Ga} \cdot 2\nu xy \quad \text{Equation 6-3}$$

$$\bar{u}_y = \frac{\pi q_0}{32Ga} \cdot \{4(2 - \nu)a^2 - (4 - 3\nu)y^2 - (4 - \nu)x^2\} \quad \text{Equation 6-4}$$

The surface displacements are then differentiated to obtain the displacement gradient field, which will then be substitute in Equations 6-5 and 6-6. Equations 6-5 and 6-6 are as per definition of Lagrange strain with the assumption of incompressible layer are described as below.

$$E_{xx} = \frac{\partial u_x}{\partial x} + 0.5 \cdot \left[\left(\frac{\partial u_x}{\partial x} \right)^2 + \left(\frac{\partial u_y}{\partial x} \right)^2 \right] \quad \text{Equation 6-5}$$

$$E_{yy} = \frac{\partial u_y}{\partial y} + 0.5 \cdot \left[\left(\frac{\partial u_x}{\partial y} \right)^2 + \left(\frac{\partial u_y}{\partial y} \right)^2 \right] \quad \text{Equation 6-6}$$

The numerical strain models for E_{xx} and E_{yy} with respect to the x and y axes are as shown in Equations 6-7 and 6-8.

$$E_{xx} = \frac{\pi q_o}{32Ga} \cdot \left\{ 2vy + 0.5 \cdot \frac{\pi q_o}{32Ga} \cdot [4v^2y^2 + 4x^2(4 - v)^2] \right\} \quad \text{Equation 6-7}$$

$$E_{yy} = \frac{\pi q_o}{32Ga} \cdot \left\{ -2(4 - 3v)y + 0.5 \cdot \frac{\pi q_o}{32Ga} \cdot [4y^2(4 - 3v)^2 + 4v^2x^2] \right\} \quad \text{Equation 6-8}$$

The numerical strain model is used to model a tribological situation, where a silicone hemi-sphere with 10% deadener sample is slid against the glass plate at steady state. The required input parameters for the numerical strain model in Equations 6-7 and 6-8 are the normal force, contact area radius, Young's modulus, dynamic coefficient of friction and Poisson's ratio, which the values inputted are tabulated in Table 6-1. Although the silicone hemi-sphere sample was applied with a normal force of 2N at static state, but an input normal force of 1.3N is chosen instead because the normal force decreased from 2N to 1.3N at state 2 due to the bending of the glass plate. The radius of the contact area is obtained from the DIC data in section 5.4.6. The inputted Young's modulus is obtained from a Dynamic Mechanical Analysis (DMA) strain sweep test performed in the mechanical engineering department in the University of Sheffield by Dr D. Tasron. The dynamic coefficient of friction inputted is obtained from section 5.4.3 of the current study. Poisson's ratio is set to be 0.3.

Typical Young's modulus of elastomers falls between 0.1 to 100 MPa (Ashby, 2011). Silicone rubber compounds from more specific studies ranged between 0.5 to 29 MPa (Suzuki et la., 2012; Ansoerge & Papailiou, 2016; Wang et al., 2016). Unlike the silicone rubber in this study, the silicone rubber compounds have additional materials mixed in to increase its mechanical properties. The Young's modulus of the silicone specimens tested by Dr D. Tasron ranged between 0.094 and 0.77 MPa depending on the amount of deadener used (Tasron, 2016). The silicone rubber with no deadener has the highest Young's modulus. It

should be noted that the process and the components used to manufacture the silicone rubber specimen in this study were the same as those made by Dr D. Tasron (Tasron, 2016).

Graphs that present both the numerical strain model and the DIC strain data were plotted to study the strain difference quantitatively. Afterwards, the strain values along the x and y position axes (along red and blue dash lines respectively in Figure 6-1) were extracted from the strain field and compared with the DIC strain values to study the strain difference numerically. In addition, a sensitivity test is performed on the numerical strain model by varying one of the three input parameters, such as, the normal force, Young's modulus or the dynamic coefficient of friction while the other input parameters remained the same values as in Table 6-1. The percentage changes of the each input parameter are -90%, -50%, 50% and 90%. The numerical model with initial input parameter values and the sensitivity test are plotted under the same graphs in the comparison with DIC strain data in Figure 6-3 and Figure 6-4. Root mean squared error (RMSE) is determined from the averaging of the square difference between the numerical strain and the experimental strain along the x and y position axes individually.

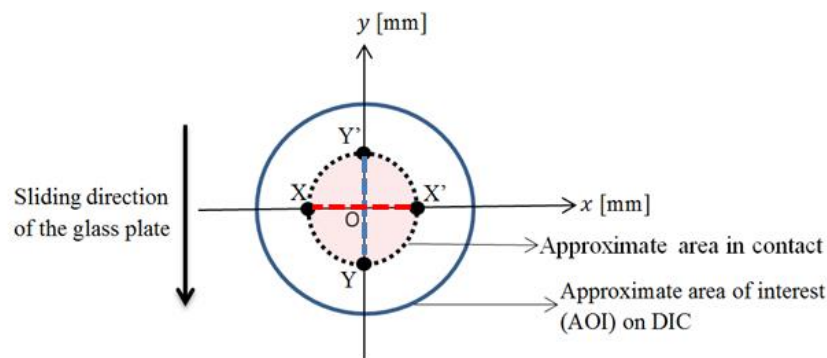


Figure 6-1, The top view of silicone hemi-sphere that illustrates the position reference axis x and y with the hint of sliding direction of the glass plate

Table 6-1, Input parameters for the numerical modelling

Specimen type	Silicone hemi-sphere with 10% Deadener
Normal force applied	1.3N
Radius of contact area	0.00293m
Young's Modulus	637988Pa
Dynamic CoF	0.84
Poisson's ratio	0.3

6.4 Results

6.4.1 Strain field profile of the silicone hemi-sphere

It should be noted that the strains presented in the result section are E_{xx} and E_{yy} , not the principal strains E_1 and E_2 .

Figure 6-2 shows the surface strain distribution within the contact area of the silicone hemisphere with 10% deadener sample from both DIC data and the numerical modelling. In the case of E_{xx} , the strain distribution pattern from the numerical modelling seems to be similar to the strain distribution pattern from DIC data as the E_{xx} strain increases horizontally along x axis from the top of the contact area ($x = 0\text{mm}$, $y = 2.9\text{mm}$) and also in the direction of glass plate along y axis (refer to Figure 6-1). In the case of E_{yy} , both DIC data and the numerical modelling have borne similarities in terms of the strain distribution pattern as well. The E_{yy} strain appears to have similar strain values along x axis and it increases along the y axis in the direction of the sliding glass plate.

E_{xx} strain line profile is extracted along x and y position axes as shown in Figure 6-3. Initial observation shows that the numerical model with initial input parameter values does not predict the experimental strain accurately. The sensitivity test shows that almost none of the predicted E_{xx} strain line profile fits the experimental strain data perfectly. However, among the three input parameters, Young's modulus parameter is more sensitive as the same percentage change in the parameter has reflected a considerable strain response in the low Young's modulus region (approximately 0.06MPa). On the other hand, the other two input parameters, normal force and coefficient of friction, have similarly low sensitivity in response to the respective percentage change.

Table 6-2 shows that the variations in the percentage change, from -90% to 90%, of the input parameters do not substantially effect the RMSE of the E_{xx} strain model. Meanwhile, the RMSE of both the normal force and coefficient of friction parameters, along both x and y position axes, have shown to decrease with positive percentage changes.

E_{yy} strain line profile along x and y position axes are shown in Figure 6-4. Initial observation shows that the numerical model with 0% change in input parameters does not give the correct strain prediction as well. The sensitivity test is able to show that the E_{yy} strain numerical model along y axis is also more sensitive to the Young's modulus parameter. Other input parameters have shown steady response under the same percentage change in

input values. From -90% to 90% change along y axis, the normal force with 90% changes, Young's modulus with -50% changes and coefficient of friction with 90% changes have the lowest RMSE value. Contrastingly, the E_{yy} strain numerical model along x axis does not seem to be affected by the variation of input parameters, which mostly are 9.5%.

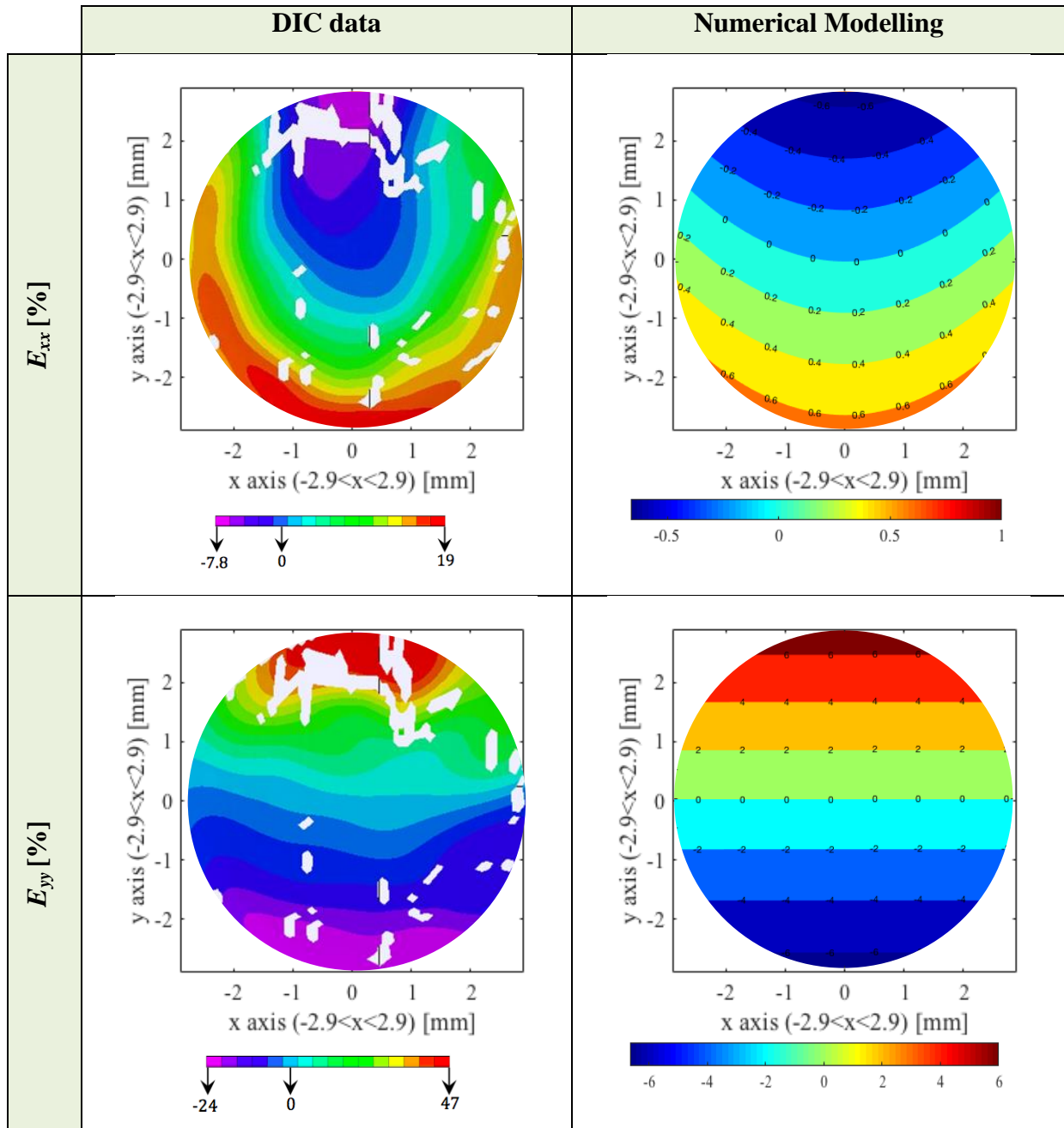


Figure 6-2, Comparison of strain distribution profile between DIC data and the numerical modelling

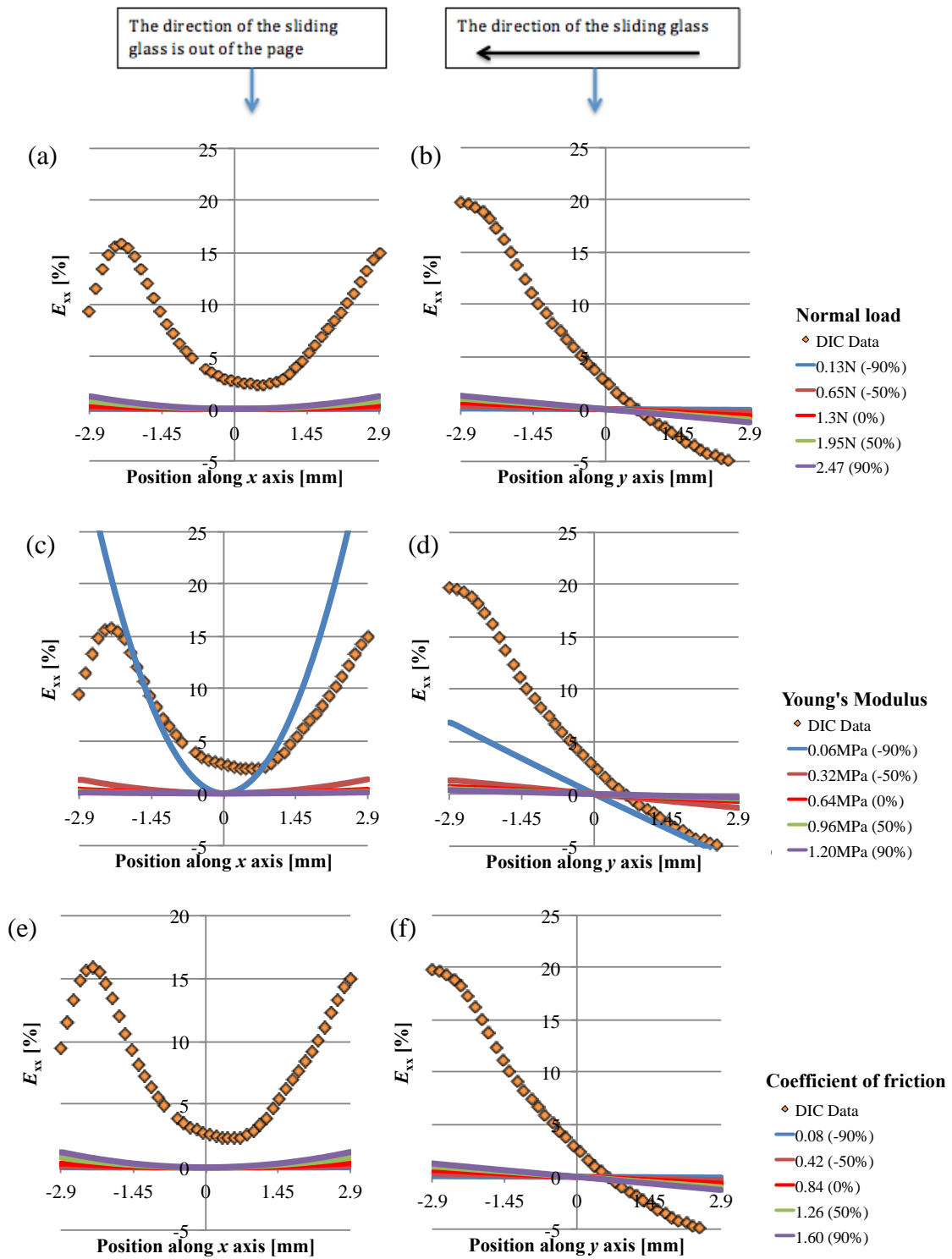


Figure 6-3, Sensitivity test of input parameters: normal force, Young's modulus and coefficient of friction of E_{xx}

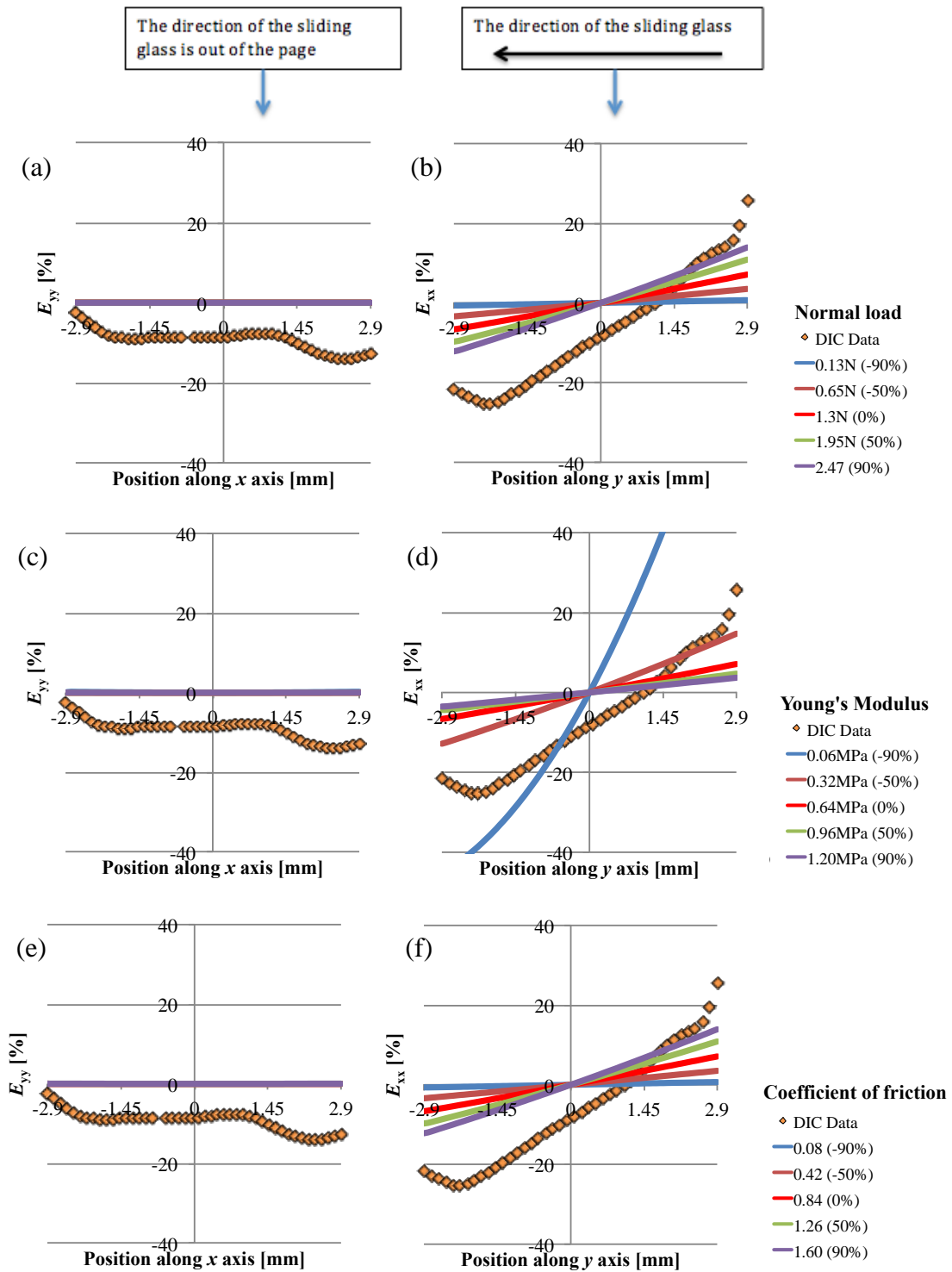


Figure 6-4, Sensitivity test of input parameters: normal force, Young's modulus and coefficient of friction of E_{yy}

Table 6-2, Root mean square error (RMSE) of the numerical strain model

		<i>E_{xx}</i> [%]		<i>E_{yy}</i> [%]	
		<i>x</i> axis	<i>y</i> axis	<i>x</i> axis	<i>y</i> axis
Initial parameters	0%	9.0	9.2	9.5	12.4
Normal force	-90%	9.2	9.5	9.5	15.5
	-50%	9.1	9.3	9.5	14.1
	50%	8.8	9.0	9.5	10.9
	90%	8.6	8.9	9.5	9.8
Young's modulus	-90%	8.1	6.4	9.6	31.1
	-50%	8.6	8.8	9.5	9.6
	50%	9.1	9.3	9.5	13.5
	90%	9.1	9.3	9.5	14.0
Coefficient of friction	-90%	9.2	9.5	9.5	15.5
	-50%	9.1	9.3	9.5	14.1
	50%	8.8	9.0	9.5	10.9
	90%	8.6	8.9	9.5	9.8

6.5 Discussion

6.5.1 *The feasibility of the theoretical strain model*

To date, Delhaye et al. (2016) has used an analysed strain model based on a Hertz traction profile (Johnson, 1985) to predict the surface strain rate of the finger pad with a smooth glass plate during the partial slip phase of the sliding interaction. This study found that the numerical model was able to predict the regions in tension or compression, but it failed to generate similar strain rate distribution as observed in the experimental strain rate distribution. Hence, it concluded that the substantial error in the full-field strain prediction was due to the assumption of the finger pad as an isotropic elastic material as finger pad skin is composed of multiple soft tissue layers of different mechanical properties. Secondly, the unsuccessful prediction is likely due to the assumption of the contact area as a circular region as the contact area of the finger pad strain rate data was clearly elliptical.

The current study also used the same analytical model, but it is used to predict the strain of the silicone samples instead of the strain rate. The Johnson model was used in this

study because it is relatively easy and straightforward to predict the strain distribution of the silicone hemi-sphere during steady sliding state. It also helps to validate the Johnson model in addition to the Delhaye et al. (2016) study. Therefore, it is suggested to use an FE approach in the future to model the silicone hemi-sphere experimental model and the finger pad to test its flexibility between the models.

In terms of the strain distribution pattern, the numerical strain model seems to be in good agreement with the experimental strain data of the silicone hemi-sphere sample because the silicone hemi-sphere samples have a circular contact area due to their spherical shape. The homogeneity and isotropic property of the silicone hemi-spheres might also be a factor that contributes towards the similarity of the modelled strain distribution. This is due to the pattern or shape of the modelled strain line profile is somewhat similar to that of DIC strain data.

However, a more in-depth investigation shows that the average RMSE from both E_{xx} and E_{yy} strain prediction (initial parameter values) along both x and y axes is $10.0 \pm 1.6\%$, which is fairly high considering the strain range of approximately -20% to 20% . Then, the sensitivity tests were performed, which the result shows the average RMSE will decrease ($\approx 9.1 - 9.2\%$) when the normal force or the coefficient of friction has a 90% increase or a 50% decrease of the Young's modulus. Considering that the normal force and the coefficient of friction were obtained from the sliding experiment of the current study, it is very unlikely that these input parameters cause a relatively high prediction error unless the force measuring plate is broken. Therefore, the most probable cause is the Young's modulus input may not be a good representative of the actual Young's modulus of the silicone hemi-sphere sample, as the strain sweep test was not done on the same silicone hemi-sphere sample in the current study. But, a more reasonable cause may be due to the shift of the point "O" (where $x = 0$, $y = 0$ and $z = 0$) on the silicone hemi-sphere sample during sliding as evidenced from the constant RMSE of E_{yy} along x axis regardless of the percentage change in the input parameters. In addition, another potential problem that needs to be considered is the possibility of uneven change of the Young's modulus of the silicone sample because the silicone hemi-sphere sample experiences both tension and compression during sliding that might result in one region having a higher Young's modulus than the opposite region.

Therefore, the future work will need to readjust/realign the dynamic point of origin to the static point of origin in Figure 6-1, assuming the point of origin of the contact shifts when

sliding occurs. This can be achieved by tracking the zero strain regions in the DIC strain data. Additionally, the numerical strain model should be employed on the other silicone hemispheres of different Young's modulus to determine if the viscoelastic properties of the material affects the RMSE of the model. In the case of numerical model for finger pad, a numerical model that is modelled for elliptical contact area could be found in Johnson's Contact Mechanics (Johnson, 1985). As for the homogeneity and isotropy of the finger pad issue, van Kuilenburg (van Kuilenburg, 2013) has proposed that the mechanical behaviour of the skin can be described by a single parameter that is the effective elastic modulus, if the contact modelling involves in a relatively small deformations. This could be helpful in the numerical model that only has one input parameter for the Young's modulus.

It is also possible to use the average strain within a contact area method to have a more quantitative study. This could help in visualising the modelling of strain behaviour of the silicone hemispheres with different stiffness.

6.6 Conclusions

The numerical strain model based on Hertz traction profile acting on a circular contact area has high potential in predicting the surface strain of the silicone hemi-sphere sample because the pattern of the strain distribution profile of the numerical strain model is very similar to the strain distribution profile from the experimental data. The next step is to improve the result of the numerical model to lower the RMSE values, by performing the sensitivity test and readjusting the initial parameter values.

Chapter 7

Natural strain of forearm skin at different postures

7.1 Introduction

The human skin is the main part of the body that interacts with a variety of materials. The human skin deforms when in contact with a counter-face material as shown in chapter 4, but the human skin can deform as well as simple movements or exercises are performed. So, this chapter will look into the strain behaviour of human skin when performing simple movements or posture changes by using 3D-digital image correlation and optical coherence tomography.

7.2 Aim and objectives

The aim of this case study was to investigate the feasibility of using OCT to reliably quantify morphological changes in the upper skin layers and sub-surface (stratum corneum, epidermis, and dermal-epidermal junction) due to natural forearm skin stretching and to correlate the results with surface strains measured by stereo digital image correlation.

The objectives of the study were to measure surface strain using DIC induced by changing the arm angle and also to determine epidermal thickness and through-plane skin layer deformation (e.g., flattening of the dermal-epidermal junction) and change in skin surface roughness from analysing OCT images.

7.3 Methodology and Experimental Set-up

7.3.1 Test subjects

This work focused on the right forearm of a 38 year old Caucasian male. The forearm was shaved in the evening before the experiment to avoid interference of the hair follicles in the OCT experiment. Then, the skin was cleaned with an alcohol wipe before the start of the experiment. Next, the right arm of the volunteer was placed in the arm holder set-up that has a vacuum pillow to minimise the sudden movement of the arm or body due to human physiology. The set-up is shown in Figure 7-1 (b) and Figure 7-2 (a). The experiment started with the initial position of the forearm at 90° flexion to the final position of the forearm at full 180° extension. OCT and DIC were used separately and further described in the following sub sections. The study protocol was approved by The University of Sheffield (Ethics Number 002074). The volunteer signed informed consent before any tests were started.

7.3.2 Stereo Digital Image Correlation (DIC) set-up

The principal of the digital image correlation has been introduced in Chapter 3.

In this study, the cameras were set-up as the Figure 7-1(b) shows. The speckles were applied on the forearm using black water-based ink (Crafters Acrylic Paint, DecoArt Inc., Stanford), which is shown in Figure 7-1(a). It was applied through the flicking of the bristles of a toothbrush. The DIC system used in this study was the VIC-3D from Correlated Solutions (version 7.2.1). The stereo angle between the two cameras used was 30° and the distance between the cameras and the volar forearm was about 350mm. This gave a field of view of 47×39 mm² with spatial pixel resolution of 0.02mm/pixel. The calibration grid

pattern used was a 2mm grid with 11×10 grid points. The outcome of the calibration score was 0.037 pixels. At the stage of data acquisition, the system was set to capture 5 images per second. For the 3D-DIC experiment, the full flexion-extension motion was monitored. In the analysis stage, subset size of 81×81 pixels was chosen, with step size set as 7 and filter size was set to 15. The noise level in the strain analysis was about 0.03-0.04%. The measurements were carried out at 20-22°C and 40-50% relative humidity.

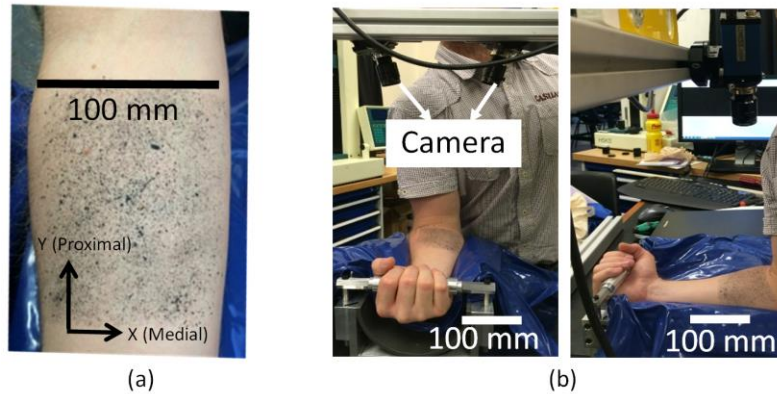


Figure 7-1, (a) The forearm with the spray pattern shown along with superimposed X-Y coordinate system defined for surface strain measurements, (b) 3D-DIC set-up showing the positioning of the cameras relative to the forearm position

7.3.3 *Optical Coherence Tomography (OCT) set-up*

An outline of the OCT measurement method and image analysis has been introduced in Chapter 3.

The OCT system used in this study was a Vivosight (Michelson Diagnostics, Kent) and it was set-up as shown in Figure 7-2 (a). In the data acquisition stage, A-scan (reflectivity) was used and the frame rate was set to 20 images per second. The images captured have a resolution of 1342×460 pixels. For stability, the hand held probe was fixed on a microscope holder.

In the OCT experiment, the images were taken at two quasi-static arm positions, at 90° flexion and 180° full extension. The OCT was used to scan ten regions of interest (ROIs) on the forearm, which are 50mm away from the arm bend, and shown in Figure 7-2 (b). The ten regions were located in an area of 25×40 mm² with distance of 5mm between them. The OCT images give a volume of 6×6×2 mm³ (width × length × depth). The measurements were carried out at 20°C and 45-50% relative humidity.

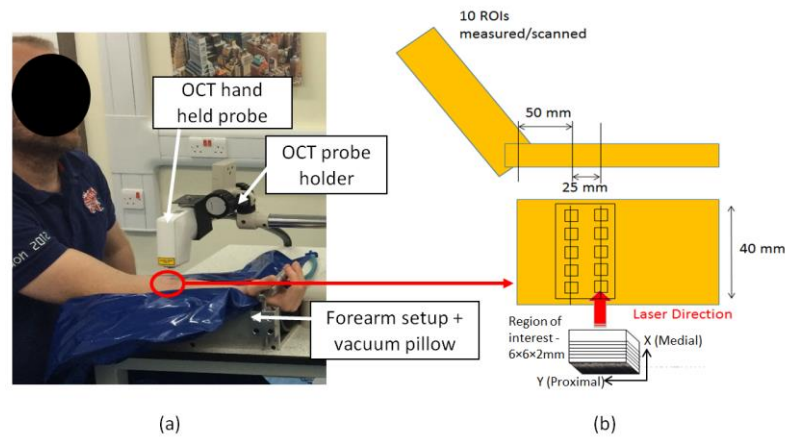


Figure 7-2: (a) OCT set-up, (b) Schematic of volar forearm: regions of interest and scan dimensions

7.4 Results

7.4.1 Surface strain behaviour of the forearm skin based on DIC data

The skin surface strain behaviour of the volar forearm at 90° flexion and 180° extension are shown in Figure 7-3. It should be noted that the surface strain data (from 3D-DIC) was determined from one undeformed image and one deformed image. Therefore, whichever image that is used as the undeformed image will be set as a “no strain” state. This would neglect the pre-strain effect on the *in-vivo* skin.

Figure 7-3(a) shows the initial condition of the arm at 90° flexion. At 180° full extension of the forearm, Lagrange strain (E_{yy}) was found to be highest towards the arm bend as shown in Figure 7-3(b).

The skin towards the elbow joint generally showed higher surface tensile strains $E_{yy} > 30\%$ as compared to the skin closer to the wrist ($E_{yy} < 20\%$). Average Lagrange strains (E_{yy}) were about 23 %.

The percentage change in compressive, tensile, shear and the principal Lagrange (E_1 , E_2) strains upon skin stretching are tabulated in Table 7-1. The strain in x and y direction are, respectively, compressive ($E_{xx} = -5.6 \pm 1.0\%$) and tensile strains ($E_{yy} = 23.3 \pm 2.2\%$) as compared to the 90° arm angle position. DIC showed that natural arm bending from 90° flexion (reference configuration) to full extension is characterised by a multiaxial surface strain distribution/state; however, compressive and shear strains were found to be relatively small (6-8%) compared to E_{yy} (>20-30%), implying that the tensile component may dominate the overall skin deformation behaviour. As shown in Table 7-1, repeatability standard

deviations were low (<2.3%), indicating a high repeatability of the strain measurements. Standard deviations within each repeated experiments (i.e., of 3 consecutive stationary images) were considerably lower (<0.2%) compared to repeatability standard deviations.

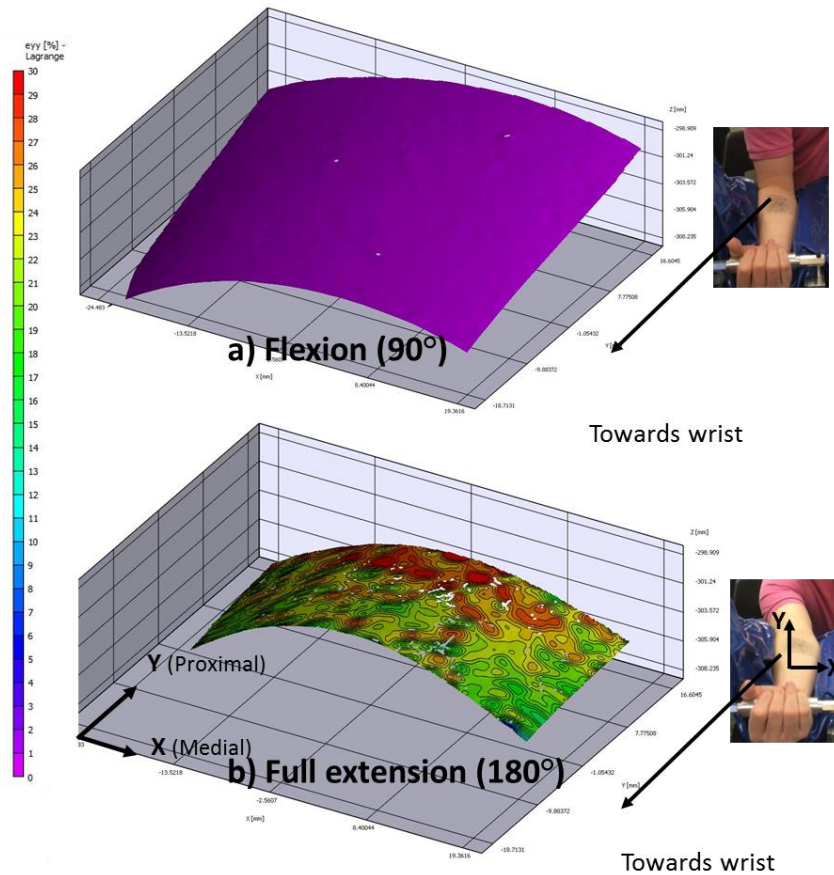


Figure 7-3: Contour plot of the skin surface strain field (E_{yy}) at (a) 90° (natural strain) and (b) induced strain through full extension at 180° arm angle

Table 7-1, Mean skin surface strains at full arm extension at 180. The values listed are mean values of 5 repeated experiments, in each of which 3 stationary images were analysed from which an average strain or area was calculated

Strain	E_{xx} [%]	E_{yy} [%]	E_{xy} [%]	E_1 [%]	E_2 [%]	Area [cm ²]
Mean	-5.6	23.3	-7.6	26.1	-8.4	5.9
S.D.	1	2.2	1.7	2.3	1.2	1.1

7.4.2 The sub-surface change of the forearm skin based on OCT images

Two examples of images taken during flexion (90°) and full extension (180°) are shown in Figure 7-4. The topography of stratum corneum and dermal-epidermal junction layers can be seen in the image of 90° arm angle. Compared to 90° flexion, both layers were smoothed during 180° full extension arm angle.

Following natural stretching and strain induced by changing the arm angle, the epidermal layer thickness reduced significantly ($p=0.001$) by 20% when the arm angle was changed between 90° flexion ($108 \pm 14 \mu\text{m}$; median: $107 \mu\text{m}$) and 180° full extension ($90 \pm 12 \mu\text{m}$; median: $89 \mu\text{m}$) as shown in Figure 7-5.

Skin roughness parameters (Ra and Rz) of the stratum corneum and dermal-epidermal junction significantly decreased by up to 45% ($p=0.001$) when the arm angle changed from 90° flexion arm angle to 180° full extension, as shown in Table 7-2 and Table 7-3. For instance, Ra changed from $14.2 \pm 2.6 \mu\text{m}$ and $15.3 \pm 3.1 \mu\text{m}$ to $8.4 \pm 2.2\mu\text{m}$ and $8.4 \pm 3.5 \mu\text{m}$ for stratum corneum and dermal-epidermal junction respectively during 180° full extension arm angle.

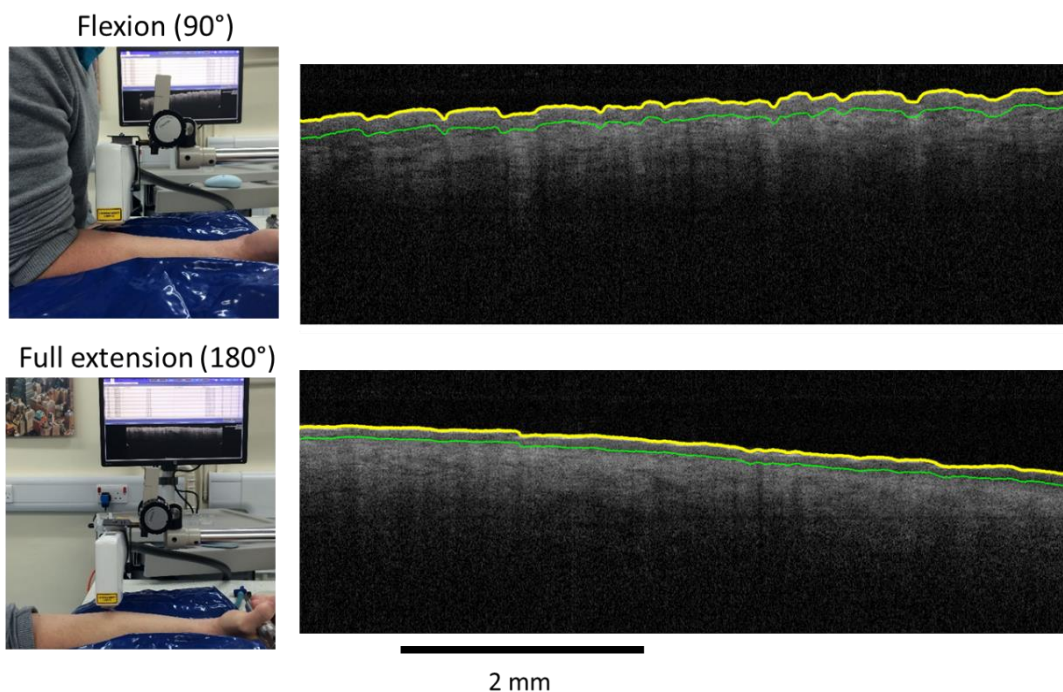


Figure 7-4: OCT images of unstretched skin (90 flexion - top) and stretched forearm skin (180 full extension - bottom), which the qualitatively smoothing of skin surface (stratum corneum) and flattening of dermal-epidermal junction can be observed.

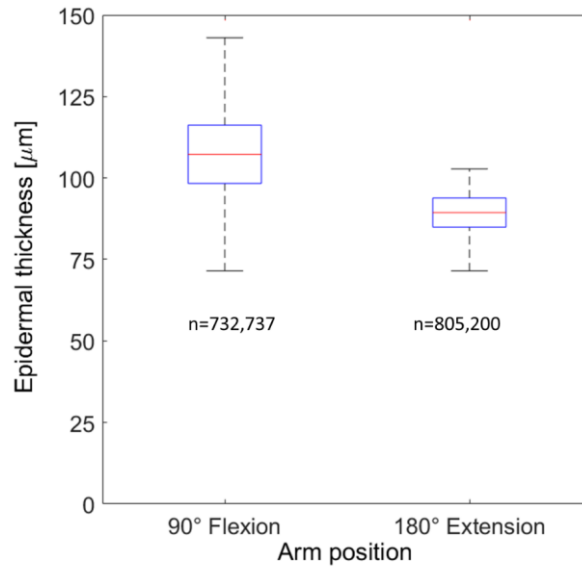


Figure 7-5: Box plot of epidermal thickness measured before and after stretching at 90° and 180°. The boxplots are made out of thickness value of in total up to 600 images, each which contains 1342 individual thickness values.

Table 7-2, Roughness parameters of stratum corneum at 90° flexion and 180° full extension. Data determined from 30 images are shown as means ± 1S.D

Stratum Corneum	Ra [μm]	Rz [μm]
90° Flexion	14.2 ± 2.6	75.7 ± 16.7
180° Full Extension	8.4 ± 2.2	38.4 ± 11.0
%Change of mean	-40.7	-49.3

Table 7-3, Roughness parameters of dermal-epidermal junction at 90° flexion and 180° full extension. Data determined from 30 images are shown as means ± 1S.D.

Dermal-epidermal Junction	Ra [μm]	Rz [μm]
90° Flexion	15.3 ± 3.1	81.4 ± 18.6
180° Full Extension	8.4 ± 3.5	40.4 ± 15.3
% change of mean	-45.5	-50.4

7.5 Discussion

7.5.1 Skin surface strains and epidermal thickness change

This study aimed to investigate the feasibility of using OCT to reliably quantify, *in vivo*, the topographical and morphological changes in upper skin layers (stratum corneum, epidermis, dermal-epidermal junction) due to natural forearm skin stretching, measured by DIC. While

several papers report on the measurements of epidermal thickness based on image analysis of OCT measurements (Neerken et al., 2004; Weissman et al., 2004; Gambichler et al., 2006; Josse et al., 2011; Hojjatoleslami & Avanaki, 2012; Abigano et al., 2013; Tsugita et al., 2013; Trohjan et al., 2015), none of these studies linked skin surface strains to epidermal layer thickness and undulation geometry change of the dermal-epidermal junction.

In the current study, upon natural stretching by changing the volar arm angle from 90° to 180° full extension, the principal tensile strain E_1 of the volar forearm increased by 26%, as shown in Figure 7-3 and Table 7-1. These volar forearm strain values are lower than skin surface strains measured in the crease of the elbow by Obropta & Newmann (2015), with principal strain values ranging from 36-60%. Differences in the anatomical region (crease of elbow), in the average age (23 year old subjects) and body composition of the subjects, or the general test procedure (Obropta & Newmann, 2015) performed an extension-flexion cycle) can be possible explanations for the higher principal skin strains measured by Obropta & Newman (2015).

In this case study with one test subject, it was found that the average epidermal thickness of the volar forearm decreased from 108 to 90 μm when the arm angle was changed from flexion to extension, thereby experiencing an increase in average skin surface strains (E_1) of 26%. To our knowledge there is surprisingly no detailed quantitative data available on the effect of *in vivo* or *in vitro* skin stretching on epidermal layer thickness and undulation geometry change of the epidermal-dermal junction. Therefore, more extended research is needed to be able to fully validate and generalise our findings. For example, it would be interesting to know the correlation with uniaxial tensile tests on *ex vivo* human skin, measuring the change in epidermal thickness upon fixing the tissue at a certain strain, or the imaging the epidermis in real time during tensile testing.

In general, the observed OCT image derived epidermal thickness values (90-108 μm) from this case study were in fairly good agreement with published data ranging from 60-128 μm . Different experimental procedures (e.g. arm angle), study populations and definitions of epidermal thickness, as well as different image processing algorithms (Neerken et al., 2004; Weissman et al., 2004; Gambichler et al., 2006; Josse et al., 2011; Hojjatoleslami and Avanaki, 2012; Abigano et al., 2013; Tsugita et al., 2013; Trohjan et al., 2015) can have influence on the measured thickness and partially explain the relatively large range of epidermal thickness determined from OCT images.

In this study, the thickness of the epidermis was determined using speckle noise reduced images, boundary tracking of stratum corneum and dermal-epidermal junction, locally weighted moving average filtering of boundary traced curved, and orthogonal vector matching between both fitted curves. Neerken et al. (2004) measured the epidermal thickness based on analysis of OCT image intensity profiles, and in this case the determination of the epidermal thickness was strongly dependant on the definition of reference markers (e.g., on top or in the valleys of dermal papillae as arbitrarily chosen by the authors such as Neerken et al., 2004). Therefore, due to the undulation of the dermal-epidermal junction, large differences can be obtained in epidermis layer thickness. For example, Weissman et al. (2004) used a novel shapelet-based image processing technique for the automatic identification of the upper and lower boundaries of the epidermis in living human skin tissue. These boundaries were used to determine epidermal thickness, with values ranging between 60 and 110 μm (Weissman et al., 2004). Although being beyond the scope of this work, it would be interesting to compare the robustness and performance of the algorithm used with the various image algorithms reported in the literature and compare all the results which histological analyses.

7.5.2 Skin topography and dermal epidermal junction geometry and undulation change

In this case study, upon changing the forearm angle from 90° bending to 180° extension, the main skin surface roughness Ra decreased from 14.2 μm to 8.4 μm , as shown in Table 7-2 and Table 7-3. The roughness Ra was found to be lower than averages values (20.5-100.2 μm in Chapter 2) measured by Egawa et al. (2002), Jacobi et al. (2004), Kampf & Ennen (2006), Li et al. (2006), Bloemen et al. (2011), Luther et al. (2012) and Tojahn et al. (2015). Different experimental techniques, such as laser scanning microscopy of silicone rubber based skin replicas in Egawa et al. (2002) and Li et al. (2006), study populations, test protocols and roughness profile algorithms (e.g. different filtering methods) used can explain this difference. The measured skin roughness Ra at full forearm extension, however, was similar to roughness ($7.2 \pm 1.3\mu\text{m}$) reported by Kottner et al. (2013).

Moreover, the mean roughness depth Rz of the dermal-epidermal junction decreased from 81.4 μm to 40.4 μm during the forearm angle change from flexion posture to extension posture, as shown in Table 7-3. Based on the definition (Equation 3-7 in Chapter 3), the mean roughness depth Rz represents the average maximum height of the derma-epidermal-junction roughness profile and concerns maximum height variations (peak-to-valley). Therefore, Rz probably overestimates a typical dermal-epidermal-junction average thickness. For example,

in a study by Neerken et al. (2004), the mean thickness of the dermal-epidermal-junction of the forearm was found to be 25 and 41 μ m in older and younger skin respectively, but the Rz of both groups was lower than the Rz values measured in this case study in the 90° arm bending position. As mentioned before, due to the undulation of the dermal-epidermal junction, large differences can be obtained in epidermis layer thickness (Neerken et al., 2004) which in return will also affect the calculation of the dermal-epidermal junction thickness and undulation geometry parameters being defines by standard roughness parameters Ra and Rz in this article.

In this flexion-to-extension forearm posture study, upon changing the forearm angle from 90° bending to 180° extension, the main skin surface profile and dermal-epidermal junction geometry parameters (Ra, Rz) decreased to a similar extent by about 41-50% as shown in Table 8-1. The observed similar percentage reduction in skin surface roughness and epidermal-dermal junction flatness/undulation (between 41-50%) upon natural skin stretching from 90° to 180° seems to be in agreement with the fact that these skin layers have the same in-plane strain because they are mechanically and structurally connected with each other. In this context, it should be pointed out that a systematic roughness offset may have been introduced into the measurement result due to the fact that the skin was compressed and folded up, causing wrinkling, in 90° bending posture, whereas the 180° full extension posture may have led to pronounced skin stretching and epidermis flattening.

Skin is a hierarchical functionally graded multilayer composite in which different skin layers are firmly connected with each other and via tendons, fascia and muscles mechanically connected to bony structures (Gerhardt et al., 2012; Lamers et al., 2013). As skin is firmly connected to the underlying body tissue structures, when the multilayer composite is subjected to body movements and global stretch, it will consequently accommodate for the exposed strain and respond in such a way that both the epidermal-dermal junction flatten and skin surface asperities smoothen out.

According to Ferguson & Barbenel (1981), during stretching of the skin the undulations of the epidermal surface and epidermal-dermal junction are flattened before elongation of the epidermal cells occurs. Moreover they suggested that the surface folds provide a reserve of tissue, allowing the epidermis to stretch without stretching or disrupting the epidermal cells. If this is true there should be a relationship between the skin extensibility and the grooves and ridges of the skin surface pattern, which produce the functional

epidermal reserve. Therefore, Ferguson & Barbenel (1981) measured forearm skin roughness at varying strain and quantified how skin stretching reduces the roughness along the stretch direction. They found a gradual decrease in surface roughness Ra from 14 μ m to 6 μ m at 10-30% strain. This result is fully in line with the observations here and data in Table 7-1, Table 7-2 and Table 7-3, showing a tendency to skin smoothing with increasing strain. Though, due to the limited strain and roughness data (only at 90° flexion and 180° extension) a mathematical correlation cannot be established in a sensible and reliable way.

It should be noted that although the epidermal and dermal-epidermal junction layer thickness detection algorithm developed has not been fully validated using for example histology, qualitative assessment of OCT images by several skin experts and authors of the present paper showed that the developed image code is sufficiently robust and sensitive to reliably identify and determine epidermis and dermal-epidermal junction thickness by automatic identification of skin structural features. Even if the code has not been fully validated, it allows reliable relative comparisons of skin layer thickness and geometry change during a flexion-extension experiment. However, as both the dermal-epidermal junction (basement membrane) and the papillary dermis are signal poor; whereas reticular is signal intense (Welzel, 2014) it cannot be ruled out that some minor contributions of the papillary dermis are included in the epidermal thickness and dermal-epidermal junction flatness determination.

7.6 Conclusions

This work has shown the feasibility to quantify the morphological skin parameters from OCT images and also the method to combine two non-invasive techniques that are 3D-DIC and OCT to investigate skin surface strain and sub-surface layer deformation of volar forearm. This study demonstrated that even simple movements such as changing arm postures, by extending the arm from natural flexion to full extension, can cause a significant change in skin surface strain, by typically 25%, and caused morphological changes in the upper skin layers – reduction of epidermal layer thickness around 20%, decrease of the dermal-epidermal junction undulation roughness between 45%-50% and also skin surface roughness between 40% - 50%. The morphological change of the skin and the strain may be connected because they are the result of the deformation of the human skin while the arm was extended.

In brief, this further demonstrates that the methodology of using high-speed imaging techniques to assess the deformation and strain in soft tissue in real-time is not limited to the study of biotribology, but both biomechanics and biotribology.

Chapter 8

Disorientation of aortic tissue fibres subjected to different loads

8.1 Introduction

This chapter investigates the potential of using confocal microscopy in biotribology experiments. As such, this research work studied the deformation of porcine aorta when damaged by a catheter tip during cardiac catheterisation procedure. Although major catheterisation damage is rare, there are certain risks in performing this procedure that might damage the blood vessel through rubbing or sliding of the catheter tip. Therefore, a damage evaluation method is needed to identify and estimate the amount of damage on porcine aorta from the deformation it sustained from the sliding of catheter tip.

8.2 Aim and objectives

The aim of this study was to investigate the possibility of and to demonstrate in-situ catheter tissue interaction using confocal microscopy on ex-vivo porcine aorta tissue.

The objectives of this study also involved determining which fluorescent dyes are more suitable for staining porcine aorta. Also, this study involved designing a feasible in-situ experimental set-up with available equipment at that time for real-time monitoring.

8.3 Methodology and experimental set-up

This section will show the methodology used to prepare the experimental set-up for the main experiment. Few pilot studies have conducted to determine the suitability of Eosin B and feasibility of in-situ tribometer.

8.3.1 Preparation of Porcine Aorta

All tissue preparation was undertaken within the fume hood according to the Human Tissue Interaction (HTI) lab protocol, no tissue was handled outside the fume hood and all tissue was transported out of the fume hood either in the tissue holder, in a petri dish or in a sealed red disposal bag

The porcine aorta had to be cut in strips of 8cm length and 3cm width, as the porcine aorta received from Hemolab, Technological University of Eindhoven, was one whole uncut porcine aorta. During preparation, the aorta was handled with care so that the innermost layer of the aorta received as little damage as possible.

The porcine aorta strips were then immersed in an Eosin B fluorescent dye solution of 100 μ M concentration overnight at 4°C. After the incubation time, the aorta strips were fixed onto a tissue holder and pre-stretched circumferentially to 15% of the original length before imaging.

8.3.2 Imaging using confocal microscopy

Detailed information regarding confocal microscopy working principal, sample preparations and the development of the image analysis has been introduced in section 3.4.

The confocal microscopy used was Spectral Confocal & Multiphoton System Leica TCS SP2.

The main experiment was to investigate two of the most important factors in contributing to catheterisation damage, which were the magnitude of force and the amount of passes. The main experiment conducted was to compare the differences of Z-stacked scan

images between undamaged porcine aorta and damaged porcine aorta across time based on the orientation of tissue fibres of porcine aorta.

The experiments conducted were divided into “Cases” of which there were 9 in total and each case had different catheterisation damage conditions.

- Case 1: 0.5N force with 1 catheterisation pass
- Case 2: 0.5N force with 5 catheterisation pass
- Case 3: 0.5N force with 10 catheterisation pass
- Case 4: 2.0N force with 1 catheterisation pass
- Case 5: 2.0N force with 5 catheterisation pass
- Case 6: 2.0N force with 10 catheterisation pass
- Case 7: 5.0N force with 1 catheterisation pass
- Case 8: 5.0N force with 5 catheterisation pass
- Case 9: 5.0N force with 10 catheterisation pass

Based on previous pilot studies, thickness of the dyed section of porcine aorta was approximately between 50 to 80 μm . The working range of the Z-stacked scan must exceed the thickness of dyed section. As such, the Z-stacked scan setting was set to have a working range of 100 μm . Secondly, the Z scan was set to have 1 μm interval between 2 consecutive images. In other words, each Z scan will give 101 images each 1 μm apart going into porcine aorta (positive z direction) as Figure 8-1 shows.

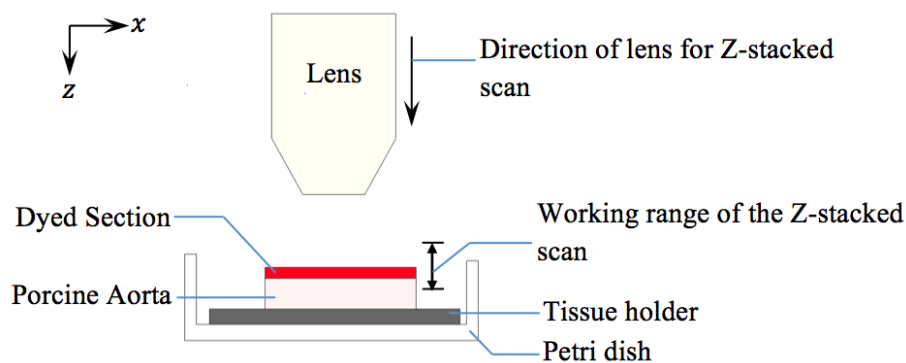


Figure 8-1, Front view of the experimental set-up

Firstly, the prepared porcine aorta sample underwent the first Z-stacked scanning, which is the undamaged Z-stacked scan. Then the x and y position values of the stage that supporting the petri dish were noted so that the lens could focus on the same area of focus as the undamaged Z-stacked scan.

The sample was then moved away from the lens by adjusting the stage in order to perform catheterisation damage on the sample. Based on case 1, force of magnitude of 0.5N was applied from point A to point B, which was considered as 1 catheterisation pass as shown in Figure 8-2. Then, the stage was moved back to its previous position as noted before within 10 seconds and turned on the live-scanning to double check if the area of focus was the same as undamaged Z-stacked scan.

Z-stacked scanning settings, which were set to run 8 separate Z-stacked scans continuously, were started after the after 10 seconds. Each Z-stacked scan that was set to scan 100 images with 1 μ m required approximately 1.88 minutes to finish. As such, relatively, first Z-stacked scan will finish at 1.88 minutes, and then, second Z-stacked scan will start from 1.89 minutes and end in 3.76 minutes. Eventually, the eighth Z-stacked scan will start from 13.16 minutes and end in 15.04 minutes as shown in Figure 8-3.

After the above procedure was finished, the sample was taken off from tissue holder and safely disposed. Then the next sample was prepared for case 2: 0.5N, 5 passes. The above processes were repeated from case 2 to case 9. This experiment was repeated 5 times. The experiments were then labelled as Set 1, Set 2, Set 3, Set 4 and Set 5.

The images collected from the main experiment were re-arranged and grouped as undamaged Z-stacked scan, damaged Z-stacked scan at T₀, damaged Z-stacked scan at T₁, damaged Z-stacked scan at T₂, damaged Z-stacked scan at T₃, damaged Z-stacked scan at T₄, damaged Z-stacked scan at T₅, damaged Z-stacked scan at T₆ and damaged Z-stacked scan at T₇ for case 1 to case 9 of all 5 set of experiments. Each Z-stacked scan has 100 images. However, only approximately 50 to 80 images had imaged tissue fibres due to the dyed thickness being approximately 50 μ m to 80 μ m. Therefore, the remaining images that were not able to show the tissue fibres were deleted prior the image analysis. Fiji is able to run directionality image analysis on a single image or the whole Z-stacked images. Therefore, a total of 9 histograms were obtained for one case and 81 histograms in total for one experiment. The histograms were required to study the directionality angle of tissue fibres at different Z-stacked height across the dyed section. Blue lines represented the surface section of the sample (surface where was in contact with in-situ tribometer and the innermost part of porcine aorta), green lines represented the middle part of dyed section and brown lines represented the deepest dyed section, as shown in Figure 8-5.

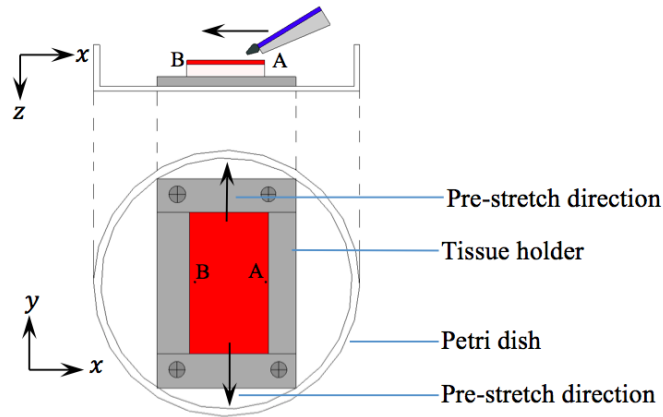


Figure 8-2, Top view and front view of the experimental set-up

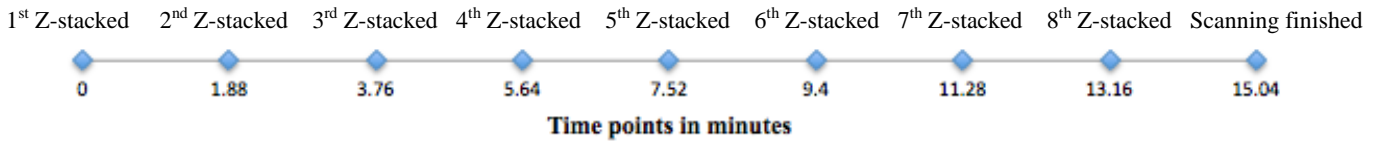


Figure 8-3, Timeline of 8 separate Z-stacked scanning

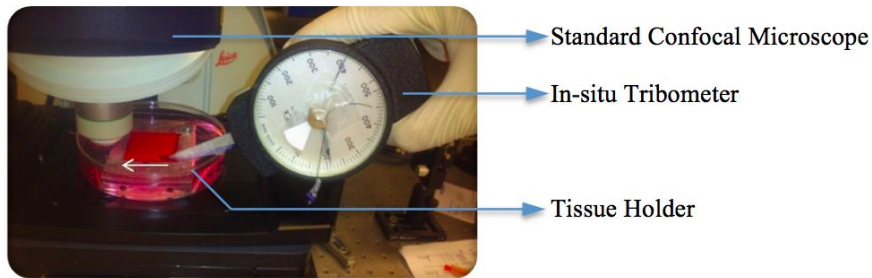


Figure 8-4, The actual experimental set-up

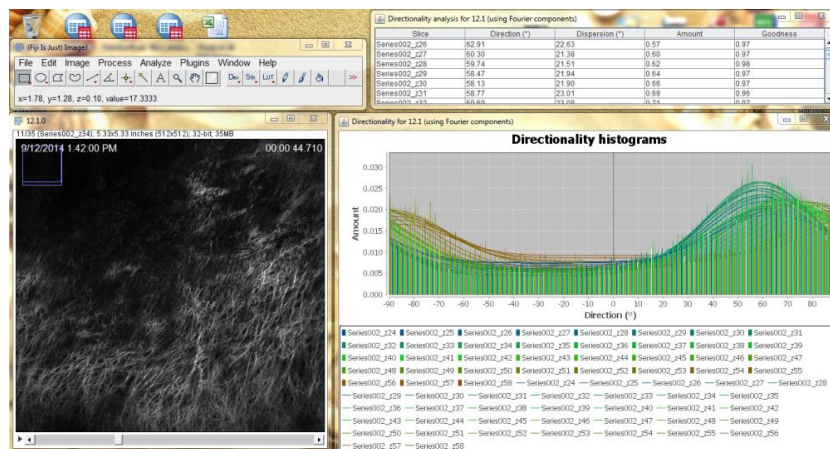


Figure 8-5, Outcome of Fiji – directionality image analysis of the Z-stacked images

8.4 Results

8.4.1 Directionality histogram of Z-stacked scan

There are three types of colours in the histograms shown: blue, green and brown, which resembles from the top layers to the bottom layers of the porcine aorta sample.

Each line in the histograms represents the dominant directionality angle of the specific image and the histogram represents the Z-stacked scan took place. As example, histograms in Figure 8-6 to Figure 8-8 were from the same experimental attempt. Histogram in Figure 8-6 is the first Z-stacked scan done on an undamaged porcine aorta sample, while histograms in Figure 8-7 and Figure 8-8 are the Z-stacked scans took place after damaged was done on the same porcine aorta sample at different time points.

8.4.2 Unique pattern of directionality histogram of each case

Every histogram groups contain 9 histograms (undamaged Z-stacked scan, damaged Z-stacked scan at T_0 , damaged Z-stacked scan at T_1 , damaged Z-stacked scan at T_2 , damaged Z-stacked scan at T_3 , damaged Z-stacked scan at T_4 , damaged Z-stacked scan at T_5 , damaged Z-stacked scan at T_6 and damaged Z-stacked scan at T_7) for each case that have their own unique pattern, which were characterised by their peak value (Y-value), position of the peak value at X-axis and the distribution curve. These could be shown by the histogram groups of Set 3, case 1: 0.5N, 1 pass (Figure 8-6, Figure 8-7, Figure 8-8), Set 1, case 4: 2N, 1 pass (Figure 8-10, Figure 8-11, Figure 8-12) and Set 1, case 7: 5N, 1 pass (Figure 8-12, Figure 8-13, Figure 8-14). Figure 8-6-Figure 8-14 show that the confocal microscopy lens was scanning at the same area of focus ($620 \times 620 \mu\text{m}$) for both undamaged Z-stacked scans and damaged Z-stacked scans.

These histogram patterns are important because the possibility of confocal microscopy lens not scanning on the same area of focus after conducting the catheterisation damage can be opted out. More importantly, these histogram patterns could also mean that the direction of orientation of tissue fibres of porcine aorta is random and different from sample to sample.

8.4.3 Inability of aortic wall tissue fibre to recover to undamaged state

Comparison of directionality histograms between undamaged aorta and damaged aorta shows that the elastin of porcine aorta is unable to recover to the undamaged state regardless of the force applied within 15 minutes, in other words, the pattern of directionality histograms of the

damaged aorta do not return to the pattern of directionality histogram of undamaged aorta. Taking Set 3, case 1: 0.5N, 1 pass (Figure 8-6 to Figure 8-8) as an example, the difference in positions between the peaks of blue and green lines are not distinctive and there are no obvious peaks for brown lines in undamaged directionality histogram as shown in Figure 8-6. However, both damaged directionality histograms at different time points (Figure 8-7, Figure 8-8) showed that the peaks of the blue lines have higher position than the peaks of green lines while there is one small peak for brown lines.

The same happens on Set 1, case 7: 5N, 1 pass (Figure 8-12-Figure 8-14) with the position of the blue lines drops below the peaks of green lines while the position of the peaks of the green lines is unchanged.

However, there are very few exceptions like Set 1, case 4: 2N, 1 pass (Figure 8-9-Figure 8-11) which shows that there was hardly any distinctive changes or differences between damaged histograms and undamaged histograms.

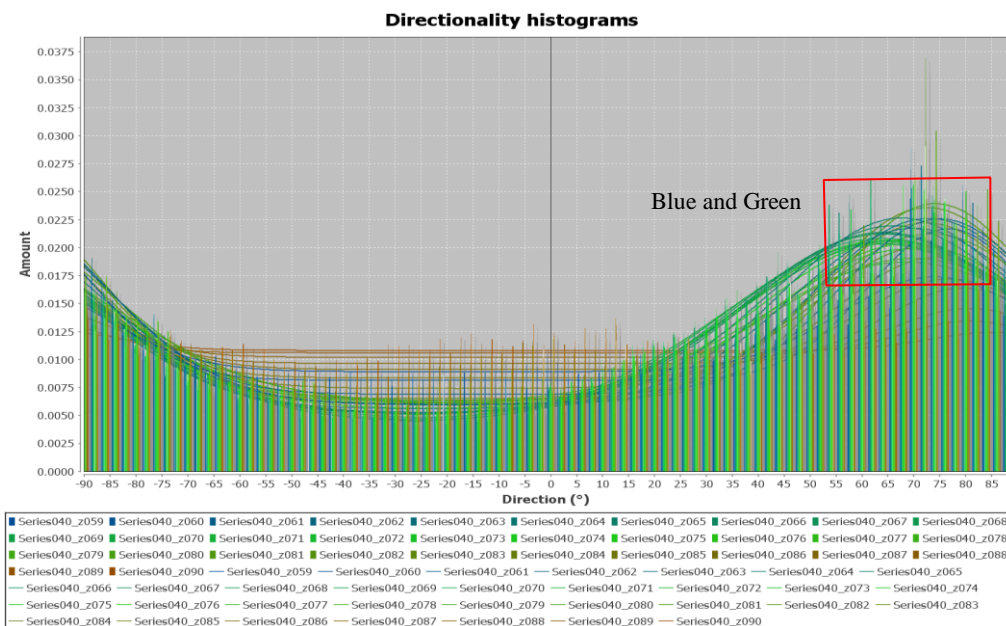


Figure 8-6, Undamaged directionality histogram for Set 3 Experiment (0.5N, 1 pass)

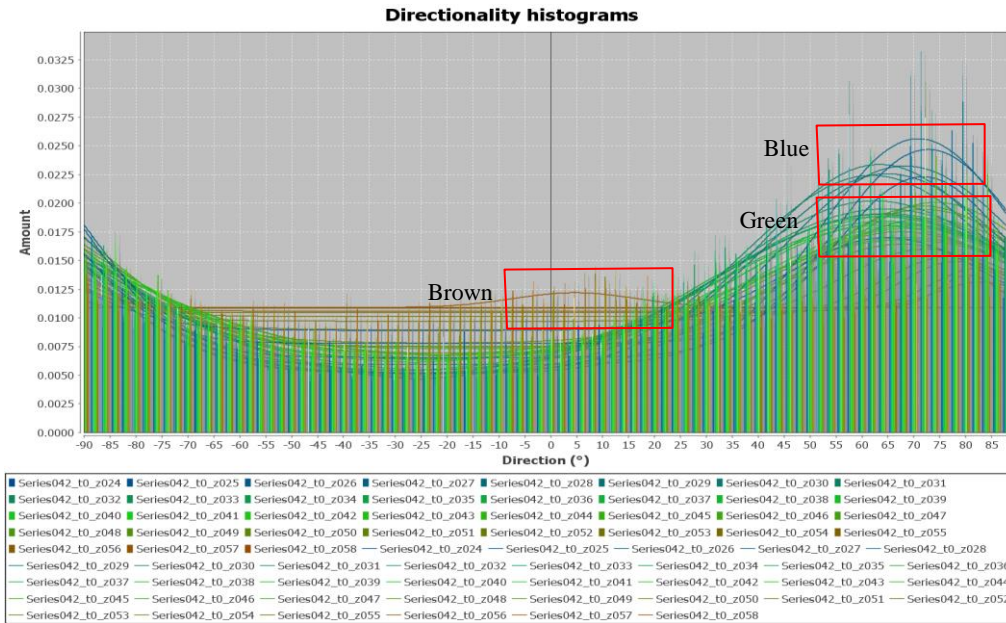


Figure 8-7, Damaged directionality histogram for Set 3 Experiment at 1.88 minute after catheterisation process (0.5N, 1 pass)

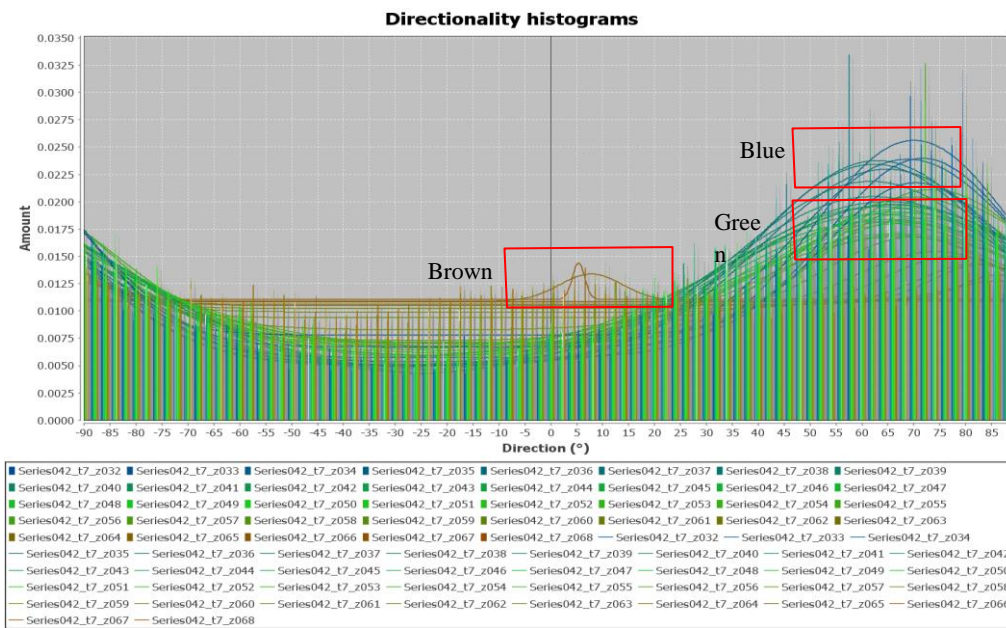


Figure 8-8, Damaged directionality histogram for Set 3 Experiment at 15 minutes after catheterisation process (0.5N, 1 pass)

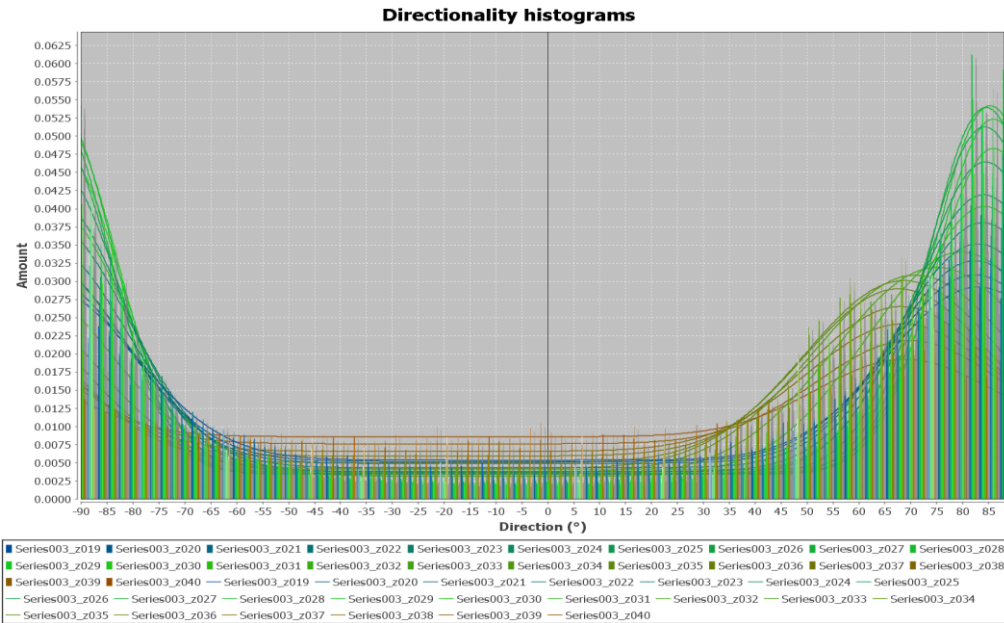


Figure 8-9, Undamaged directionality histogram for Set 1 Experiment (2.0N, 1 pass)

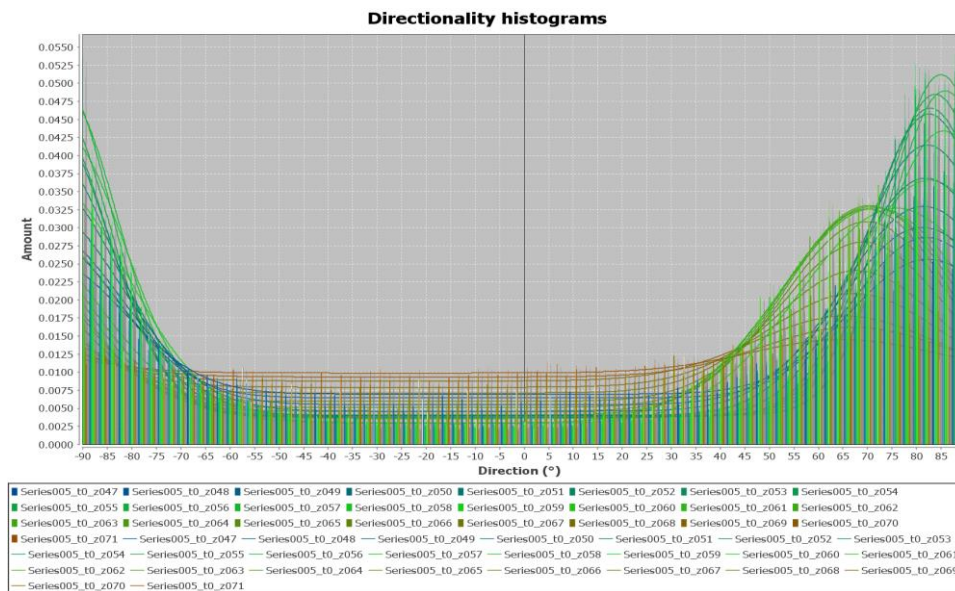


Figure 8-10, Damaged directionality histogram for Set 1 Experiment at 1.88 minutes after catheterisation process (2.0N, 1 pass)

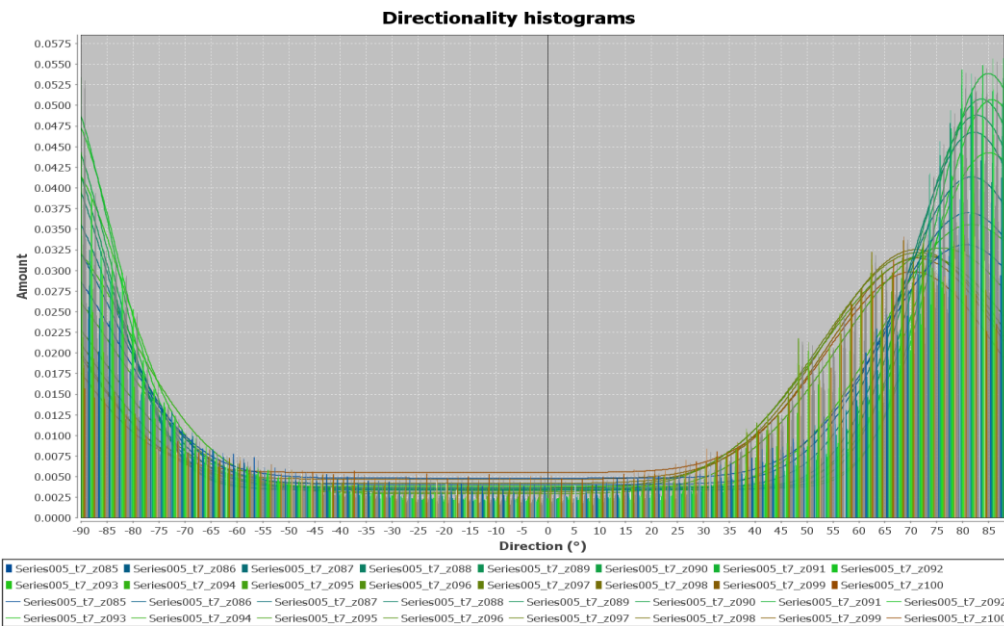


Figure 8-11, Damaged directionality histogram for Set 1 Experiment at 15 minutes after catheterisation process (2.0N, 1 pass)

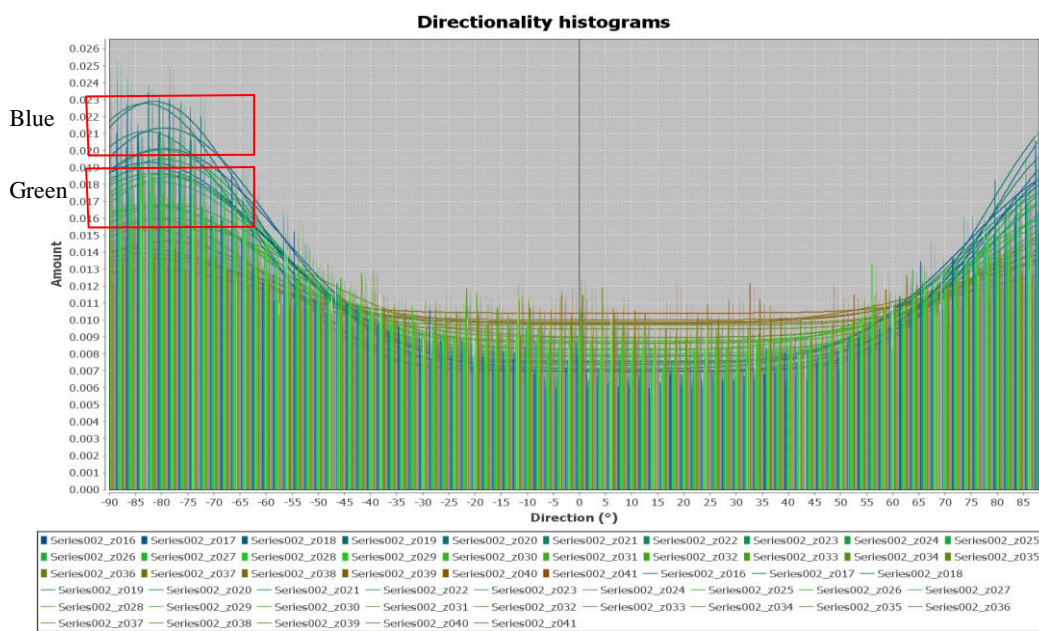


Figure 8-12, Undamaged directionality histogram for Set 1 Experiment (5.0N, 1 pass)

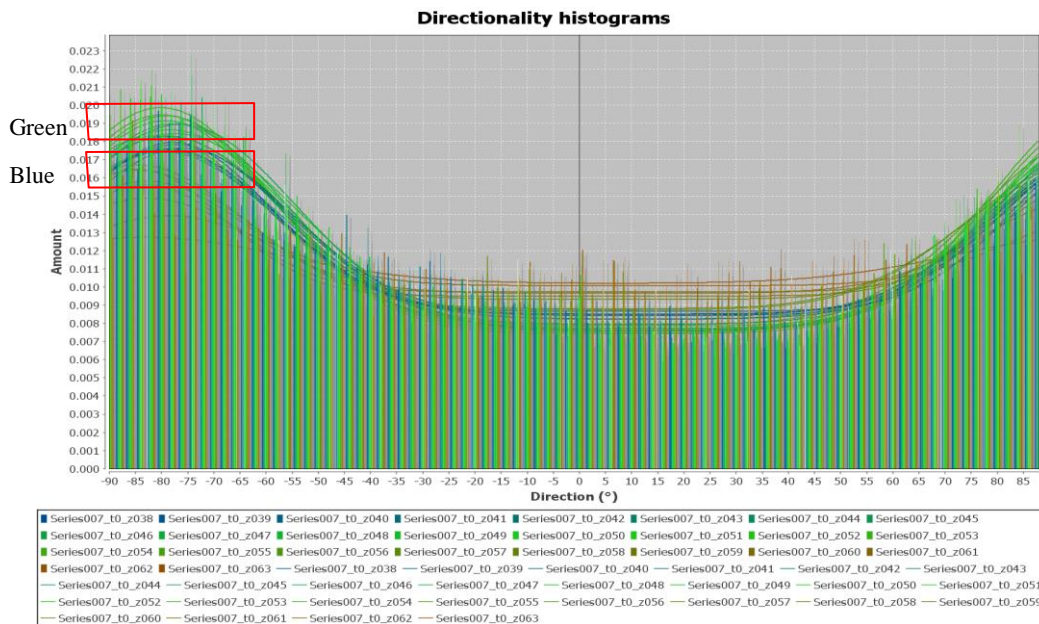


Figure 8-13, Damaged directionality histogram for Set 1 Experiment at 1.88 minutes after catheterisation process (5.0N, 1 pass)

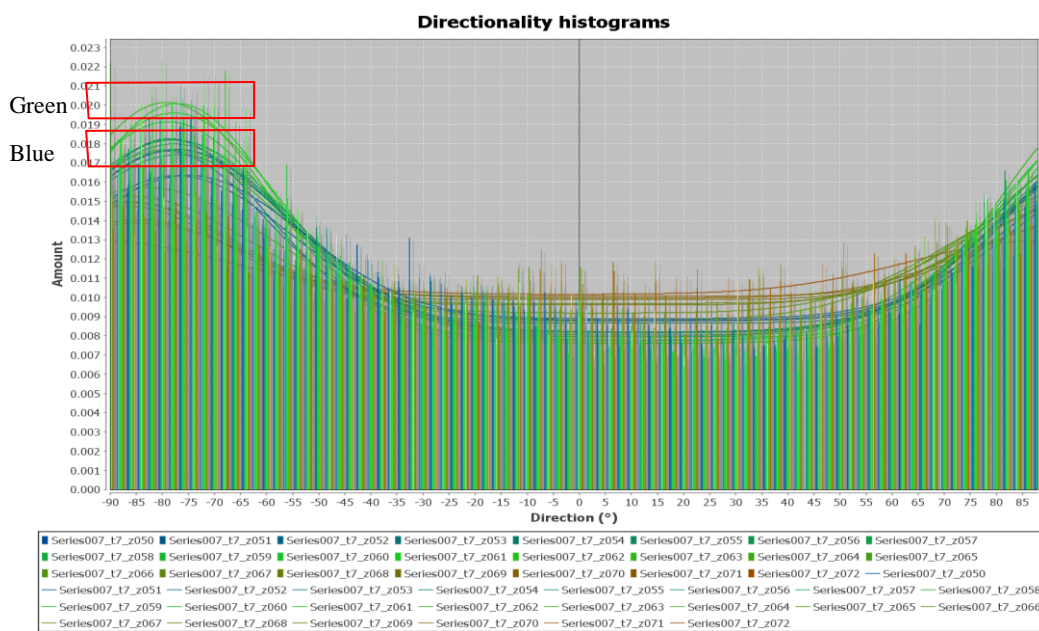


Figure 8-14, Damaged directionality histogram for Set 1 Experiment at 15 minutes after catheterisation process (5.0N, 1 pass)

8.4.4 Comparison of mean directionality angle of each set

This section examines the comparison of mean directionality angle of each histogram between undamaged Z-stacked scan and damaged Z-stacked scan at undamaged Z-stacked scan T_0 , T_1 , T_2 , T_3 , T_4 , T_5 , T_6 and T_7 . Figure 8-15 gives an overview of change in mean directionality angles for case 1. The change of the directionality angle against the time points of each is presented in Appendix G. In general, the change in mean directionality angle of

every case does not converge. In other words, the mean directionality angle of most of the cases does not have considerable change at T_0 and does not show any converging signs. One of the two possibilities is that porcine aorta samples did not undergo a recovery progress. A second possibility is that the mean directionality angle method is not suitable to represent the recovery progress of porcine aorta tissue samples. However, there are few cases that have considerable change in mean directionality angle ($>5^\circ$) but the change does not converge to the undamaged mean directionality angle.

In addition, case 9: 5N, 10 passes is a special case whereby most of the samples were perforated during the application of damage and only 2 samples from Set 2 and Set 4 were not perforated as shown in Figure G-9 in Appendix G.

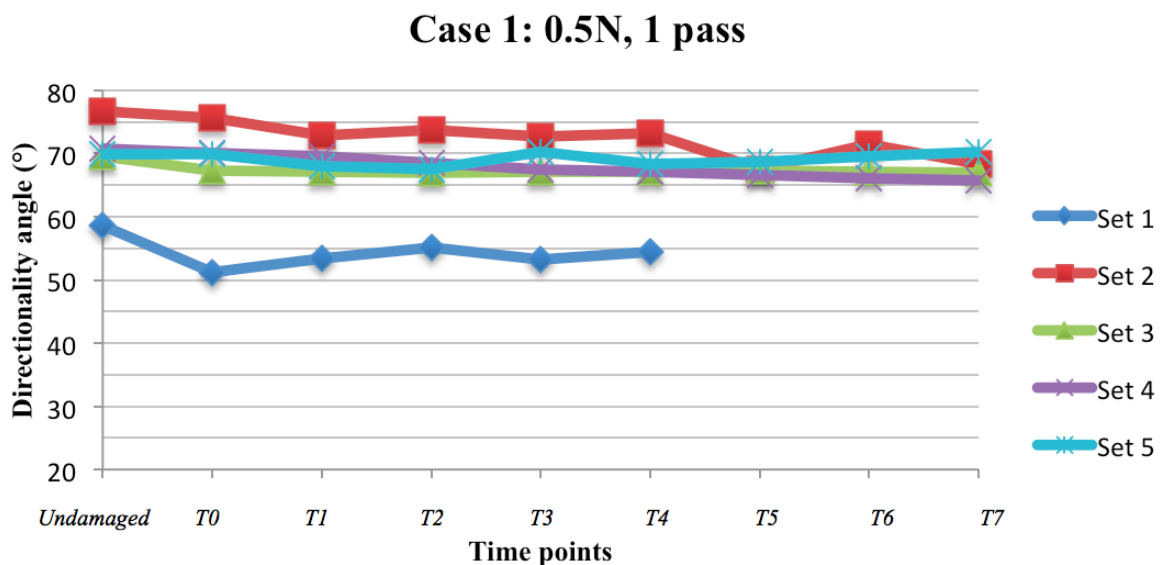


Figure 8-15, Comparison of mean directionality angle of 5 sets of experiments for case 1: 0.5N, 1 pass

8.4.5 Recovery progress of tissue fibres based on the direction angle difference ($\theta_{undamaged} - \theta_{Tn}$) for each case

As mentioned in section 8.3.4, the difference in directionality angle was used to study the recovery progress of porcine aorta tissue fibres. Therefore, it was predicted that porcine aorta would have recovered when time point, $|\Delta\theta_{Tn}|$, is equal to or near to 0 for consecutive time points. However, this prediction was not achieved as shown in Table 8-1.

The values of mean directionality angle difference, $|\Delta\theta_{Tn}|$, in Table 8-1 were taken from all 5 sets of experiments. By assuming that porcine aorta tissue fibres will deform and recover to its original state, Table 8-1 gives an overview of recover progress for different

damage conditions. Table 8-1 also shows that the recovery progress of all 9 damage conditions are not consistent, not showing any pattern or trend to imply how porcine aorta tissue fibres would recover. This might give a hint that there are other factors governing the recovery progress of porcine aorta tissue fibres.

Table 8-2, Table 8-3 and Table 8-4 show the mean and standard deviation of 3 different time points, T_0 , T_4 , T_7 , and how they were obtained from all 5 sets of experiments. Among all 9 damage conditions, standard deviation of Case 3: 0.5N, 10 pass, Case 4: 2N, 1 pass, and Case 9: 5N, 10 pass are larger than other 6 damage conditions. Case 3: 0.5N, 10 pass and Case 4: 2N, 1 pass was more likely had been influence by the human errors, while Case 9: 5N, 10 pass was due to the perforation of porcine aorta tissue samples.

Table 8-1, Recovery progress based on the amount of mean directionality angle change

			$ \Delta\theta_{T_0} $	$ \Delta\theta_{T_1} $	$ \Delta\theta_{T_2} $	$ \Delta\theta_{T_3} $	$ \Delta\theta_4 $	$ \Delta\theta_{T_5} $	$ \Delta\theta_{T_6} $	$ \Delta\theta_{T_7} $
Case 1	0.5N	1 pass	2.3°	2.9°	2.7°	3.1°	3.0°	4.2°	3.2°	4.1°
Case 2	0.5N	5 pass	1.4°	1.2°	1.2°	1.2°	1.7°	1.3°	1.8°	1.8°
Case 3	0.5N	10 pass	8.8°	6.6°	6.4°	8.1°	6.5°	8.1°	7.4°	6.6°
Case 4	2N	1 pass	5.9°	5.9°	5.6°	6.4°	6.2°	8.1°	6.8°	6.0°
Case 5	2N	5 pass	1.9°	1.5°	2.3°	3.0°	2.2°	1.2°	1.0°	1.6°
Case 6	2N	10 pass	2.5°	1.9°	2.2°	2.1°	2.7°	2.0°	2.4°	2.3°
Case 7	5N	1 pass	2.4°	3.0°	2.8°	2.7°	3.2°	3.0°	3.5°	3.7°
Case 8	5N	5 pass	2.3°	1.1°	2.3°	1.5°	3.1°	3.9°	4.7°	3.9°
Case 9	5N	10 pass	26.2°	28.9°	25.8°	25.6°	7.6°	10.0°	9.1°	9.8°

Table 8-2, Amount of mean directionality angle change at T_0 with respect to $T_{undamaged}$

			Set 1	Set 2	Set 3	Set 4	Set 5	Mean	S.D.
Case 1	0.5N	1 pass	7.4°	1.0°	2.2°	0.7°	0.1°	2.3°	2.9°
Case 2	0.5N	5 pass	1.0°	3.8°	0.6°	1.5°	0.1°	1.4°	1.4°
Case 3	0.5N	10 pass	9.2°	8.3°	23.6°	2.0°	0.7°	8.8°	9.1°
Case 4	2N	1 pass	24.2°	2.3°	2.3°	0.6°	0.3°	5.9°	10.3°
Case 5	2N	5 pass	6.6°	0.2°	2.0°	0.2°	0.7°	1.9°	2.7°
Case 6	2N	10 pass	8.6°	0.4°	1.9°	0.3°	1.4°	2.5°	3.5°
Case 7	5N	1 pass	2.5°	3.8°	0.8°	2.4°		2.4°	1.2°
Case 8	5N	5 pass	7.3°	0.2°	0.4°	1.4°		2.3°	3.4°
Case 9	5N	10 pass	64.2°	13.3°		1.1°		26.2°	33.5°

Table 8-3, Amount of mean directionality angle change at T₄ with respect to T_{undamaged}

			Set 1	Set 2	Set 3	Set 4	Set 5	Mean	S.D.
Case 1	0.5N	1 pass	4.2°	3.4°	2.4°	3.7°	1.5°	3.0°	1.1°
Case 2	0.5N	5 pass	2.3°	3.7°	0.2°	2.0°	0.2°	1.7°	1.5°
Case 3	0.5N	10 pass	10.8°	6.7°	12.7°	2.0°	0.4°	6.5°	5.3°
Case 4	2N	1 pass	24.1°	1.8°	2.5°	0.5°	2.1°	6.2°	10.0°
Case 5	2N	5 pass	7.6°	0.3°	2.7°	0.0°	0.6°	2.2°	3.2°
Case 6	2N	10 pass	9.7°	0.3°	2.2°	0.4°	1.0°	2.7°	4.0°
Case 7	5N	1 pass	4.3°	4.9°	1.0°	2.7°		3.2°	1.7°
Case 8	5N	5 pass	10.0°	0.3°	1.5°	0.6°		3.1°	4.6°
Case 9	5N	10 pass		14.9°		0.3°		7.6°	10.3°

Table 8-4, Amount of mean directionality angle change at T₇ with respect to T_{undamaged}

			Set 1	Set 2	Set 3	Set 4	Set 5	Mean	S.D.
Case 1	0.5N	1 pass		8.3°	2.6°	5.1°	0.5°	4.1°	3.3°
Case 2	0.5N	5 pass	0.5°	4.8°	0.8°	0.8°	2.0°	1.8°	1.8°
Case 3	0.5N	10 pass		6.1°	16.9°	2.3°	1.3°	6.6°	7.1°
Case 4	2N	1 pass	23.1°	0.3°	0.2°	0.6°		6.0°	11.4°
Case 5	2N	5 pass	2.9°	1.0°	3.3°	0.3°	0.6°	1.6°	1.4°
Case 6	2N	10 pass	7.2°	0.6°	2.2°	0.7°	0.9°	2.3°	2.8°
Case 7	5N	1 pass	5.2°	5.4°	1.4°	2.7°		3.7°	2.0°
Case 8	5N	5 pass	7.9°	1.0°	6.2°	0.4°		3.9°	3.8°
Case 9	5N	10 pass		17.6°		2.1°		9.8°	10.9°

8.5 Discussion

8.5.1 Suitability of Eosin B in Imaging Surface or Subsurface of Porcine Aorta

Waheed's study suggests that Eosin B is capable of staining arginine, lysine and histidine (Waheed et al., 2000). These proteins do not exist in elastin fibres or exist in a very small amount. However, these proteins exist in collagen fibres although they are not as abundant as other proteins, in the porcine aorta wall. This suggests that the tissue fibres stained are not elastin fibres in this study, which contradicts Megen's study that used Eosin to stain elastin fibres (Megens et al., 2007)

In addition, Figure 8-17 that was obtained from Tsamis's study also showed that the inner layer (intima) is comprised of mainly a single layer of endothelial cells, a thin basal

membrane and a sub-endothelial layer full of collagen fibrils (Tasmis et al., 2013). Therefore, this might suggest that the tissue fibre imaged could be collagen fibrils. However, it is unknown if the aortic wall of porcine aorta is composed of collagen or elastin fibres or both. Zeeman et al. (1998) confirmed that Eosin B is able to stain the collagen in the aortic wall, but elastin is less likely. But the middle part of porcine aorta sample shown in Figure 8-16, which is composed mostly of collagen fibres, is not stained with Eosin B. This could be supported by another study that stated elastic fibres are stained with Eosin probably due to the high density and low permeability of these structures (Goldstein, 1969).

From these, it can be concluded that Eosin B is able to stain the tissue fibres of the porcine aortic wall, which could comprise of both elastin and collagen fibres.

Additionally, during the initial experiments, the results were able to show the endothelial cells on the intima layer as shown in Figure 8-18 due to the ability of Eosin B to stain cytoplasm of cells. In addition, the shape of the cells images in Figure 8-18(a) and (b) are similar to endothelial cells illustrated in Figure 8-17.

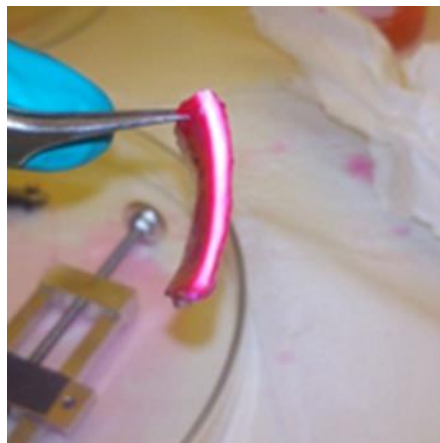


Figure 8-16, The stained porcine aorta sample that is cut open to investigate the depth of Eosin B stain

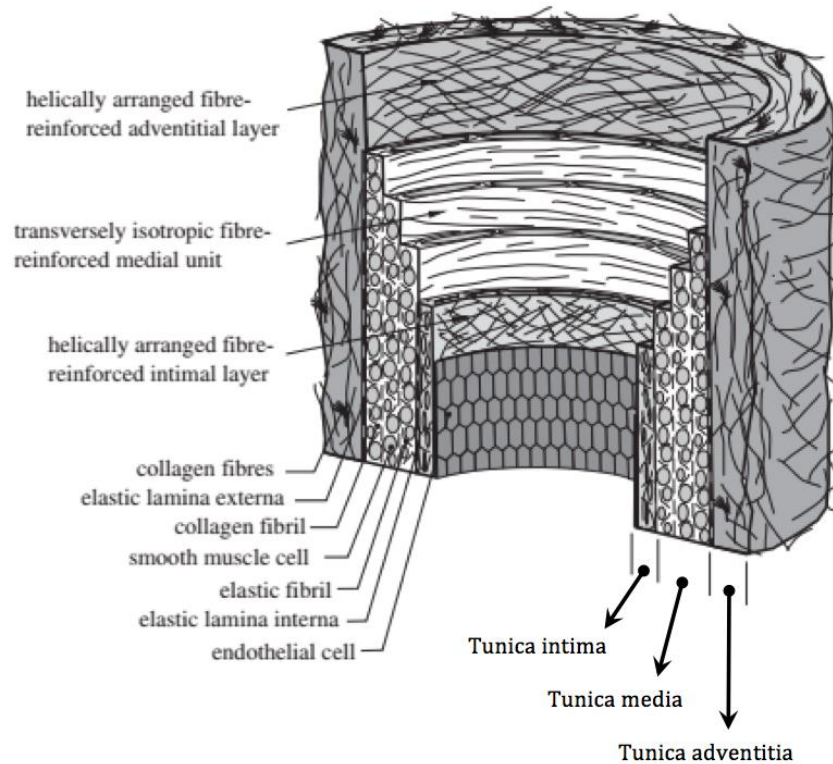


Figure 8-17, The detailed structure of the layers of porcine aorta (Tsamis et al., 2013)

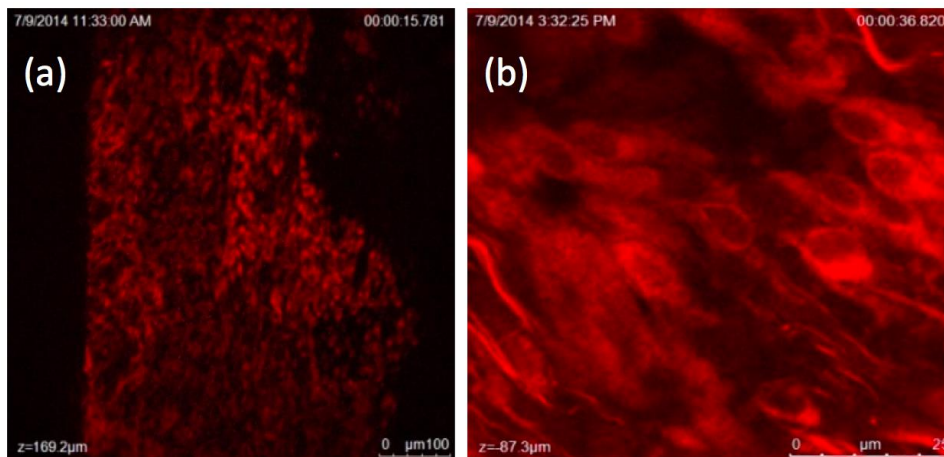


Figure 8-18, (a) The endothelial cells stained with Eosin B imaged using standard confocal microscopy (b) The endothelial cells were magnified

8.5.2 Recovery of aortic wall tissue fibre

Based on the directionality histograms of tissue fibres for case 1 to case 9 of 5 sets of experiments show that the respective directionality histograms pattern of each and every case are unique and therefore this has ruled out the assumption that the orientation of porcine aorta tissue fibres is the same across all samples. It was previously hypothesized that the directionality angle of tissue fibres should remain constant due to the pre-stretch of aorta samples throughout the experiment. However, directionality histograms and the images

obtained from confocal microscope have shown that the directionality of the tissue samples vary for every different tissue sample used.

The first method of analysing the recovery of the tissue sample was through directionality histograms, which show the directionality of the tissue samples before and after the rubbing of a catheter. There are slight to moderate changes on the directionality angle and the amount of the tissue fibres at that direction. The tissue samples are known to be able to recover when the damaged directionality histograms of tissue samples are identical or similar to their respective undamaged directionality histogram however the damaged directionality histograms do not show even the slightest recovery even after approximately 15 minutes.

The no-recovery progress also can be observed using the comparison of figures of mean directionality angle for every case and experimental sets. In brief, the figure of comparison of mean directionality angle for all 9 cases and 5 experimental sets show that the mean directionality angle of the tissue fibres of the 8th damaged Z scan is not the same as the undamaged directionality angle of the tissue fibres. In addition, the trend lines of the figures do not show any recovery signs. There are 2 possibilities explaining this situation. Firstly, it could be that the orientation of tissue fibres would take a longer period to recover, which was more than 15 minutes. Second possibility is that it could be that the tissue fibres had already recovered the instant the in situ tribometer finished applying the catheterisation damage on the samples.

These methods show that the aortic wall fibres might not be a suitable mean to measure the recovery of porcine aorta after catheterisation process. Even if aortic wall tissue might recover to an undamaged state, it definitely takes longer than 15 minutes. It is also uncertain if the deformation will have an effect on the directionality of the tissue fibres, but deformation will have an effect on the amount of tissue fibres of specific directionality. This could explain why there are changes in the amount of tissue fibres in the directionality histograms. When deformation occurs, the tissue fibres will be either being pushed away or go further down due to the pressing normal force, as such, the amount of tissue fibres of specific directionality will change.

8.5.3 Real-time monitoring of porcine aorta tissue fibres

The main result showed that the porcine aorta tissue fibres did not recover within 15 minutes. However, it is uncertain whether the tissue fibres had recovered or returned to their original

orientation the instant after the application of catheterisation damage finished and before the Z-stacked scanning took place.

Therefore, it was of interest to investigate how the porcine aorta tissue fibres behaved or recovered in the period between the application of catheterisation damage and the first damaged Z-stacked scanning. However, it was very difficult to achieve due to two main problems.

Firstly, confocal microscope is not able to obtain any image of tissue fibres when there is an object between the tissue sample and the lens. Therefore, it is impossible to use confocal microscope to obtain any images during the application of catheterisation damage. Secondly, confocal microscope is not able to automatically focus at the same layer of the porcine aorta as porcine aorta sample will deform during the application of catheterisation damage due to the normal force, and will take time to return to undeform state. Therefore, it requires confocal microscopy to run a Z-stacked scan on the porcine aorta sample, however, Z-stacked scan will not give accurate real time monitoring as each Z-stacked scan takes 1.88 minutes to finish scanning. As such, confocal microscopy will take 1.88 minute to scan the same layer with every consecutive scans.

Y-stacked scanning of confocal microscope was previously used to scan the porcine aorta sample from the side view to give more accurate real time monitoring on the change of orientation of tissue fibres without concerning the deformation of porcine aorta samples. However, the images obtained were blurred and were not able to improve by changing various scanning settings.

In regards to subsurface real time monitoring, Optical Coherence Tomography (OCT) is a good alternative that can be used to study the subsurface condition of porcine aorta sample. However, OCT is not able to produce imaged that can show such details of tissue fibres in comparison to confocal microscopy.

Therefore, further research should focus if tissue fibre is really a necessary to study the recovery progress of porcine aorta, and also to discover if there are alternatives that can be used to measure and represent the recovery progress of damaged porcine aorta.

8.6 Conclusions

Throughout this study, it is shown that the directionality of the aortic wall fibres might not be a suitable scale to measure the recovery progress of porcine aorta. Firstly, it is time

consuming for the recovery progress to finish considering if the ex-vivo tissue samples do recover. In addition, it is unsure if the porcine aorta had recovered the instant before the Z-stacked scan took place. Secondly, confocal microscopy is not able to provide accurate real time monitoring on the changes of orientation of porcine aorta tissue fibres.

Further improvements on the experiment results and experiment set-up are limited as there are currently no appropriate equipment (2-Photon Confocal Fibre Scanner) and materials (Fluorescent Dyes that can stain the whole porcine aorta). Therefore, accurate real time imaging on en-vivo experiment is difficult to achieve currently. However, this study still shows that the results obtained from real time imaging are of great value.

Chapter 9

Discussion

9.1 Introduction

This research has so far covered and studied several different studies, which are the strain behaviour of finger pad and silicone hemi-sphere while in contact with a counter-face material, the strain behaviour of the forearm while performing simple movements without interacting with a counter-face material and the deformation of the porcine aorta from catheterisation process. Therefore, this chapter aims to look at the bigger picture and discuss the connections between the work packages in this research from chapter 4 to chapter 8. As this research was more focused in exploring the usage of different imaging techniques in biotribology and biomechanics experiments, a summary of the imaging techniques used and their respective limitations are shown in this chapter. In addition, this chapter will summarise the strain behaviour of the human finger pad skin in contact with a counter-face material.

9.2 A summary of real-time imaging techniques in studying the deformation of soft tissues

One of the main outputs of the current project is to explore how various imaging techniques can be used in bio-tribology because these imaging techniques are not traditionally designed for bio-tribological experiments.

Therefore, various imaging techniques introduced in this study have been useful in revealing the morphology of the soft tissues. For example, OCT was able to capture the interaction between finger pad and transparent counter-face materials such as glass plate or plastic plate without much loss on the image quality. This imaging technique could even show the interaction between a finger pad and a transparent material with lubrication, as shown in Figure 9-1. This could lead to potential research opportunities in human skin biotribology in the future, which will be further discussed in section 9.3. Most importantly, these imaging techniques are able to produce real-time images that can monitor and show how the finger pad or soft tissues behave or react to different stimulations, such as a sliding test or a simple posture changing test. Also, the imaging techniques used in this research are non-invasive to the human body.

However, the imaging techniques that use light as a medium are also limited in the study of biotribology mainly due to the properties of light. In this research, for OCT and confocal microscopy, it was difficult to produce high quality images without trade-offs. For instance, due to the fact that OCT and 3D-DIC can only be used with a transparent counter-face material, the scope of research on interacting materials is limited to either transparent glass or plastic material although human skin has different touch perception when come into contact with all kinds of materials like metal, ceramics, woods etc. The study in Chapter 7 that focused on the change in morphology of forearm skin by changing its posture is an example, proved that the same imaging methodology was easier to use on an experiment without interacting materials and high quality images were easier to obtain. Another limitation is the properties of light, like reflection, refraction and diffusion. This is the main reason why a thin plate was used as the interacting material with finger pad in this research. The study on water lubrication during the interaction between finger pad and glass was not pursued as well, due to the severe light refraction during 3D-DIC experiments.

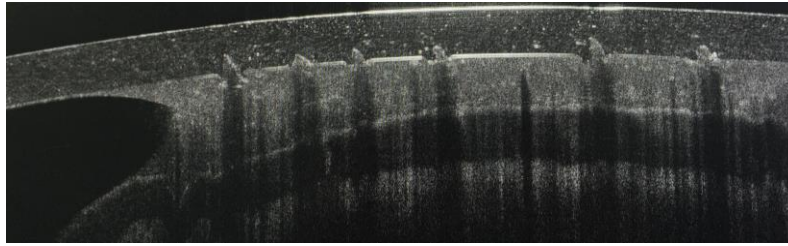


Figure 9-1, OCT image of finger pad, plastic glass and water layer

9.2.1 3D-Digital Image Correlation (DIC)

3D-Digital Image Correlation has been used to study the strain of the human skin in biotribology experiment (sliding interaction between glass plate and finger pad) and biomechanics experiment (posture change of the forearm). There are several stages in using 3D-DIC in the experiment, which are the samples preparation, cameras set-up and calibration, images acquisition and post-processing. After the post-processing, the 3D-DIC will show how the surface strain profile of the finger pad and the forearm changes in response to the change in the external environment in real-time.

The limitation of this imaging technique is that it is only able to look at the surface deformation of the soft tissues. Research work that is particularly interested in the subsurface deformation of soft tissues can consider using Optical Coherence Tomography or Digital Volume Correlation (DVC). DVC works similarly to DIC, however, this image technique analyses the cross sectional images (tomographic images) of the soft tissues to visualise the strain profile of the soft tissue in three axes. 3D-DIC is only able to visualise the surface strain profile of the soft tissue in two axes.

The other limitation, which is more specific to biotribology experiment, is the change of the surface properties during a sliding experiment. As 3D-DIC requires black speckles to be painted on the soft tissues during the sample preparation stage, it will have an effect on the sliding performance of the finger pad on the glass plate. This effect was reduced in this research by not applying the white background paint that was popularly done in other DIC experiments, which was deemed possible because the human skin used in this study has a light colour background in comparison to the black speckles. In the silicone hemi-sphere and glass plate study, the white background of the silicone hemi-sphere was done by mixing a tiny drop of white paint with the silicone mixture during the manufacturing stage instead of painting a white paint on the silicone hemi-sphere.

9.2.2 *Optical Coherence Tomography (OCT)*

Optical Coherence Tomography (OCT) is a non-invasive imaging technique that can show the surface and subsurface morphology of biological tissues. In this research, it is able to show the epidermal and dermal region of the human skin and their morphologic changes in response to the change in external environment in real-time. Commercially available OCT is a user-friendly imaging technique that does not require any camera calibration or set-up. However, complicated settings can be changed accordingly for advanced users. The software that comes with the OCT can only show and capture the condition of the skin without any post-processing features. So the OCT images captured are post-processed by using different software in this research, which is Matlab. After the post-processing, the OCT images can show the surface roughness of the human skin and the roughness of the dermal-epidermal junction of the skin.

The only limitation of using this imaging technique is that it is not possible to extract the strain values from the images. The OCT images had been previously analysed using DIC software, but no useful results were obtained because the speckles in the OCT images were too small and not unique, so the DIC software was not able to track the movement of the speckles from the OCT images.

The second limitation, which is more specific to biotribology experiments, the interacting material must be transparent in nature so that the light can travel through it. In addition, only thin glass plate can be used in the finger pad and glass sliding experiment. This is due to the fact that the thick glass has a striking effect on the laser light that is detrimental to the quality of the OCT images. This effect is still reflected on the thin glass, but to a lesser amount.

9.2.3 *Confocal microscopy*

Confocal microscopy scans the soft tissues with a focused beam and builds up the image point by point. Sample preparation is required in using this imaging technique on soft tissue. The soft tissue is required to be stained with a fluorescent dye overnight so that the fluorescent material can be attached on the tissue fibres during the imaging. Therefore, due to the potential health hazards on human skin using this method, porcine aorta was used instead in the biotribology experiment.

Confocal microscopy was the first imaging technique used in this project. Due to the difficulty of getting real-time deformation measurements and lengthy sample preparations,

confocal microscopy was not further pursued. On the other hand, OCT and 3D-DIC were suggested and investigated extensively in the remaining of the project.

Similar to OCT, confocal microscopy is only able to show and capture the condition of the tissue fibres without advanced post-processing features. So the confocal images were analysed using Fiji software and the orientation of the tissue fibres was extracted from the confocal images.

The limitation of the confocal microscopy is that it cannot show the strain of the tissue fibres before and after the sliding of the catheter tip on the porcine aorta. Therefore, the deformation or the damages of the tissue fibres can only be assessed by the orientation of the tissue fibres.

A study by Hendriks et al. (2011) had designed a portable miniaturised confocal microscopy, which could be attached on a tribo-meter. However, this was not successful because the device has a very short focal length - $100\mu\text{m}$, so the device touching the sample during image acquisition was unavoidable. This performance of the device is being further improved, which there will be a possibility that the confocal microscopy can still be used in real-time recording of the tribological experiment in the future.

9.3 From human skin to soft tissue simulant to theoretical model

The imaging techniques, as discussed in previous section, were all used to study the deformation and strain behaviour of the soft tissue during tribological interaction with other material. Confocal microscopy was used on porcine aorta and catheter tip. Optical Coherence Tomography and 3D-Digital Image Correlation were used on human finger pad and glass plate. Additionally, OCT and 3D-DIC were also used on non-tribological experiment, which is the forearm study in Chapter 7.

This research was initially focused on the measurement of strain on the finger pad undergoing sliding with a glass plate, in which Chapter 5 has shown that the strain profile of the finger pad would change from static to dynamic state. Although the finger pad surface strain behaviour does not seem to correlate with its frictional behaviour, the dynamic state strain profile has clearly shown that a region of finger pad was in tension while the other was in compression. However, this experiment was limited by the small measured strain values, which was easily affected by the unintentional self-vibration of the finger pad of the

volunteer. Therefore, this led to the testing of a more stable experimental sample, which was the soft tissue simulant – silicone rubber.

A silicone hemi-sphere was a stable experimental sample, which the strain profile showed almost no noisy strain values. However, the silicone hemi-spheres made in Chapter 6 were not a perfect simulation of the finger pad due to a few reasons. Firstly, the silicone hemi-sphere did not have ridges. Finger ridges played a very important role in interaction with other materials as shown in finger pad friction studies from Liu (2012) and Tomlinson (2009). Secondly, the silicone hemi-sphere made was a homogeneous isotropic material, but the human skin was composed of different layers of materials with different mechanical properties. Thirdly, the amount of the silicone in the hemi-sphere sample was limited and the size was smaller in comparison to the size of the finger pad. Therefore, a small size sample tends to experience a larger amount of strain because there is a limited amount of the material to share the strain. Despite the limitations of the silicone hemi-sphere, the strain profiles of the silicone hemi-spheres still served as a good reference and a starting point in understanding the strain behaviour of the finger pad under tribological interactions.

As the next step after the experimental soft tissue simulant, a study was conducted to investigate the feasibility of using the theoretical strain modelling, based on contact mechanics by Johnson (1987), to predict the strain profile and values of the silicone hemi-sphere under tribological interactions. The pilot study showed that the theoretical strain modelling was adequate to predict the strain profile of the silicone hemi-sphere but it was not used to compare with the strain profile of the finger pad due to certain limitations. The limitations are similar to why silicone hemi-sphere was not suitable to represent finger pad during tribological interaction. Firstly, the theoretical strain model was modelled under the assumption of homogeneous isotropic material, which human skin was not a homogenous material. Secondly, the theoretical strain model was modelled for a sphere in contact, however the shape of the finger pad in contact was elliptical. A study on strain profile of finger pad by Delhaye (2016) has also concluded that the theoretical strain modelling, based on Hertzian contact, was not suitable to predict complex strain profiles such as the finger pad during tribological interaction.

9.4 Strain study of soft tissue

Although the deformation of human skin does not play a significant role in tribological interactions with a smooth plate, a human always can feel the pulling sensation on the finger

pad even when a smooth plate is sliding. The previous studies have already built up the fact that one side of the human skin will be in tension while the other side is in compression against a sliding plate (Kwiatkowska et al., 2009, Delhayé et al., 2016). However this research is one of the earlier works that can clearly visualise the strain distribution of the human skin during tribological interactions in real-time by using 3D-DIC. It is shown that although strain distribution of the finger pad in contact is complex and may have slight variation with each experimental attempt but the overall strain profile is similar, especially the locations of the human skin in tension and compression, which is always aligned with the direction of the sliding of the plate (Delhayé et al., 2016).

The main problem with a non-uniform strain distribution is the method to quantify the strain values. The most straightforward method is to average the strain values as in a study by Delhayé et al. (2016), which has quantified the strain by reporting the average strain in within the contact region. However, strain averaging might lead to the misrepresentation of the strain condition because a study done by Jacquemoud et al. (2007) discovered that there is a distinctive difference between ultimate global longitudinal strain (Green-Lagrange strain, 9.5%) and the ultimate local longitudinal strain (Green Lagrange strain, 24%), which were obtained from the LVDT of the tensile machine and the DIC respectively. Averaging the strain within contact area is a good starting point to show the big picture of the strain changes against the normal load, however, essential information on the effects from other parameters, like relative humidity, external temperature, sliding speed, age, gender, ethnicity etc. may be lost (Liu, 2013). Therefore, this study had shown the general strain distribution profile, the strain profile along position axis and also the averaging of strain within the contact area of the finger pad to perform a detailed analysis on the strain changes of the finger pad during a sliding interaction.

It is known that the condition of the finger pad can vary vastly as human skin is highly dependent on the internal and external environment (Liu, 2012; Tomlinson, 2009; Adams, 2007). This will be reflected in the strain behaviour of the finger pad as well. However, this research was a starting point to develop imaging methodologies for obtaining the strain profile of the finger pad consistently and reliably, which is why there were only few parameters altered during experiments. Future work will involve investigating more parameters and the consistency of the strain profiles by repeating the experiments.

In addition to the strain of human skin during sliding on the smooth glass, a pilot study in Chapter 4 has looked into the study of human skin while sliding against plates of uneven surfaces. So, in order to increase the friction between the finger pad and interacting material, one of the methods include increase the roughness of the interacting material to a roughness threshold that introduces an interlocking mechanism between the human skin and the interacting material. Tomlinson (2009) has particularly investigated the interlocking mechanism between the finger pad and the ridged plate ($R = 1.19 - 98.42\mu\text{m}$) during sliding interaction. In addition, Derler et al. (2009) have shown that how finger pad frictional behaviour changes with the roughness of the interacting material. The pilot study in Chapter 4 has opened up the possibility to capture and record the motion of the human skin interacting with materials of different roughness in real-time. Although there will be limitations as discussed in section 4.5.7, but the effect of the interlocking mechanism on the human skin can be further investigated and, most importantly, visualised using the imaging technique - optical coherence tomography.

Chapter 10

Conclusions and Future work

10.1 Introduction

This final chapter first lists the key findings of each imaging techniques used throughout the research. Then it goes through the main highlights of the deformation and strain behaviour of the soft tissues and the tissue simulant undergoing tribological interactions or just plain simple movement. The final section of the chapter shows the next steps of this research that could help in further developing the understanding of deformation and strain of soft tissues in various circumstances.

10.2 Conclusions

10.2.1 Real-time imaging techniques

10.2.1.1 3D-Digital Image Correlation

3D-DIC is very useful in computing real-time full-field surface strain of the experimental subject that shows how the strain varies in response to different internal and external conditions. It can be used on both soft tissues and tissue simulants undergoing tribological interaction with a counter-face material, although it is limited only to smooth transparent materials.

Traditional 3D-DIC system is not suitable for determining strain of finger pad ridges and it is also not suitable for use on highly deformable viscoelastic materials, for instance silicone hemi-sphere with 20% deadener, due to extreme shearing that occurs in the middle region of the contact

It is feasible to measure the contact area of soft tissue or tissue simulants in contact with the glass plate using the 3D-DIC position data.

10.2.1.2 Optical Coherence Tomography

OCT is useful in the study of morphological changes of human skin, like the change in skin roughness and the thickness of the epidermal-dermal layer of human skin, in response to different internal and external conditions. It is a real-time imaging technique although post-processing is required to accurately determine the mean and standard deviation of skin roughness and thickness.

This research shows that the OCT can be used in a tribological study between human skin and grooved plates in addition to smooth transparent glass

10.2.1.3 Confocal microscopy

Confocal microscopy is useful in looking at the microscopic deformation of tissue fibres of soft tissues. However, fluorescent dyes are required for the imaging. It is the most difficult imaging technique to achieve real-time imaging of deformation of soft tissue due to the scanning distance and the scanning speed

10.2.2 Frictional behaviour, strain behaviour, morphological changes and surface moisture changes of finger pad with tribological interactions

Based on the study done on one experimental subject, there are connections between the frictional and the strain behaviour of the finger pad as the average strain within the contact area has a linear relationship with the normal load applied. The power-law relationship between the dynamic coefficient of friction and the normal load of the finger pad shows that the adhesion is the predominant friction mechanism in the sliding interaction of a finger pad with a smooth glass plate. Soaked finger pad has a higher dynamic coefficient of friction than the natural finger pad, however, the soaked finger from the 3D-DIC test has similar dynamic coefficient of friction with the natural finger pad due to the longer acclimatisation period, different environmental conditions and the change in surface conditions by the speckles application. The general principal strain profile of the finger pad in contact was able to show which region was in tension or in compression and also the surface strain at the edge of the contact area was higher than the middle region of the contact area.

The methodology of water application on the finger pad is essential in the future study as the surface moisture level of the finger pad was highly affected by the acclimatisation period even though the finger pad had been exposed to long period of water soaking.

The relationship between the apparent contact area of the finger pad and the normal load can be described using a power-law equation. Moreover, the friction has a linear relationship with the apparent contact area of the finger pad. The real-apparent contact area ratio has hints of relationship with the moisture condition, although the apparent contact area does not seem to influence it. The sliding state of the finger pad appears to have a minimal effect on the contact area.

The roughness profile has the potential to be used as a parameter in the sliding interaction between the finger pad and a smooth glass plate. It is expected to be relatable to the real contact area that affects the frictional behaviour of the finger pad. However, it needs more experimental data to be validated.

10.2.3 Frictional behaviour and strain behaviour of silicone hemi-sphere with tribological interactions and its theoretical modelling

The frictional and the strain behaviour of the silicone hemi-spheres are relatable because the normal load has a linear relationship with the average strain of the contact area and the shear load in the dynamic state has caused a substantial change in the strain behaviour of the

silicone hemi-spheres. The frictional behaviour of the silicone hemi-sphere with a smooth glass plate is dominated by the adhesion mechanism based on the exponent from a power-law relationship between the dynamic coefficient of friction and the normal force. Further work shows that the coefficient of friction is directly proportional to the stiffness of the silicone samples with a negative gradient regardless of the amount of deadener in the mixture. The strain behaviour of the silicone hemi-spheres in contact is largely characterised by the high strain at the edge of the contact and low strain in the middle of the contact, similar to the finger pad. High average surface strain values (E_1 strain: 8 to 52%, E_2 strain: -6 to -16%) on the silicone hemi-sphere samples may be explained by the adhesive hysteresis effect, which is defined as the phenomenon where taking apart two contact surfaces dissipates more energy than bringing both together (Qian & Yu, 2013).

The contact area of the silicone hemi-spheres and the normal load applied can be related by using power-law relationship. Additionally, the shear force is shown to have a linear relationship with the apparent contact area in the dynamic state. The contact area of the silicone hemi-sphere samples with higher stiffness decreases during sliding is due to the recovery of the silicone sample, as the bending stiffness of the glass decreases. On the other hand, the silicone sample with 15% deadener increases is likely due to the slow recovery of the silicone hemi-sphere at the compression part of the contact while the “in tension” part of the silicone hemi-sphere got into contact with the glass during sliding.

The homogenous silicone hemi-spheres used in this study are able to simulate the frictional behaviour of a finger pad at different moisture conditions. However, there are rooms for improvements in simulating the strain behaviour, the stiffness profile and the apparent contact area of the finger pad. The main challenges are the homogeneous properties, the size and geometry, and the surface roughness of the silicone hemi-spheres.

The theoretical strain modelling of contact mechanics (Johnson, 1982) is able to predict the pattern of the strain distribution profile of the silicone hemi-sphere although it still requires more work to accurately predict the strain values due to limitations such as the bending effect of the plate and the change of material properties when one region is in tension and the other in compression.

10.2.4 Strain behaviour and morphological changes of forearm movement without tribological interactions

It is feasible to quantify the morphological skin parameters from OCT images and also the method to combine two non-invasive techniques that are DIC and OCT to investigate skin surface strain and sub-surface layer deformation of volar forearm.

Simple movements such as extension and flexion of the arm will cause considerable strain on the forearm region, approximately 25%, and caused morphological changes in the upper skin layers, which result in the decrease of skin surface roughness between 40% - 50%, the decrease of epidermal layer thickness approximately 20% and the decrease of the dermal-epidermal junction undulation roughness between 45%-50%.

10.2.5 Deformation of porcine aorta tissue fibres due to catheterisation damage

Porcine aorta tissue fibres were unable to recover to their undamaged state after tribological damage in 15 minutes, which could be explained by two possibilities. Firstly, the tissue fibres needed a longer time to recover. Secondly, the tissue fibres have recovered as much as they could the moment the tribological interaction was finished. Therefore, aortic wall fibres might not be a suitable mean to measure the recovery of porcine aorta that experienced damage from catheterisation process

10.3 Future work

10.3.1 Real-time imaging techniques

10.3.1.1 3D-Digital Image Correlation

More work/experiments are needed to understand why 3D-DIC is not able to compute dynamic strain profiles of high viscoelastic materials like silicone-hemispheres with a high percentage of deadener.

The use of high-speed camera for 3D-DIC to study the effect of relative sliding speed on the strain profile of finger pad or silicone hemisphere can prove advantageous as the sliding speed is one of the main factors in biotribology. For the particular interests in the study of surface strain of the finger pad ridges, 3D-DIC system with higher magnification cameras, such as VIC-3D MicroTM, can be explored.

10.3.1.2 Optical Coherence Tomography

Much higher C-scan scanning speed is required to study the contact condition of finger pad during sliding in real-time. More importantly, more ideas are required to optimise the OCT

system in capturing the whole contact area of the finger pad. The main purpose is to validate the connection of the real contact area with other variables, such as, the moisture level and the stiffness of the finger pad. A more feasible approach may focus on imaging smaller contact area that fits into the scanning range of the OCT system during the sliding interaction with the glass plate in static or dynamic state. Monitoring the real and apparent contact area of the finger in real time may prove to be difficult unless a more advanced OCT system is designed and manufactured.

10.3.1.3 Confocal microscopy

Look into a more reliable imaging method to obtain real-time tissue damage visualisation data. Regardless, the miniaturised confocal microscopy can still be explored if the scanning speed is increased and the vulnerability to environmental disturbance, such as the vibration from the surrounding, is improved.

10.3.2 Frictional and strain behaviours of finger pads and silicone hemi-spheres

A study that performs the stiffness test and sliding tests using the imaging methodologies in this study on more volunteering subjects to investigate the frictional and strain behaviours of the finger pads from a wider human population, which different gender, age, ethnicity groups etc. may have a certain effect on the behaviours. In the meantime, additional work is needed to increase the strain profile database of the finger pad, which can be achieved by exploring the effect of various other parameters, such as the high normal load region, relative sliding speed, moisture level before the sliding test, the environmental temperature etc.

A multi-layered silicone hemi-sphere should be studied next to investigate if the gap difference in the strain profiles between a finger pad and a silicone hemi-sphere can be reduced without jeopardising the successful simulation of the frictional behaviour in this study. A silicone replica of a finger pad can be explored as well after the study on the multi-layered silicone hemi-sphere.

10.3.3 Theoretical strain model of the silicone hemi-sphere

More work is needed to improve the theoretical strain of the silicone hemi-sphere that can predict a relatively accurate strain profile of the homogenous silicone hemi-sphere, a multi-layered silicone hemi-sphere and the silicone replica of a finger pad.

10.3.4 Morphological change of finger pad

Further investigation of the morphology of finger pad ridges when sliding against grooved plate by exploring a variety of patterned glass and corrugated plastic sheets, which a visualisation database of morphological change of finger pad can be built. In addition, the study of the lubrication on finger pad can be included in the visualisation database of morphological change of finger pad.

10.3.5 Moisture level of the finger pad

Further investigations required to study the effect of different water application methods and also the length of acclimatisation period on the finger pad. Also, a study is needed to standardise the water application method to efficiently control the moisture level of the finger pad before the sliding test. It could be very advantageous if a device or a method can be manufactured or designed to monitor the moisture level of the finger pad in real time.

10.3.6 Contact area measuring method

Additional work is required to improve the apparent contact area measurement from the 3D-DIC data in order to get a more accurate contact area reading. This can be compared to the experimental data obtained using OCT (refer to section 10.3.1.2). Uncertainty and errors quantification test should be performed in the future work as well.

References

- Abignano G., Aydin, A. Z., Castillo-Gallego, C., Liakouli, V., Woods, D., Meekings, A., Wakefield, R. J., McGonagle, D. G., Emery, P. & Del Galdo, F. (2013). Virtual skin biopsy by optical coherence tomography: the first quantitative imaging biomarker for scleroderma. *Annals of the Rheumatic Diseases*, 72, 1845-1851.
- Adams, M. J., Briscoe, B. J., & Johnson, S. A. (2007). Friction and lubrication of human skin. *Tribology Letter*, 26(3), 239-253.
- Adams, M. J., Johnson, S. A., Lefevre, P., Levesque, V., Hayward, V., André, T., et al. (2012). Finger pad friction and its role in grip and touch. *Journal of The Royal Society Interface*, 10(80), 1-19.
- Agache, P., Monneur, C., Leveque, J., & Rigal, J. (1980). Mechanical Properties and Young's modulus of human skin in vivo. *Archives of Dermatological Research*, 269(3), 221-232.
- Alawi, S. A., Batzm, S., Rawert-Huber, J., Fluhr, J. W., Lademann, J., & Ulrich, M. (2015). Correlation of optical coherence tomography and histology in microcystic adnexal carcinoma: a case report. *Skin Research and Technology*, 21(1), 15-17.
- André, T. M., Lefvre, P., & Thonnard, J. L. (2009). A continuous measure of fingertip friction during precision grip. *Journal of Neuroscience Methods*, 179, 224-229.
- Annaidh, A. N., Bruyere, K., Destrade, M., Gilchrist, M. D., & Ottenio, M. (2012). Characterization of the anisotropic mechanical properties of excised human skin. *Journal of the Mechanical Behaviour of Biomedical Materials*, 5, 139-148.
- Ansorge, S. & Papailiou, K. (2016). Mechanical properties of silicone rubber under high loadings of alumina trihydrate filler. *Journal of Elastomers & Plastics*, 48(4), 354-382.
- Archard, J. F. (1957). Elastic deformation and the laws of friction. *Proceedings of the Royal Society of London. Series A, Mathematics and Physical Science*, 243(1233), 190-205.
- Ashby, M. F. (2011). *Materials selection in mechanical design 4th edition*. Butterworth-Heinemann (Elsevier).
- Asserin, J., Zahouani, H., Humbert, P., Couturaud, V., & Mougín, D. (2000). Measurement of the friction coefficient of the human skin in vivo: quantification of the cutaneous smoothness. *Colloids and surfaces B: Biointerfaces*, 19, 1-12.
- Australian Microscopy and Microanalysis Research Facility (2014). *Confocal Microscopy*. Retrieved February 3rd, 2014, from MyScope - training for advanced research: <http://www.ammrf.org.au/myscope/confocal/confocal/>

- Azadani, A. N., Chitsaz, S., Matthews, P. B., Jaussaud, N., Leung, J., Tsinman, T., et al. (2012). Comparison of mechanical properties of human ascending aorta and aortic sinuses. *The Annals of Thoracic Surgery*, 93, 87-94.
- Bader, D. L., & Bowker, P. (1983). Mechanical characteristics of skin and underlying tissues in vivo. *Biomaterials*, 4(4), 305-308.
- Barboriak, D. P., Padua, A. O., York, G. E., & Macfall, J. R. (2005). Creation of DICOM - Aware Applications Using ImageJ. *Journal of Digital Imaging*, 18(2), 91-99.
- Barel, A., Courage, W., & Clarys, P. (1995). Suction method for measurement of skin mechanical properties: the cutometer. In J. Serup, & G. B. Jemec, *Handbook of Non-invasive Methods and the Skin*. Boca Raton: CRC Press.
- Barton, J. K., Gossage, K. W., Xu, W., Ranger-Moore, J. R., Saboda, K., Brooks, C. A., et al. (2003). Investigating sun-damaged skin and actinic keratosis with optical coherence tomography: a pilot study. *Technology in Cancer Research & Treatment*, 2(6), 525-534.
- Barros, R. C., Van Kooten, T. G. & Veeregowda, D. H. (2015). Investigation of friction-induced damage to the pig cornea. *The Ocular Surface*, 13 (4), 315-320.
- Berillis, P. (2013). The role of collagen in the aorta's structure. *The Open Circulation and Vascular Journal*, 6, 1-8.
- Bloemen, M. C., Gerven, M. v., Wal, M. v., Verhaegen, P. D., & Middelkoop, E. (2011). An objective device for measuring surface roughness of skin and scars. *J. Am. Acad. Dermatol.*, 64(4), 706-715.
- Bostan, L. E., Taylor, Z. A., Carré, M. J., Macneil, S., Franklin, S. E., & Lewis, R. (2016). A comparison of friction behaviour for ex vivo human , tissue engineered and synthetic skin. *Tribology International*, 103, 487-495.
- Bostan, L. E., Noble, C., Smulders, N., Lewis, R., Carré, M. J., Franklin, S., Green, N. H. & Macneil, S. (2017). Measurement of friction-induced changes in pig aorta fibre organization by non-invasive imaging as a model for detecting the tissue response to endovascular catheters. *Biotribology*, 12, 24-32.
- Bowden, F. P., & Tabor, D. (1954). *Friction and Lubrication of Solids*. London: Oxford University Press.
- Brown, I. (1973). A scanning electron microscope study of the effects of uniaxial tension on human skin. *British Journal of Dermatology*, 89, 383-393.
- Byers, R. A., Tozer, G., Brown, N. J., & Matcher, S. J. (2016). High-resolution label-free vascular imaging using a commercial, clinically approved dermatological OCT scanner. In: *Proceedings of the International Society for Optics and Photonics*. San Francisco: SPIE.

- Carré, M. J., Tan, S. K., Mylon, P. T. & Lewis, R. (2017). Influence of medical gloves on fingerpad friction and feel. *Wear*, 376-377, 324-328.
- Changizi, M., Weber, R., Kotecha, R. & Palazzo, J. (2011). Are wet-induced wrinkled fingers printe rain treads?, *Brain, Behaviour and Evolution*, 77, 286-290.
- Childs, T. H., & Henson, B. (2007). Human tactile perception of screen printed surfaces: self report and contact mechanics experiments. *Proceedings of the Institution of Mechanical Engineers, Part J: Journal of Engineering Tribology*, 221(3), 427-441.
- Choudhury, N., Bouchot, O., Rouleau, L., Tremblay, D., Cartier, R., Butany, J., et al. (2009). Local mechanical and structural properties of healthy and diseased human ascending aorta tissue. *Cardiovascular Pathology*, 18, 83-91.
- Coleman, A. J., Richardson, T. J., Orchard, G., Uddin, A., Choi, M. J., & Lacy, K. E. (2013). Histological correlates of optical coherence tomography in non-melanoma skin cancer. *Skin Research and Technology*, 19(1), 10-19.
- Collins, J. A., Munoz, J.-V., Patel, T. R., Loukas, M., & Tubbs, R. S. (2014). The anatomy of the aging aorta. *Clinical Anatomy*, 27, 463-466.
- Collins, T. J. (2007). ImageJ for microscopy. *Biotechniques*, 43, 25-30.
- Comaish, S., & Bottoms, E. (1971). The skin and friction: derivations from Amontons' laws, and the effects of hydration and lubrication. *British Journal of Dermatology*, 84(37), 37-43.
- Cottenden, D. J. & Cottenden, A. M. (2013). A study of friction mechanisms between a surrogate skin (Lorica soft) and nonwoven fabrics. *Journal of the Mechanical Behaviour of Biomedical Materials*, 28, 410-426.
- Cua, A. B., Wilhelm, K.-P. & Maibach, H. I. (1990). Frictional properties of human skin: relation to age, sex and anatomical region, stratum corneum hydration and transepidermal water loss. *British Journal of Dermatology*, 123, 473-479.
- Daly, C. H. (1982). Biomechanical properties of dermis. *The Journal of Investigative Dermatology*, 79, 17-20.
- Dandekar, K., Raju, B. I., & Srinivasan, M. A. (2003). 3-D finite-element models of human and monkey fingertips to investigate the mechanics of tactile sense. *Journal of Biomechanical Engineering*, 125, 682-691.
- De Graaf, K. (1998). *Human Anatomy, fifth edition*. McGraw-Hill.
- Delalleau, A, Josse, G, Laggarde, J.-M., Zahouani, H., & Bergheau, J.-M. (2008). A nonlinear elastic behaviour to identify the mechanical parameters of human skin *in vivo*. *Skin Research and Technology*, 14, 152-164.

- Deleau, F., Mazuyer, D., & Koenen, A. (2009). Sliding friction at elastomer/glass contact: influences of the wetting conditions and instability analysis. *Tribology International*, 42, 149-159.
- Delhaye, B., Lefevre, P., & Thonnard, J.-L. (2014). Dynamics of fingertip contact during the onset of tangential slip. *Journal of The Royal Society Interface*, 11, 1-11.
- Delhaye, B., Barrea, A., Edin, B. B., Lefevre, P., & Thonnard, J.-L. (2016). Surface skin measurements of fingertip skin under shearing. *Journal of The Royal Society Interface*, 13(115), 1-11.
- Denk, W., Strickler, J. H., & Webb, W. W. (1990). Two-photon laser scanning fluorescence microscopy. *248*, 73-76.
- Derler, S., Gerhardt, L.-C., Lenz, A., Bertaux, E., & Hadad, M. (2009). Friction of human skin against smooth and rough glass as a function of the contact pressure. *Tribology International*, 42, 1565-1574.
- Derler, S. & Gerhardt, L.-C. (2012). Tribology of skin: Review and analysis of experimental results for the friction coefficient of human skin. *Tribology Letter*, 45, 1-27.
- Derler, S., Rossi, R. M. & Rotaru, G.-M. (2015). Understanding the variation of friction coefficients of human skin as a function of skin hydration and interfacial water films. *Proceeding IMechE Part J: J Engineering Tribology*, 229(3), 285-293.
- Deserno (n Lehmann), T. M., Handels, H., Maier-Hein (ne Fritzsche), K. H., Mersmann, S., Palm, C., Tolxdorff, T., Wagenknecht, G. & Wittenberg T. (2013). Viewpoints on Medical Image Processing: From Science to Application. *Current Medical Imaging Reviews*, 9, 79-88.
- Dinç, O. S., Ettles, C. M., Calabrese, S. J., & Scarton, H. A. (1991). Some parameters affecting tactile friction. *Journal of Tribology*, 113, 512-517.
- Diridollou, S., Patat, F., Gens., F., Vaillant, L., Black, D., Lagarde, J. M., et al. (2000). In vivo model of the mechanical properties of the human skin under suction. *Skin Research and Technology*, 6(4), 214-221.
- Dobrin, P. B., Baker, W. H., & Gley, W. C. (1984, April). Elastolytic and collagenolytic studies of arteries. Implications for the mechanical properties of aneurysms. *Archives of Surgery*, 119(4), 405-409.
- Dobrin, P., & Gley, W. (1985). Elastase, collagenase and the radial elastic properties of arteries. *Experientia*, 41(8), 1040-1042.
- Dowson, D. (1997). Tribology and the skin surface. In K.-P. Wilhelm, P. Elsner, E. Berardesca, & H. I. Maibach, *Bioengineering of the skin: skin surface imaging and analysis* (pp. 159-179). Boca Raton: CRC Press.

- Dowson, D., & Wright, V. (1973). Bio-tribology. In *Proceedings of the Conference on The Rheology of Lubrication, The Institute of Petroleum, The Institution of Mechanical Engineers, and the British Society of Rheology*, 81-88.
- Egawa, M., Oquiri, M., Kuwahara, T., & Takahashi, M. (2002). Effect of exposure of human skin to a dry environment. *Skin Research and Technology*, 8(4), 212-218.
- Elkhyat, A., Mac-Mary, S., & Humbert, P. (2009). Skin wettability and friction. In: Barel, A.O., Paye, M., Maibach, H.I. (eds.). *Handbook of Cosmetic Science and Technology* (Informa Healthcare, New York), 427–436.
- Enfield, J., Jonathan, E., & Leachy, M. (2011). In vivo imaging of the microcirculation of the volar forearm using correlation mapping optical coherence tomography (OCT). *Biomedical Optics Express*, 2(5), 1184-1193.
- Escoffier, C., Rigal, J. d., Rochefort, A., Vasselet, R., Leveque, J.-L., & Agache, P. G. (1989). Age-related mechanical properties of human skin: an in vivo study. *The Society for Investigative Dermatology*, 93(3), 353-357.
- Fercher, A. F. (2010). Optical coherence tomography - development, principles, applications. *Zeitschrift für Medizinische Physik*, 20(4), 251-276.
- Ferrara, A., Morganti, S., Totaro, P., Mazzola, A., & Auricchio, F. (2016). Human dilated ascending aorta: mechanical characterization via uniaxial tensile tests. *Journal of The Mechanical Behaviour of Biomedical Materials*, 53, 257-271.
- Genovese, K., Montes, A., Martinez, A., & Evans, S. I. (2015). Full-surface deformation measurement of anisotropic tissues under indentation. *Medical Engineering & Physics*, 37(5), 484-493.
- Gerhardt, L.-C., Strässle, V., Lenz, A., Spencer, N. D. & Derler, S. (2008). Influence of epidermal hydration on the friction of human skin against textiles. *Journal of The Royal Society Interface*, 5, 1317-1328.
- Gerhardt, L.-C., Schmidt, J., Sanz-Harrera, J. A., Baaijens, F. P., Ansari, T., Peters, G. W., et al. (2012). A novel method for visualising and quantifying through-plane skin layer deformations. *Journal of The Mechanical Behaviour of Biomedical Materials*, 14, 199-207.
- Gibb, L., & Matthews, D. (n.d.). *Two Photon Microscopy and Second Harmonic Generation*.
- Goldstein, D. J. (1969). The fluorescence of elastic fibers stained with Eosin and excited by visible light. *The Histochemical Journal*, 1, 187-198.
- Gorodetsky, R., Andriessen, A., Polyansky, I., & Vexler, A. (1999). Measurement of breast skin viscoelasticity and a pilot study on the potential radioprotective effect of a zinc-based cream. *Journal of Wound Care*, 8(10), 514-518.

- Grahame, R. (1969). Elasticity of human skin in vivo. A study of the physical properties of the skin in rheumatoid arthritis and the effect of cortocosteroids. *Annals of physical medicine, 10*(3), 130-136.
- Grant, R. A. (1966). Variations in the amino acid composition of aortic elastin from different species. *The British Journal of Experimental Pathology, 47*(2).
- Greenwood, J. A., & Tabor, D. (1958). The friction of hard sliders on lubricated rubber: the importance of deformation losses. *Proceedings of the Physical Society of London, 71*, 989-1001.
- Gundiah, N., Ratcliffe, M. B., & Pruitt, L. A. (2007). Determination of strain energy function for arterial elastin: experiments using histology and mechanical tests. *Journal of Biomechanics, 40*(3), 586-594.
- Han, H. Y., Shimada, A., & Kawamura, S. (1996). Analysis of friction on human fingers and design of artificial fingers. In *IEEE International Conference on Robotics and Automation, Minneapolis, Minnesota*, 3061-3066.
- Han, J., Nishiyama, S., Yamazaki, K., & Itoh, R. (2008). Ergonomic design of beverage can lift tabs based on numerical evaluations of fingertip discomfort. *Applied Ergonomics, 39*(2), 150-157.
- Hatze, H. (1974). The Meaning of the Term "Biomechanics". *Journal of Biomechanics, 7*, 189-190.
- Hendriks, B. H., Bierhoff, W. C., Horikx, J. J., Desjardins, A. E., Hezemans, C. A., 'T Hooft, G. W., et al. (2011). High-resolution resonant and nonresonant fiber-scanning confocal microscope. *Journal of Biomedical Optics, 16*(2), 1-8.
- Hendriks, F. M., Brokken, D., Oomens, C. W., Bader, D. L., & Baaijens, F. P. (2006). The relative contributions of different skin layers to the mechanical behaviour of human skin invivo using suction experiments. *Medical Engineering & Physics, 28*, 259-266.
- Holzapfel, G. A. & Gasser G. C. (2001). A viscoelastic model for fiber-reinforced composites at finite strains: Continuum basis, computational aspects and applications. *Computational Methods in Applied Mechanics and Engineering, 190*, 4379-4403
- Holzapfel, G. A. (2001). Biomechanics of soft tissue. In J. Lemaitre, *Handbook of material behaviour models 1st Edition* (pp. 1057-1071). Academic Press.
- Jacobi, U., Chen, M., Frankowski, G., Sinkgraven, R., HUnd, M., Rzany, B., et al. (2004). In vivo determination of skin surface topography using an optical 3D device. *Skin Research and Technology, 10*, 207-214.
- Jacquemoud, C., Bruyere-Garnier, K., & Coret, M. (2007). Methodology to determine failure characteristics of planar soft tissues using a dynamic tensile test. *Journal of Biomechanics, 40*, 468-475.

- Jerrams, S. J. (2004). Friction and adhesion in rigid surface indentation of nitrile rubber. *Materials and Design*, 26, 251-258.
- Johnson , S. A., Gorman, D. M., Adams, M. J., & Briscoe, B. J. (1993). The friction and lubrication of human stratum corneum . *Leeds-Lyon symposium on tribology*, Amsterdam: Elsevier Science Publishers, 663-672.
- Johnson, K. L. (1985). *Contact Mechanics*. Cambridge University Press.
- Johnson, K. O., & Phillips, J. R. (1981). Tactile spatial resolution. III. a continuum mechanics model of skin predicting mechanoreceptor responses to bars, edges, and gratings. *Journal of Neurophysiology*, 46, 1204-1225.
- Josse, G., George, J., & Black, D. (2011). Automatic measurement of epidermal thickness from optical coherence tomography images using a new algorithm. *Skin Research and Technology*, 17(3), 314-319.
- Kampf, G., & Ennen, J. (2006). Regular use of a hand cream can attenuate skin dryness and roughness caused by frequent hand washing. *BMC Dermatology*, 6, 1.
- Kao, A. P., Connelly, J. T., & Barber, A. H. (2016). 3D nanomechanical evaluations of dermal structures in skin. *Journal of the Mechanical Behavior of Biomedical Materials*, 57, 14-23.
- Kareklas, K., Nettle, D. & Smulders, T. V. (2013). Water-induced finger wrinkles improve handling of wet objects. *Biology Letter*, 9, 20120999.
- Kehtarnavaz, N., & Gamadia, M. (2006). *Real-Time Image and Video Processing: From Research to Reality*. Morgan & Claypool.
- Kim, J., Hong, J.-W., & Baek, S. (2013). Longitudinal differences in the mechanical properties of the thoracic aorta depend on circumferential regions. *Journal of Biomedical Materials Research*, 101A(5), 1525-1529.
- Kottner, J., Schario, M., Garcia Bartels, N., Pantchechnikova, E., Hillmann, K., & Blume-Peytavi, U. (2013). Comparison of two in vivo measurements for skin surface topography. *Skin Research Technology*, 19(2), 84-90.
- Kraus, M. F., Potsaid, B., Mayer, M. A., Bock, R., Baumann, B., Liu, J. J., et al. (2012). Motion correction in optical coherence tomography volumes on a per A-scan basis using orthogonal scan patterns. *Biomedical Optics Express*, 3(6), 1182-1199.
- Kuilenburg, J., Masen, M., & Van der Heide, E. (2013). The role of the skin microrelief in the contact behaviour of human skin: Contact between the human finger and regular surface textures. *Tribology International*, 65, 81–90.
- Kwiatkowska, M., Franklin, S. E., Hendriks, C. P., & Kwiatkoswki, K. (2009). Friction and deformation behaviour of human skin. *Wear*, 267, 1264-1273.

- Lamers, E., Kempen, T. v., Baaijens, F. P., Peters, G. W., & Oomens, C. W. (2013). Large amplitude oscillatory shear properties of human skin. *Journal of The Mechanical Behaviour of Biomedical Materials*, 28, 462-470.
- Lanir, Y., & Fung, Y. C. (1974). Two-dimensional mechanical properties of rabbit skin - II. Experimental Results. *Journal of Biomechanics*, 7, 171-182.
- Li, L., Mac-Mary, S., Marsaut, D., Sainthillier, J. M., Nouveau, S., Gharbi, T., et al. (2006). Age-related changes in skin topography and microcirculation. *Archives of Dermatological Research*, 297(9), 412-416.
- Lichtman, J. W. (1994). Confocal microscopy. *Scientific American*, 271(2), 40.
- Lichtman, J. W. (1994, August). Confocal Microscopy. *Scientific American*.
- Lillie, M. A., Shadwick, R. E., & Gosline, J. M. (2010). Mechanical anisotropy of inflated elastic tissue from the pig aorta. *Journal of Biomechanics*, 43(11), 2070-2078.
- Limbirt, G. & Kuhl, E. (2018). On skin microrelief and the emergence of expression micro-wrinkles. *Soft Matter*, 14 (8), 1292-1300.
- Lin H.-T., Hong T.-F. & Li W.-L. (2015). Grip performance affected by water-induced wrinkling of fingers. *Tribology Letter*, 58:38, 1-9.
- Liu, X. (2013). *Understanding the effect of skin mechanical properties on the friction of human finger pad*. The University of Sheffield, Mechanical Engineering. White Rose eTheses Online.
- Liu, X., Carré, M. J., Zhang, Q., Lu, Z., Matcher, S. J., & Lewis, R. (2017). Measuring contact area in a sliding human finger-pad contact. *Skin Research and Technology*, 24(1), 31-44.
- Liu, X., Gad, D., Lu, Z., Lewis, R., Carré, M. J., & Matcher, S. J. (2015). The contributions of skin structural properties to the friction of human finger-pads. *Proceeding IMechE Part J:J Engineering Tribology*, 229(3), 294-311.
- Liu, X., Lu, Z., Lewis, R., Carré, M. J., & Matcher, S. J. (2013). Feasibility of using optical coherence tomography to study the influence of skin structure on finger friction. *Tribology International*, 63, 34-44.
- Love, A. E. (1952). *A Treatise on the Mathematical Theory of Elasticity 4th Edition*. Cambridge: University Press.
- Luboz, V., Petrizelli, M., Bucki, M., Diot, B., Vuillerme, N. & Payan, Y. (2014). Biomechanical modelling to prevent ischial pressure ulcers. *Journal of Biomechanics*, 47, 2231-2236.

- Luther, N., Darvin, M. E., Sterry, W., Lademann, J., & Patzelt, A. (2012). Ethnic differences in skin physiology, hair follicle morphology and follicular penetration. *Skin Pharmacol Physiol*, 25, 182-191.
- Marcellier, H., Vescovo, P., Varchon, D., Vacher, P., & Humbert, P. (2001). Optical analysis of displacement and strain fields on human skin. *Skin Research and Technology*, 7, 246-253.
- Masters, B. R., So, P. T., & Gratton, E. (1997, June). Multiphoton excitation fluorescence microscopy and spectroscopy of in vivo human skin. *Biophysical Journal*, 72(6), 2405-2412.
- Megens, T. R., Egbrink, M. G., Cleutjens, J. P., Kuijpers, M. J., Schiffers, H. P., Merks, M., Slaaf, D. W., & van Zandvoort, M. A. M. J. (2007). Imaging collagen in Intact Viable Healthy and Atherosclerotic Arteries Using Fluorescently Labeled CNA35 and Two-Photon Laser Scanning Microscopy. *Molecular Imaging*, 6(4), 247-260.
- Minsky, M. (1988). Memoir on Inventing the Confocal Scanning Microscope. *10*, 128-138.
- Moore, D. F. (1972). *The friction and lubrication of elastomers*. New York: Pergamon Press Inc.
- Mossel, W. P., & Roosen, C. G. (1994). Friction and the skin. *Contemporary Ergonomics*, 1, 353-358.
- Nachman, M., & Franklin, S. E. (2016). Artificial skin model simulating dry and moist in vivo human skin friction and deformation behaviour. *Tribology International*, 97, 431-439.
- Neerken, S., Lucassen, G. W., Bisschop, M. A., Lenderink, E., & Nuijs, T. A. (2001). Characterization of age-related effects in human skin: a comparative study that applied confocal laser scanning microscopy and optical coherence tomography. *Journal of Biomedical Optics*, 9(2), 274-281.
- Nonomura, Y., Fujii, T., Arashi, Y., Miura, T., Maeno, T., Tahiro, K., et al. (2009). Tactile impression and friction of water on human skin. *Colloids Surf. B: Biointerface*, 69, 264-267.
- Obropta, E. W., & Newman, D. J. (2015). A comparison of human skin strain fields of the elbow joint for mechanical counter pressure space suit development. *2015 IEEE Aerospace Conference*.
- Pailler-Mattei, C., Bec, S., & Zahouani, H. (2008). In vivo measurements of the elastic mechanical properties of human skin by indentation test. *Medical Engineering and Physics*, 30(5), 599-606.
- Pawley, J. B. (1990). *Handbook of Biological Confocal Microscopy*. Plenum Press.

- Persson B. N. J. (2008). Capillary adhesion between elastic solids with randomly rough surfaces. *Journal of Physics: Condensed Matter*, 20, 1-11.
- Pomerantz, R., Zell, D., McKenzie, G., & Siegel, D. M. (2011). Optical coherence tomography used as a modality to delineate basal cell carcinoma prior to mohs micrographic surgery. *Case Reports in Dermatology*, 3(3), 212-218.
- Proksch, E., Brandner, J. M., & Jensen, J.-M. (2008). The skin: an indispensable barrier. *Experimental Dermatology*, 17, 1063-1072.
- Ramalho, A., Silva, C. L., & Thomas, T. R. (2005). On in-vivo skin topography metrology and replication techniques. *Journal of Physics: Conference Series*, 13, 325-329.
- Reu, P. (2012). Hidden components of 3D-DIC: interpolation and matching - part 2. *Experimental Techniques*, 36(3), 3-4.
- Reu, P. (2012). Hidden components of 3D-DIC: triangulation and post-processing - part 3. *Experimental Techniques*, 36(4), 3-5.
- Reu, P. (2012). Hidden components of DIC: calibration and shape function - part 1. *Experimental Techniques*, 36(2), 3-5.
- Reu, P. (2015). All about speckles: contrast. *Experimental Techniques*, 39, 1-2.
- Reu, P. (2015). All about speckles: speckle density. *Experimental Techniques*, 39, 1-2.
- Rigal, J. d., Escoffier, C., Querleux, B., Faivre, B., Agache, P., & Leveque, J.-L. (1989). Assessment of aging of the human skin by in vivo ultrasonic imaging. *The Society for Investigate Dermatology*, 93(5), 621-625.
- Ross, M. H., & Pawlina, W. (2006). *Histology: a text and atlas: with correlated cell and molecular biology*. Philadelphia, Pa. ; London: Lippincott Williams & Wilkins.
- Rossetti, F. C., Depieri, L. V., & Bently, M. V. (2013). Confocal Laser Scanning Microscopy as a Tool for the Investigation of Skin Drug Delivery Systems and Diagnosis of Skin Disorders. In N. Lagali, *Confocal Laser Microscopy - Principles and Applications in Medicine, Biology, and the Food Sciences*. InTech.
- Eliceiri, K. W. & Rueden, C. (2005). Tools for visualizing multidimensional images from living specimens. *Photochemistry and Photobiology*, 81(5), 1116-1122.
- Sáez P. & Zöllner A. M. (2017). Mechanics reveals the biological trigger in wrinkly fingers. *Annals of Biomedical Engineering*, 45 (4), 1039-1047.
- Sanders, R. (1973). Torsional elasticity of human skin in vivo. *Pflugers Archiv*, 342(3), 255-260.
- Sattler, E. C., Kastle, R., & Welzel, J. (2013). Optical coherence tomography in dermatology. *Journal of Biomedical Optics*, 18(6).

- Schatten, G., & Pawley, J. (1988). Advances in optical, confocal, and electron microscopic imaging for biomedical researchers. *Science*, 239(4841), G164.
- Schindelin, J., Arganda-Carreras, I., Frise, E., Kaynig, V., Longair, M., Pietzsch, T., Preibisch, S., Rueden, C., Saalfeld, S., Schmid, D., Tinevez, J. Y., White, D. J., Hartenstein, V., Eliceiri, K., Tomancak, P. & Cardona, A. (2012). Fiji: an open-source platform for biological-image analysis. *Nature Methods*, 9(7), 676-682.
- Shier, D., Butler, J., & Lewis, R. (2015). *Hole's Human Anatomy and Physiology 128th edition*. McGraw-Hill.
- Silver, F. H., Freeman J. W. & DeVore D. (2001). Viscoelastic properties of human skin and processed dermis. *Skin Research and Technology*, 7, 18-23.
- Stein, W. H., & Miller, Jr., E. G. (1938). The Composition of Elastin. *The Journal of Biological Chemistry*, 125, 599-614.
- Suzuki N., Kiba S., Kamachi Y., Miyamoto N. & Yamauchi Y. (2012). Unusual reinforcement of silicone rubber compounds containing mesoporous silica particles as inorganic fillers. *Physics Chemistry Chemistry Physics*, 14, 3400-3407.
- Tasron, D. N. (2013). *Understanding the issues related to maintaining foot health within an in-shoe environment*. Ph.D. Thesis, Dept. Mech. Eng., University of Sheffield.
- Tomlinson, S. E. (2009). *Understanding the friction mechanisms between the human finger and contacting surfaces*. Ph.D. Thesis, Dept. Mech. Eng., University of Sheffield.
- Tomlinson, S. E., Carré, M. J., Lewis, R., & Franklin, S. E. (2011). Human finger contact with small, triangular ridged surfaces. *Wear*, 271(9-10), 2346-2353.
- Tsamis A., Krawiec J. T. & Vorp D. A. (2013). Elastin and collagen fibre microstructure of the human aorta in ageing and disease: a review. *Journal of the Royal Society Interface*, 10, 1-22.
- Van De Graaff, K. M. (1998). *Concepts of Human Anatomy & Physiology Fifth Edition*. McGraw-Hill.
- Veijgen, N. K., Masen, M. A. & van der Heide, E. (2013). Relating friction on the human skin to the hydration and temperature of the skin. *Tribology Letter*, 49, 251-262.
- Waheed, A., Rao, K. S., & Gupta, P. D. (2000). Mechanism of Dye Binding in the Protein Assay Using Eosin Dyes. *Analytical Biochemistry*, 287, 73-79.
- Wang S., Chen X., Liu S., Zhu F. & Liu X. (2016). Estimation of homogenized Young's modulus of silicone /phosphor composite considering random dispersion and size variation of phosphor particles. *Journal of Composite Materials*, 50 (14), 1981-1988.

- White, J. G., Amos, W. B., & Fordham, M. (1987). An evaluation of confocal versus conventional imaging of biological structures by fluorescence light microscopy. *The Journal of Cell Biology*, *105*(1), 41-48.
- Zafar, H., Enfield, J., O'Connell, M.L., Ramsay, B., Lynch, M., Leahy, M.J., 2014. Assessment of psoriatic plaque in vivo with correlation mapping optical coherence tomography. *Skin Res. Technol.*, *20* (2), 141–146.
- Zeeman, R., Dijkstra, P. J., van Wachem, P. B., Luyn, M. J., Hendriks, M., Cahalan, P. T., et al. (1970). Cross-linking and modification of porcine aortic heart valves. In R. Zeeman, *Cross-linking of Collagen-Based Materials*. Medtronic Bakken Research Center B.V. Maastricht, The Netherlands.
- Zhang, Y., Wu, G., Wei, H., Guo, Z., Yang, H., He, Y., Xie, S., 2014. Continuous non-invasive monitoring of changes in human skin optical properties during oral intake of different sugars with optical coherence tomography. *Biomed. Opt. Express*, *5* (4), 990–999.

Appendix A: Derivation of the theoretical strain model

Love (1952) proposed that the three axial elastic displacement at any point, as shown in Figure A-1, can be described below using the potential functions defined in equation A-4, equation A-6, equation A-7 and equation A-8.

$$u_x = \frac{1}{4\pi G} + \left\{ 2 \frac{\partial F}{\partial z} - \frac{\partial H}{\partial x} + 2\nu \frac{\partial \psi_1}{\partial x} - z \frac{\partial \psi}{\partial x} \right\} \quad \text{Equation A-1}$$

$$u_y = \frac{1}{4\pi G} + \left\{ 2 \frac{\partial G}{\partial z} - \frac{\partial H}{\partial y} + 2\nu \frac{\partial \psi_1}{\partial y} - z \frac{\partial \psi}{\partial y} \right\} \quad \text{Equation A-2}$$

$$u_z = \frac{1}{4\pi G} + \left\{ \frac{\partial H}{\partial z} + (1 - 2\nu)\psi - z \frac{\partial \psi}{\partial z} \right\} \quad \text{Equation A-3}$$

$$\psi_1 = \frac{\partial F_1}{\partial x} + \frac{\partial G_1}{\partial y} + \frac{\partial H_1}{\partial z} \quad \text{Equation A-4}$$

$$\psi = \frac{\partial \psi_1}{\partial x} = \frac{\partial F}{\partial x} + \frac{\partial G}{\partial y} + \frac{\partial H}{\partial z} \quad \text{Equation A-5}$$

$$F = \frac{\partial F_1}{\partial z} = \int_S \int q_x(\xi, \eta) \cdot \ln(\rho + z) \, d\xi d\eta \quad \text{Equation A-6}$$

$$G = \frac{\partial G_1}{\partial z} = \int_S \int q_y(\xi, \eta) \cdot \ln(\rho + z) \, d\xi d\eta \quad \text{Equation A-7}$$

$$H = \frac{\partial H_1}{\partial z} = \int_S \int p(\xi, \eta) \cdot \ln(\rho + z) \, d\xi d\eta \quad \text{Equation A-8}$$

$$F_1 = \iint_S q_x(\xi, \eta) \cdot \Omega \, d\xi d\eta \quad \text{Equation A-9}$$

$$G_1 = \iint_S q_y(\xi, \eta) \cdot \Omega \, d\xi d\eta \quad \text{Equation A-10}$$

$$H_1 = \iint_S p(\xi, \eta) \cdot \Omega \, d\xi d\eta \quad \text{Equation A-11}$$

$$\Omega = z \cdot \ln(\rho + z) - \rho \quad \text{Equation A-12}$$

$$\rho^2 = (\xi - x)^2 + (\eta - y)^2 + z^2 \quad \text{Equation A-13}$$

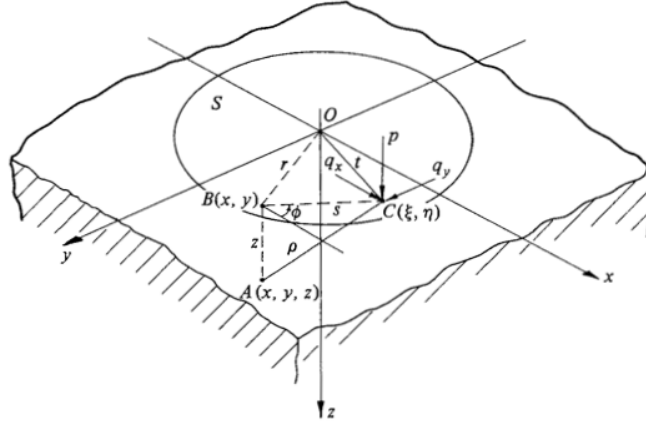


Figure A-1, Illustration of tractions on the circular contact region (Johnson, 2004)

To simulate a smooth homogenous silicone hemi-sphere in contact with a smooth rigid plate, only the tangential traction $q_y(\xi, \eta)$ acting over loaded area S is investigated, so the traction $q_x(\xi, \eta)$ and pressure $p(\xi, \eta)$ are 0.

$$F_1 = H_1 = F = H = 0 \quad \text{Equation A-14}$$

$$\psi_1 = \frac{\partial G_1}{\partial y} \quad \text{Equation A-15}$$

$$\psi = \frac{\partial^2 G_1}{\partial y \partial z} \quad \text{Equation A-16}$$

$$u_x = \frac{1}{4\pi G} + \left\{ 2\nu \frac{\partial^2 G_1}{\partial x \partial y} - z \frac{\partial^3 G_1}{\partial x \partial y \partial z} \right\} \quad \text{Equation A-17}$$

$$u_y = \frac{1}{4\pi G} + \left\{ 2 \frac{\partial^2 G_1}{\partial z^2} + 2\nu \frac{\partial^2 G_1}{\partial y^2} - z \frac{\partial^3 G_1}{\partial y^2 \partial z} \right\} \quad \text{Equation A-18}$$

$$u_z = \frac{1}{4\pi G} + \left\{ (1 - 2\nu) \frac{\partial^2 G_1}{\partial y \partial z} - z \frac{\partial^3 G_1}{\partial y \partial z^2} \right\} \quad \text{Equation A-19}$$

Differentiate G_1 accordingly

$$G_1 = \iint_S q_y(\xi, \eta) \cdot \{z \cdot \ln(\rho + z) - \rho\} d\xi d\eta \quad \text{Equation A-20}$$

$$u_x = \frac{1}{4\pi G} \iint_S q_y(\xi, \eta) \cdot \left\{ \frac{(\xi-x)(\eta-y)}{\rho^3} - (1-2\nu) \frac{(\xi-x)(\eta-y)}{\rho(\rho+z)^2} \right\} d\xi d\eta \quad \text{Equation A-21}$$

$$u_y = \frac{1}{4\pi G} \iint_S q_y(\xi, \eta) \cdot \left\{ \frac{1}{\rho} + \frac{1-2\nu}{\rho+z} + \frac{(\xi-y)^2}{\rho^3} - \frac{(1-2\nu)(\xi-y)^2}{\rho(\rho+z)^2} \right\} d\xi d\eta \quad \text{Equation A-22}$$

$$u_z = \frac{1}{4\pi G} \iint_S q_y(\xi, \eta) \cdot \left\{ \frac{(\xi-y)z}{\rho^3} - \frac{(1-2\nu)(\xi-y)}{\rho(\rho+z)} \right\} d\xi d\eta \quad \text{Equation A-23}$$

To investigate the surface condition on the contact surface, z is equal to 0. At this point, only u_x and u_y are focused

$$\bar{u}_x = \frac{1}{4\pi G} \iint_S q_y(\xi, \eta) \cdot \left\{ 2\nu \frac{(\xi-x)(\eta-y)}{\rho^3} \right\} d\xi d\eta \quad \text{Equation A-24}$$

$$\bar{u}_y = \frac{1}{4\pi G} \iint_S q_y(\xi, \eta) \cdot \left\{ \frac{1-\nu}{\rho} + \frac{\nu(\xi-y)^2}{\rho^3} \right\} d\xi d\eta \quad \text{Equation A-25}$$

The surface traction profile was as described below

$$q_x(x, y) = q_0 \left(1 - \frac{x^2+y^2}{a^2} \right)^{1/2} \quad \text{Equation A-26}$$

$$q_0 = \frac{3\mu P}{2\pi a^2} \quad \text{Equation A-27}$$

Further integrate to the area S (within the circle)

$$\bar{u}_x = \frac{\pi q_0}{32Ga} \cdot 2\nu xy \quad \text{Equation A-28}$$

$$\bar{u}_y = \frac{\pi q_0}{32Ga} \cdot \{4(2-\nu)a^2 - (4-3\nu)y^2 - (4-\nu)x^2\} \quad \text{Equation A-29}$$

Green-Lagrange strain as defined below,

$$E_{xx} = \frac{\partial u_x}{\partial x} + 0.5 \cdot \left[\left(\frac{\partial u_x}{\partial x} \right)^2 + \left(\frac{\partial u_y}{\partial x} \right)^2 \right] \quad \text{Equation A-30}$$

$$E_{yy} = \frac{\partial u_y}{\partial y} + 0.5 \cdot \left[\left(\frac{\partial u_x}{\partial y} \right)^2 + \left(\frac{\partial u_y}{\partial y} \right)^2 \right] \quad \text{Equation A-31}$$

$$E_{xy} = 0.5 \cdot \left[\frac{\partial u_x}{\partial y} + \frac{\partial u_y}{\partial x} \right] + 0.5 \cdot \left[\frac{\partial u_x}{\partial x} \cdot \frac{\partial u_x}{\partial y} + \frac{\partial u_y}{\partial x} \cdot \frac{\partial u_y}{\partial y} \right] \quad \text{Equation A-32}$$

Substitute the differentiation into Green-Lagrange strain

$$E_{xx} = \frac{\pi q_o}{32Ga} \cdot \left\{ 2vy + 0.5 \cdot \frac{\pi q_o}{32Ga} \cdot [4v^2y^2 + 4x^2(4-v)^2] \right\} \quad \text{Equation A-33}$$

$$E_{yy} = \frac{\pi q_o}{32Ga} \cdot \left\{ -2(4-3v)y + 0.5 \cdot \frac{\pi q_o}{32Ga} \cdot [4y^2(4-3v)^2 + 4v^2x^2] \right\} \quad \text{Equation A-34}$$

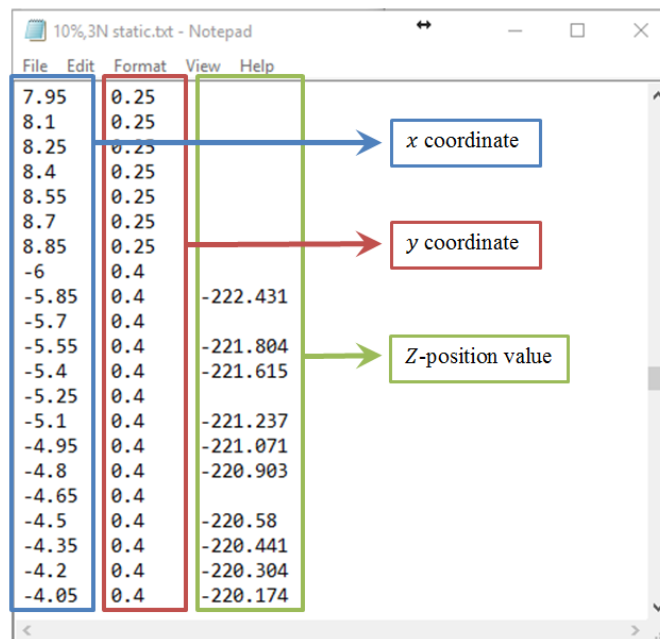
$$E_{xy} = 0.5 \cdot \frac{\pi q_o}{32Ga} \cdot \left\{ 4vx - 8x + \frac{\pi q_o}{32Ga} \cdot [(4-3v)(4-v)4xy + 4v^2xy] \right\} \quad \text{Equation A-35}$$

Appendix B: Measuring the apparent contact area from 3D-DIC data

Firstly, a “.txt” file was saved from the VIC-3D software that showed the x, y coordinates of the finger pad or the silicone hemi-sphere and their respective Z-position value, as shown in Figure B-1. The three columns in the figure were comprised of 100 slices of cross sectional data in one silicone hemi-sphere at a specific time point. In this example, the data was obtained when the silicone hemi-sphere was in the static state.

Then, the “.txt” file was imported into Matlab as a “numerical matrix” with a variable named as “t”, as shown in Figure B-2. It is important to replace the blank cells in the variable with “0” value.

The Matlab script file 1 (shown in this section) was then used to separate the whole column of x, y, z data (10000×3) into 100 cross sectional slices of x, y, z data (100×3). Then, another Matlab scrip file named “start_finish” was used to find the 2 boundary points from each cross section, as shown in Figure B-3. The boundary points were then plotted in a new excel file and an elliptical equation of best fit was used to describe the size of the apparent area of the silicone hemi-sphere.



x coordinate	y coordinate	Z-position value
7.95	0.25	
8.1	0.25	
8.25	0.25	
8.4	0.25	
8.55	0.25	
8.7	0.25	
8.85	0.25	
-6	0.4	
-5.85	0.4	-222.431
-5.7	0.4	
-5.55	0.4	-221.804
-5.4	0.4	-221.615
-5.25	0.4	
-5.1	0.4	-221.237
-4.95	0.4	-221.071
-4.8	0.4	-220.903
-4.65	0.4	
-4.5	0.4	-220.58
-4.35	0.4	-220.441
-4.2	0.4	-220.304
-4.05	0.4	-220.174

Figure B-1, a “.txt” file that has the three axial coordinates for the shape of a silicone hemi-sphere

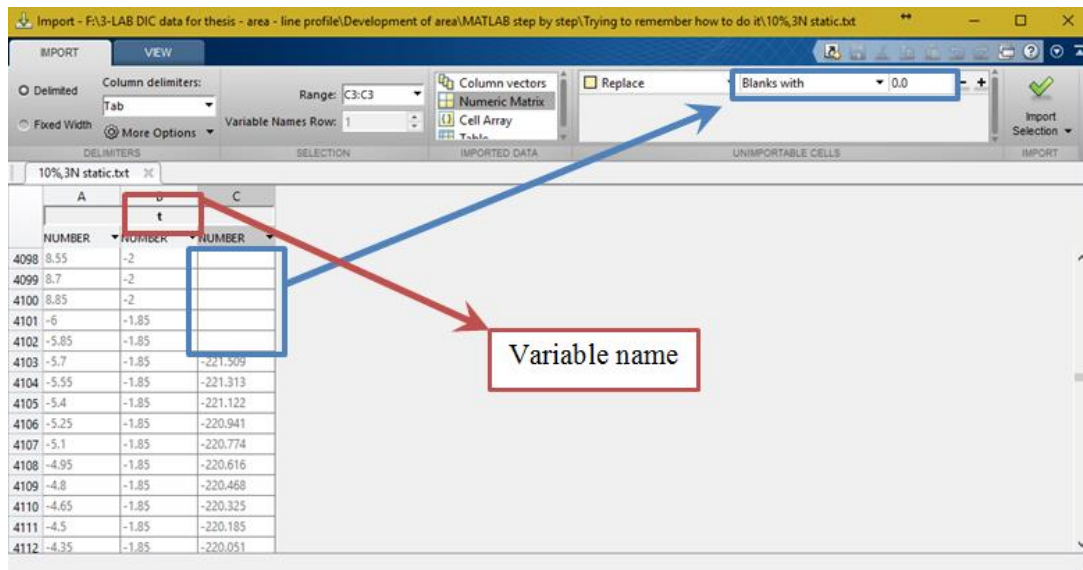


Figure B-2, Importing ".txt" file into Matlab

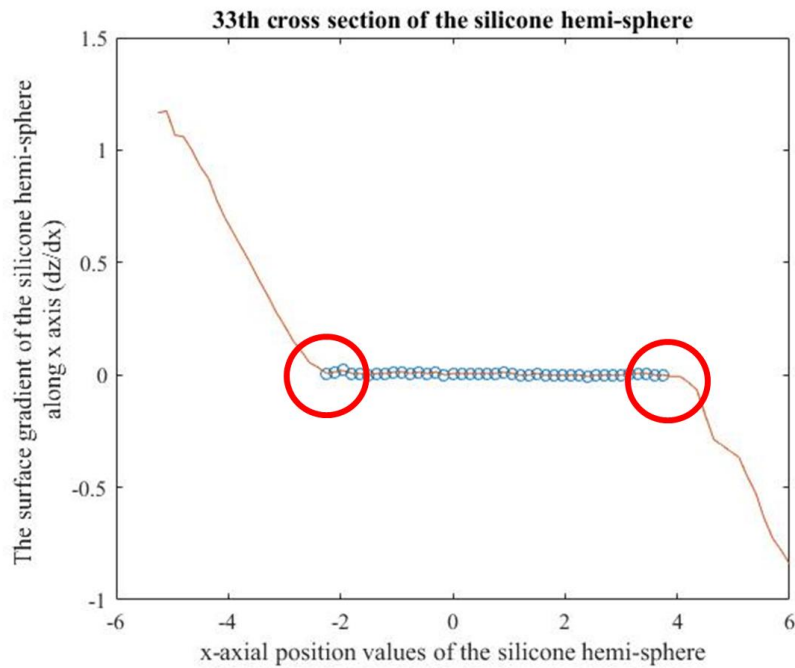


Figure B-3, The process of finding the 2 boundary points from the 33th cross section of the silicone hemi-sphere

Matlab script file 1: "code_image_z1.m"

```

l = length(t)
count = l/100; % 100 refers to how many data points per column
for i = 1:count
    new(:, :, i) = t( ((i-1) *100 + 1) : (i*100) , : );
end

```

```
save('S10_3_dynamic','new')
```

Matlab script file 2: “start_finish”

```
clear
clc

for count_o = 1:100 % 1:100 -> start at 30th fig and finish at 100th
    hold off

    load S10_3_dynamic;
    count2 = [];
    new1 = new(:, :, count_o);
    new1 = [new1(:, 1), new1(:, 3)];

    i1 = 1;
    for i = 1:length(new1)
        if new1(i, 2) == 0
            count2 (i1) = i;
            i1 = i1+1;
        end
    end
    new1(count2, :) = [];

    new_3 = sortrows(new1, 1);

    new_4 = diff(new_3(:, 2)) ./ diff(new_3(:, 1));

    count3 = 1000;
    count2 = 1;

    for i3 = 1:length(new_4)
        if isinf(new_4(i3))
            count3(count2) = i3;
            count2 = count2+1;
        end
    end
    new_5 = [new_3(1:end-1, 1), new_4, new_3(1:end-1, 2)];

    if count3 == 1000
        count7 = 1;
    else
        new_5(count3, :) = [];
    end

    count6 = 1000;
    count2 = 1;
    for i3 = 1:length(new_5)
        if isnan(new_5(i3, 2))
            count6(count2) = i3;
            count2 = count2+1;
        end
    end
    if count6 == 1000
        count8 = 1;
    else
        new_5(count6, :) = [];
    end
end
```



```

t = new_5(:,1);
shear = new_5(:,2);

samplingfreq = 1/mean(diff(t)); % calculate the sampling frequency

cutoff_freq = 0.5; % input your cut off frequency
[b a] = butter(2,cutoff_freq/samplingfreq*2); % butterworth filter
shear_fil = filtfilt(b,a,shear); % define the filtered data

plot(t,shear_fil)

shear_fill1 = diff(shear_fil)./diff(t);

for i6 = 1:length(t)
    if abs(shear_fill1(i6)) < 0.1
        start_point = i6;
        break
    end
end

for i6 = 1:length(t)
    i7 = length(t) - i6;
    if abs(shear_fill1(i7)) < 0.1
        end_point = i7;
        break
    end
end

plot(t(start_point:end_point),shear(start_point:end_point),'o')
hold on
plot(t,shear)
title(num2str(count_o))
pause

start(:,count_o) = [t(start_point) new_5(start_point,3)];
finish(:,count_o) = [t(end_point) new_5(end_point,3)];
end

```

Appendix C: Strain line profile of the finger pads

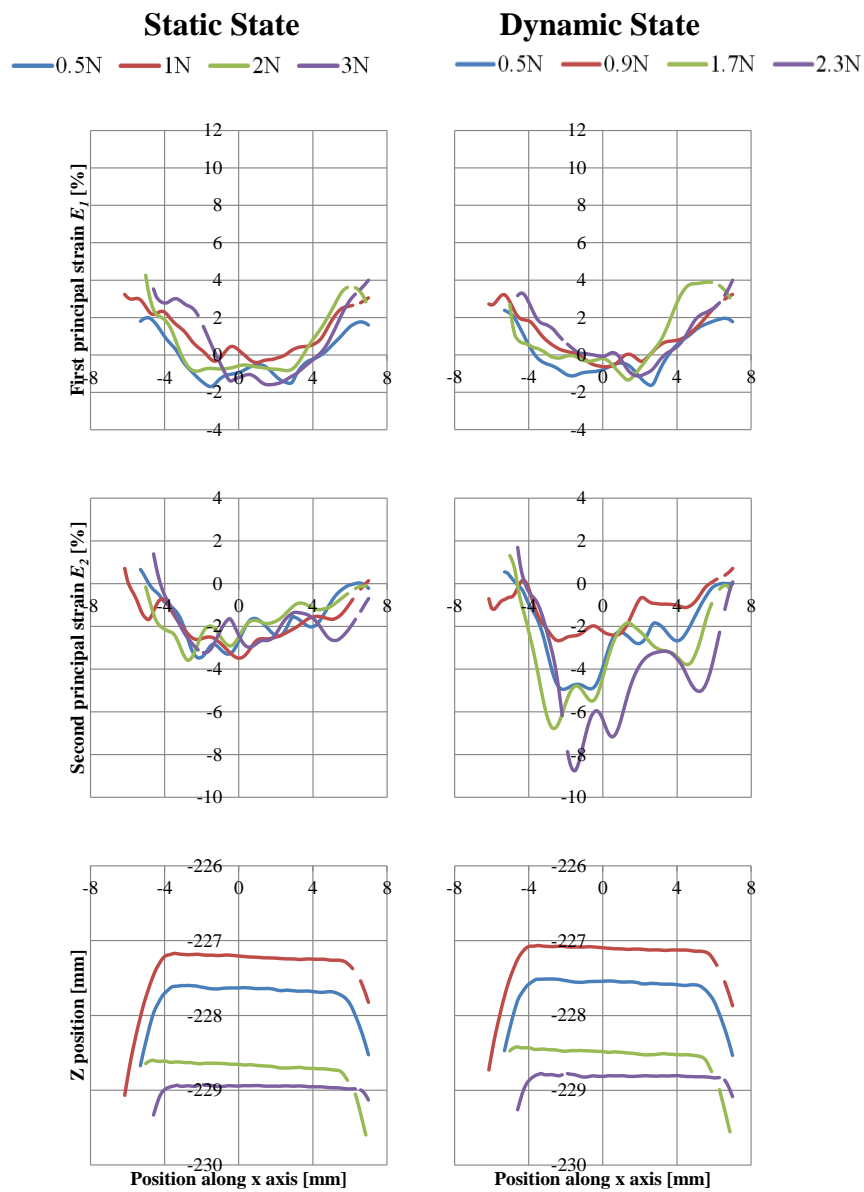


Figure C-1, Surface strains of the dry finger pad along x axis

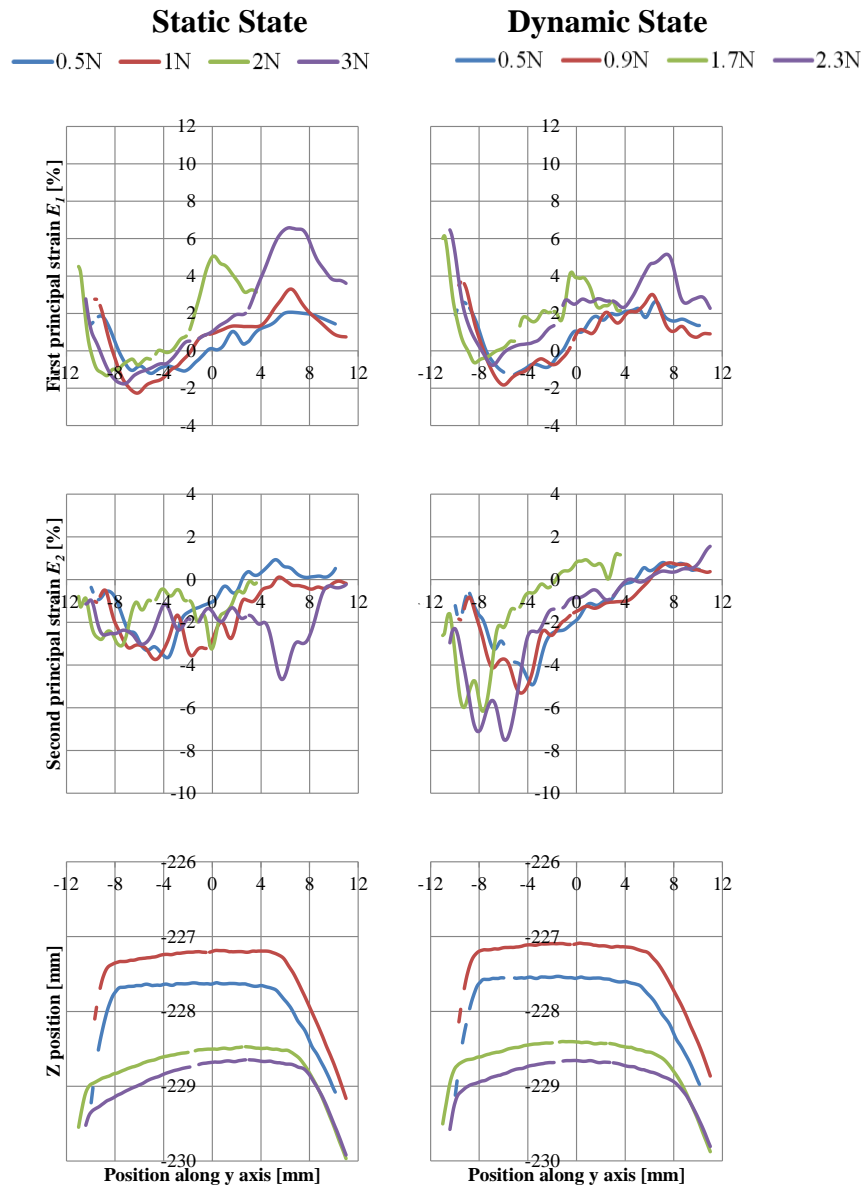


Figure C-2, Surface strains of the dry finger pad along y axis

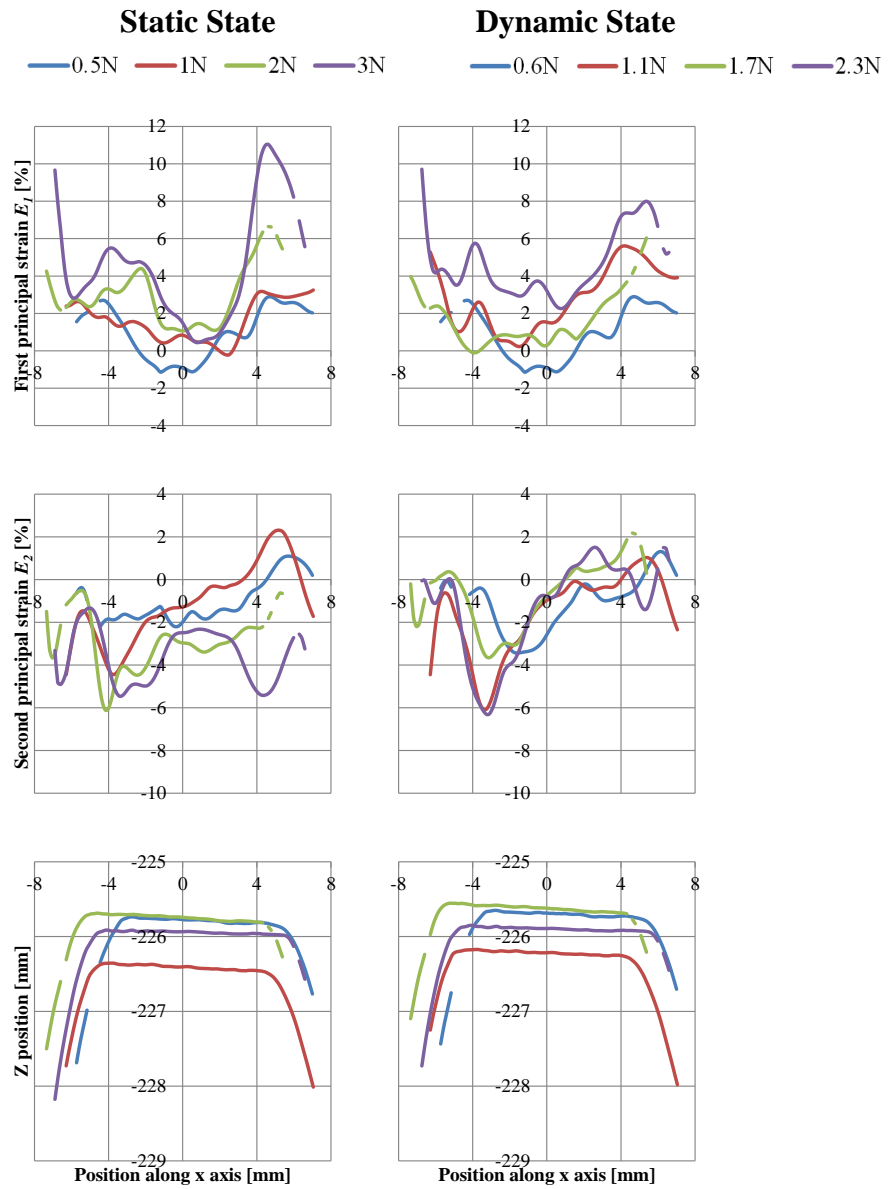


Figure C-3, Surface strains of the moist finger pad along x axis

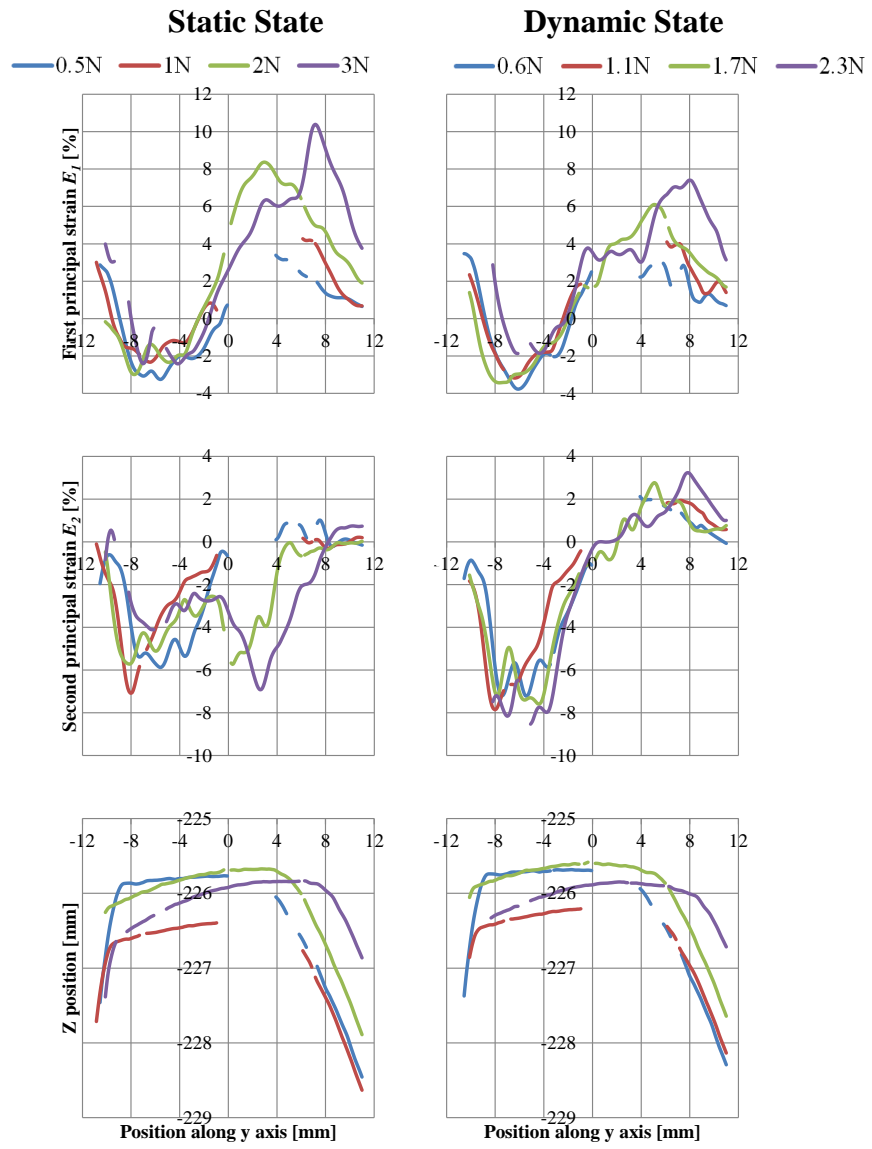


Figure C-4, Surface strains of the moist finger pad along y axis

Appendix D: The moisture levels of the finger pads at different tests

Table D-1, Moisture level of the natural finger pad during stiffness test

Natural finger pad	Moisture level [AU]
Before experiment	38.2±5.7
After experiment	46±8.7

Table D-2, Moisture level of the soaked finger pad during stiffness test

Soaked finger pad	Moisture level [AU]
Before treated	46.8±7.3
After treated	56.8±13.3
Before experiment	30.6±3.1
After experiment	42.6±3.3

Table D-3, Moisture level of the natural finger pad during 3D-DIC sliding experiment

Natural finger pad		Moisture level [AU]
0.5N	Before experiment	17.4±1.7
	After experiment	18.2±3.1
1N	Before experiment	15.6±1.5
	After experiment	16.2±3.2
2N	Before experiment	14.8±1.3
	After experiment	17.8±2.2
3N	Before experiment	17.8±1.8
	After experiment	17.6±3.4

Table D-4, Moisture level of the soaked finger pad during 3D-DIC sliding experiment

Soaked finger pad		Moisture level [AU]
0.5N	Before water application	44.8±4.3
	After water application	26.0±2.9
	Before painting	25.0±5.6
	After painting	20.8±5.4
	Before experiment	25.0±4.9
	After experiment	28.0±6.4
1N	Before water application	34.4±6.2
	After water application	26.4±3.0
	Before painting	26.6±3.6
	After painting	19.8±6.0
	Before experiment	22.8±4.6
	After experiment	25.2±5.9
2N	Before water application	38.4±1.8
	After water application	31.0±4.1
	Before painting	25.2±4.4
	After painting	17.8±1.8
	Before experiment	16.4±4.8
	After experiment	16.0±2.5
3N	Before water application	31.8±5.3
	After water application	29.2±2.7
	Before painting	19.6±2.4
	After painting	14.2±2.0
	Before experiment	15.2±3.3
	After experiment	18.8±4.6

Table D-5, Moisture level of the natural finger pad during OCT sliding experiment

Natural finger pad		Moisture level [AU]	
		Position 1	Position 2
0.5N	Before experiment	37.4±3.5	34.2±2.4
	After experiment	40.4±5.1	44.4±3.8
1N	Before experiment	40.4±4.1	32.4±2.3
	After experiment	44.0±5.7	41.8±7.0
2N	Before experiment	36.6±2.3	36.8±4.8
	After experiment	43.2±6.0	45.4±5.7
3N	Before experiment	39.2±4.8	44.0±3.7
	After experiment	48.2±6.7	44.8±7.2

Table D-6, Moisture level of the soaked finger pad during OCT sliding experiment

Soaked finger pad		Moisture level [AU]	
		Position 1	Position 2
0.5N	Before water application	42.2±3.6	27.6±1.1
	After water application	46.0±9.4	40.6±9.3
	Before experiment	23.6±1.8	23.8±4.3
	After experiment	31.0±4.8	24.2±2.2
1N	Before water application	33.8±4.3	24.6±3.0
	After water application	32.2±3.7	47.6±8.6
	Before experiment	23.4±2.6	25.6±2.5
	After experiment	27.4±1.3	27.4±3.2
2N	Before water application	33.0±3.4	25.4±1.7
	After water application	41.8±8.1	41.0±3.9
	Before experiment	24.0±1.9	29.0±1.4
	After experiment	29.4±2.6	34.6±4.5
3N	Before water application	28.6±2.1	27.6±2.5
	After water application	43.2±7.4	36.4±5.4
	Before experiment	21.8±2.4	30.2±3.1
	After experiment	30.2±4.4	31.8±4.1

Appendix E: Roughness profiles of the finger pads

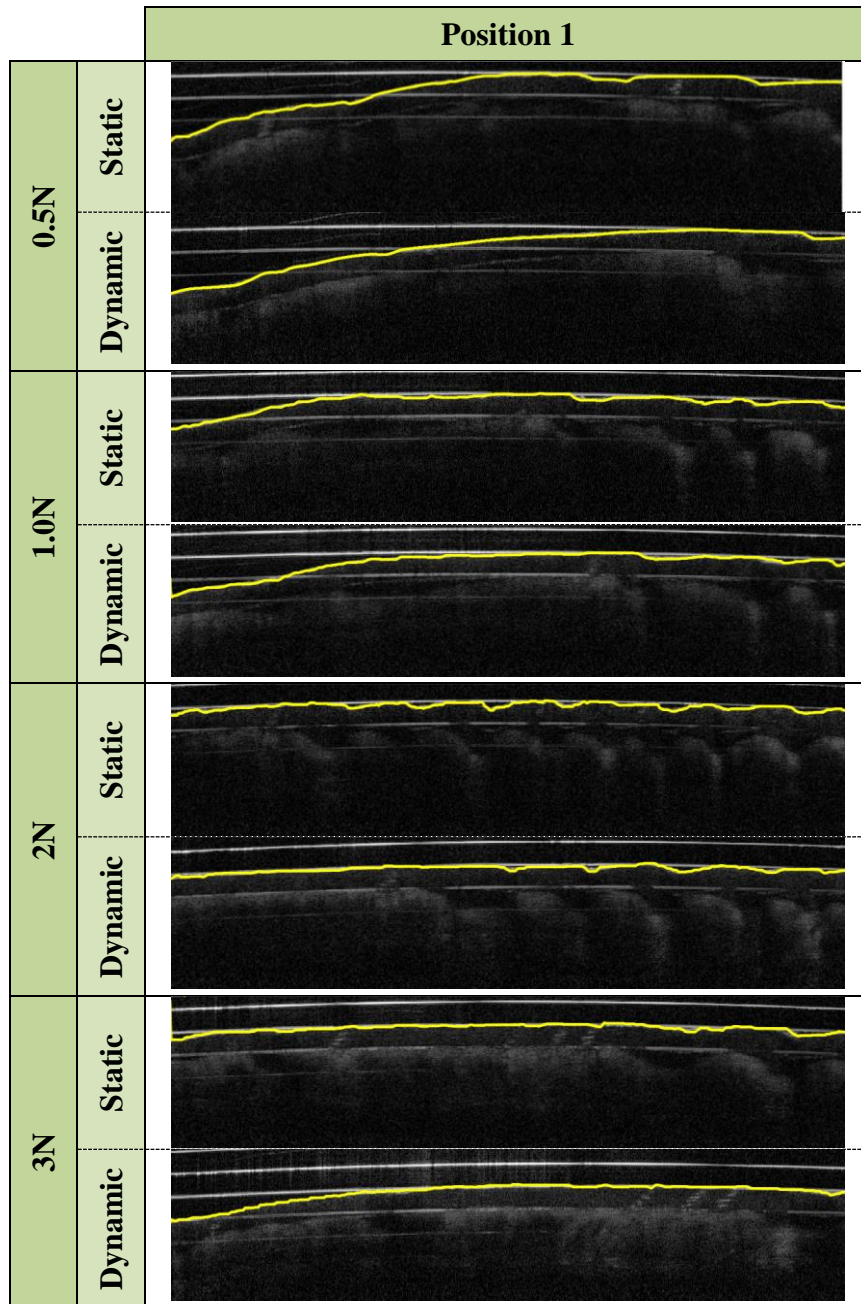


Figure E-1, OCT images of position 1 of the natural finger pad

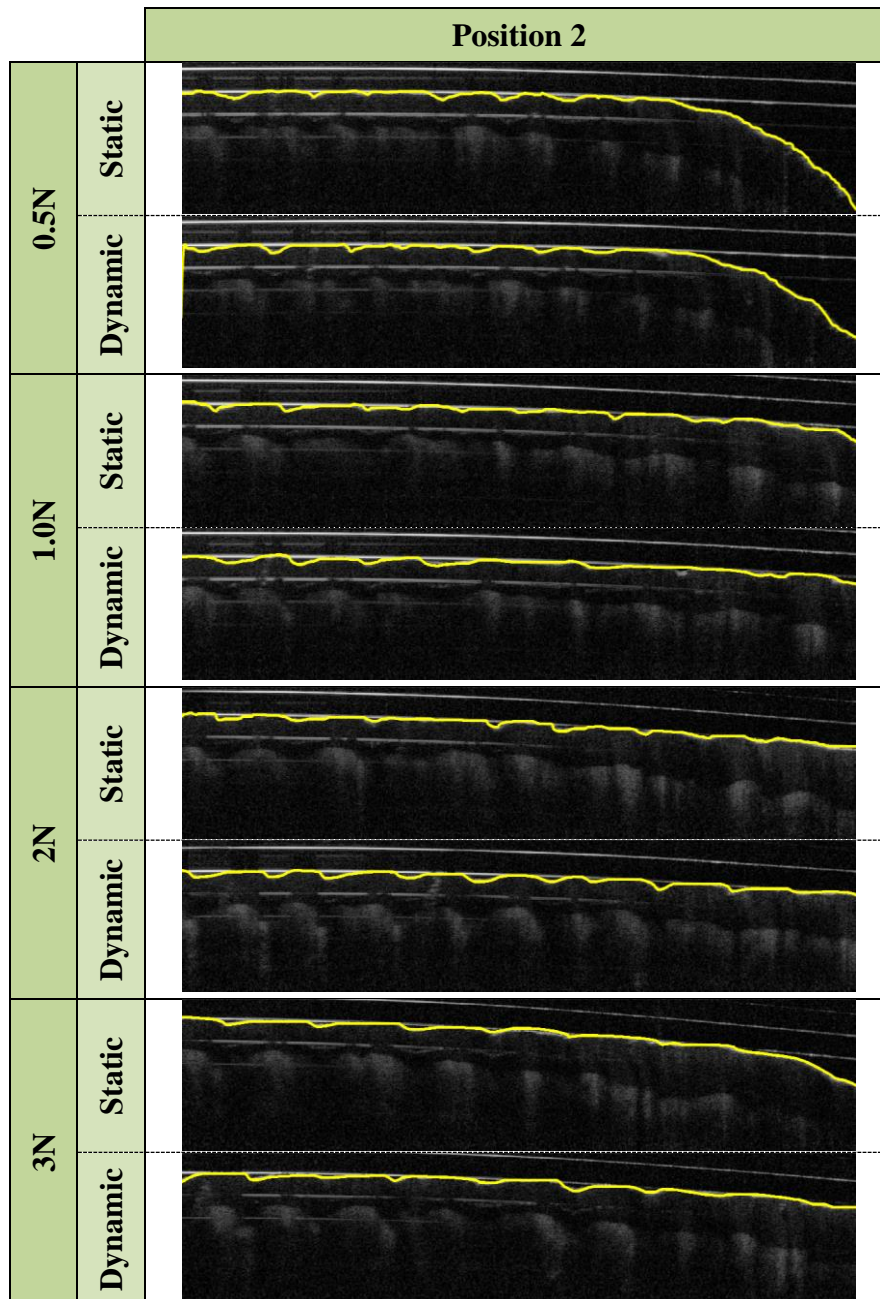


Figure E-2, OCT images of position 1 of the natural finger pad

Table E-1, The roughness of the position 1 and position 2 of natural finger pad

			Ra [μm]		Rz [μm]	
			Position 1	Position 2	Position 1	Position 2
Normal load	0.5 N	Static	4.07±0.32	7.84±0.39	13.65±0.92	26.64±1.86
		Dynamic	2.28±0.04	7.64±0.52	9.37±0.67	26.17±1.00
	1N	Static	3.11±0.31	2.90±0.12	12.77±0.67	14.39±0.45
		Dynamic	2.60±0.33	3.44±0.11	10.52±0.60	14.55±1.05
	2N	Static	3.33±0.14	2.91±0.20	14.58±0.93	13.18±1.19
		Dynamic	2.29±0.21	3.55±0.30	9.92±0.73	14.91±0.21
	3N	Static	2.07±0.32	3.76±0.10	8.81±1.59	14.68±0.61
		Dynamic	1.54±0.15	3.12±0.16	8.04±1.07	13.21±0.62

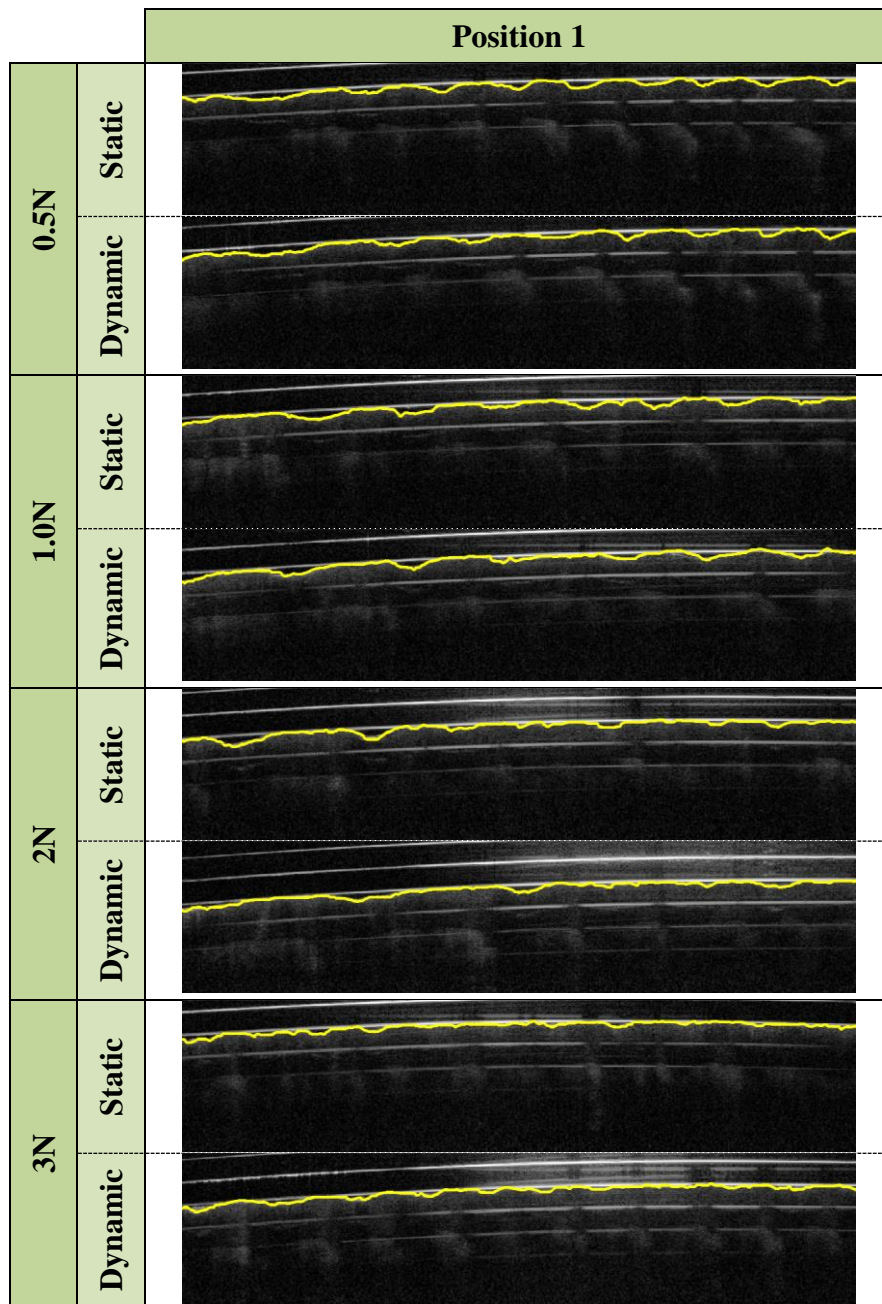


Figure E-3, OCT images of position 1 of the soaked finger pad

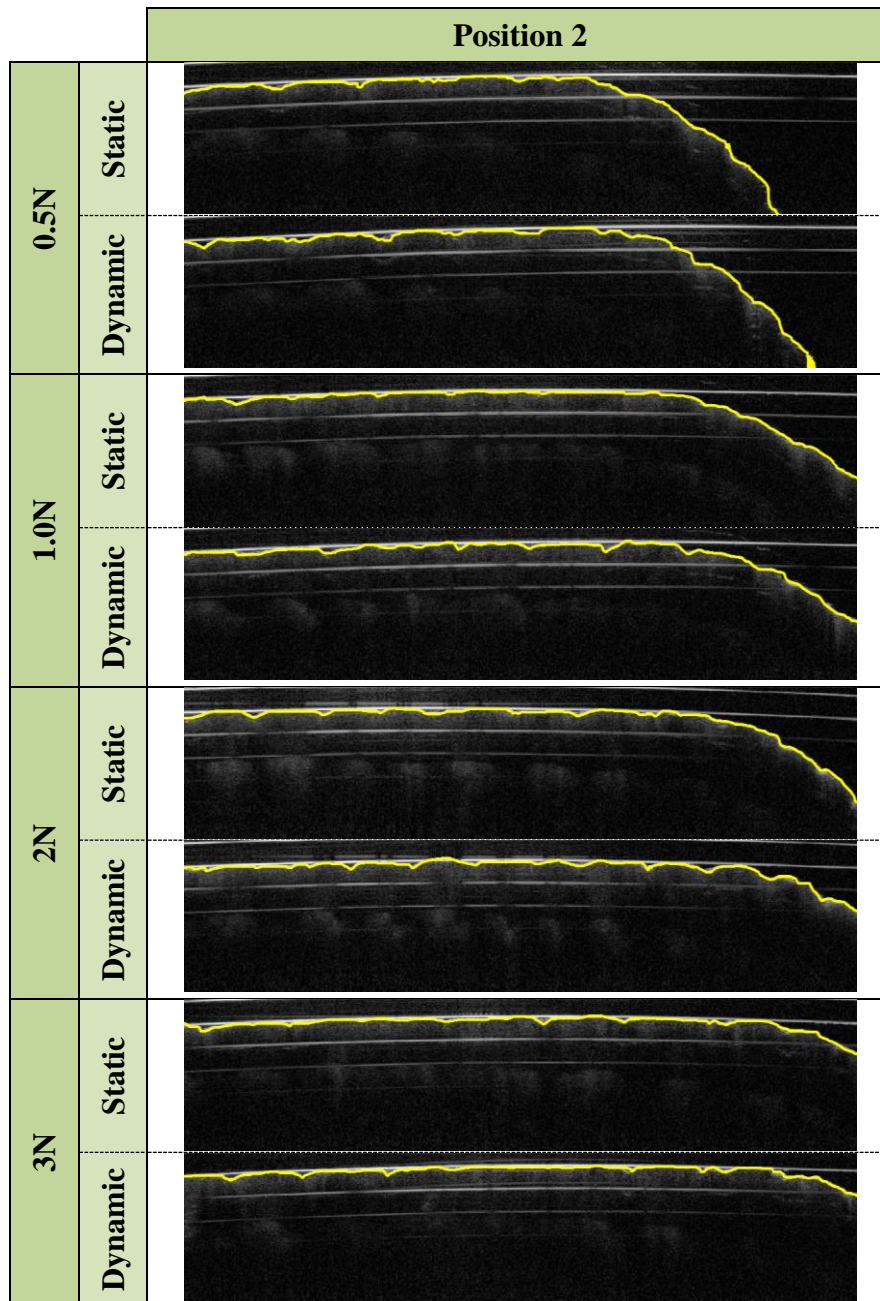


Figure E-4, OCT images of position 2 of the soaked finger pad

Table E-2, The roughness of the position 1 and 2 of soaked finger pad

		Ra [μm]		Rz [μm]	
		Position 1	Position 2	Position 1	Position 2
0.5N	Static	4.29±0.09	8.86±0.90	17.28±0.77	41.48±9.43
	Dynamic	4.07±0.15	10.86±0.38	16.15±0.75	38.60±0.93
1N	Static	4.38±0.07	5.40±0.36	17.87±0.82	16.77±1.48
	Dynamic	4.08±0.14	5.10±0.43	17.26±0.82	18.97±0.70
2N	Static	3.90±0.33	7.74±0.47	17.70±0.78	27.90±0.66
	Dynamic	3.63±0.17	4.96±0.26	17.30±1.75	20.47±0.91
3N	Static	2.36±0.19	3.91±0.29	12.65±1.19	18.73±1.11
	Dynamic	2.59±0.20	3.43±0.34	12.36±1.37	15.02±0.97

Appendix F: Strain line profiles of the silicone hemi-spheres

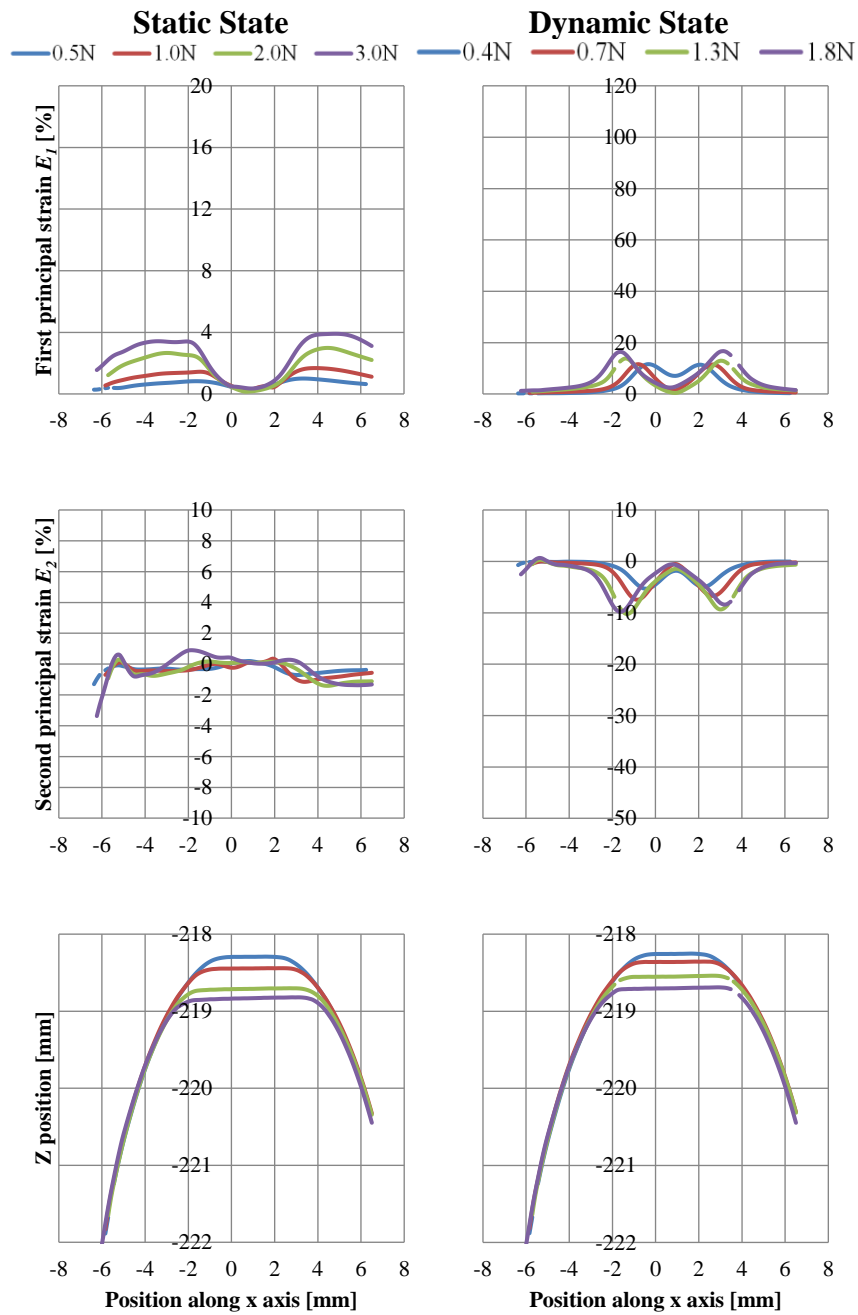


Figure F-1, Strain line profile of silicone hemi-sphere with 0% deadener along x axis

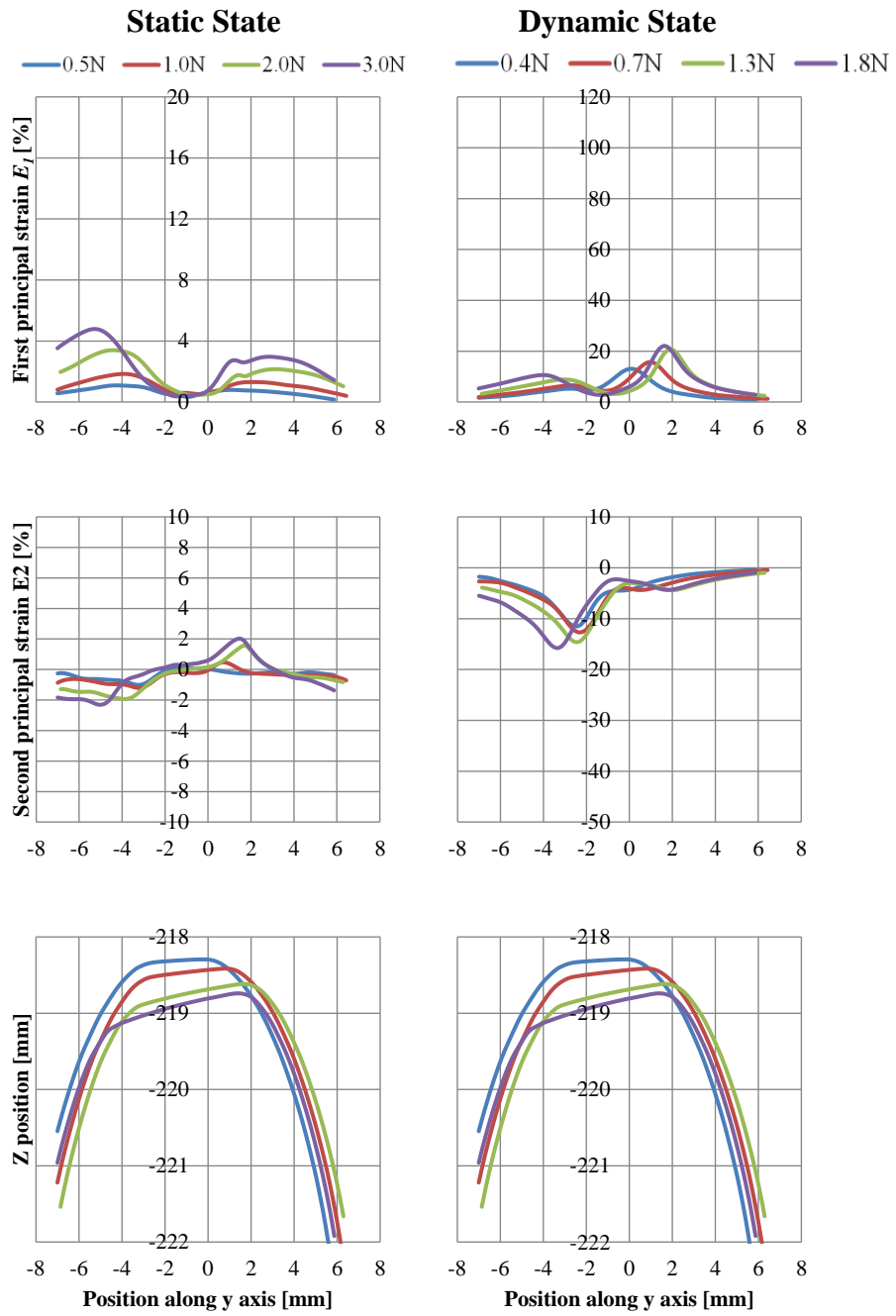


Figure F-2, Strain line profile of silicone hemi-sphere with 0% deadener along y axis

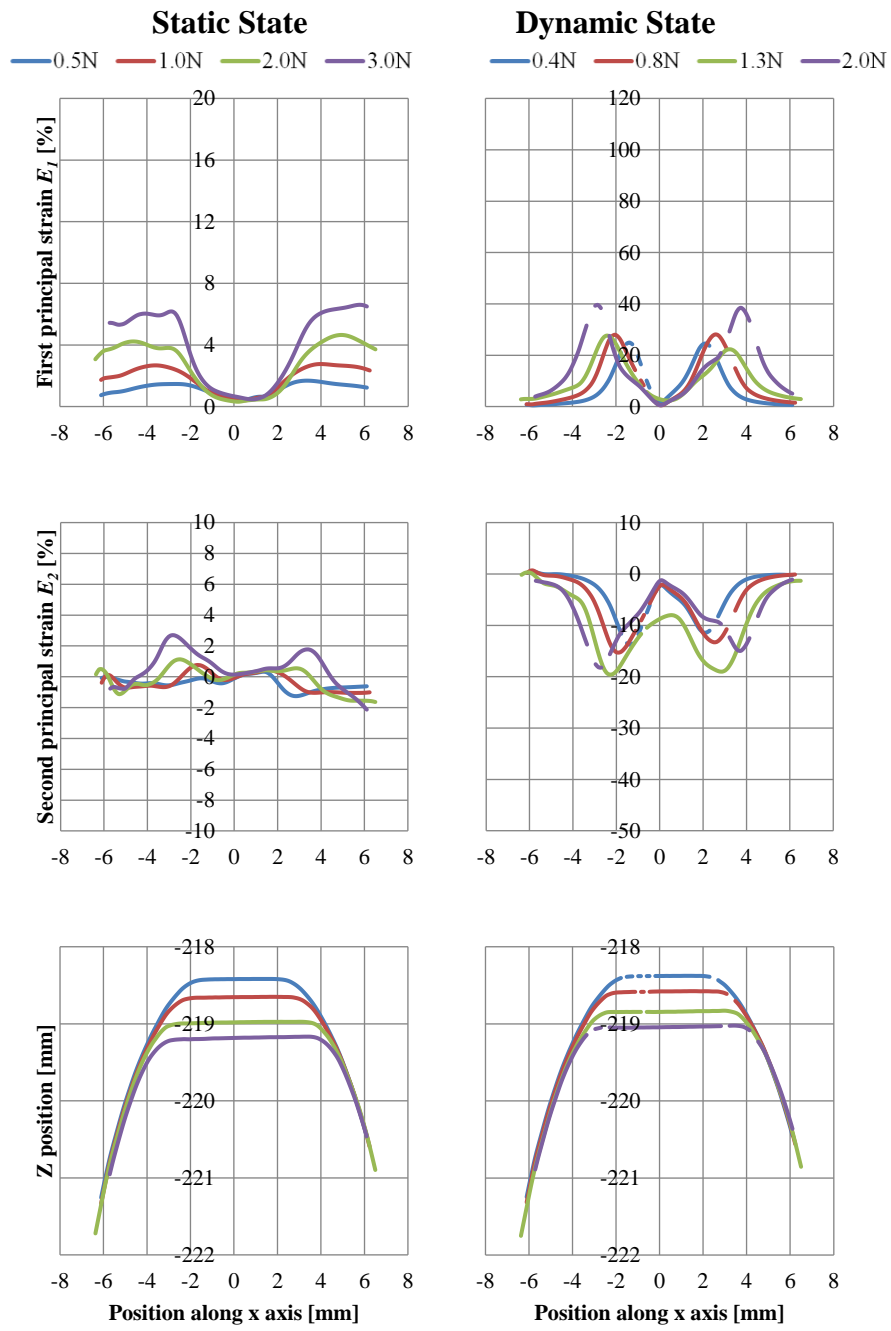


Figure F-3, Strain line profile of silicone hemi-sphere with 10% deadener along x axis

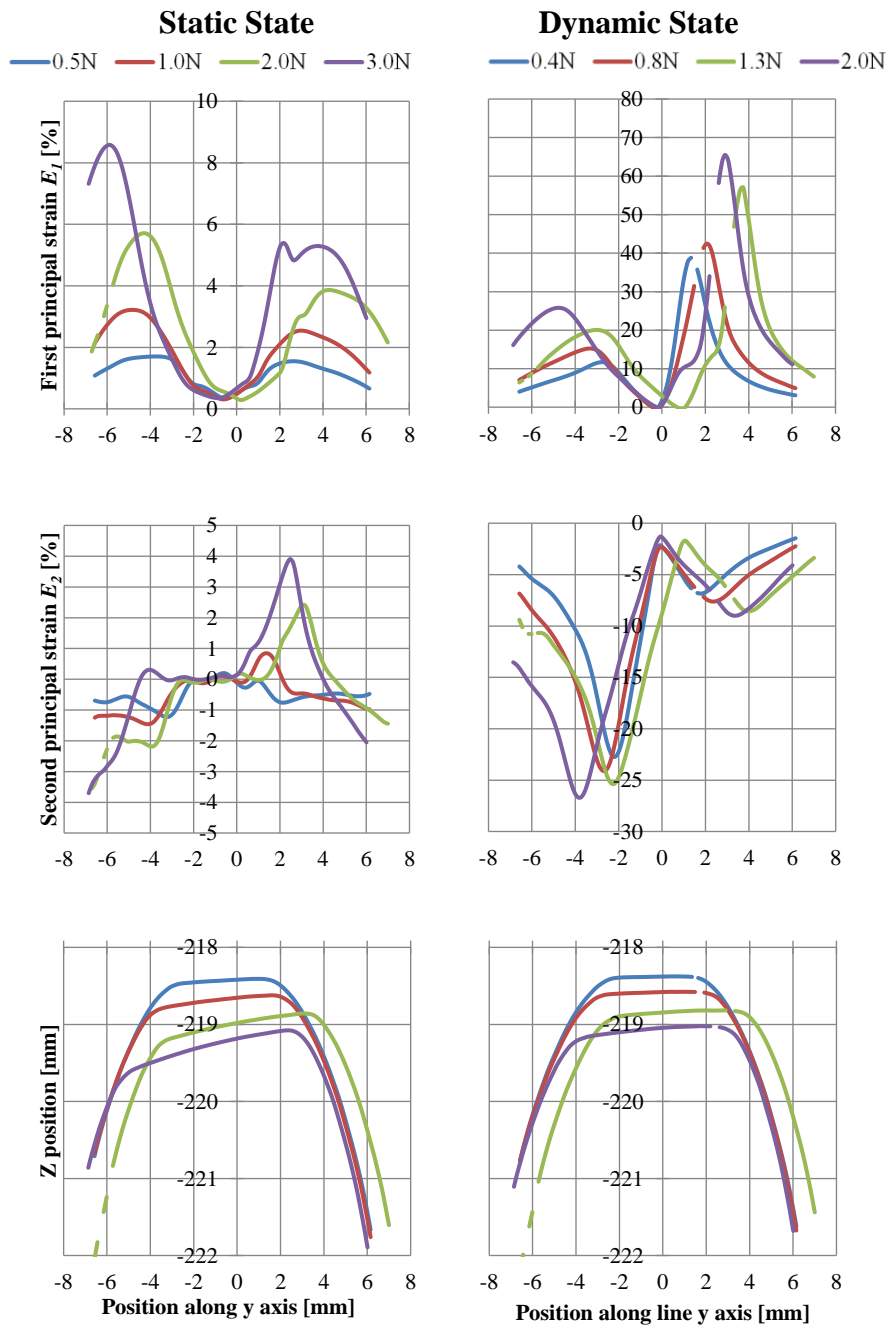


Figure F-4, Strain line profile of silicone hemi-sphere with 10% deadener along y axis

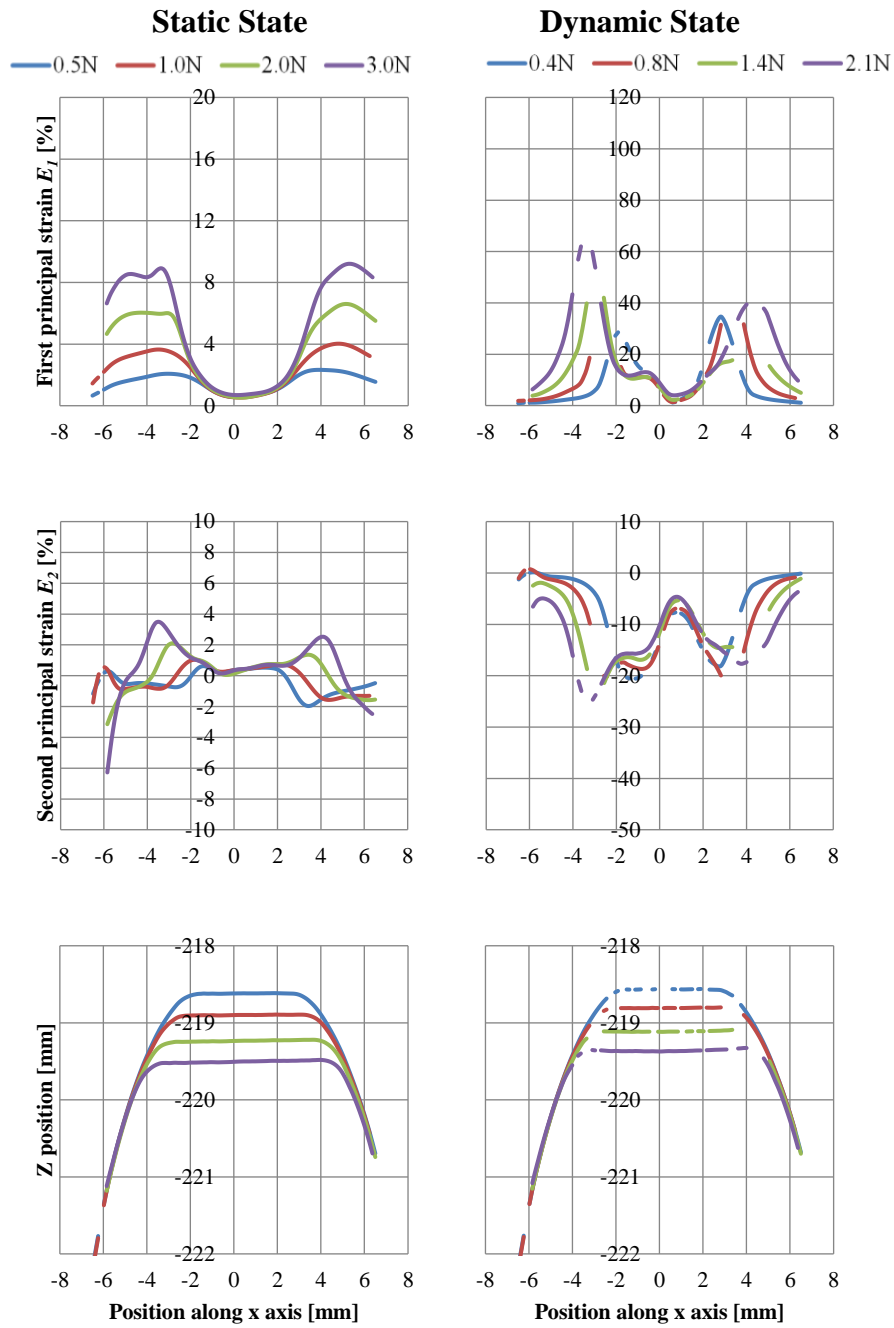


Figure F-5, Strain line profile of silicone hemi-sphere with 15% deadener along x axis

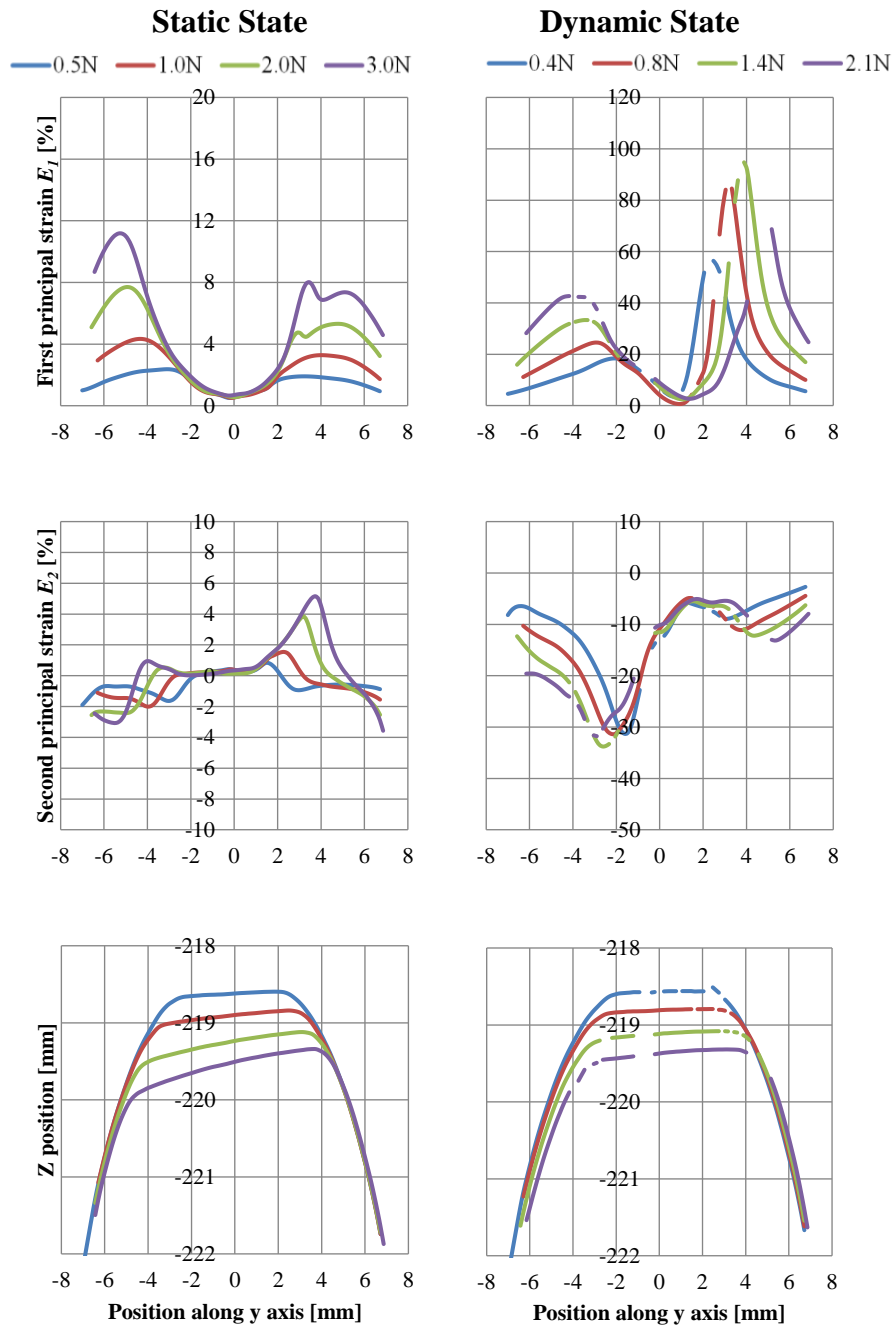


Figure F-6, Strain line profile of silicone hemi-sphere with 15% deadener along y axis

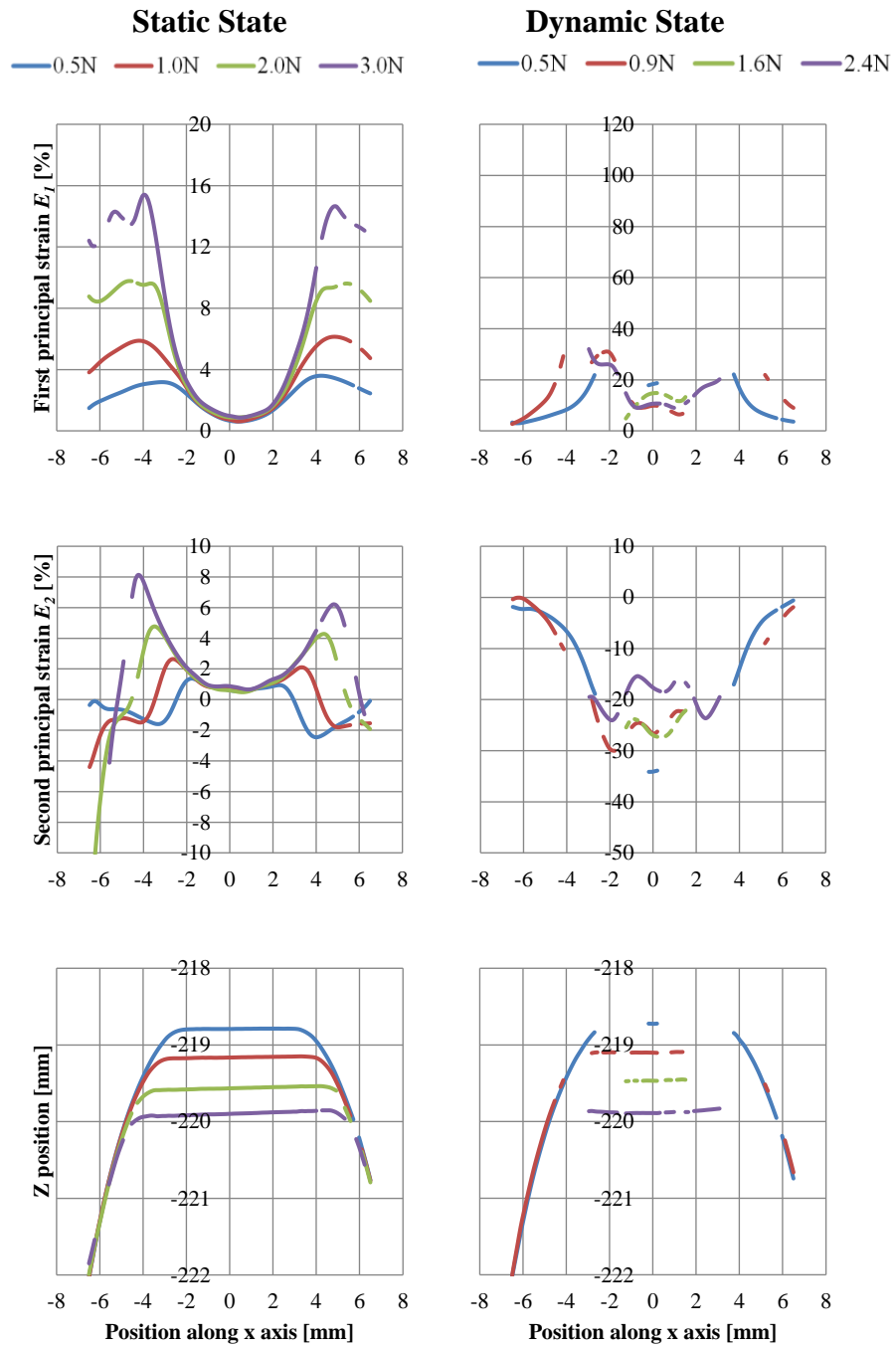


Figure F-7, Strain line profile of silicone hemi-sphere with 20% deadener along x axis

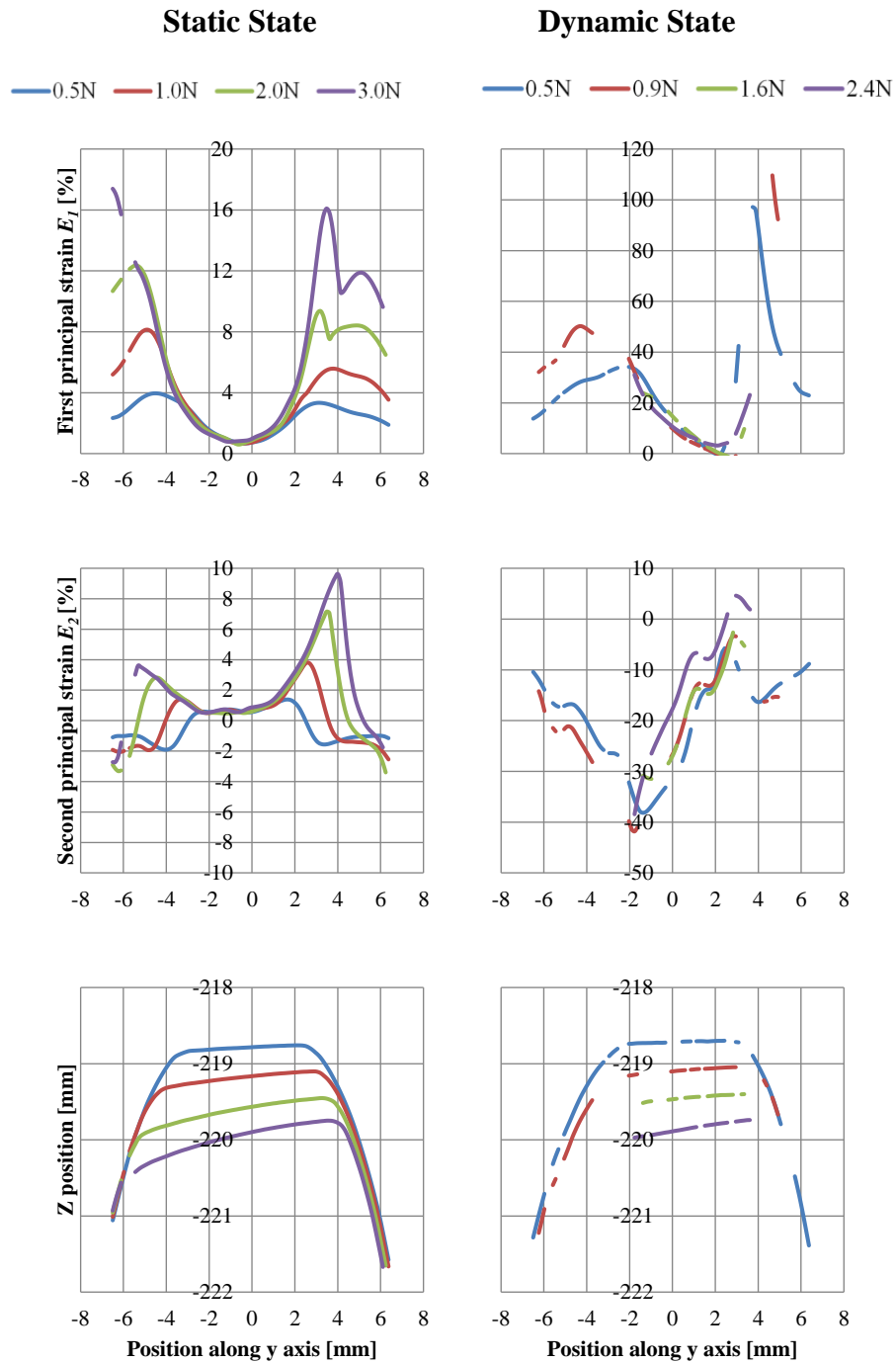


Figure F-8, Strain line profile of silicone hemi-sphere with 20% deadener along y axis

Appendix G: Temporal evolution of the orientation of the porcine aorta tissue fibres

Case 1: 0.5N, 1 pass

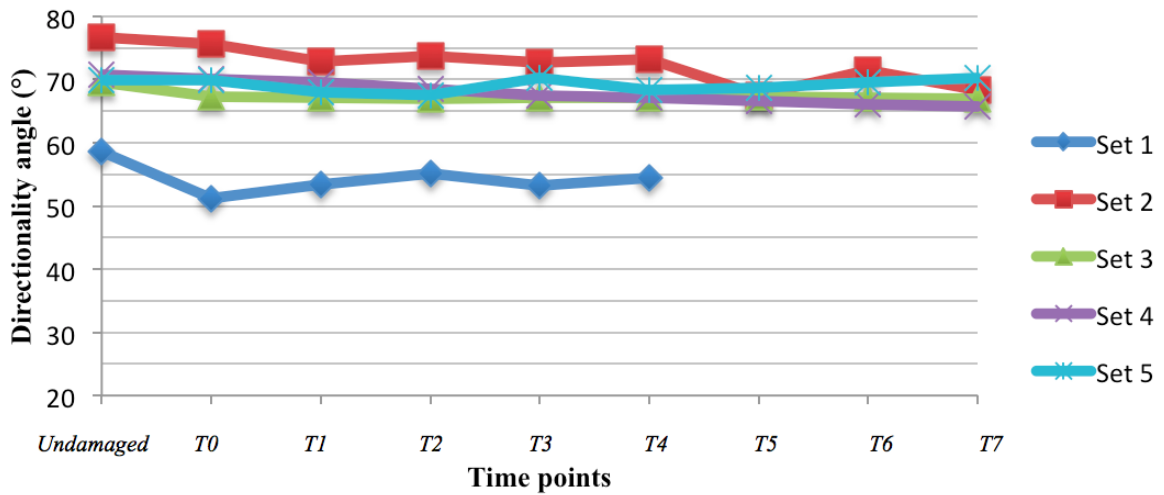


Figure G-1, Comparison of mean directionality angle of 5 sets of experiments for case 1: 0.5N, 1 pass

Case 2: 0.5N, 5 pass

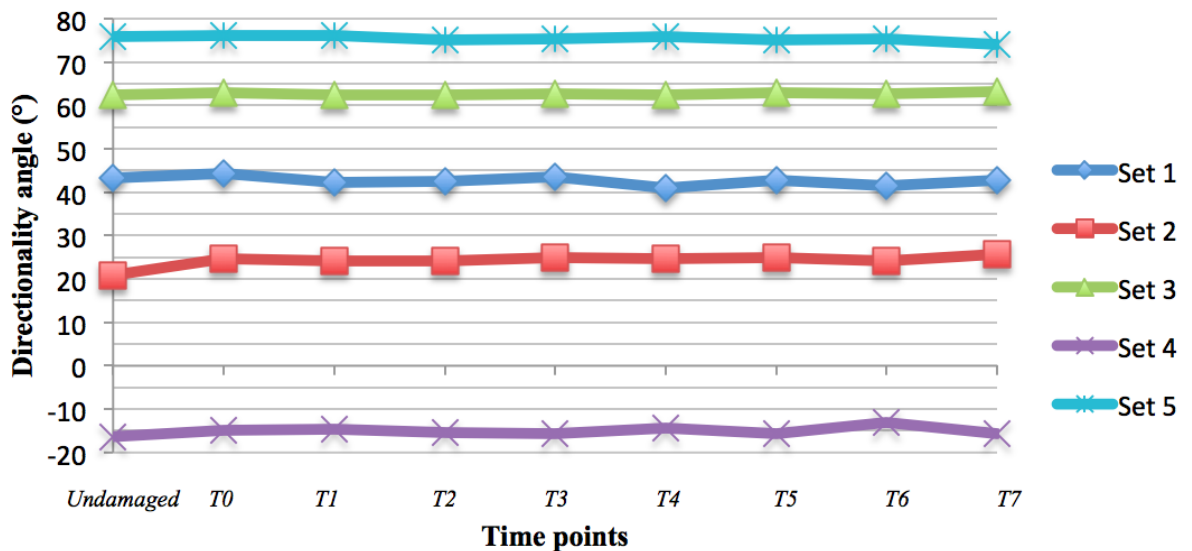


Figure G-2, Comparison of mean directionality angle of 5 sets of experiments for case 2: 0.5N, 5 passes

Case 3: 0.5N, 10 pass

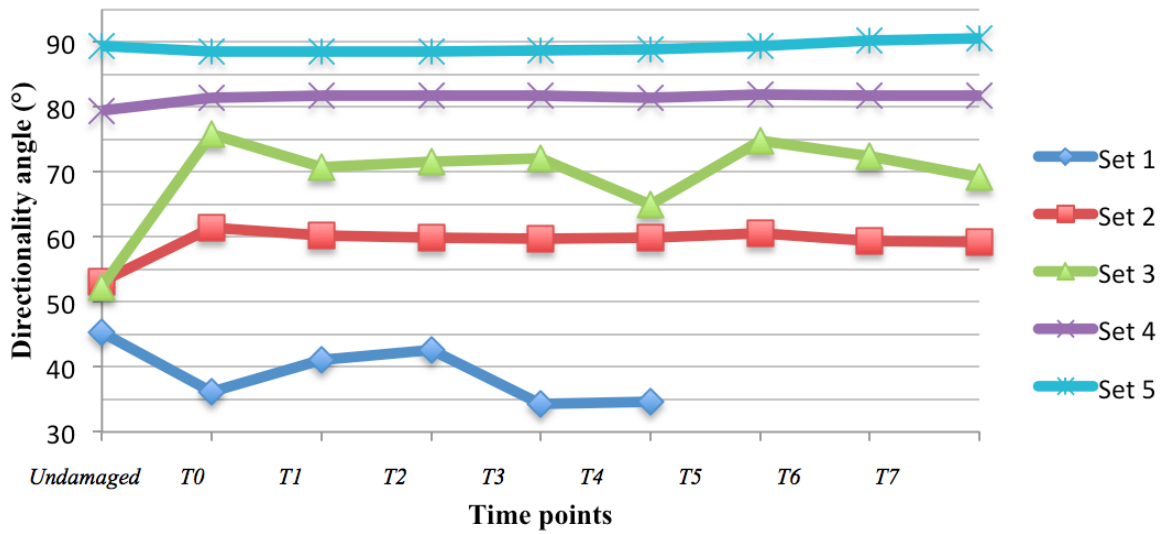


Figure G-3, Comparison of mean directionality angle of 5 sets of experiments for case 3: 0.5N, 10 passes

Case 4: 2N, 1 pass

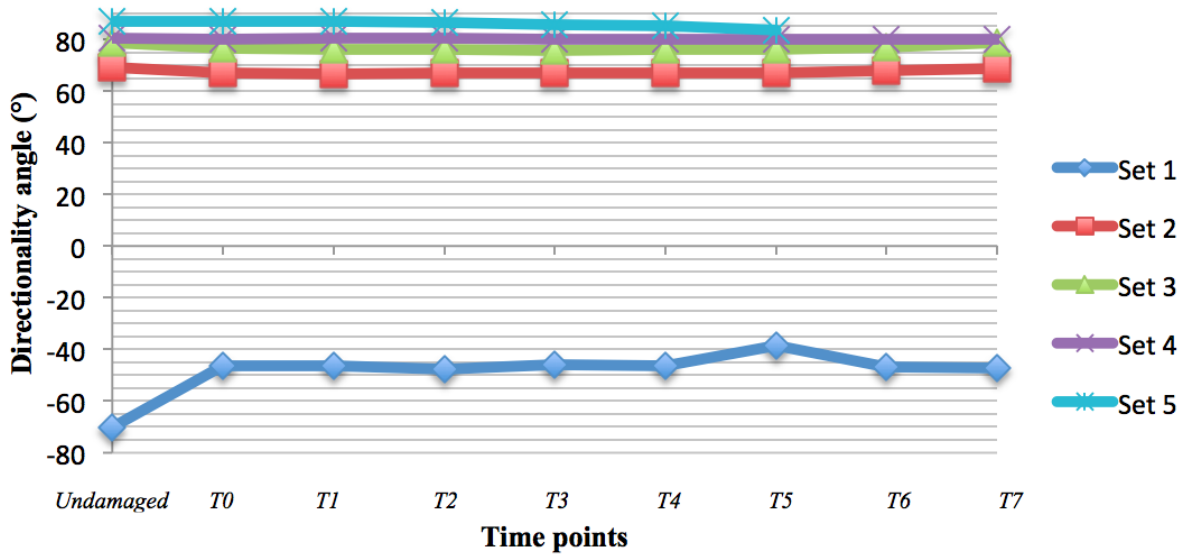


Figure G-4, Comparison of mean directionality angle of 5 sets of experiments for case 4: 2N, 1 pass

Case 5: 2N, 5 pass

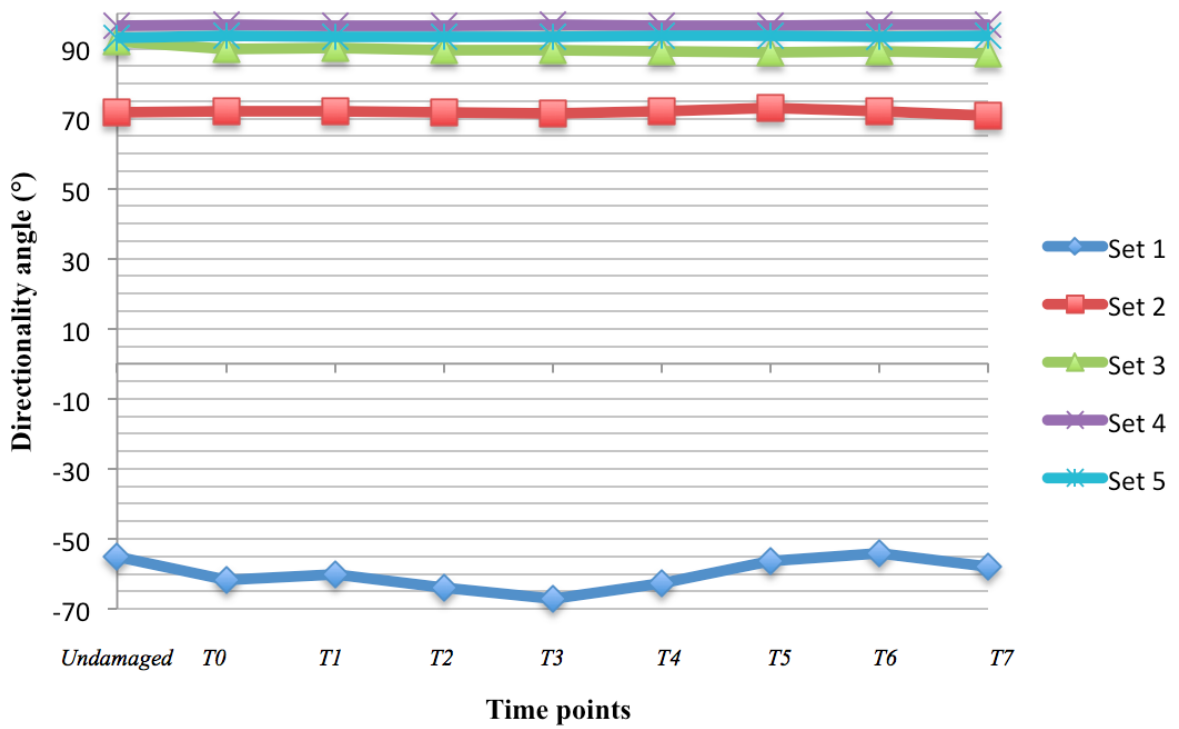


Figure G-5, Comparison of mean directionality angle of 5 sets of experiments for case 5: 2N, 5 passes

Case 6: 2N, 10 pass

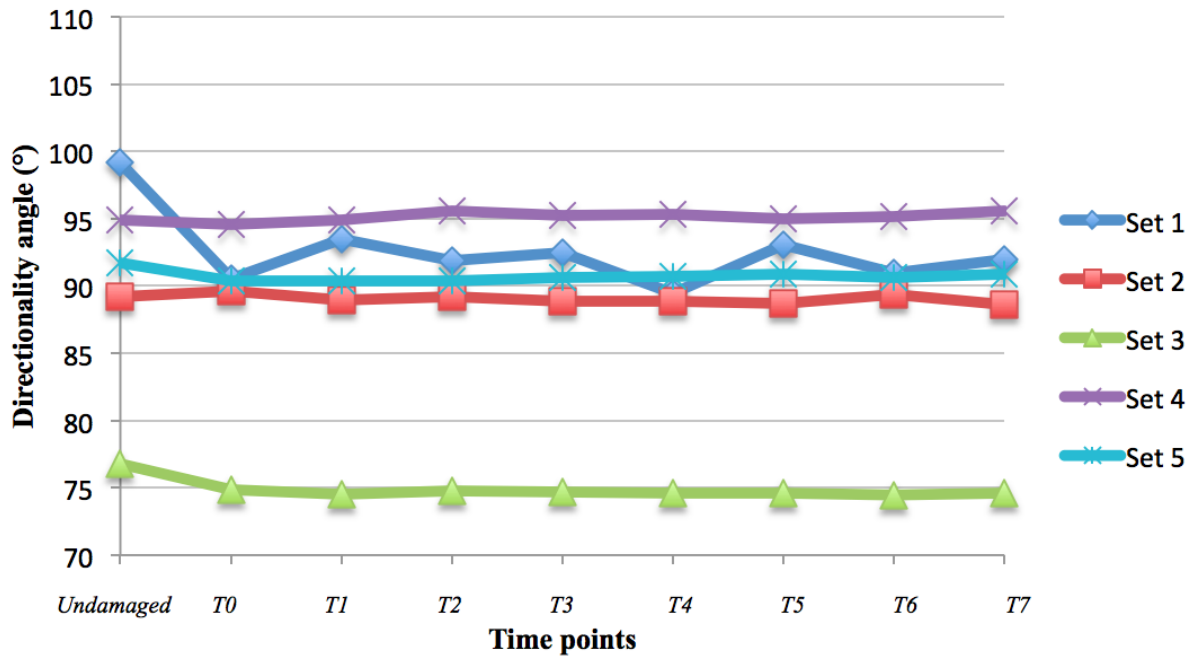


Figure G-6, Comparison of mean directionality angle of 5 sets of experiments for case 6: 2N, 10 passes

Case 7: 5N, 1 pass

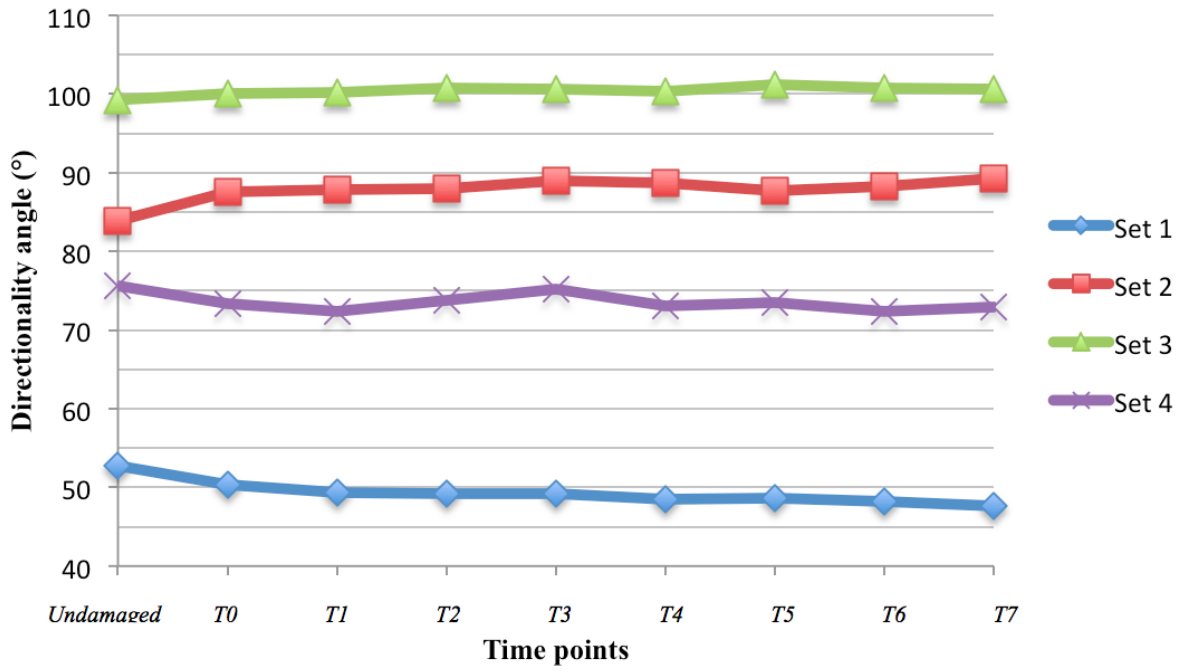


Figure G-7, Comparison of mean directionality angle of 4 sets of experiments for case 7: 5N, 1 pass

Case 8: 5N, 5 pass

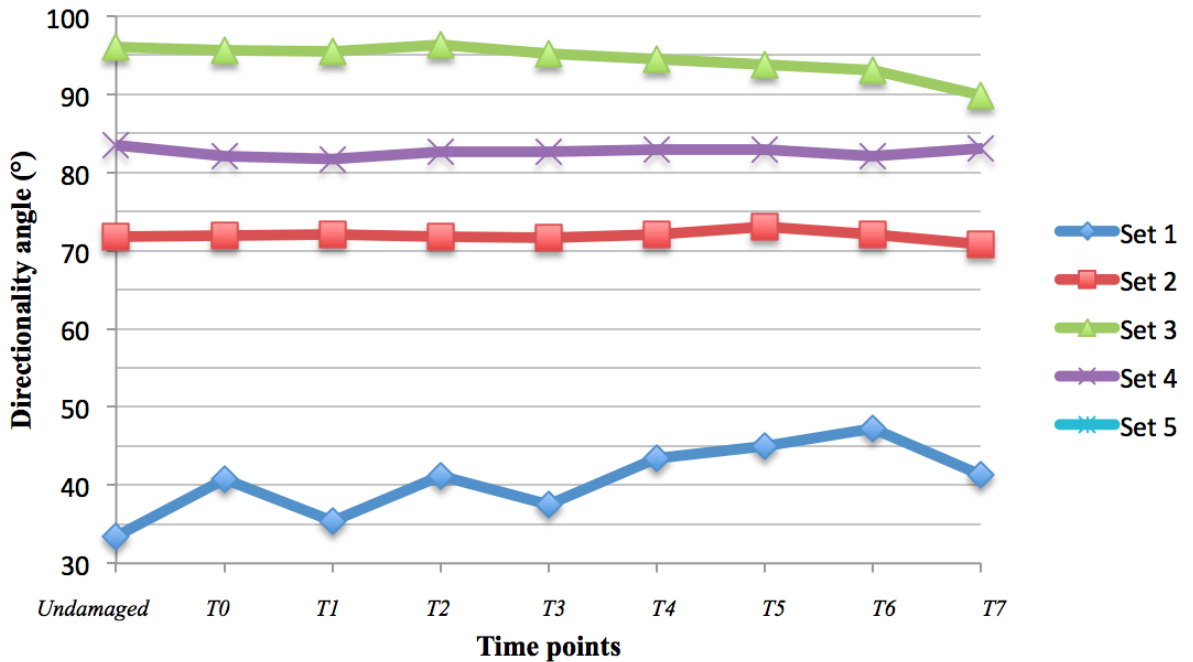


Figure G-8, Comparison of mean directionality angle of 4 sets of experiments for case 8: 5N, 5 passes

Case 9: 5N, 10 pass

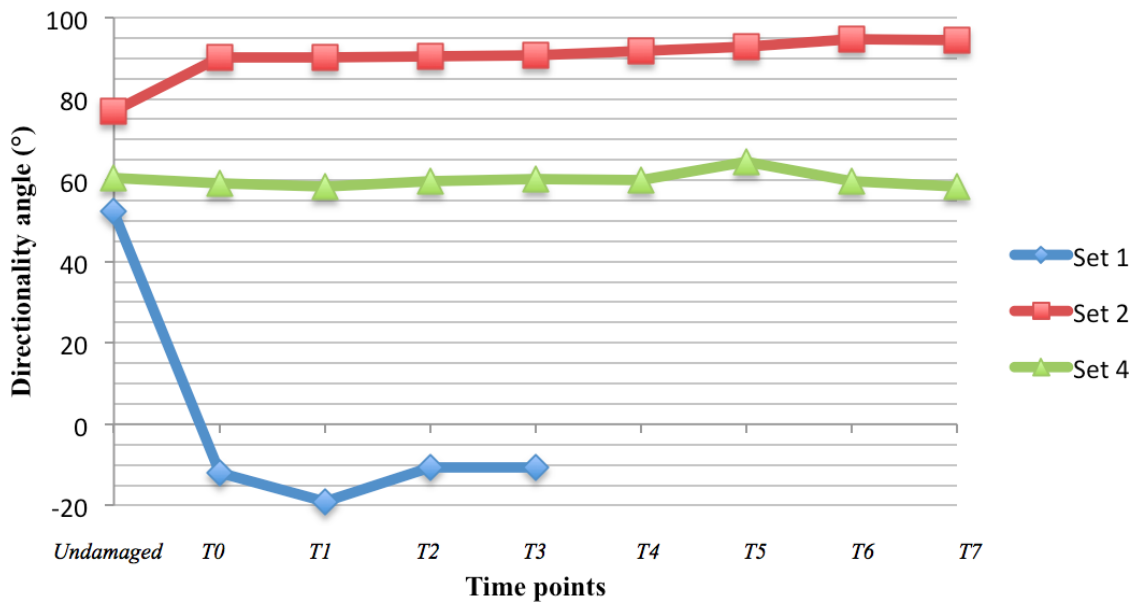


Figure G-9, Comparison of mean directionality angle of 3 sets of experiments for case 9: 5N, 10 passes